

Département de Chimie
Université de Fribourg (Suisse)

Construction of a New Forward
and Backward Scattering Raman
Optical Activity Spectrometer and
Graphical Analysis of Measured
and Calculated Spectra for
(*R*)-[²H₁,²H₂,²H₃]-Neopentane

THÈSE

présentée à la faculté des Sciences de l'Université
de Fribourg (Suisse) pour l'obtention du grade de
Doctor rerum naturalium

JACQUES HAESLER
de Lütschental (BE)

Thèse N° 1509
Imprimerie St-Paul, Fribourg
2006

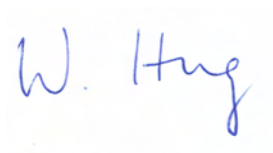
Acceptée par la Faculté des Sciences de l'Université de Fribourg (Suisse)
sur la proposition du jury composé de MM.

Composition du Jury :

Prof. Dr. T. A. Jenny, Université de Fribourg, président du jury,
Prof. Dr. W. Hug, Université de Fribourg, Département de Chimie,
directeur de thèse, rapporteur,
Prof. Dr. A. Weis, Université de Fribourg, Département de Physique,
corapporteur,
Prof. Dr. B. Champagne, Facultés Universitaires Notre-Dame de la Paix,
Laboratoire de Chimie Théorique Appliquée, Namur (Belgique), corapporteur.

Fribourg, le 16 mars 2006.

Le Directeur de thèse



Prof. Dr. Werner Hug

Le Doyen



Prof. Marco Celio

À Marcel,
parti trop tôt.

Table of Contents

| | |
|----------------------------------------------------------|-----------|
| Table of Contents | i |
| Acknowledgments | v |
| Résumé | vii |
| Abstract | ix |
| | |
| I Introduction | 1 |
| | |
| 1 Introduction to Raman Optical Activity | 3 |
| 1.1 Optical Activity and Chirality | 3 |
| 1.2 Chirality in Everyday Life | 6 |
| 1.3 Raman and ROA in Short | 8 |
| 1.3.1 Vibrational Raman Scattering | 8 |
| 1.3.2 Raman Optical Activity (ROA) | 10 |
| 1.3.3 Theoretical Aspects | 11 |
| 1.3.4 Experimental Aspects | 12 |
| 1.3.5 Computational Aspects | 15 |
| 1.4 Scope of Application of ROA | 17 |
| 1.5 Future of ROA | 18 |
| | |
| II Theory | 21 |
| | |
| 2 Vibrational Raman Scattering | 23 |
| 2.1 Introduction | 23 |
| 2.2 Quantum Mechanical Theory | 24 |
| 2.3 Born-Oppenheimer and Placzek Approximation | 25 |
| | |
| 3 Raman Optical Activity Scattering | 29 |
| 3.1 Introduction | 29 |

| | | |
|------------|-------------------------------------------------------|-----------|
| 3.2 | Born-Oppenheimer and Placzek Approximation | 31 |
| 4 | Raman and ROA Intensities | 33 |
| 4.1 | Illumination-Observation Geometry | 33 |
| 4.2 | Raman and ROA Invariants | 35 |
| 4.3 | Scattering Cross Sections | 37 |
| III | Experiment | 41 |
| 5 | Basics of ROA Spectrometers | 43 |
| 5.1 | History | 43 |
| 5.2 | Practical Limitations of ROA Measurements | 44 |
| 5.2.1 | The Exciting Laser Source | 45 |
| 5.2.2 | The Sample | 45 |
| 5.3 | The Three Circular Polarisation Schemes | 46 |
| 5.3.1 | Incident Circular Polarisation (ICP) | 46 |
| 5.3.2 | Scattered Circular Polarisation (SCP) | 47 |
| 5.3.3 | Dual Circular Polarisation (DCP) | 48 |
| 6 | Offset Problems in ROA | 51 |
| 6.1 | Elimination of Deterministic Offsets in ROA | 51 |
| 6.2 | Creating the Virtual Enantiomer | 52 |
| 6.3 | The 2- and 4-phase Offset Correction Scheme | 54 |
| 7 | A Novel SCP ROA Spectrometer | 57 |
| 7.1 | Basis of the Spectrometer | 58 |
| 7.2 | Optical description | 59 |
| 7.2.1 | Spectrograph and CCD Detector | 60 |
| 7.2.2 | Cross-section Transformer Fiber Optics | 62 |
| 7.2.3 | Light Collection | 65 |
| 7.2.4 | Circular Polarisation Analyser | 67 |
| 7.2.5 | Correction Scheme Optics | 68 |
| 7.2.6 | Exciting Laser Light | 69 |
| 7.2.7 | Sample Cell and Temperature Control | 71 |
| 7.3 | Data Acquisition System | 72 |
| 7.3.1 | Basic Acquisition Cycle | 74 |
| 7.3.2 | Timing Units and 8-cycles | 75 |
| 7.3.3 | Complete Acquisition Cycle | 76 |
| 7.3.4 | CCD Readout and Binning | 77 |
| 7.3.5 | The 16 Buffers | 79 |

| | | |
|-----------|------------------------------------------------------|------------|
| 8 | Instrumental Performances | 81 |
| 8.1 | Backscattering SCP Spectra | 81 |
| 8.1.1 | Degree of Circularity | 82 |
| 8.1.2 | Raman Optical Activity | 86 |
| 8.2 | Forward Scattering SCP Spectra | 96 |
| 8.2.1 | Degree of Circularity | 96 |
| 8.2.2 | Raman Optical Activity | 96 |
| | | |
| IV | Computation | 119 |
| | | |
| 9 | Computational Approach | 121 |
| 9.1 | Raman Optical Activity | 121 |
| 9.1.1 | Harmonic Force Field | 122 |
| 9.1.2 | Gradient of Electronic Tensors | 123 |
| | | |
| 10 | VOAView: a Graphical User Interface | 125 |
| 10.1 | Installing and Launching VOAView | 126 |
| 10.2 | Main Features of VOAView | 127 |
| 10.2.1 | Input File | 128 |
| 10.2.2 | Vibrational Analysis | 129 |
| 10.2.3 | Molecular Structure | 129 |
| 10.2.4 | Vibrational Normal Modes | 130 |
| 10.2.5 | Scattering Cross Sections | 133 |
| 10.2.6 | Group Coupling Matrices (GCM) | 134 |
| 10.2.7 | Atomic Contribution Patterns (ACP) | 135 |
| 10.2.8 | Further Options | 138 |
| 10.2.9 | Output File | 140 |
| 10.3 | Main Features of VOAPlot | 140 |
| 10.4 | Simulating a Voigt Profile | 141 |
| 10.5 | IR and VCD | 149 |
| 10.5.1 | Expressions for VOAView | 149 |
| 10.5.2 | Expressions for VOAPlot | 150 |
| | | |
| V | Applications | 151 |
| | | |
| 11 | Neopentane and Neopentane-d_{12} | 153 |
| 11.1 | Geometry and Conformation | 154 |
| 11.2 | Vibrational Frequencies | 155 |
| 11.3 | Raman Spectra | 162 |
| 11.3.1 | Assignment for Neopentane | 162 |

| | | |
|-----------|----------------------------------------------------------------------------------------------------------------|------------|
| 11.3.2 | Assignment for Neopentane- d_{12} . | 168 |
| 12 | (<i>R</i>)-[$^2\text{H}_1$, $^2\text{H}_2$, $^2\text{H}_3$]-Neopentane | 177 |
| 12.1 | Publication in <i>Int. J. Quantum Chem.</i> | 177 |
| 12.2 | Geometry and Conformations of (<i>R</i>)-[$^2\text{H}_1$, $^2\text{H}_2$, $^2\text{H}_3$]-neopentane | 199 |
| 12.3 | Vibrational frequencies | 200 |
| 12.4 | Simulation of Raman and ROA Spectra | 200 |
| VI | Appendices | 211 |
| A | ROA Spectrometer | 213 |
| B | Additional Spectra | 217 |
| C | VOAView | 223 |
| D | Computations | 231 |
| E | DALTON vs. Gaussian03 | 235 |
| | Conclusion and Outlook | 237 |
| | References | 239 |
| | List of Abbreviations | 250 |
| | Curriculum Vitae | 251 |

Remerciements

Je tiens tout d'abord à remercier mon directeur de thèse, le professeur Werner Hug, de l'Université de Fribourg (Suisse). Sa passion et son dévouement sans égal pour la spectroscopie d'activité optique vibrationnelle Raman (ROA) m'ont été transmis avec conviction, et je lui en suis particulièrement reconnaissant.

Je remercie le professeur Benoît Champagne des Facultés Universitaires Notre-Dame de la Paix de Namur (Belgique) ainsi que le professeur Antoine Weis de l'Université de Fribourg pour avoir accepté et accompli leur rôle de corapporteur. Je remercie également le Prof. Titus A. Jenny pour avoir présidé le jury ainsi que le Prof. Thomas Bally pour ses corrections linguistiques.

Je tiens à remercier tout particulièrement Markus Racheter et Olivier Graber, pour leur participation active à la réalisation de notre spectromètre, mais également pour les bons moments passés ensemble. Un grand merci à Alphonse Crottet et Oswald Raetzo des différents ateliers mécaniques.

L'accomplissement de cette thèse dois beaucoup à mon prédécesseur, le docteur Gérard Zuber, que je remercie du fond du cœur pour sa disponibilité ainsi que pour tous ces conseils. Je remercie le professeur Benoît Champagne, le docteur Olivier Quinet et Vincent Liégeois pour notre étroite collaboration et pour les bons moments partagés.

Je remercie chaleureusement Marion Heckenroth, László Mercs, Aurélie Poulain et Claudio Gandolfi, l'équipe du café du matin, Oliver Graber, Verena

Schwalm, Anne Schuwey et Freddy Nydegger, ainsi que les différents adeptes de la course à pied de notre département.

Mes remerciements s'adressent également aux différentes personnes ayant contribué de près ou de loin à la réalisation de cette thèse: Prof. Christian Bochet, Dr. Emmanuel Riguet, Ivan Schindelholz, Dmytro Dudenko, Maxim Fedorovsky, Elena Hasanova, Dr. Christine Deillon, Dr. Svetlana Živanov, Dr. Krzysztof Piech, Dr. Pavel Bednarek, Olivier Aebischer, Rafaël Nussbaum, Pio Bättig, Joël Kühni, Frederic Birbaum, Claire-Lise Ciana, Emerith Brügger, Hubert Favre, Xavier Hanselmann, Lucienne Rouiller, Noël Chassot, Michel Piccand, Inge Müller ainsi que tous ceux que j'aurais omis de citer.

Une pensée toute particulière est réservée à mon amie Valérie, pour m'avoir supporté et accompagné durant ces 4 ans. Ma maman ainsi que son ami Jean, mon frère Cédric, sa femme Florence et leurs enfants Hugo et Mathieu, toute ma famille ainsi que tous mes proches sont également chaleureusement remerciés.

Finalement, je tiens à remercier le Fond National Suisse de la Recherche Scientifique ainsi que le Canton de Fribourg pour leur financement.

Résumé

La construction d'un instrument unique au monde pour la détermination de la configuration absolue de composés chiraux, par spectroscopie d'activité optique vibrationnelle Raman (AOVR), constitue la majeure partie du travail réalisé durant cette thèse. Le développement d'un programme informatique muni d'une interface graphique, ainsi que son utilisation dans l'analyse comparative de résultats expérimentaux et computationnels, présentent les capacités de cette méthode encore trop peu connue.

Le Professeur Hug possède un spectromètre d'AOVR, issu de son propre développement, situé à l'Université de Zürich. Cet appareil fait office de référence dans le domaine de l'AOVR et est utilisé de nos jours pour des mesures de routine. Dans le but de continuer le développement de la méthode et profitant des technologies existantes, un nouveau spectromètre d'AOVR a été construit dans nos laboratoires de Fribourg durant cette thèse. La géométrie de mesure standard a dans un premier temps été reprise, elle correspond à une mesure en diffusion retour avec analyse du contenu de polarisation circulaire de la lumière diffusée ($SCP(\pi)$). Cette géométrie de mesure a ensuite été complétée par la première implémentation d'un arrangement en diffusion avant $SCP(0)$. La mise en place de cette extension a été réalisée sur le même appareil que précédemment cité, ce qui fait de lui le seul instrument au monde capable d'effectuer des mesures d'AOVR selon ces deux arrangements. Des mesures de composés d'importance biologique comme la vitamine C et la L-alanine ont été effectuées pour la première fois en diffusion avant.

Les spectres ROA correspondant sont d'ailleurs de haute qualité. La diffusion avant semble également posséder de réels avantages, comme une simplification générale des spectres ainsi qu'une sensibilité moindre face aux influences de solvants. Il est dès lors évident que la mise en place de cette nouvelle méthode de mesure profite à la toute la communauté scientifique active dans le domaine de l'AOVR.

Les conditions de mesures ont été étendues par rapport à l'instrument de référence grâce au développement d'un porte-cellule à température contrôlée. Toutes nos cellules y sont acceptées, notamment celles à base de micro-capillaires. Ces avancées techniques ont permis d'effectuer les premières mesures de composés gazeux à température ambiante. Il s'agit de mesures réalisées à 0°C du 2,2-diméthylpropane (néopentane) et de son homologue deutéré.

Un isotopomère intéressant de ces deux molécules, le (*R*)-[²H₁,²H₂,²H₃]-néopentane, chiral par substitution isotopique, a fait l'objet d'une analyse théorique de la mesurabilité de son activité optique vibrationnelle. Cette molécule de symétrie T_d est considérée comme un archétype, car ne devant son activité optique qu'à une distribution chirale des masses de ses noyaux, alors que son environnement électronique est purement achiral. Une nouvelle méthode de simulation des spectres d'AOVR développée durant cette thèse, par l'approximation de fonctions de Voigt à l'aide de simples gaussiennes, qui tient compte des largeurs différentes des bandes isotropes et anisotropes, laissent supposer que notre spectromètre constitue le seul instrument au monde capable de déterminer la configuration absolue du (*R*)-[²H₁,²H₂,²H₃]-néopentane, et ce en dépit des effets d'annulation et de compensation dues à la présence de 9 rotamères. Sa synthèse est en cours et nous espérons pouvoir confirmer nos simulations dans un avenir proche.

Abstract

The construction of a unique instrument for the determination of the absolute configuration of chiral compounds, by means of Raman optical activity (ROA) spectroscopy, represents the main achievement of this thesis. The development of a program with a graphical interface, which incorporates previously but also newly developed graphical tools, as well as its application in comparative studies of experimental and computed data, illustrates the power of ROA in general.

Professor Hug had developed an ROA spectrometer at the University of Zürich. This instrument is still considered as a reference in the ROA community and is used nowadays for routine measurements. In order to continue its development, and taking advantage of the existing technologies, a new ROA spectrometer has been constructed in Fribourg during this thesis. First, the standard geometry of measurement was chosen, which corresponds to scattered circular polarisation recorded in backscattering ($\text{SCP}(\pi)$). Secondly, this geometry was extended for the first time by a forward scattering scheme ($\text{SCP}(0)$). This extension was realised on the same instrument, which is now the only ROA spectrometer in the world on which both kinds of measurements are possible. In particular, the forward scattering mode was used for the first time to record high quality ROA spectra of biologically relevant compounds. Forward scattering seems to feature interesting advantages, such as a general simplification of the spectra and a reduced sensitivity to the influence of solvent molecules. The ROA community will certainly benefit from that first implementation of

SCP(0).

Furthermore, the range of measuring conditions has been extended thanks to the development of a temperature regulated sample holder, which accepts all our measurement cells, in particular those based on disposable capillaries. These technical advances made it possible to measure for the first time 2,2-dimethylpropane (neopentane) and its deuterated homologue at 0°C, both of which are gases at room temperature.

An interesting isotopomer of these latter compounds, chiral by isotopic substitution, is (*R*)-[²H₁,²H₂,²H₃]-neopentane. A complete analysis of the vibrational optical activity measurability of this compound has been achieved. Within T_d symmetry, this molecule is considered as a chiral archetype, as its chirality arises solely by the mass distribution of its nuclei, while its electron distribution is completely achiral. The careful simulation of its ROA spectra, by the use of approximated line shapes of the Voigt type, and by taking into account the different bandwidths of isotropic and anisotropic bands, showed that our spectrometer should be the only apparatus in the world capable to determine the absolute configuration of (*R*)-[²H₁,²H₂,²H₃]-neopentane, despite extensive cancellation and compensation effects due to the presence of 9 rotamers. The synthesis of this compound is in progress and we hope to confirm our simulations in a near future.

Part I

Introduction

Chapter 1

Introduction to Raman Optical Activity

Raman optical activity (ROA), as its name tells us, deals with substances that do interact differently with right and left circularly polarised light, a behaviour called *optical activity*. ROA spectroscopy is a well suited method for the determination of the three-dimensional structure of optically active, i.e. *chiral* compounds.

1.1 Optical Activity and Chirality

The term *chiral* is derived from the Greek word *kheir* meaning "hand" and apparently was coined by Lord Kelvin in 1884 [1], in his Baltimore lectures on "Molecular Dynamics" and the "Wave Theory of Light", in which he stated: "*I call any geometrical figure, or group of points, chiral, and say it has chirality, if its image in a plane mirror, ideally realised, cannot be brought to coincide with itself*". In group theory, chirality is defined in a geometrical way: "*Molecules with no improper axis of rotation are said to be chiral*".

The first observation of the differing interaction with right and left cir-

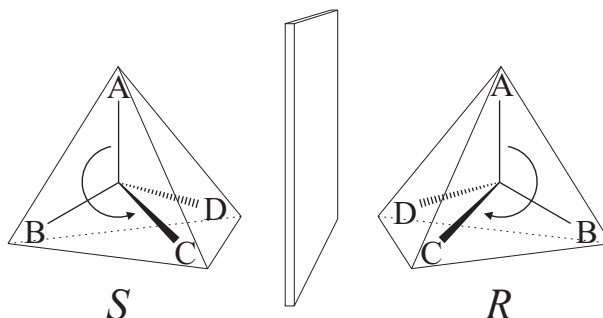
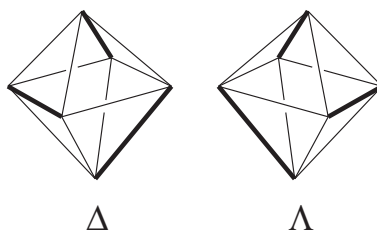


Figure 1.1: Cahn, Ingold and Prelog R/S sequence rules. Priority from A to D

cularly polarised light goes back to the beginning of the 19th century, when Arago [2] described the faculty of crystalline quartz to rotate the plane of polarisation of linearly polarised light, as do also certain organic liquids described in a paper of Biot [3]. This rotation is due to a differing index of refraction for right and left circularly polarised light¹.

In chemistry, the most common type of "chirality" is observed when a carbon atom has four different groups attached to it. This carbon atom is then described as an *asymmetric*, chiral, or stereogenic centre. The concept of "asymmetry" was developed by J. H. van't Hoff [5] and J. A. Le Bel [6] in 1874, following the resolution by Louis Pasteur of a mixture of tartaric acid salt isomers during the period 1848-1853, in which he picked out the differing crystal types by hand, doing so on the basis of the differing physical appearance of the salt crystals. Pasteur recognised that the two types of crystals rotated plane polarised light differently (one to the left and the other to the right) and that it must be due to an asymmetric grouping of atoms in the optically active molecules, a result he described in lectures for the *Société Chimique de Paris* (1860). Following Kekule's recognition in 1858 that carbon has a valence of

¹Linearly polarised light is composed of an equal amount of right and left circular light [4].

Figure 1.2: Δ/Λ nomenclature in $\text{Ru}(\text{bipy})_3$

four [7], van't Hoff and Le Bel independently recognised that, when four different groups are attached to a carbon atom and are arranged at the corners of a tetrahedron (Fig. 1.1), then the arrangement can be in the form of two different non-superimposable mirror images, as are your left and right hand, and therefore the two molecules are chiral. Such pairs of molecules are called *enantiomers*.

It is also possible for a molecule to be chiral without any tetrahedral chiral centres. Examples include 1,1'-bi-2-naphthol (BINOL) and 1,3-dichloro-allene which have axial chirality (but no improper axis of rotation), and the famous $[\text{Ru}(\text{2,2'}\text{-bipyridine})_3]^{2+}$ complex, with its three bipyridine units located on the edges of an octahedron (Fig. 1.2), which belongs to the highly symmetric D_3 point group.

In the early days, chemists often assigned trivial names to differentiate these isomers, and enantiomers generally were specified by *d*- (dextrorotary, from the Greek *dextro*: right) and *l*- (levorotary, from the Greek *leavo*: left) based on which direction the molecule rotates plane polarised light. Cahn, Ingold and Prelog [8] then devised a system (Fig. 1.1), assigning sequence rules based on decreasing atomic number (and rates of substitution for atoms of the same atomic number) for projection formulae, that allows the absolute assignments of configurations. They proposed the terms *R* (for the Latin *rectus*: right) and

S (for the Latin *sinister*: left).

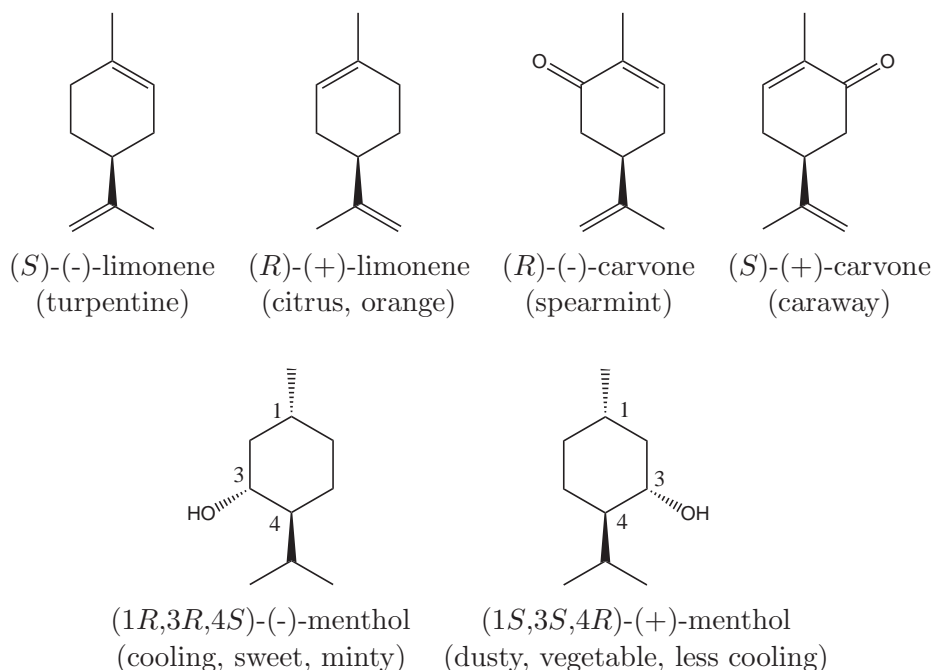
1.2 Chirality in Everyday Life

Determination of the absolute configuration of chiral molecules can be of critical importance in chemistry and biochemistry. Life and chirality are strictly connected. It is generally recognised that enantiomers may have different effects when interacting with living beings. Many biologically active molecules are chiral, including the naturally occurring amino acids and vitamins. Interestingly, on earth, these compounds are mostly homochiral, that is all have the same absolute configuration. The origin of homochirality in the biological world is the subject of vigorous debate, but is a sign that chirality plays an important role in everyday life. Many coordination compounds are also chiral, for example the above $[\text{Ru}(\text{2,2'}\text{-bipyridine})_3]^{2+}$ complex, in which the bipyridine ligands adopt a propeller-like arrangement. Many active compounds from the pharmaceutical industry are chiral, and their physiological and pharmacological activity is often related to the chirality of the receptors they are interacting with. Enzymes, which are themselves always chiral, often distinguish between the two enantiomers of a chiral substrate.

Other biological processes may be triggered by only one of the two possible enantiomers of a chiral molecule, often being unresponsive to the other enantiomer. Many chiral drugs must be made with high enantiomeric purity due to toxic activity of the "wrong" enantiomer. An example is thalidomide, which is *racemic*, that is, it contains both left and right handed isomers in equal amounts. One enantiomer is effective against morning sickness (*R*-thalidomide), whereas the other is teratogenic (*S*-thalidomide). It should be

noted that the enantiomers are converted into each other *in vivo*. That is, if a human is given one enantiomer of thalidomide, both isomers can be found in the serum. Hence, administering only one enantiomer will not prevent the teratogenic effect in humans in this particular case.

It has been recognised by chemists in the flavour & fragrance industry since the beginning of the 20th century that certain enantiomeric chemicals, such as menthol and carvone, had different organoleptic properties. In fact, by the 1960's, a number of processes had been developed for the synthesis of the desired (-)-menthol, with its strong cooling effect, from optically active terpenoids, and both (-)-carvone and (+)-carvone were being manufactured from (+)- and (-)-limonene, respectively.



One must make a clear distinction between conformation and configuration when discussing chirality in a molecular context. Conformations are temporary positions of atoms in a molecule, as a result of bond rotation, bending, or stretching while no bonds are broken. Configurations are structures of a

molecule which are assumed not to be interconvertible under ambient conditions. Enantiomers, and other optically active isomers such as diastereoisomers, are examples of configurational isomers.

1.3 Raman and ROA in Short

A short introduction to spontaneous vibrational Raman and Raman optical activity is given here. The reader is asked to read Part II and III, for more detailed theoretical and experimental considerations, respectively.

1.3.1 Vibrational Raman Scattering

When monochromatic radiation of frequency ν_0 is incident on a non-absorbing sample molecule (gases or liquids in our case), most of it is transmitted without any change but, in addition, some scattering of the radiation occurs. We consider that the molecule in its initial vibrational state has an energy $E_i = h\nu_i$. The interaction of the radiation with this molecule leads to annihilation of one incident photon of energy $h\nu_0$, creation of a new photon of energy $h\nu_S$, and the transition of the molecule between the different $3N - 6$ ($3N - 5$ for linear molecules) vibrational levels with energy E_i and E_f , the initial and final states, respectively (Fig. 1.3). In the overall process, energy must be conserved and the vibrational transition energy is defined as

$$\begin{aligned} E_{fi} &= E_f - E_i \\ &= h\nu_{fi} = h(\nu_0 - \nu_S) \end{aligned} \quad (1.1)$$

As E_f can be greater or less than E_i , ν_{fi} can be positive or negative. It is

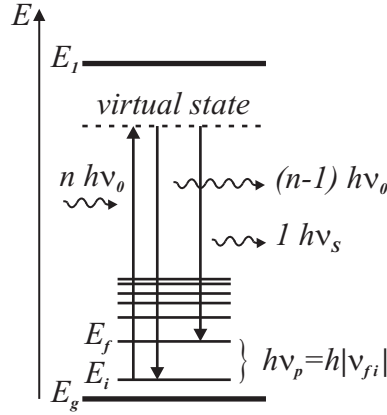


Figure 1.3: Simple energetic diagram illustrating the Raman scattering process.

convenient to introduce ν_p which is the magnitude of ν_{fi} , that is

$$\nu_p = |\nu_{fi}| \quad (1.2)$$

The absorption of a quantum of energy $h\nu_0$ does not induce a resonant transition to a real electronic state, and the incident photon is not absorbed in the strict spectroscopic sense, as there is no conservation of energy in this stage of the process. Such an absorption is called *virtual absorption* and the resulting state is described as a *virtual state*. The role of the incident radiation is rather to perturb the molecule and open the possibility of spectroscopic transitions other than direct absorption.

The scattering process involves two photons, one incident and one scattered. It describes *Rayleigh scattering* (also called elastic scattering), the process described by Lord Rayleigh which accounts for the blue colour of the sky, when $f = i$ ($\nu_S = \nu_0$), and *Raman scattering* (also called inelastic scattering), from its discoverer C. V. Raman, when $f \neq i$. For Raman scattering, if $E_f > E_i$, then $\nu_S = \nu_0 - \nu_p$ and we have Stokes Raman scattering; if $E_f < E_i$, then $\nu_S = \nu_0 + \nu_p$ and we have the much weaker inelastic anti-Stokes Raman scattering (Fig. 1.4). The scattering process occurs in all directions but both the intensity and

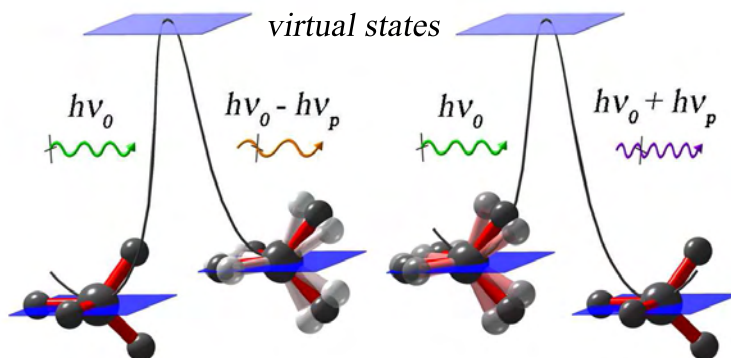


Figure 1.4: Energetic diagram of the Stokes (left) and anti-Stokes (right) Raman scattering process.

polarisation of the scattered radiation depend on the direction of observation. The small amount of radiation that is scattered at some different wavelength (Stokes and anti-Stokes Raman scattering) is approximatively only 1×10^{-7} [9] of the total scattered radiation.

1.3.2 Raman Optical Activity (ROA)

Raman optical activity (ROA) is a special case of normal Raman scattering. It measures vibrational optical activity by means of a small difference in the intensity of Raman scattering from chiral molecules for right and left circularly polarised incident light or, alternatively, a small circularly polarised component in the scattered radiation. The ratio of ROA to Raman scattering is known as the Δ -value, and amounts in general to less than 5×10^{-3} , thus meaning that Raman optical activity is an extremely weak process, and therefore subject to experimental artifacts.

1.3.3 Theoretical Aspects

Light scattering has its origin in oscillating multipoles induced in a molecule by the incident electromagnetic radiation. For the great majority of cases, like normal vibrational Raman scattering, it is sufficient to consider only the frequency-dependent linear induced electric dipole $\boldsymbol{\mu}$ as a source of radiation.

$$\boldsymbol{\mu} = \boldsymbol{\alpha} \cdot \boldsymbol{E} \quad (1.3)$$

where $\boldsymbol{\alpha}$ is the molecular polarisability tensor and \boldsymbol{E} the electric field of the incident monochromatic radiation. A molecular vibration p , described by the normal coordinate Q_p , can be observed in Raman spectroscopy only if it modulates to first order the molecular polarisability:

$$\left(\frac{\partial \alpha}{\partial Q_p} \right)_0 \neq 0 \quad (1.4)$$

where the index 0 indicates $Q_p=0$. If the symmetry of the normal mode is such that this condition is fulfilled, then the transition is said to be allowed or *Raman active*; if it is not fulfilled, it is said to be forbidden or *Raman inactive*.

However, for the scattering by chiral systems it is necessary to consider not only the induced electric dipole, but also the induced magnetic dipole and the induced electric quadrupole. These multipoles, which are induced by the interaction of the field of radiation with the material system [10], are described, for the off resonance case [11], through three transition polarisability tensors: $\boldsymbol{\alpha}$ (electric dipole - electric dipole transition polarisability tensor), \boldsymbol{G}' (purely imaginary electric dipole - magnetic dipole transition polarisability tensor) and \boldsymbol{A} (electric dipole - electric quadrupole transition polarisability tensor).

For a given circular polarisation scheme and geometry of observation (both described in the next section), the scattering sum (Raman) and scattering dif-

ference (ROA) intensity of an isotropic ensemble of molecules are given through appropriate linear combinations of Raman and ROA invariants, respectively, arising from the spatial average of mixed products between the three transition polarisability tensors. In the off-resonant Raman case, and if real wave functions are considered, two Raman invariants are identified: a^2 and β^2 , the isotropic and anisotropic part of the polarisability tensor α , respectively. For the ROA case, three invariants are identified: two of them arise from the contraction of α with \mathbf{G}' , that is, the isotropic aG' and anisotropic $\beta_{G'}^2$. The last ROA invariant is the result of the contraction of α with \mathbf{A} , the anisotropic β_A^2 .

1.3.4 Experimental Aspects

We have so far described the light scattering process in terms of the frequency ν . For the treatment of spectroscopic processes, it is more convenient to use the angular frequency $\omega = 2\pi c_0/\lambda = 2\pi\nu$ (in rad s^{-1}), where c_0 is the speed of light in the vacuum, rather than the frequency ν (in Hz). However it is standard practice in vibrational spectroscopy to use the wavenumber $\tilde{\nu} = 1/\lambda$ (in cm^{-1}), λ being the wavelength in cm, to discuss spectra.

Normal vibrational Raman scattering can be measured by observing the scattered radiation in all directions. Three preferred geometries are mostly used (Fig. 1.5) and are described by the angle θ between the incident and scattered radiation, namely forward scattering ($\theta = 0$), right-angle scattering ($\theta = \pi/2$) and backscattering ($\theta = \pi$).

As we measure Raman optical activity, the circular content of the radiation has to be analysed. There are three different circular polarisation schemes by which spontaneous ROA scattering can be measured, namely incident circular

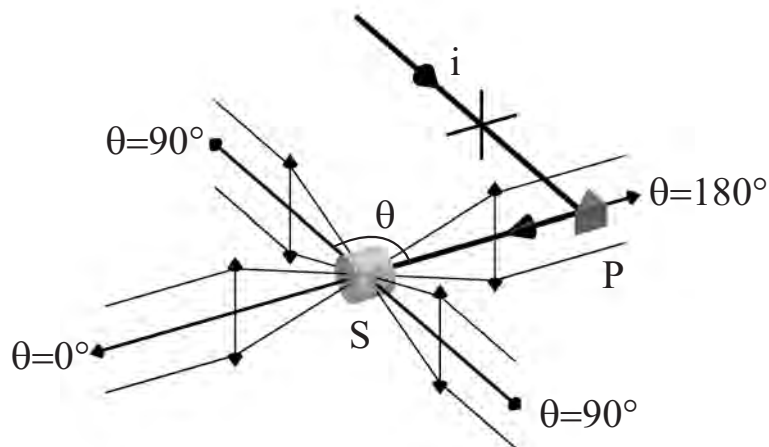


Figure 1.5: Geometries for the observation of Raman scattering. *i*: incident radiation; *P*: prism deflecting incident radiation; *S*: sample; θ : angle between incident and scattered radiation.

polarisation (ICP), scattered circular polarisation (SCP) and dual circular polarisation (DCP_I and DCP_{II}), depending on the circular polarisation content of the incident as well as of the scattered radiation. The corresponding Raman and ROA spectra, or CIS and CID² (for circular intensity sum and difference, respectively), are obtained by adding and subtracting the scattered intensity as defined in Figure 1.6. The sign convention commonly accepted for presenting circular difference scattering intensities is right³ minus left circular. The general sign convention for molecular quantities in the field of optical activity, on the other hand, is left minus right circular.

Typical Raman and ROA spectra, measured in the backscattering circular polarisation geometry ($SCP(\pi)$), are illustrated in Fig. 1.7. As excited state do not have an infinite lifetime, i.e., their energy is not exactly defined, an uncertainty ΔE exists and the transitions are associated with a distribution of

²CID has two definitions: $I_R - I_L$ or $(I_R - I_L)/(I_R + I_L)$ [10], the later corresponding to the Δ -value which we use.

³The polarisation is said to be right-handed (R) when, to an observer looking in the direction from which the radiation is coming, the end point of the electric vector turns in the clockwise sense.

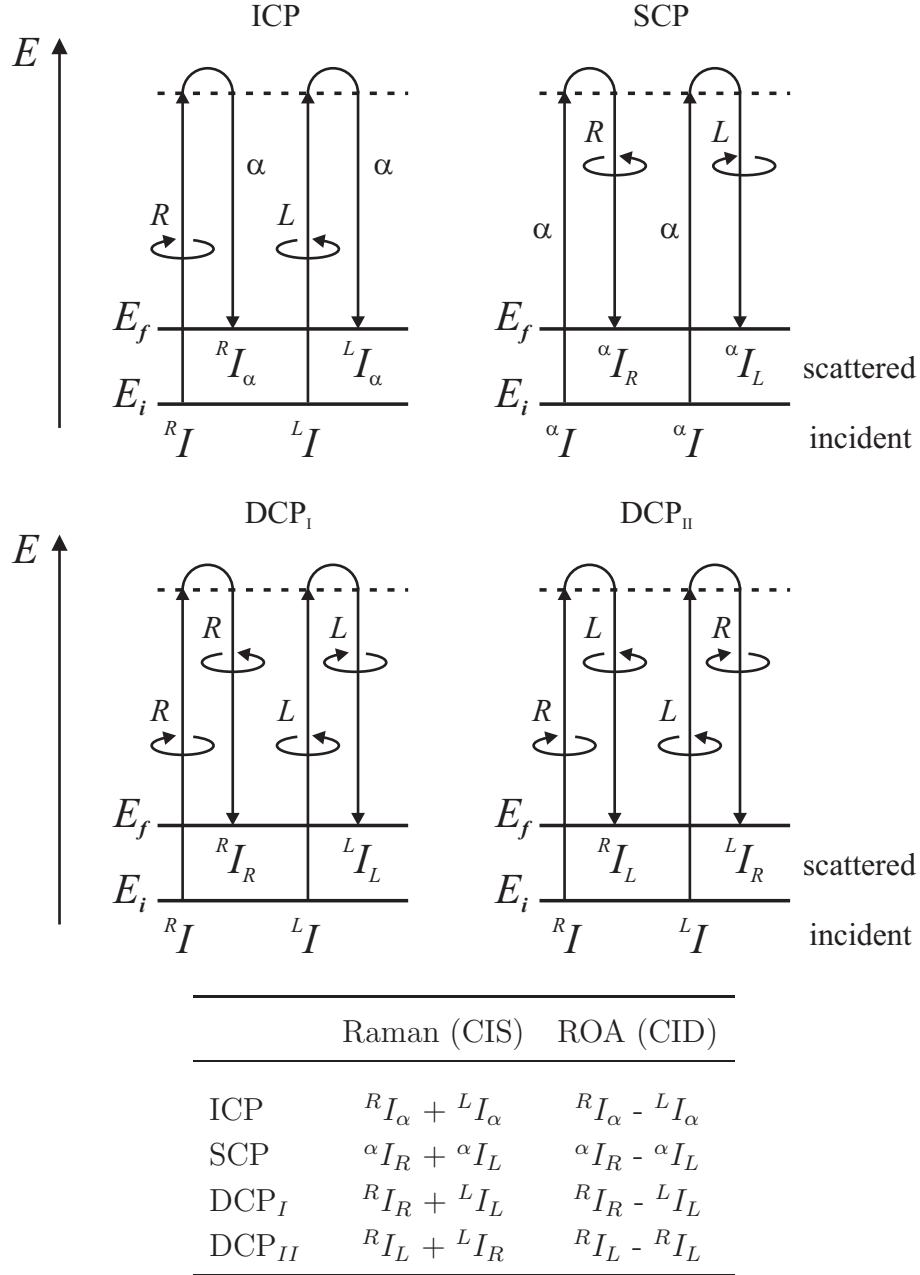


Figure 1.6: Energy levels and polarisation states for the measurement of ROA adapted from [12]. Superscripts refer to the polarisation state of the incident radiation, and subscripts refer to the scattered radiation. R: right-circular; L: left-circular; α : linear polarisation, can be \parallel , \perp to the plane of observation, or n for naturally (unpolarised) incident radiation.

wavenumbers around a central value. This so-called natural line broadening is one of the many factors that contribute to the intrinsic line shape. Vibrational spectra are represented by plotting the measured or calculated intensity in function of the wavenumber shift associated with each vibrational transition. For a particular vibrational transition p , the corresponding wavenumber shift $\Delta\tilde{\nu}_p$ is

$$\Delta\tilde{\nu}_p = \tilde{\nu}_0 \pm \tilde{\nu}_S = \frac{1}{\lambda_0} \pm \frac{1}{\lambda_S} \quad (1.5)$$

It has been recommended by the International Union of Pure Applied Chemistry (IUPAC) [13] that Stokes Raman spectra should be plotted with the abscissa linear in the wavenumber shift, increasing to the left (such that the energy increases to the right), and the ordinate linear and proportional to the intensity.

1.3.5 Computational Aspects

The computation of Raman and ROA intensities has first been achieved through the development of theoretical models, of which one can cite the two group model [14, 15] and the bond polarisability model [15, 16]. A decisive improvement in this field has been the introduction of *ab initio* calculations, where force field and polarisability tensors were evaluated at the Hartree-Fock level of theory [17, 18, 19]. Implementation of post-Hartree-Fock methods such as MP2 [20, 21] and of density functional theory (DFT) [21, 22] for the computation of force fields has sensibly improved the quality of computed spectra. The computation of larger molecules has recently become possible with the development by Zuber et al. [23] of small basis sets that are able to reproduce spectra with comparable quality as those predicted with large reference basis

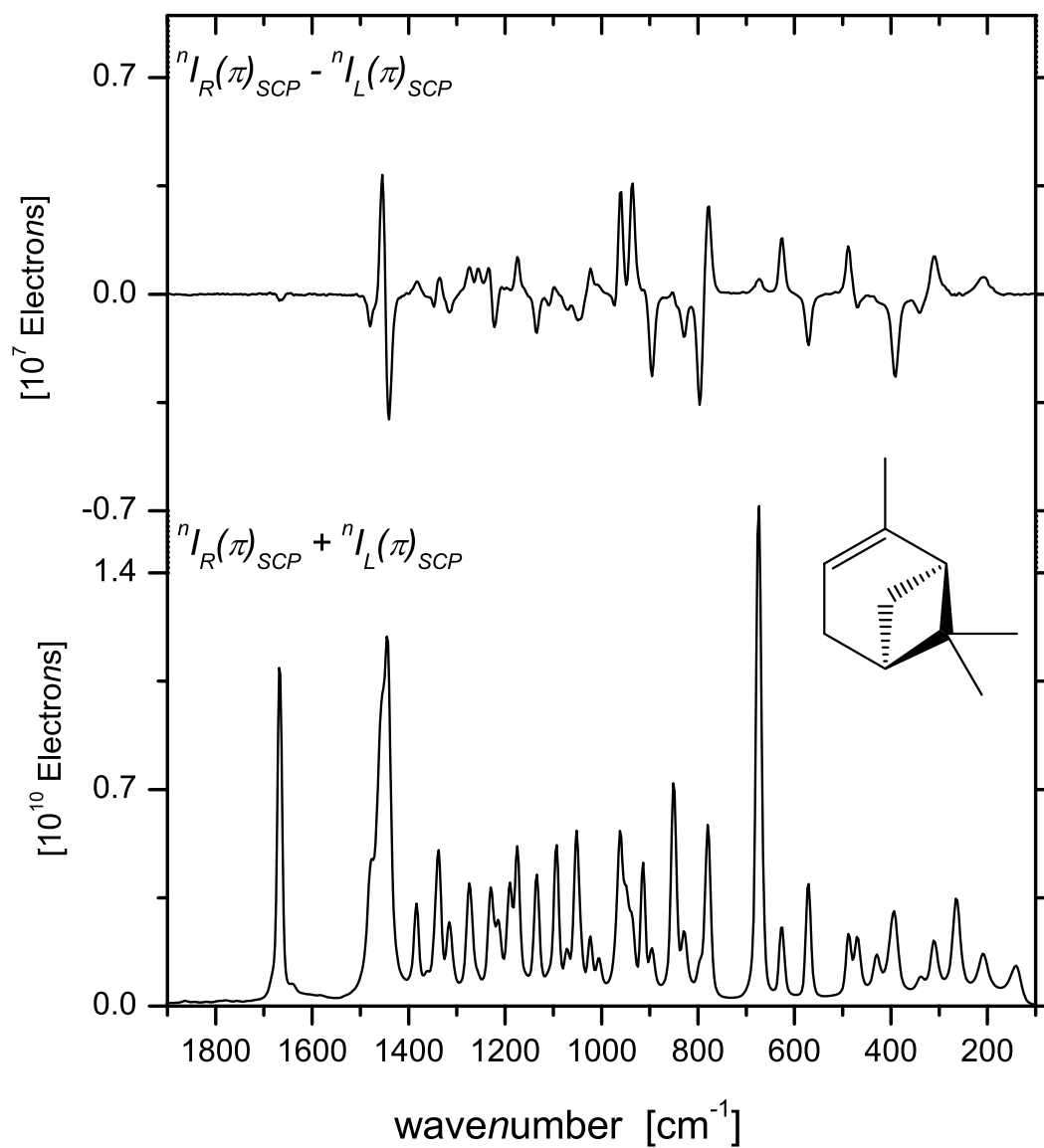


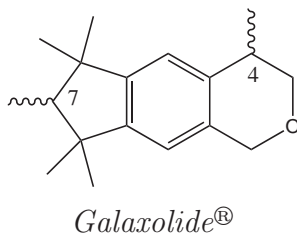
Figure 1.7: Typical experimental SCP(π) Raman (bottom) and ROA (top) spectra of (-)- α -pinene taken on our instrument in Fribourg. Excitation wavelength 532 nm, laser power at sample 300 mW, sample illumination time 20 min.

sets like Dunning’s aug-cc-pVDZ [24] or Sadlej’s [25]. More recently, evaluation of the polarisability tensors at the DFT level has become accessible in computational packages like DALTON [26] and Gaussian03 [27].

1.4 Scope of Application of ROA

The scope of application of optical activity, until the last quarter of the 20th century, has been limited to the probing of electronic chirality by the means of optical rotation and its dispersion (optical rotatory dispersion, ORD), and circular dichroism (CD), the difference in absorption for right and left circular light demonstrated by Cotton [28] in 1896. Nuclear magnetic resonance (NMR), under certain conditions, and X-ray crystallography, are also methods used in the determination of the three-dimensional structure of chiral systems. In the 1970’s, it became possible to probe vibrational optical activity (VOA) with two novel chiroptical methods: Raman optical activity (ROA) and vibrational circular dichroism (VCD), the differing amount of light absorbed for right and left incident circularly polarised light.

These two VOA spectroscopic methods have proven, over the last decade, their potential in conformational and structural analysis of biologically relevant molecules like amino-acids [29, 30], peptides [31, 32, 33], polypeptides [34, 35], proteins [36, 37, 38, 39], nucleic acids [40] and viruses [40, 41, 42]. Raman optical activity is a powerful technique when the configurational and conformational identity of chiral molecules [12, 43, 44] of pharmaceutical importance [12, 45, 46] has to be elucidated. An example is a compound commonly used in the fragrance industry, *Galaxolide*[®], which was studied in our laboratories by means of ROA spectroscopy [23].



It has been shown [47] that only two of the four stereoisomers of *Galaxolide*® have the desired fragrance with an important odour threshold, namely the two diastereoisomers (4*S*,7*S*)- and (4*S*,7*R*)-*Galaxolide*®. Both of them have two conformations, with a ψ -axial or ψ -equatorial methyl group in position 4. Zuber et al. succeeded in determining the absolute configuration of both stereogenic centres by taking into account the equilibrium between the conformers.

1.5 Future of ROA

The beginning of the 21st century is a turning point in the survey, and we hope the expansion, of Raman optical activity. One of the most important developments in the field of ROA is indisputably the recent construction of a backscattering circular polarisation spectrometer SCP(π) by Hug and Hangartner [48], its improvements in term of offsets [49], and the commercialisation by BioTools Inc. (Wauconda, IL, USA) [50], in collaboration with Critical Link Inc. (Syracuse, NY, USA) [51], of the *ChiralRaman*TM instrument which is largely inspired by the setup designed by Hug. An extension of Hug's spectrometer is presented in this work, with the capability to measure, for the first time, SCP forward scattering. Another key development for ROA to become more popular is the availability of dynamic polarisability tensors for the incident light frequency and the elimination of the gauge dependance in the evaluation of the optical activity tensor \mathbf{G}' , which was first implemented [52]

in the DALTON program. A further improvement is the possibility to evaluate polarisability tensors by DFT methods, as implemented in the DALTON and Gaussian03 calculation packages.

To be able to measure and simulate ROA spectra is one thing, but it is another to be able to interpret correctly the plethora of available information. Work has been done in this field, and a useful program with a graphical interface for facilitating this aspect is presented in this work.

All elements required for this method to become largely recognised over the world are now available: a full theoretical description of the ROA phenomenon, a research-level commercial ROA instrument, accessible *ab initio* calculation packages and new graphical intuitive tools for a better understanding and interpretation of calculated and measured spectra. Even if more work still has to be done, and is actually done [53], for a better and easier understanding of ROA spectra, we believe that Raman optical activity will be, in a near future, a reference and world-wide recognised method for configuration and conformational studies of chiral systems.

Part II

Theory

Chapter 2

Vibrational Raman Scattering

2.1 Introduction

When monochromatic laser radiation, of frequency ω_0 and irradiance \mathcal{I} ¹, is incident on a material system, scattered radiation is produced, among which some arises from inelastic vibrational Raman scattering. The latter process consists of a number of different vibrational frequency components, of frequency ω_S and radiant intensity I ². The origin of the scattered radiation is known to be the oscillating electric and magnetic multipole moments induced in the molecule by the electromagnetic fields of the incident radiation. The most important one is the induced oscillating electric dipole, responsible for the normal vibrational Raman scattering. The simultaneous presence of the induced oscillating magnetic dipole and electric quadrupole, much weaker, account for Raman optical activity scattering.

¹The irradiance \mathcal{I} has units of W m^{-2}

²The radiant intensity I has units of W sr^{-1}

2.2 Quantum Mechanical Theory

Quantum mechanical theory, based on time-dependent perturbation theory, makes it possible to obtain expressions for the first-order induced complex transition electric dipole moment $\tilde{\boldsymbol{\mu}}_{fi}$ and hence, the transition polarisability $\tilde{\boldsymbol{\alpha}}_{fi}$, for vibrational Raman scattering. A comprehensive theoretical treatment of the Raman effect can be found in Ref. [9], which makes use of the harmonic electric and mechanic approximations³, and the following basic description is based on it.

To maintain generality in the treatment of the incident electromagnetic radiation, the electric field amplitude is first considered to be complex and $\tilde{\boldsymbol{\mu}}_{fi}$ is given by

$$\tilde{\boldsymbol{\mu}}_{fi} = \left\langle \Psi_f^{(1)} | \hat{\boldsymbol{\mu}} | \Psi_i^{(0)} \right\rangle + \left\langle \Psi_f^{(0)} | \hat{\boldsymbol{\mu}} | \Psi_i^{(1)} \right\rangle \quad (2.1)$$

where $\hat{\boldsymbol{\mu}}$ is the electric dipole moment operator, $\Psi_i^{(0)}$ and $\Psi_f^{(0)}$ are the unperturbed time-dependent wave functions of the initial state i and final state f , respectively, and $\Psi_i^{(1)}$ and $\Psi_f^{(1)}$ the corresponding first-order perturbed time-dependent wave functions, obtained by solution of the time-dependent Schrödinger equation

$$\hat{H}_0 + \hat{H} |\Psi\rangle = i \frac{\partial}{\partial t} |\Psi\rangle \quad (2.2)$$

where \hat{H}_0 is the unperturbed molecular hamiltonian and \hat{H} the radiation field/material system interaction hamiltonian, which is considered to be entirely electric dipole in nature $\hat{H} = \hat{H}_\mu$.

³The higher order terms which are not taken into account in this treatment account for the presence of overtones, combination bands and Fermi resonances.

For vibrational transitions which involve no change of the electronic state (i.e., $i_e = f_e$), where $\hbar\omega_0 > \hbar\omega_{fi}$ (off-resonance), and according to Placzek (1934), the Stokes and anti-Stokes Raman part of the μ component (x , y or z) of the real induced transition electric dipole moment is

$$(\mu_\mu)_{fi} = \frac{1}{2\hbar} \sum_{j \neq i, f} \left[\frac{\langle f | \hat{\mu}_\mu | j \rangle \langle j | \hat{\mu}_\nu | i \rangle}{\omega_{ji} - \omega_0 - i\Gamma_j} + \frac{\langle f | \hat{\mu}_\nu | j \rangle \langle j | \hat{\mu}_\mu | i \rangle}{\omega_{ji} + \omega_0 + i\Gamma_j} \right] \tilde{E}_\nu \exp(-i\omega st) + \text{complex conjugate} \quad (2.3)$$

where the simplified notations $|i\rangle$ stands for $|\Psi_i\rangle$, $|f\rangle$ for $|\Psi_f\rangle$ and $|j\rangle$ for $|\Psi_j\rangle$, where j is the virtual transition state. Summation goes over the states j , which carry the restriction $j \neq i, f$, as the contribution from states i and f are found to be zero in most situations. From Eq. (2.3), the general transition polarisability tensor $(\tilde{\alpha})_{fi}$ is introduced, with components $(\tilde{\alpha}_{\mu\nu})_{fi}$ defined as

$$(\tilde{\alpha}_{\mu\nu})_{fi} = \frac{1}{\hbar} \sum_{j \neq i, f} \left[\frac{\langle f | \hat{\mu}_\mu | j \rangle \langle j | \hat{\mu}_\nu | i \rangle}{\omega_{ji} - \omega_0 - i\Gamma_j} + \frac{\langle f | \hat{\mu}_\nu | j \rangle \langle j | \hat{\mu}_\mu | i \rangle}{\omega_{ji} + \omega_0 + i\Gamma_j} \right] \quad (2.4)$$

2.3 Born-Oppenheimer and Placzek Approximation

To make the general formula in Eq. (2.4) more tractable, the Born-Oppenheimer approximation is made, which enables the electronic and nuclear motions to be decoupled. The j th state is first expanded into its electronic, vibrational and rotational parts, and the Born-Oppenheimer approximation enables us to write

$$|j\rangle = |j_e\rangle |j_v\rangle |j_r\rangle \quad (2.5)$$

The energy corresponding to state $|j\rangle$ is analogously decomposed

$$\omega_j = \omega_{j_e} + \omega_{j_v} + \omega_{j_r} \quad (2.6)$$

In vibrational Raman scattering, the rotational structure is not resolved and the scattering may be described by transition of the type $f_e f_v \leftarrow i_e i_v$ (e being the electronic ground state). Eq. 2.4 is then given by

$$\begin{aligned}
 (\alpha_{\mu\nu})_{f_e f_v \leftarrow i_e i_v} &= \frac{1}{\hbar} \sum_{\substack{j_e j_v \neq \\ i_e i_v, f_e f_v}} \left[\frac{\langle f_v | \langle f_e | \hat{\mu}_\mu | j_e \rangle | j_v \rangle \langle j_v | \langle j_e | \hat{\mu}_\nu | i_e \rangle | i_v \rangle}{\omega_{j_e i_e} + \omega_{j_v i_v} - \omega_0 - i\Gamma_{j_e j_v}} \right. \\
 &\quad \left. + \frac{\langle f_v | \langle f_e | \hat{\mu}_\nu | j_e \rangle | j_v \rangle \langle j_v | \langle j_e | \hat{\mu}_\mu | i_e \rangle | i_v \rangle}{\omega_{j_e i_e} + \omega_{j_v i_v} + \omega_0 + i\Gamma_{j_e j_v}} \right] \quad (2.7)
 \end{aligned}$$

By applying the Placzek transition polarisability approximation, i.e., by confining the general case to those cases for which $f_e = i_e = e_g$, that is, the initial and final vibrational state belong to the non-degenerated electronic ground state, and considering the off resonance case, the polarisability tensor defined in Eq. (2.7) can be simplified. A detailed analysis [9] shows that in the denominators, $\omega_{j_v i_v}$, $\omega_{j_v f_v}$, and $i\Gamma_{j_e j_v}$ are negligible compared to ω_0 and $\omega_{j_e i_e}$. Under these assumptions and considering the wave functions to be real, Eq. (2.7) becomes

$$(\alpha_{\mu\nu})_{f_v i_v} = \frac{2}{\hbar} \sum_{j_e \neq i_e} \omega_{j_e i_e} \left[\frac{\langle f_v | \langle i_e | \hat{\mu}_\mu | j_e \rangle \langle j_e | \hat{\mu}_\nu | i_e \rangle | i_v \rangle}{\omega_{j_e i_e}^2 - \omega_0^2} \right] \quad (2.8)$$

Eq. (2.8) can be simplified by introducing the purely electronic dynamic transition polarisability operator $\hat{\alpha}_{\mu\nu}^e(Q)$, the nuclei being fixed in a configuration Q , so that only electrons are free to move.

$$(\alpha_{\mu\nu})_{f_v i_v} = \langle f_v | \hat{\alpha}_{\mu\nu}^e(Q) | i_v \rangle \quad (2.9)$$

$$\hat{\alpha}_{\mu\nu}^e = \frac{2}{\hbar} \sum_{j_e \neq i_e} \omega_{j_e i_e} \left[\frac{\langle i_e | \hat{\mu}_\mu | j_e \rangle \langle j_e | \hat{\mu}_\nu | i_e \rangle}{\omega_{j_e i_e}^2 - \omega_0^2} \right] \quad (2.10)$$

For a specific vibrational transition $f_v \leftarrow i_v$, where only the vibrational quantum number v_p associated with the normal coordinate Q changes, $\hat{\alpha}_{\mu\nu}^e(Q)$

can be expanded as a Taylor series in Q

$$\hat{\alpha}_{\mu\nu}^e(Q) = (\alpha_{\mu\nu}^e)_0 + \sum_p \left(\frac{\partial \alpha_{\mu\nu}^e}{\partial Q_p} \right)_0 \hat{Q}_p \quad (2.11)$$

where the expansion is only to first-order, and the derivative with subscript 0 is taken at the nuclear equilibrium position ($Q_p=0$). Introducing Eq. (2.11) into (2.9) gives

$$(\alpha_{\mu\nu})_{f_v i_v} = \langle f_v | (\alpha_{\mu\nu}^e)_0 | i_v \rangle + \sum_p \left(\frac{\partial \alpha_{\mu\nu}^e}{\partial Q_p} \right)_0 \langle f_v | Q_p | i_v \rangle \quad (2.12)$$

The first term in (2.12) is responsible for Rayleigh scattering, as in the harmonic approximation $\langle f_v | Q_p | i_v \rangle$ vanishes for $f_v = i_v$. The second term accounts for normal vibrational Raman scattering, as the first term is zero, due to the orthogonality condition of the harmonic oscillator eigenfunctions f_v and i_v . Vibrational Raman scattering is thus non-zero provided that

$$\left(\frac{\partial \alpha_{\mu\nu}^e}{\partial Q_p} \right)_0 \neq 0 \quad (2.13)$$

The first-order derivatives of $\alpha_{\mu\nu}^e$ in (2.12) can be expressed in terms of cartesian displacement vectors (as obtained from *ab initio* calculations), through the relation $\Delta \mathbf{x} = \mathbf{L}^x \cdot \mathbf{Q}_p$ [54]

$$\begin{aligned} \left(\frac{\partial \alpha_{\mu\nu}^e}{\partial Q_p} \right)_0 &= \sum_{\alpha,i} \left(\frac{\partial \alpha_{\mu\nu}^e}{\partial x_i^\alpha} \right)_0 \left(\frac{\partial x_i^\alpha}{\partial Q_p} \right)_0 \\ &= \sum_{\alpha,i} \left(\frac{\partial \alpha_{\mu\nu}^e}{\partial x_i^\alpha} \right)_0 L_{\alpha i, p}^x \end{aligned} \quad (2.14)$$

where $\mathbf{L}_{\alpha, p}^x$, the Cartesian displacement vector of nucleus α , with mass m_α in normal mode p , is normalised so that

$$\sum_{\alpha,i} m_\alpha (L_{\alpha i, p}^x)^2 = 1 \quad (2.15)$$

Chapter 3

Raman Optical Activity Scattering

3.1 Introduction

In order to account for Raman scattering by chiral molecules, according to Long [9], the purely dipole moment nature of the perturbed hamiltonian in Eq. (2.2) has to be extended so that it involves the magnetic dipole operator \hat{H}_m , as well as the electric quadrupole operator \hat{H}_θ

$$\hat{H}_0 + \hat{H} |\Psi\rangle = i \frac{\partial}{\partial t} |\Psi\rangle \quad (3.1)$$

$$\hat{H} = \hat{H}_\mu + \hat{H}_m + \hat{H}_\theta \quad (3.2)$$

It is useful to develop Eq. (3.2) to reproduce the general definition of the three operators

$$\hat{H} = -\hat{\mu}_\mu(E_\mu)_0 - \hat{m}_\mu(B_\mu)_0 - \frac{1}{3}\hat{\Theta}_{\mu\nu}(E_{\mu\nu})_0 \quad (3.3)$$

where the index μ refers to the three cartesian components x , y and z , the index 0 indicates that the quantity in question is taken at the molecular origin, and

a summation over repeated Greek subscripts is assumed implicitly (Einstein convention). The multipole moment operators occurring in Eq. (3.2) are given by

$$\hat{\mu}_\mu = - \sum_i r_{i_\mu} \quad (3.4)$$

$$\hat{m}_\mu = - \frac{1}{2} \sum_i \epsilon_{\mu\nu\lambda} r_{i_\nu} p_{i_\lambda} \quad (3.5)$$

$$\hat{\Theta}_{\mu\nu} = - \frac{1}{2} \sum_i (3r_{i_\mu} r_{i_\nu} - r_i^2 \delta_{\mu\nu}) \quad (3.6)$$

in atomic units ($e = \hbar$, $m_e = 1$), where particle i at \mathbf{r}_i has charge e , mass m_e and momentum \mathbf{p}_i . $\epsilon_{\mu\nu\lambda}$ is the antisymmetric unit tensor of Levi-Civita and $\delta_{\mu\nu}$ is the Kronecker symbol.

In order to calculate the intensity of the scattered radiation, general expressions for the three first-order induced time-dependent transition moments have to be evaluated: the electric dipole transition moment $(\tilde{\boldsymbol{\mu}})_{fi}$, the magnetic dipole transition moment $(\tilde{\boldsymbol{m}})_{fi}$ and the electric quadrupole transition moment $(\tilde{\boldsymbol{\Theta}})_{fi}$ given in Ref. [9]. In the off-resonance case, considering the wave functions to be real and applying the hermitian properties of the different transition moment operators, three polarisability tensors are identified: $(\tilde{\boldsymbol{\alpha}})_{fi}$, the electric dipole - electric dipole polarisability tensor, $(\tilde{\boldsymbol{G}})_{fi}$, the electric dipole - magnetic dipole optical activity tensor, and $(\tilde{\boldsymbol{A}})_{fi}$, the electric dipole - electric quadrupole optical activity tensor. For the general case where the wave functions are taken to be complex, they are obtained by time-dependent perturbation theory

$$(\tilde{\alpha}_{\mu\nu})_{fi} = \frac{1}{\hbar} \sum_{j \neq i, f} \left[\frac{\langle f | \hat{\mu}_\mu | j \rangle \langle j | \hat{\mu}_\nu | i \rangle}{\omega_{ji} - \omega_0 - i\Gamma_j} + \frac{\langle f | \hat{\mu}_\nu | j \rangle \langle j | \hat{\mu}_\mu | i \rangle}{\omega_{ji} + \omega_0 + i\Gamma_j} \right] \quad (3.7)$$

$$(\tilde{G}_{\mu\nu})_{fi} = \frac{1}{\hbar} \sum_{j \neq i, f} \left[\frac{\langle f | \hat{\mu}_\mu | j \rangle \langle j | \hat{m}_\nu | i \rangle}{\omega_{ji} - \omega_0 - i\Gamma_j} + \frac{\langle f | \hat{m}_\nu | j \rangle \langle j | \hat{\mu}_\mu | i \rangle}{\omega_{ji} + \omega_0 + i\Gamma_j} \right] \quad (3.8)$$

$$(\tilde{A}_{\mu\nu\lambda})_{fi} = \frac{1}{\hbar} \sum_{j \neq i, f} \left[\frac{\langle f | \hat{\mu}_\mu | j \rangle \langle j | \hat{\Theta}_{\nu\lambda} | i \rangle}{\omega_{ji} - \omega_0 - i\Gamma_j} + \frac{\langle f | \hat{\Theta}_{\nu\lambda} | j \rangle \langle j | \hat{\mu}_\mu | i \rangle}{\omega_{ji} + \omega_0 + i\Gamma_j} \right] \quad (3.9)$$

3.2 Born-Oppenheimer and Placzek Approximation

The general transition tensors given by Eqs. (3.7) to (3.9) can be reduced to vibrational transition tensors in which the electronic parts of the tensors are regarded as operators, in analogy with what has been done in chapter 2, section 2.3. These operators are functions of the normal coordinate Q_p and induce the vibrational transitions. Raman optical activity scattering can thus also be treated using Placzek theory. The result of these approximation, treated in the same way as for $(\tilde{\alpha}_\mu)_{fi}$, shows that the additional contributions to vibrational Raman scattering by chiral systems involves terms of the type

$$\left(\frac{\partial \alpha_{\mu\nu}^e}{\partial Q_p} \right)_0 \left(\frac{\partial \mathcal{A}_{\mu\nu}^e}{\partial Q_p} \right)_0 = \sum_{\alpha, i} \left(\frac{\partial \alpha_{\mu\nu}^e}{\partial x_i^\alpha} \right)_0 \left(\frac{\partial \mathcal{A}_{\mu\nu}^e}{\partial x_j^\beta} \right)_0 L_{\alpha i, p}^x L_{\beta j, p}^x \quad (3.10)$$

where $\mathcal{A}_{\mu\nu}^e$ is the contraction of the electric dipole - electric quadrupole polarisability tensor with the antisymmetric unit tensor of Levi-Civita: $\mathcal{A}_{\mu\nu}^e = \epsilon_{\mu\lambda\kappa} A_{\lambda\kappa\nu}^e$.

The treatment of the complex transition tensors $(\tilde{\mathbf{G}})_{fi}$ is different, because the operators involved are of the types $\hat{\boldsymbol{\mu}}$ and $\hat{\boldsymbol{m}}$, the latter being purely imaginary. Thus, when the wave function are real, the real parts of this transition tensors are zero, and hence $(\tilde{G}_{\mu\nu})_{fi} = -i(G'_{\mu\nu})_{fi}$, so that $(\tilde{G}_{\mu\nu})_{fi}$ is now purely imaginary. The additional contribution to vibrational Raman scattering by chiral systems is thus of the type

$$\left(\frac{\partial \alpha_{\mu\nu}^e}{\partial Q_p} \right)_0 \left(\frac{\partial G_{\mu\nu}^{\prime e}}{\partial Q_p} \right)_0 = \sum_{\alpha, i} \left(\frac{\partial \alpha_{\mu\nu}^e}{\partial x_i^\alpha} \right)_0 \left(\frac{\partial G_{\mu\nu}^{\prime e}}{\partial x_j^\beta} \right)_0 L_{\alpha i, p}^x L_{\beta j, p}^x \quad (3.11)$$

For chiral contributions to be different from zero, the associated derivatives which appear in Eqs. (3.10) and (3.11) must be non-zero.

Chapter 4

Raman and ROA Intensities

In a light scattering experiment, the intensity of the scattered radiation is measured relative to a space-fixed (laboratory) coordinate system. They are determined by the optical field and the products of the polarisability tensors components, averaged over all orientations of the molecule relative to the space-fixed axes. This isotropic averaging gives rise to rotational invariants of the polarisability tensors, described in section 4.2, the linear combinations of which will account for Raman and ROA intensities.

4.1 Illumination-Observation Geometry

The illumination-observation geometry (Fig. 4.1) is given by the orientation of the unit vector n_S , defining the direction of propagation of the scattered radiation relative to the unit vector n_i for the incident radiation. The relative orientation is given by the angle θ . n_S and n_i define the scattering plane and are related to the space-fixed coordinate system. The scattering material is considered to be at the origin O of the cartesian laboratory axes and the propagation of the incident radiation is chosen parallel to the z axis.

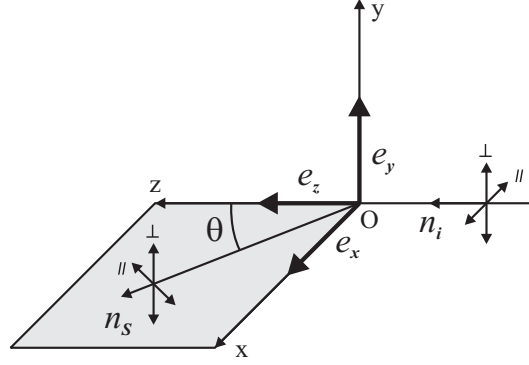


Figure 4.1: Space-fixed cartesian axis system x, y, z associated with unit vectors e_x, e_y , and e_z

The states of polarisation, the propagation vectors and the angular dependence of the incident and scattered radiation may be expressed in a single, composite intensity symbol. As an example, the incident radiation (i) is chosen to propagate along the z axis and linearly polarized parallel to the scattering plane. The polarisation of the scattered (s) radiation is observed along the x axis ($\theta = \pi/2$), and perpendicular to the scattering plane. The resulting symbol is

$$I(\pi/2, \perp^s, \parallel^i) \quad \text{or} \quad \parallel I_{\perp}(\pi/2) \quad (4.1)$$

The first symbol is used in Ref. [9]. We will use a different notation, where the superscript describes the states of polarisation of the incident radiation and the subscript that of the scattered radiation. It is well suited for use with scattering system consisting of freely oriented molecules where the intensity is expressed in terms of tensor invariants which do not require cartesian axis labels.

4.2 Raman and ROA Invariants

Raman and ROA scattering arise from the three induced transition multipole moments given in Ref. [9]: the induced electric dipole transition moment $(\tilde{\mu}_{\mu_0})_{fi}$, the induced magnetic dipole transition moment $(\tilde{m}_{\mu_0})_{fi}$ and the induced electric quadrupole $(\tilde{\Theta}_{\mu\lambda_0})_{fi}$ transition moment. As all three moments are properties of one and the same molecule, the electric fields they radiate are phase related, and thus their amplitudes must be combined before the scattered intensity can be calculated.

The illumination-observation situation defined by the symbol in Eq. (4.1) is first considered, which represents one of the geometries used in early work on ROA. $\tilde{E}_{y_0}^s$, the total amplitude of the y component of the electric field of the scattered radiation, at a distance x from the origin O, along the x axis, is given by [9]

$$\begin{aligned} \tilde{E}_{y_0}^s = & \frac{k}{x} \left\{ (\alpha_{yx})_{fi} - \frac{1}{c_0} [(G'_{yy})_{fi} - (G'_{xz})_{fi}] \right. \\ & \left. - \frac{i\omega_0}{3c_0} [(A_{yzx})_{fi} - (A_{xyx})_{fi}] \right\} \tilde{E}_{x_0}^i \end{aligned} \quad (4.2)$$

where

$$k = \frac{\omega_0^2}{4\pi\epsilon_0 c_0^2} = \frac{\omega_0^2 \mu_0}{4\pi} \quad (4.3)$$

ϵ_0 and μ_0 are the electric permittivity and the magnetic permeability of the vacuum, respectively. The radiant intensity I_y (power per unit of solid angle) of the scattered radiation for a single space-fixed molecule is given by the product

$$I_y = \frac{1}{2\mu_0 c_0} \tilde{E}_{y_0}^s \tilde{E}_{y_0}^{s*} \quad (4.4)$$

By forming this kind of products, a considerable number of terms will be produced. However, some of them can be disregarded and others result in zero values [9] when averaged over all orientations.

If the wave functions are taken to be real, half of the quadratic terms vanish because of their much weaker contribution. If, furthermore, the antisymmetric parts are disregarded, only eight isotropic averages have to be considered. Moreover, if it is assumed that the final state $|f\rangle$ is not very different from the initial state $|i\rangle$, and if it is assumed that the off-resonance case is applied, then the hermitian properties of the operators involved in the tensors $(\tilde{\mathbf{G}})_{fi}$ and $(\tilde{\mathbf{A}})_{fi}$ may be considered to be applied in a good approximation to optically active Raman scattering. Thus, the total number of independent invariants is finally reduced to five: a^2 , the isotropic, and β^2 , the anisotropic invariant of the molecular electric dipole - electric dipole transition tensor; aG' and β_G^2 , the isotropic and anisotropic invariant due to cross products of the latter tensor with the electric dipole - magnetic dipole transition tensor; and β_A^2 , the anisotropic invariant due to its cross products with the electric dipole - electric quadrupole transition tensor. The five invariants used here are identical to the invariants a^2 , β^2 , aG' , γ_G^2 and γ_A^2 introduced in ROA by Long [9], except for $\gamma_A^2 = 3\beta_A^2$.

We introduce now the reduced invariants J_p , which do not include integration over wave functions, whose general components $\alpha\beta$, in terms of the cartesian displacement vectors $\mathbf{L}_{\alpha,p}^x$, can be written as

$$J_{\alpha\beta,p} = \mathbf{L}_{\alpha,p}^x \cdot \mathbf{V}(\mathfrak{J})_{\alpha\beta} \cdot \mathbf{L}_{\alpha,p}^x \quad (4.5)$$

They can be considered as the constituent invariant terms, attributable to the vibrational motion of nuclei α and β , which compose the five global

molecular Raman and ROA invariants \mathfrak{I} (i.e., a^2 , β^2 , aG' , β_G^2 and β_A^2), defined as

$$\mathfrak{I}(f_v \leftarrow i_v) = \langle f_v | Q_p | i_v \rangle^2 \sum_{\alpha, \beta} J_{\alpha\beta, p} \quad (4.6)$$

where the value of the integral over wave functions for a fundamental transition is given by

$$\langle f_v | Q_p | i_v \rangle^2 = \frac{\hbar}{2\Delta\omega_p} = \frac{\hbar}{400\pi c_0 \Delta\tilde{\nu}_p} \quad (4.7)$$

whith $\Delta\tilde{\nu}_p$ given in cm^{-1} . The elements of the electronic second-rank tensors, or dyadics, $\mathbf{V}(\mathfrak{I})_{\alpha\beta}$, have the form

$$V(a^2)_{\alpha i, \beta j} = \frac{1}{9} \sum_{\mu, \nu} \left(\frac{\partial \alpha_{\mu\mu}^e}{\partial x_i^\alpha} \right)_0 \left(\frac{\partial \alpha_{\nu\nu}^e}{\partial x_j^\beta} \right)_0 \quad (4.8)$$

$$V(\beta^2)_{\alpha i, \beta j} = \frac{1}{2} \sum_{\mu, \nu} \left[3 \left(\frac{\partial \alpha_{\mu\nu}^e}{\partial x_i^\alpha} \right)_0 \left(\frac{\partial \alpha_{\mu\nu}^e}{\partial x_j^\beta} \right)_0 - \left(\frac{\partial \alpha_{\mu\mu}^e}{\partial x_i^\alpha} \right)_0 \left(\frac{\partial \alpha_{\nu\nu}^e}{\partial x_j^\beta} \right)_0 \right] \quad (4.9)$$

$$V(aG')_{\alpha i, \beta j} = \frac{1}{9} \sum_{\alpha, \beta} \sum_{\mu, \nu} \sum_{i, j} \left(\frac{\partial \alpha_{\mu\mu}^e}{\partial x_i^\alpha} \right)_0 \left(\frac{\partial G'_{\nu\nu}}{\partial x_j^\beta} \right)_0 \quad (4.10)$$

$$V(\beta_{G'}^2)_{\alpha i, \beta j} = \frac{1}{2} \sum_{\mu, \nu} \left[3 \left(\frac{\partial \alpha_{\mu\nu}^e}{\partial x_i^\alpha} \right)_0 \left(\frac{\partial G'_{\mu\nu}}{\partial x_j^\beta} \right)_0 - \left(\frac{\partial \alpha_{\mu\mu}^e}{\partial x_i^\alpha} \right)_0 \left(\frac{\partial G'_{\nu\nu}}{\partial x_j^\beta} \right)_0 \right] \quad (4.11)$$

$$V(\beta_A^2)_{\alpha i, \beta j} = \frac{\omega_0}{2} \sum_{\alpha, \beta} \sum_{\mu, \nu} \sum_{i, j} \left(\frac{\partial \alpha_{\mu\mu}^e}{\partial x_i^\alpha} \right)_0 \left(\frac{\partial A_{\nu\nu}^e}{\partial x_j^\beta} \right)_0 \quad (4.12)$$

4.3 Scattering Cross Sections

The radiant intensity I of the radiation scattered by a single molecule is directly proportional to the irradiance \mathcal{I} of the incident radiation. It is useful to introduce scattering cross-sections because they are molecular quantities that

are independent of \mathcal{J} . The proportionality factor is the differential scattering cross section $d\sigma$ [9]

$$d\sigma = \frac{I}{\mathcal{J}} \quad (4.13)$$

in $\text{m}^2 \text{sr}^{-1} \text{molecule}^{-1}$, and the total scattering cross-section σ is obtained by

$$\sigma = \int_0^{4\pi} d\sigma d\Omega \quad (4.14)$$

where $d\Omega$ is an element of the solid angle.

The particular case defined in Eq. (4.1) is now considered, with the difference that the incident radiation is taken either right or left circularly polarised, corresponding to polarised ICP($\pi/2$). The irradiance \mathcal{J} of the time-dependent electric field of the incident electromagnetic radiation is given by

$$\mathcal{J} = \frac{1}{2} c_0 \epsilon_0 (E_0)^2 \quad (4.15)$$

Introducing Eq. (4.2) into (4.4), and combining it with Eq. (4.15), results in expressions for the differential cross-section in Eq. (4.13), for right and left incident polarised radiation. These results are given in the form of the sum and difference differential scattering cross-sections, which account for Raman and ROA scattering, respectively. It is assumed that the molecules are freely rotating, so that isotropic averages can be taken. The quadratic terms arising from Eq. (4.4), the spatial averages of which are zero or negligible, are omitted, as has been explained in section 4.2. The remaining isotropic averages are expressed in terms of the five invariants defined in Eq. (4.6), and the formulae for Raman and ROA differential scattering cross-section for the polarised

ICP($\pi/2$) geometry become

$$\begin{aligned} d\sigma_{\perp}(\pi/2)_{ICP} &= {}^R d\sigma_{\perp}(\pi/2) + {}^L d\sigma_{\perp}(\pi/2) \\ &= 2K_p [45a^2 + 7\beta^2] d\Omega \end{aligned} \quad (4.16)$$

$$\begin{aligned} -\Delta d\sigma_{\perp}(\pi/2)_{ICP} &= {}^R d\sigma_{\perp}(\pi/2) - {}^L d\sigma_{\perp}(\pi/2) \\ &= \frac{4K_p}{c_0} [45aG' + 7\beta_G^2 + \beta_A^2] d\Omega \end{aligned} \quad (4.17)$$

where the constant K_p is defined as

$$\begin{aligned} K_p &= \frac{1}{90} \left(\frac{\mu_0}{4\pi} \right)^2 \omega_p^3 \omega_0 \\ &= \frac{10^7}{9} \pi^2 \mu_0^2 c_0 \tilde{\nu}_p^3 \tilde{\nu}_0 \end{aligned} \quad (4.18)$$

$$\tilde{\nu}_p = \frac{\omega_0}{200\pi c_0} \pm \Delta\tilde{\nu}_p \quad (4.19)$$

where $\Delta\tilde{\nu}_p$ is the Raman frequency shift (in cm^{-1}) and μ_0 the permeability of the vacuum.

A minus sign has been included for the difference expression in Eq. (4.17), because the sign convention in ROA for presenting data is opposite to the one used in optical activity in general. $-\Delta d\sigma$ corresponds to the ROA convention to represent the data for right circular radiation minus the data for left circular radiation, with $\Delta d\sigma$ defined in agreement with the standard convention left minus right used for molecular quantities in optical activity.

Similar derivations have been done for the other geometries of observation. The resulting Raman and ROA differential scattering cross-sections used in this work are given by the general formulae

$$d\sigma(\theta) = K_p [c_1 a^2 + c_2 \beta^2] d\Omega \quad (4.20)$$

$$-\Delta d\sigma(\theta) = \frac{K_p}{c_0} [c_3 aG' + c_4 \beta_{G'}^2 + c_5 \beta_A^2] d\Omega \quad (4.21)$$

The linear combination coefficients c_i of invariants used in Eqs. (4.20) and (4.21) are resumed in table 4.1.

| | | | Coefficients of | | | | |
|-----|-----------|--------------------------------------------|-----------------|-----------|-------|-------------|-------------|
| | | | a^2 | β^2 | aG' | β_G^2 | β_A^2 |
| SCP | (π) | ${}^n d\sigma(\pi)_{SCP}$ | 90 | 14 | | | |
| | | $-\Delta {}^n d\sigma(\pi)_{SCP}$ | | | | 48 | 16 |
| SCP | (0) | ${}^n d\sigma(0)_{SCP}$ | 90 | 14 | | | |
| | | $-\Delta {}^n d\sigma(0)_{SCP}$ | | | 360 | 8 | -8 |
| ICP | $(\pi/2)$ | $d\sigma_{\perp}(\pi/2)_{ICP}$ | 90 | 14 | | | |
| | | $-\Delta d\sigma_{\perp}(\pi/2)_{ICP}$ | | | 180 | 28 | 4 |
| | | $d\sigma_{\parallel}(\pi/2)_{ICP}$ | | 12 | | | |
| | | $-\Delta d\sigma_{\parallel}(\pi/2)_{ICP}$ | | | | 24 | -8 |

Table 4.1: Linear combinations coefficients of Raman and ROA invariants for SCP(π , 0) and ICP($\pi/2$) geometry. n stands for naturally (unpolarised) incident radiation, \perp and \parallel stand for scattered radiation analysed perpendicular and parallel to the scattering plane, respectively.

The differential scattering cross-sections in Eqs. (4.20) and (4.21) are valid for a temperature $T = 0$ K. For $T \neq 0$ K, the population of the initial vibrational state has to be taken into account, by multiplying these expressions by the Boltzman factor K_{Boltz} , which for Stokes scattering is given by

$$K_{Boltz} = \frac{1}{1 - \exp(100hc_0\Delta\tilde{\nu}_p/kT)} \quad (4.22)$$

in SI units, where $\Delta\tilde{\nu}_p$ is given in cm^{-1} .

Part III

Experiment

Chapter 5

Basics of ROA Spectrometers

5.1 History

Efforts in trying to observe molecular vibrational chirality have been made during the 20th century, e.g. in the group of Kastler [55] and Günthard [56, 57], but they were all unsuccessful. The situation changed with an important technological breakthrough, the invention of the argon ion laser by William Bridges at Hughes Aircraft in 1964, which led to a renewal of the quest for measuring optically active light scattering. In 1971, Barron and Buckingham [10] theoretically demonstrated the possibility of measuring vibrational Rayleigh and Raman optical activity, followed two years later by the work of Barron et al. [58, 59], who were the first to observe vibrational optical activity of molecular origin by Raman optical activity (ROA) scattering in the visible, with their Coherent Radiation Laboratories Model 52A argon laser. Only about a year later, Holzwarth et al. [60] extended VOA spectroscopy to the infrared, with the first measurement of vibrational circular dichroism (VCD). Higher quality VCD data over a broader spectral region were then obtained by Nafie et al. [61]. On the ROA side, Hug et al. [62] were the first to record entire ROA spectra.

Since the 1970s considerable instrumental advances have been made on the measurement of ROA. To the original ICP right angle depolarised scattering arrangement, polarised right angle scattering [63], backscattering [64, 65], and forward scattering [66] have been added and will be described later in this work. To complete the list of the most important developments in ROA instrumentation, one should cite the introduction of solid-state detectors (self-scanned diode arrays were first used in multichannel Raman spectroscopy [63, 67]), the invention of dual circular polarisation ROA by Nafie et al. [68, 69], the development of the dual-channel design coupled with high-throughput spectrograph by Hug and Hangartner [48] in 1999 and finally the invention of the virtual enantiomer offset correction scheme [49] proposed by Hug. This work presents the second ROA spectra ever measured in forward scattering, which represents the very first measurements of forward SCP ROA.

5.2 Practical Limitations of ROA Measurements

The measurement of Raman optical activity is not a trivial matter, and it is subject to a number of inherent practical limitations spectroscopists have to cope with.

The optical activity one measures represents the difference in interaction of right and left circularly polarised radiation with chiral molecules. This tiny difference is obtained by subtracting two much larger quantities, which differ by one part in a thousand or less for typical interactions in the visible part of the spectrum. ROA is favoured over VCD, because the signal-to-noise ratio decreases as the wavelength of the probing radiation increases, an advantage which is partly balanced by the increasing weakness of the spontaneous Raman

scattering signal with wavelength.

5.2.1 The Exciting Laser Source

Choosing the laser probing wavelength requires some consideration. The Raman scattered energy for a constant exciting energy varies as λ^{-4} with the wavelength λ of the scattered radiation. For a detector yielding a signal proportional to the number of detected photons, the exciting energy required for a constant signal therefore varies as the inverse third power of the wavelength. In addition, the variation with wavelength of the Δ -value, the ratio of ROA to Raman scattered radiation, has to be considered. An ultraviolet source at 266 nm, compared to an infrared 1.06 μm exciting laser, will thus yield a 1000 times stronger signal [70]. In this comparison, the quantum efficiency of the detector and throughput of the spectral analysing system are not taken into account. In addition, laser power is not the only consideration in ROA. Offset problems, sample decomposition, fluorescence and other features do also play a crucial role in choosing the right laser. A good but not completely ideal value of 532 nm is commonly chosen. We are still waiting on laser in the orange to red part of the visible electromagnetic spectrum, with an acceptable spectral linewidth and output power, to eliminate fluorescence problems.

5.2.2 The Sample

The latter problem leads us to take the sample into account. Absence of any dust is an absolute necessity in slow modulation ROA instruments, but the simultaneous detection of right and left circular scattered radiation has improved this aspect [48]. Additionally, small amounts of absorption of the exciting laser light by the sample causes thermal lensing, a source of possible offsets and a

reduction in signal strength. Last but not least, in a multichannel experiment, strong solvent bands can saturate the detector at specific wavelengths. This can lead to offsets throughout the spectra and requires a reduction of sample illumination time before detector readout, increasing the total recording time. Solving the problem of strong solvent bands could be realised by mechanically preventing the scattered radiation of such bands to reach the CCD detector. More work has to be done in this respect. Strong solvent bands may also obscure interesting spectral ranges.

5.3 The Three Circular Polarisation Schemes

5.3.1 Incident Circular Polarisation (ICP)

As mentioned in chapter 1, section 1.3, there are three different polarisation geometries by which ROA can be measured. The first and original one is the so called incident circular polarisation (ICP) scheme (Fig. 5.1), in which the incident radiation is modulated between right and left circular, but the scattered radiation is not analysed with respect to its circular content. Originally, the depolarised right-angle scattering ($\theta = \pi/2$) was the standard geometry of measurement, with the analyser oriented parallel to the scattering plane [58, 59] (ICP_{||}($\pi/2$)). Thanks to collecting optics designed to reduce instrumental artifacts [63, 67, 71], ICP could be extended to polarised right-angle scattering (ICP_⊥($\pi/2$)). The two latter schemes were replaced by backscattering ICP [64, 65, 72] (ICP(π)) in standard instruments [73, 74, 75] because of its enhancement in signal-to-noise ratio, although right-angle scattering is still of great interest when trying to isolate individual scattering components in combination with SCP. Forward ICP has also been implemented once [66], but this

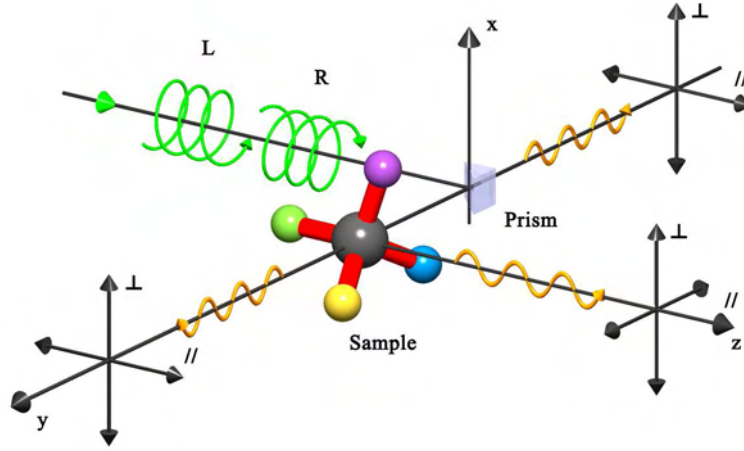


Figure 5.1: Forward, right-angle and backward incident circular polarisation $ICP_{\parallel,\perp}(0, \pi/2, \pi)$ arrangement.

geometry did not persuade VOA scientists. The only published measurements were those of *trans*-pinane and β -pinene.

5.3.2 Scattered Circular Polarisation (SCP)

The scattered circular polarisation (SCP) ROA was the first to be predicted qualitatively [76] in 1969, but it was only described six years later [77]. In this geometry, the circular polarisation of the scattered radiation is analysed, while the incident radiation is chosen to be linearly or naturally polarised (Fig. 5.2). The first SCP instrument built was an $SCP(\pi/2)$ [69, 78]. Although its construction was considered very simple, the development of SCP instrumentation was stopped, as it was first erroneously assumed to yield two times weaker signals than it actually does [79, 80]. By recording simultaneously right and left scattered radiation, Hug et al. were the first to measure backscattering SCP ROA [48], the arrangement most commonly used nowadays which has become commercially available (Biotoool Inc., Wauconda, IL, USA). No implementation

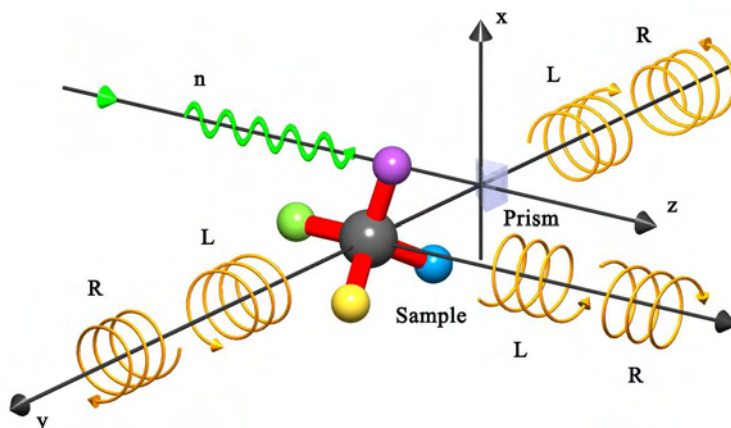


Figure 5.2: Forward, right-angle and backward scattered circular polarisation SCP(0, $\pi/2$, π) arrangement.

of forward scattering SCP ROA has been published so far.

5.3.3 Dual Circular Polarisation (DCP)

Dual circular polarisation (DCP) was the last geometry to be theoretically described [68], to be experimentally predicted [78] and to be implemented [69]. In DCP, the circular content of the scattered radiation is analysed, while the circular polarisation of the incident radiation is synchronously modulated. In DCP_I, the circularity of the incident and of the detected radiation are of the same kind, while in DCP_{II} they are opposite. The latter vanish in the far from resonance limit. DCP_I represents a combination of ICP and SCP, but with a higher ratio of ROA to Raman intensity. In its first implementation, backward scattering was preferred, as ICP(π) was the actually favoured geometry, which could also be recorded on this instrument.

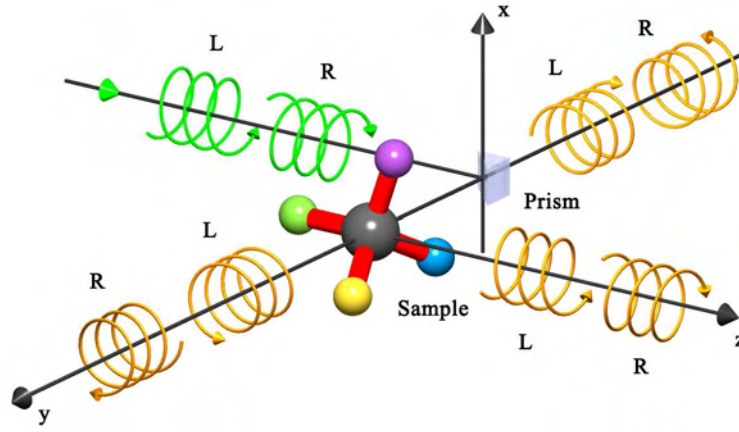


Figure 5.3: Forward, right-angle and backward dual circular polarisation $\text{DCP}_{I,II}(0, \pi/2, \pi)$ arrangement.

Chapter 6

Offset Problems in ROA

As mentioned before, the SCP ROA arrangement developed by Hug et al. [48] has become the standard and commercially accessible way to measure Raman optical activity. Implementation of a revolutionary offset correction scheme definitely made SCP(π) the reference ROA measurement technique.

6.1 Elimination of Deterministic Offsets in ROA

The ratio of the difference to the sum of right and left scattered radiation measured in optical activity spectroscopy lies at the root of the difficulty of the measurement of all forms of optical activity. Shot noise, low frequency flicker noise, and spurious results due to instrumental artifacts have been a steady companion to vibrational optical activity measurements since their inception. Shot noise, which follows a Gaussian distribution, increases as the square root of measurement time, with signal-to-shot noise ratio improving at the same rate, while improvement of the signal-to-flicker noise with time is known to be slow or nonexistent. Influence of systematic instrumental offset, in turn, cannot be reduced with time, nor can it be detected by comparison of subsequent measurements.

Specific solutions are known for the elimination of this latter deterministic offset in the measurement of our particular form of optical activity [64, 71]. One approach to detect and eliminate the presence of deterministic offset has been to measure both enantiomorphous forms of a molecule, under identical conditions, and to subtract their spectra [69]. This cancels offsets other than those due to the differing chiroptical properties of the two optical antipodes. However, this method requires the availability of both enantiomers and is therefore far from satisfactory. Hug et al. demonstrated that one can achieve the same result with a sole enantiomer, by the optical "creation" of the other, i.e., by optically creating its "virtual enantiomer".

6.2 Creating the Virtual Enantiomer

The creation of a virtual enantiomer uses a property of half-wave retarders. They act as circularity converters, by transforming right into left and left into right circularly polarised radiation, and of mirroring the plane of polarisation of linearly polarised radiation with respect to half-wave plate's fast axis.

Illustrating this correction scheme is easier if one first considers only the optical rotation of linearly polarised radiation by a chiral sample. The use of a single half-wave plate after the sample is sufficient to simulate the optical antipode to a subsequent linear polarisation analyser. However, the full simulation of an optical antipode, also towards the radiation source, requires two half-wave plates, one before, and the other after the sample.

A simple way to implement the idea of the virtual enantiomer in SCP backscattering is shown in Fig. 6.1. A single movable half-wave plate fulfills the function of a circularity converter ($CC_{1,2}$) for the incident and scattered radia-

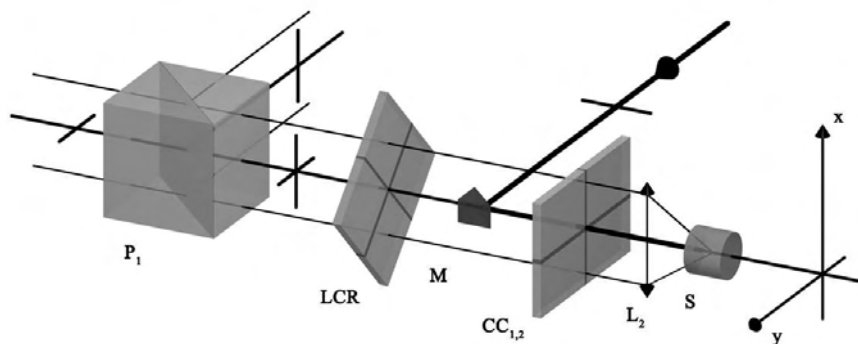


Figure 6.1: Simple implementation of the circularity conversion in ROA backscattering. **S**: sample. **L₂**: lens for focusing the exciting and collecting the scattered radiation. **CC_{1,2}**: circularity converter used for incident and scattered radiation. **M**: mirror for 90° incident radiation deflection. **LCR**: liquid crystal retarder used as the circular polarisation analyser in combination with the polarising cube **P₁**.

tion. If the plate is precise, and in the absence of chromaticity, the subtraction of the data obtained with and without the half-wave plate corrects parasitic net circular components that might be present in the exciting radiation, as well as an unequal response to right and left circular radiation by the circular polarisation analyser (LCR: liquid crystal retarder).

Most circular polarisation analysers are sensitive to the orientation of linearly polarised radiation. In an experiment in which the circular intensity difference is measured, and where optical rotation is an unwelcome phenomenon, linear polarisation of the exciting radiation is therefore undesirable. Other sources of linear or elliptical radiation are stray birefringence, oblique reflection (which can occur in lenses or in the sample cell itself) and an imperfect half-wave retardation of the circularity converters. In order to reduce the effect of linear polarisation, exciting radiation in which all directions of linear polarisation are equally probable can be used. To generate such an exciting radiation, it is straightforward to rotate a half-wave plate at a specific angular

velocity ω . Such a rotating half-wave plate is called a linear rotator, in order to distinguish its action from that of a true polarisation scrambler.

6.3 The 2- and 4-phase Offset Correction Scheme

Combining all these considerations, offsets falling below the presently measurable level can be achieved by the design shown in Fig.6.2, which is also the design used in our new ROA spectrometer. It consists of two independently movable circularity converters, one simulating the optical antipode in the exciting radiation (CC_1) and the other in the scattered radiation (CC_2), complemented by two counter-rotating linear rotators in the exciting radiation (LR_1 and LR_2), and a single one in the scattered radiation (LR_3). The only task of LR_3 is to eliminate small components of linear polarisation produced by the imprecision of other optical elements. Remaining offsets caused by the circular polarisation analyser are mainly eliminated by the dual arm design [48, 70] of our instrument, which allow the simultaneous recording of right and left circularly polarised scattered radiation.

The idea of correcting offsets by the creation of the virtual enantiomer requires two measurements, patterned [00] and [11], with the circularity converter in the incident radiation (CC_1) moving like the lower bit, and the converter in the scattered radiation (CC_2) described by the higher bit. It has been shown that this is only true for perfect optical elements. For real elements, a net circular component in the exciting radiation, even if a very high-quality linear polariser is used, is unavoidable. Correcting this major offset source is better achieved through a four-phase scheme, i.e., [00], [01], [10], [11], where the circularity converter in the incident radiation is moved at a higher frequency

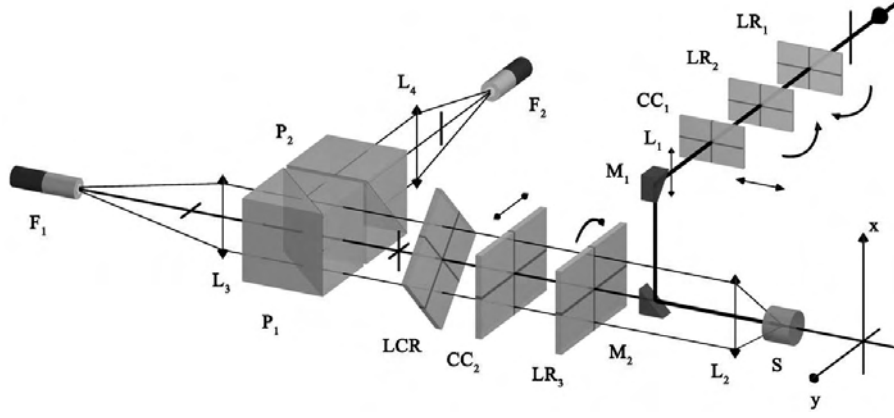


Figure 6.2: Optical arrangement of the backscattering part of our actual ROA spectrometer in Fribourg. \mathbf{M}_1 , \mathbf{M}_2 : mirror for 90° polarisation neutral beam deflection. \mathbf{LR}_1 , \mathbf{LR}_2 : high-speed counter-rotating linear rotator. \mathbf{LR}_3 : slow-rotating linear rotator. \mathbf{P}_2 : second polarising cube used to compensate the difference in extinction of \mathbf{P}_1 for the two orientation of linear radiation. \mathbf{L}_3 , \mathbf{L}_4 : lens for focusing linear radiation splitted by \mathbf{P}_1 and \mathbf{P}_2 into the two fiber optics, \mathbf{F}_1 and \mathbf{F}_2 , of our dual-arm design. Other optical elements as in Fig.6.1.

because of its smaller size. Finally, an offset free ROA spectrum is obtained by the addition and subtraction of the different recorded intensity (Eq. 6.1).

$$I = -\frac{1}{4}\{I[00] + I[01] - I[10] - I[11]\} \quad (6.1)$$

The signs, as indicated, take care of the interconversion of right and left circular radiation by the linear rotator LR_3 and the circularity converter CC_2 in the scattered radiation.

Chapter 7

A Novel High-throughput SCP ROA Spectrometer

As pointed out earlier, the novel original instrument based in Prof. Hug's lab in Zürich (Switzerland), is now used for routine measurements of biological compounds. It is still considered to be a reference instrument for judging the reliability of measurements made on other spectrometers worldwide.

One does not like to make changes in a perfectly working instrument. Replacing or adding optical components in an optical path is not trivial. It often implicates lots of adjustments, without any warranty of recovering the original capabilities of the spectrometer. It is also at high risk to move such sensitive components. Thus it is preferable to build a completely new experiment, and this is precisely what has been done in Fribourg during the work described here. The resulting instrument is mainly based on the previous one; it uses the same timing logic¹ for the acquisition, but adds new features, of which forward scattering is the most important one.

¹For the ROA instrument in Zürich, all the timing logic was implemented in hand-wired electronics by Hug [48].

7.1 Basis of the Spectrometer

Advances made in spectrograph and detector technology, due to the introduction of volume phase holographic (VPH) transmission gratings and notch filters, and also of large surface area, high quantum efficiency, low noise CCD sensors, were exploited at best to design this novel high-throughput spectrometer. Solutions were found for reducing the influences of less desirable characteristics of such modern spectrometer components, like image distortion in the spectrograph and the slow read-out of the detector.

The standard way to measure ROA was to make two measurements, one for right and one for left circularly polarised radiation, and their modulation to increase the sensitivity. Dust, thermal Schlieren and variations in the background fluorescence of the sample give rise to intensity variations between these modulation half-cycles. Reduction of low-frequency noise, often termed $1/f$ or flicker-noise, is achieved by splitting the detector surface into two halves, one for recording the right and one for the left circular signal. Once filled, both halves are read out in the same read-out cycles. This is the basic idea of the dual branch design of this instrument depicted in Fig. 7.1: one of the two optical branches transmits the right circular component (I_R) of the Raman scattered radiation to one half of the detector, and the remaining branch the left circular (I_L) to the other half. The two halves of the CCD detector and the two optical branches will however never be perfectly balanced, but the influence of slight differences between them can be eliminated by interconverting the role of the two branches. This can be accomplished by optical switching, without any moving mechanical parts, by interchanging the slow and fast axes of the liquid crystal retarder.

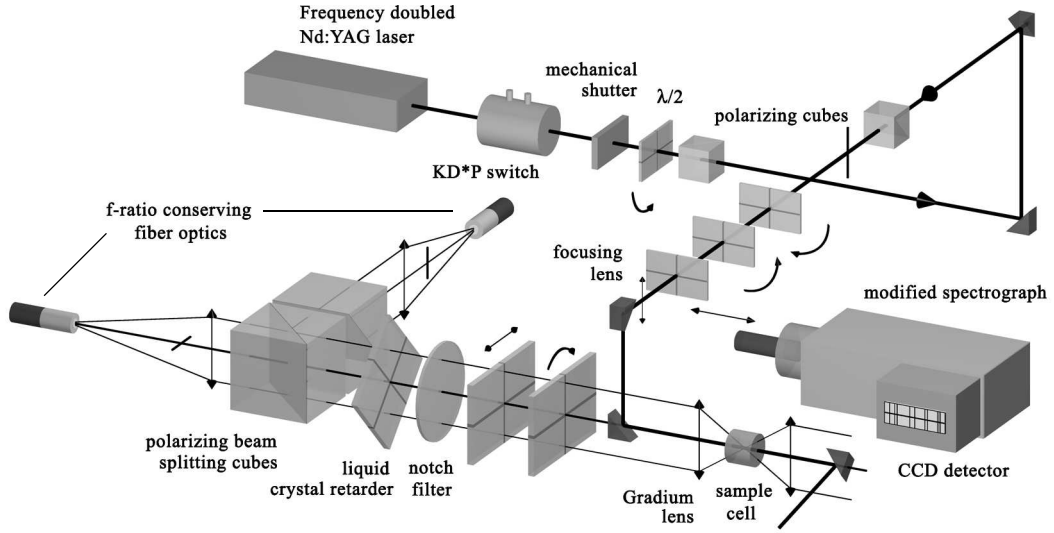


Figure 7.1: Simplified overview of our SCP ROA instrument. Only the backscattering part is depicted. The forward part is a mirror image of the backward part, with the addition of a small mirror coated 45° rod lens after the forward collection lens. Optical components as in Fig. 6.2.

7.2 Optical description

This novel backward and, for the first time, forward scattered circular polarisation spectrometer consists of the following components: 532nm exciting laser radiation, non-imaging light collection, dual-arm design, cross-section transforming fiber optics light guides, high-throughput modified spectrograph and CCD detection. For convenience and simplicity, most of the figures illustrating the instrument are principally devoted to the backscattering geometry. The only difference arising in the forward scattering direction is the deflection of the incident laser beam by a small mirror coated, 45° rod lens (Edmund Optics, Barrington, NJ, USA).

The instrument, illustrated in the central part of this work, is mounted on an optical breadboard (120 x 240 cm), in an air-conditioned room where

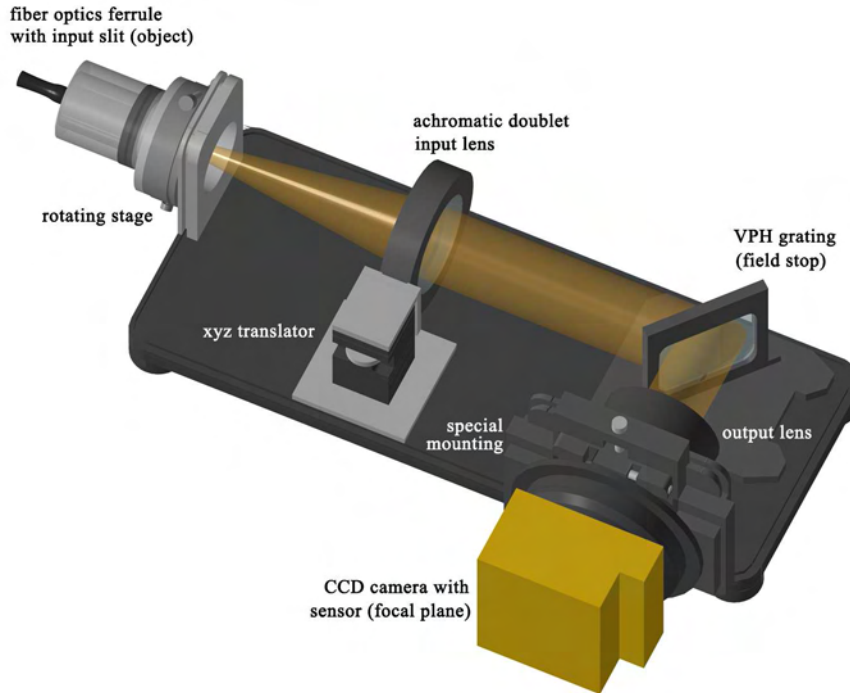


Figure 7.2: Illustration of our modified Kaiser Holospec $f/1.8i$ spectrograph.

a vertical laminar flow of filtered air limits the amount of dust. The height of the optical axis is set to 40 mm above the stainless steel optical X26 rails (Newport, Irvine, CA, USA).

7.2.1 Spectrograph and CCD Detector

The first aspect one has to consider in building such an instrument is the choice of a suitable spectrograph/CCD detector combination, keeping in mind that one has to match its étendue and to illuminate the CCD detector entirely. Such considerations have often been neglected, and very expensive CCD detectors with a 6-8 mm width have been used, but with only a strip of 1 mm actually being illuminated.

Our choice, depicted in Fig. 7.2, has been to use a CCD camera from

Wright Instruments (Enfield, Middlesex, UK), equipped with a CCD30-11-0-232 sensor form EEV, with an array of 1024 x 256 square pixels ($26 \mu\text{m}$), and an imaging area of $26.63 \times 6.66 \text{ mm}$ (177.2 mm^2). The CCD camera is held by a special mount, allowing vertical translation and rotation for an easier alignment of the sensor. Finding the focal plane is achieved by an adjustment tool on the Nikon Nikkor 85 mm 1:1.4 output objective. An electromechanical shutter (Prontor, Bad Wildbad, Germany) is mounted on the spectrograph's input and used in the calibration and alignment procedure to prevent light from falling onto the CCD during readout.

A high output speed is a most desirable characteristic of the spectrograph, as it allows to keep the detector size small. On the other side, a high input speed reduces the object size (entrance slit), but involves complex optics. We opted for a soft approach by using a modified Kaiser Holospec f/1.8*i* spectrograph. From a detailed analysis, it was decided to replace the original input optics ($f=85 \text{ mm}$, f/1.8 lens) by a 200 mm focal length achromatic doublet. With an unchanged 85 mm focal length and f/1.4 output lens, this requires an f number of 3.3 for the input lens (60 mm aperture). A schematic view of this arrangement is shown in Fig. 7.3. In that actual spectrograph, it is the VPH transmission grating (G) size ($\sim 60 \text{ mm}$ height), and not the output optics, which limits the étendue by cutting off marginal rays. The resulting average input f number value is slightly below f/4.

In order to cover the entire vibrational spectrum, two different gratings can be used. Both are from the same manufacturer as the spectrograph itself (Kaiser Optical Systems Inc., Ann Arbor, MI, USA). The first and most frequently used one covers the spectrum from 0 to 2400 cm^{-1} (532 to 610 nm) and the second one from 1555 to 3825 cm^{-1} (580 to 668 nm). Switching from

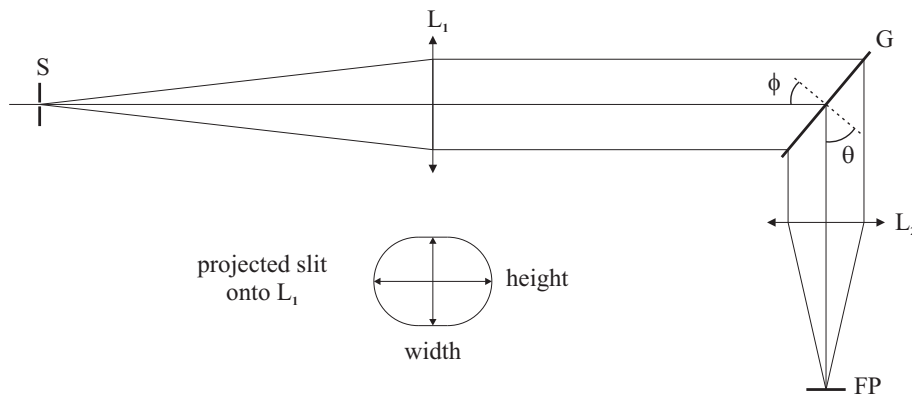


Figure 7.3: Schematic view of the Kaiser VPH planar transmission grating spectrograph with modified input optics. **S**: input slit; **L₁**: input achromatic doublet; **G**: VPH transmission grating; **L₂**: output lens; **FP**: output focal plane.

one grating to the other requires a re-calibration of the spectrograph with a low-pressure Neon discharge lamp (L.O.T.-Oriol AG, Switzerland) placed at the sample's position.

7.2.2 Cross-section Transformer Fiber Optics

With a 6.66 mm high CCD detector in the focal plane, and a demagnification of 200/85, the slit (object) length amounts to 15.66 mm. As the only practical way for matching the étendue of such a spectrograph is the use of fiber optics, and as in backscattering ROA a cross-section transformer is unavoidable, the input slit is formed by a column of 2 x 31 low numerical aperture ($NA = 0.22$, i.e., $\Phi = 6.35^\circ$ in air) fibers with buffer and core diameters of 245 μm and 215 μm , respectively. The upper and lower halves of the column of fibers are separated by a 300 μm spacer so that a length of 15.5 mm results. The image of the slit viewed by the chosen 200 mm input lens is thus 60 mm long and 44.8 mm broad. The use of a cross-section transformer does not permit a variation of the slit's width, and our choice of fiber size and input focal length

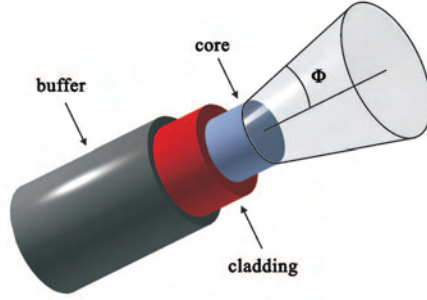


Figure 7.4: Fiber optics are composed of a core surrounded by a higher refractive index cladding and are protected by a robust buffer. Guided light exits the core with a half-opening angle Φ .

corresponds to a $72 \mu\text{m}$ slit width as referred to the standard 85 mm input focal length used in the Holospec $f/1.8i$. It provides a resolution of about 7 cm^{-1} , which is a good value for Raman optical activity solution spectra.

In order to compensate the parabolic distortion of the straight slit image caused by the VPH transmission grating, as do other ordinary plane gratings [81], the individual fibers are aligned along a parabolic line with the opposite curvature (Fig. 7.5), resulting in a straight slit image on the CCD detector. For simplicity, the parabola section is approximated by a circle section whose radius is 108.5 mm. At the high- and low-wavenumber limit, the distortion is slightly under- and overcorrected, respectively. A special ferrule holds these 62 individual fibers in the desired shape as depicted in Fig. 7.5.

Collecting a regular cone of radiation at the fiber optics entrance has been shown to be very important in backward and forward scattering [71, 79, 82]. In this view, we decided to arrange the fibers in the semi-ordered way shown in Fig. 7.5. The two entrance cross-sections of the fiber optics are hexagons with the six corners cut off, which yield the 2×31 fibers we need to form the spectrograph entrance slit for our chosen resolution, CCD size and image demagnification. There is essentially no focal ratio degradation [83] in the very

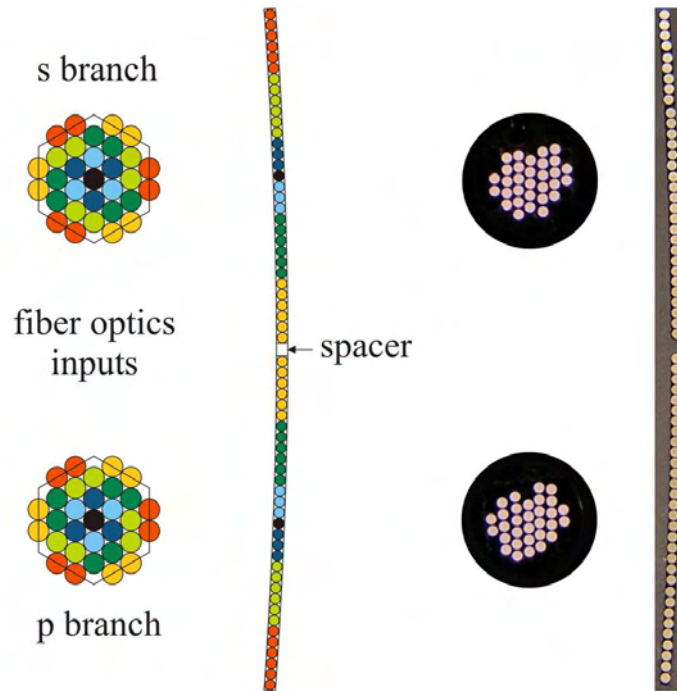


Figure 7.5: Detailed view of the fiber optics cross-section transformer. Left: schematic design of both fiber inputs and of the curved slit ($R=108.5$ mm). Right: pictures of both fiber inputs and of the curved slit. It looks evident that the input's hexagonal shape has not been manufactured correctly. The vertical alignment of the fibers is correct but not the horizontal one.

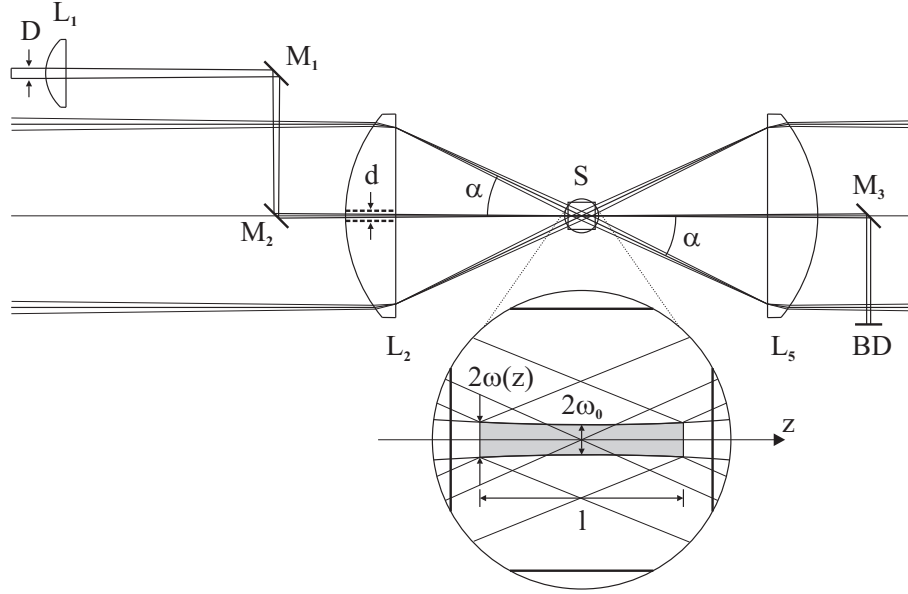


Figure 7.6: Schematic view of the light collection design. **D**: laser beam diameter($1/e^2$); **d**: hole diameter drilled in the Gradium lens **L₂**; α : cone half-angle of the collected scattered radiation; **M₃**: mirror coated, 45° rod lens for exciting beam deflection; **BD**: beam dump; **l**: length of the collected light segment; $2\omega_0$: focused beam waist; $2\omega(z)$: beam waist at the end of the segment. Other optical elements as in Fig. 6.2.

high quality fiber optics, so that this is also the f number by which the radiation enters the spectrograph. This will be important in the light collection design. Such fiber optics are clearly difficult to fabricate, but we found a company (Multimode, East Hanover, NJ, USA) willing and able to do it. The first two parts for the Zürich instrument were of good faction, but the further ones, despite an improved fabrication process promised by the company, were of minor quality, and this caused a considerable delay for the implementation of the forward scattering geometry.

7.2.3 Light Collection

The overall light collection is non-imaging and part of it is illustrated in Fig. 7.6. The 1.5 mm diameter 532 nm green laser beam is focused into the sample

through a 100 mm focal length and 10 mm diameter BK-7 plano-convex lens (L_1). The focused beam is deflected by a polarisation neutral combination of two special Silflex MKII coated prisms (Balzers) fabricated in the same batch (M_1, M_2) and passes through a 1.5 mm diameter hole drilled in a 30 mm diameter and f/1.1 Gradium lens (L_2) from Lightpath Technology (Albuquerque, NM, USA). This design avoids offset sources like Raman light scattered by the collection lens and elliptical light generated by stray birefringence. As the optics is non-imaging, light is collected from an approximately 3 mm long segment centred in length with respect to the waist of the focused beam which amounts to a value of about $2\omega_0 = 45\mu\text{m}$,

$$2\omega_0 = \frac{8\lambda}{\pi} \left(\frac{F}{D} \right)^2 \quad (7.1)$$

where λ and D are the exciting wavelength and beam diameter (at $1/e^2$), and F the focal length of the focusing lens.

The waist diameter does not matter in such an arrangement. It could nevertheless be adjusted by replacing the focusing lens, but it is sufficiently large to yield a long enough and reasonably collimated segment for an eventual operation in a 90° scattering geometry. To evaluate the degree of collimation of this segment (Fig. 7.6), one can calculate the beam diameter $2\omega(z)$ at the distance $z = 1.5$ mm from the beam waist by means of Gaussian optics [84],

$$\omega^2(z) = \omega_0^2 \left[1 + \left(\frac{\lambda z}{\pi \omega_0^2} \right)^2 \right] \quad (7.2)$$

obtaining a value of $2\omega(1.5) = 50\mu\text{m}$, which is smaller than the $64\mu\text{m}$ calculated at the Rayleigh range (3 mm), the distance over which the beam's cross-sectional area doubles.

The back- and forward scattered radiation is collected in a cone with half-angle $\alpha = 24^\circ$. In the backscattering direction, the collimated beam of scattered radiation, from which the light falling onto the deflection prism M_2 is lost, passes first through two retarder plates belonging to the offset correction scheme (LR_3 and CC_2). In the forward scattering part, light is collected in a similar way by a 30 mm Gradium lens, and the exciting laser beam is deflected by a mirror coated, 4 mm diameter 45° rod lens (M_3), from Edmund Optics. Rayleigh radiation is then mostly eliminated by a notch filter from Kaiser Opticals, polarisation analysed as described below and finally focused for each detection branch by a 40 mm diameter, $f = 100$ mm achromatic doublet, onto the fiber optics inputs. At this point, the average f number is 3.65, slightly below the one of the spectrograph's input, a value which is not, as said before, degraded by the fiber optics.

7.2.4 Circular Polarisation Analyser

The circularly polarised scattered radiation is converted by the liquid crystal retarder into light which is linearly polarised at $+45^\circ$ or -45° with respect to the retarder's fast axis, depending on whether it is right or left circular. The two orientations of the transmitted linearly polarised radiation are then separated by a 40 mm polarising beam splitting cube (P_1) depicted in Fig. 7.7. The p-polarised transmitted radiation has a degree of purity higher than 99.95%, according to the manufacturer (Halle, Berlin, Germany). The deviated s-polarised radiation (99.9% reflectivity) is contaminated with up to 3% of p polarisation. In order to equilibrate the transmission characteristics of the two branches, the polarisation of the s-branch is "cleaned" with a second cube (P_2).

The transmission of the two branches cannot be balanced exactly, one there-

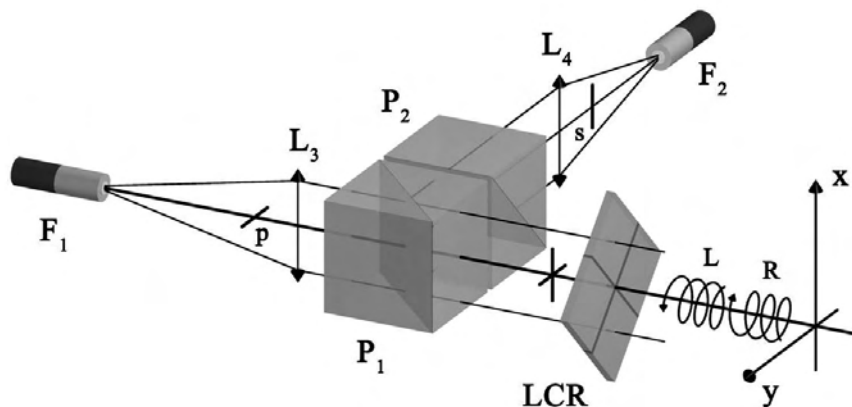


Figure 7.7: Circular polarisation analyser. F_1 , F_2 : fiber optics input collecting the p- resp.and the s-polarised light, respectively. Other optical elements as in Fig. 6.2

fore has to modulate the polarisation of the light they collect. This is achieved by electrical switching of the fast and slow axes in the liquid crystal retarder. In one of the switching positions, right circularly polarised is converted into p-polarised radiation. Conversely it is converted into s-polarised radiation in the other switching position, thus interchanging the role of each branch. The use of LCRs (Meadowlark Optics, Frederick Co, USA) provides an elegant way of achieving this, albeit at the cost of precision. When switched, LCRs show a deviation of the direction of the induced axes of up to 4° and a difference in transmission of about 2‰ [48]. The manufacturer did his best to reduce the deviation problem and thanks to the dual-arm design we could use them in our instrument.

7.2.5 Correction Scheme Optics

The virtual enantiomer correction scheme described in Section 6.2 is composed of a total of five $\lambda/2$ retarder plates. The first two, LR_1 and LR_2 , are small (5 mm diameter) precision low order retarders (Halle) mounted on modified

brushless servo-motors from Minimotor SA (Croglio, Switzerland), fitted by us with hollow axles². The third, CC_1 , similar to the first two, is mounted on a mechanical part, designed by us, whose arm is pushed in and out of the beam path by an eccentric disk. The last two are cemented zero order waveplates (Casix Inc., Fujian, China) with a clear aperture of 33 mm and are mounted in a special slow rotator (LR_3) and in a moving arm (CC_2), respectively, both designed by us.

7.2.6 Exciting Laser Light

As mentioned in Section 5.2, the 532 nm exciting laser wavelength is now commonly used in ROA spectroscopy. It is worth to note that Hug [48] was the first to dare using a solid-state exciting laser, at a time when others did not venture to do so. Our new instrument also profits from this kind of laser, providing high output power and narrow spectral linewidth, crucial in Raman spectroscopy. Our approach is nevertheless quite unique.

We settled on a picosecond Cheetah-X, frequency doubled, high average power, diode-pumped solid-state (DPSS) laser system using patented SESAM[®] [85] technology from Time-Bandwidth Products AG (Zürich, Switzerland). This choice was driven by the plan to try and measure non-linear ROA in a subsequent experiment.

The Cheetah-X works on longitudinal diode pumping of a Neodymium doped Yttrium Vanadate (Nd:YVO_4) crystal, emitting at 1064 nm (Fig. 7.8). The light pulses are frequency doubled by a non-linear lithium triborate (LBO) second harmonic generation (SHG) crystal, resulting in the desired 532 nm.

²Hollow axles and other mechanical parts were manufactured by Markus Racheter.

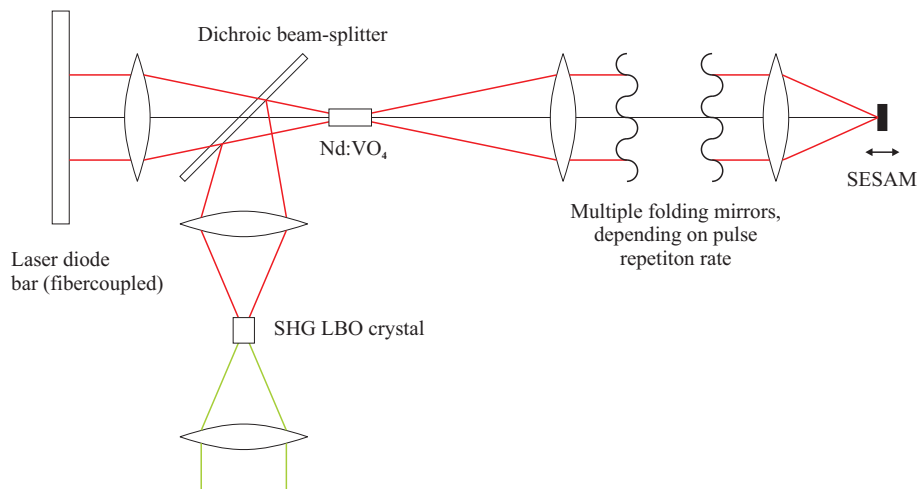


Figure 7.8: Schematic beam path of the Cheetah-X laser system.

The power supply and the laser head are water cooled, using a closed loop water circulating system which is temperature stabilised by a thermoelectric chiller. The SHG crystal is mounted in an oven and maintained at a temperature of 156.1°C for maximum efficiency. The maximum average output power obtained with this laser is 2.85 W.

The output beam is TEM_{00} ($M^2 < 1.1$) and horizontally polarised (100:1), with a spectral full width at half maximum (FWHM) of 0.043 nm (0.15 cm^{-1}). Modulation of the output power is achieved by rotating a $\lambda/2$ retarder plate in front of a polarising cube.

Switching the laser beam on and off during an acquisition cycle is achieved at the laser's output by a patented shutter (NM Laser Products Inc., Sunnyvale, CA, USA), which uses a cantilever flexure blade that is magnetic, has good thermal conductivity, provides excellent spring properties, and is optically coated. This optical blade is magnetically pulled to the open position by a closely coupled cylindrical toroid electromagnet. We also have a transverse KD*P switch, but the use of this extremely rapid shutter has been shown not

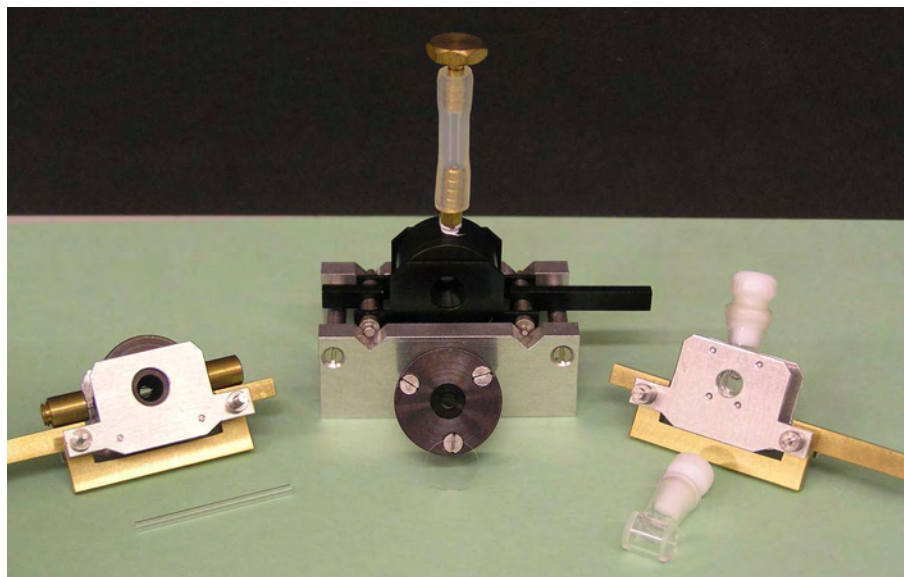


Figure 7.9: Picture of our sample cells. Left: disposable capillary cell and its holder. Middle: high-precision 21 to 27 μl cell. The upper cell in its holder is the aluminium one, for temperature controlled measurement. Right: Routine 120 μl macro cell with its holder.

to be as crucial as it was thought to be, especially when using the benefit of the *dark jump* (see Section 7.3).

With our instrument, ROA is for the first time measured using a non continuous wave laser.

7.2.7 Sample Cell and Temperature Control

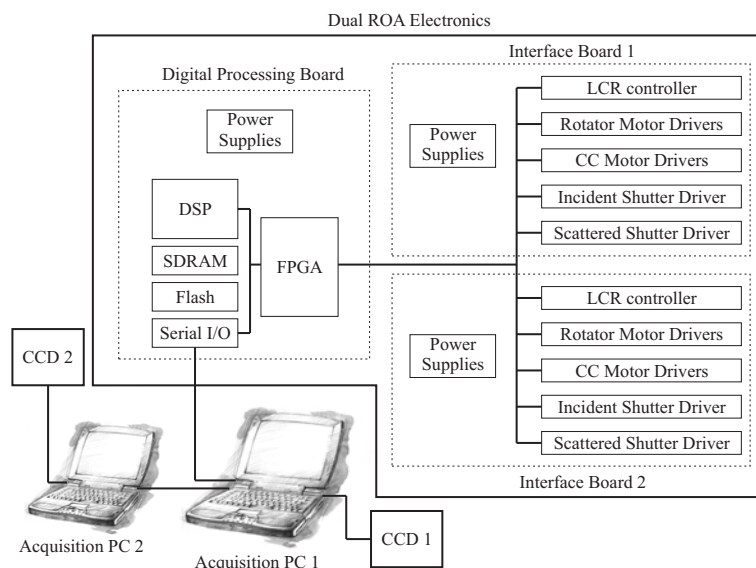
Our instrument is designed to accept different kinds of sample cells (Fig. 7.9). A high precision cell developed by Hug and Racheter, and modified in this work for temperature regulated measurements, whose volume ranges from 21 to 27 μl , depending on the cell's path length l . The cell's axis is oriented parallel to the direction of propagation of the exciting radiation. Measurements can also be recorded in a high precision 35 μl custom-made cylindrical cell (Helma, Müllheim, Germany) or in disposable, 1.3 mm inner and 1.7 mm outer

diameter, micro capillaries (Hirschmann, Eberstadt, Germany). For routine measurements of less expensive compounds, a bigger, 5 mm diameter, 6 mm long and 120 μ l cell is available.

In order to measure sensitive or highly volatile compounds, as well as protein water solutions, a temperature controlling cage has been developed, accepting all the previously mentioned cells (Fig. 7.9). Temperatures in the range of +80° to -30°C can be maintained by blowing a stream of dry air onto the sample cell. The temperature controlled air is obtained by the mean of an XR11851 Air Jet Crystal Cooler (FTS Systems Inc., Stone Ridge, NY, USA) and blown onto the sample from the top of an isolating cage. Moisture freezing on the 30 mm collection lens and other optics is avoided by blowing room temperature dry air through the cage's walls and by aspiration of more than the total amount of blown air, thus creating a small underpressure inside the cage.

7.3 Data Acquisition System

The overall data acquisition and architecture of our dual ROA (backward / forward scattering or linear / non-linear scattering) instrument is illustrated by the block diagram in Fig. 7.10. Two computers (acquisition PC 1 and PC 2), on which the acquisition software is installed, are connected via a dedicated ethernet link. The first PC communicates via a low speed RS232C serial bus with the instrument's electronics developed for us by Critical Link Inc. (Syracuse, NY, USA) and the data acquisition process for CCD camera 1 takes place via integrated camera electronics from Wright Instruments Ltd. The second PC communicates with the electronics via the acquisition PC (ethernet



link) and has the same camera electronics integrated for reading out CCD camera 2.

The dual ROA electronics is composed of three boards. It replaces the functions of the hand-wired electronics developed by Hug and still used in our instrument located in Zürich. The Digital Processing board is designed around a Texas Instruments high performance floating point Digital Signal Processor (DSP) TMS320C6712. The DSP is primarily responsible for running the instrument's electronics as well as communicating with the acquisition PC 1 and the two interface boards. The DSP receives commands from the acquisition PC 1 and manages the acquisition cycle with an on-board Field-Programmable Gate Array (FPGA). The latter is based on a Xilinx XC2S100 module with 90 available I/O lines and 100 K programmable cells. The FPGA accepts commands from the DSP and controls all the opto-mechanical components via the interface boards, which include motor and shutter drivers, as well as LCR drivers. The LCR portion includes a temperature controller and an A/D

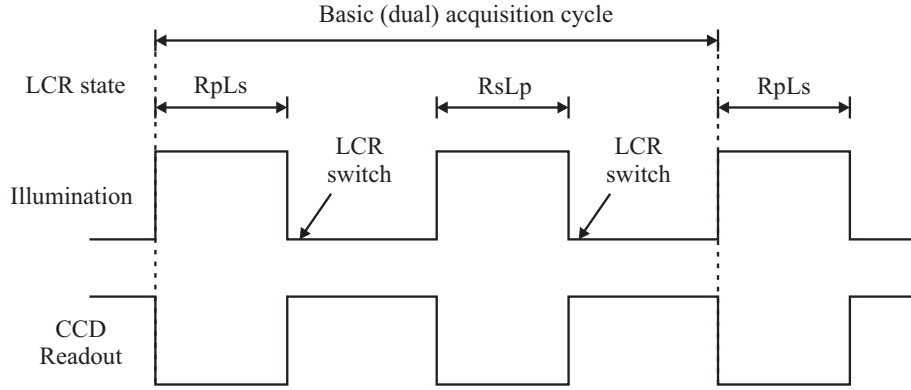


Figure 7.11: Time diagram of a basic acquisition cycle.

converter for LCR temperature monitoring.

7.3.1 Basic Acquisition Cycle

A basic acquisition cycle (Fig. 7.11), without any correction scheme except for the dual branch design, requires exposure of the CCD, electrical switching of the liquid crystal retarder to interconvert the two branches, reading of the CCD with exposure switched off, and repeating this sequence.

The LCR switching is not time critical, it is done at the start of the readout period, which provides sufficient time for the LCR to settle into its new state. In state one (RpLs), the circular polarisation analyser passes the right circular component of the scattered radiation by the p branch and the left circular by the s branch. Light from the p branch is guided to the upper half of the CCD detector and light from the s branch to the lower half, yielding simultaneously the two sets of data I_R^p and I_L^s . Switching the LCR to state two (RsLp) yields I_R^s and I_L^p . The Raman and ROA spectra, in other words the sum and difference intensities, are calculated by the computer from the last four sets of data.

$$I_R + I_L = \frac{1}{2} (I_R^p + I_L^s + I_R^s + I_L^p) \quad (7.3)$$

$$I_R - I_L = \frac{1}{2} [(I_R^p - I_L^s) + (I_R^s - I_L^p)] \quad (7.4)$$

7.3.2 Timing Units and 8-cycles

In the more complex acquisition timing involved by the virtual enantiomer correction scheme, in which linear rotators have to be synchronised, all the timing intervals generated by the FPGA are measured in basic timing units (TUs), whose value amounts to 1/218th of a second, or approximately 4.59 ms. It corresponds to half the length of the period of our reference frequency of 109 Hz, chosen in order to avoid interferences from 50 and 60 Hz line frequencies. In our design, the rotation speed of the three linear rotators are chosen in such a way that the orientation of all these elements repeats itself after 16 TUs, or 73.4 ms. Such a block of TUs is called a timing block (TB) and it represents the shortest possible duration for an exposure window, while the time required for readout amounts to at least 2 TBs. Depending on the sample and CCD saturation, the length of an exposure window is constrained to a multiple of TBs, in order to guarantee averaging over all polarisation states produced by the rotation of the three linear rotators.

During readout of the CCD, the scattered radiation is prevented from reaching it by switching off the laser (dark window), thus allowing a blanking of all the CCD surface and reducing the sample's irradiation time. The mechanical shutter we use shows a small systematic difference in the opening and closing speed, resulting in a small excess of one polarisation state of a pair of orthogonal linear polarisation states, and could therefore be a source of offsets if a timing trick, the *dark jump* [49], would not have been implemented: the length of each readout window following a dual acquisition cycle is automatically in-

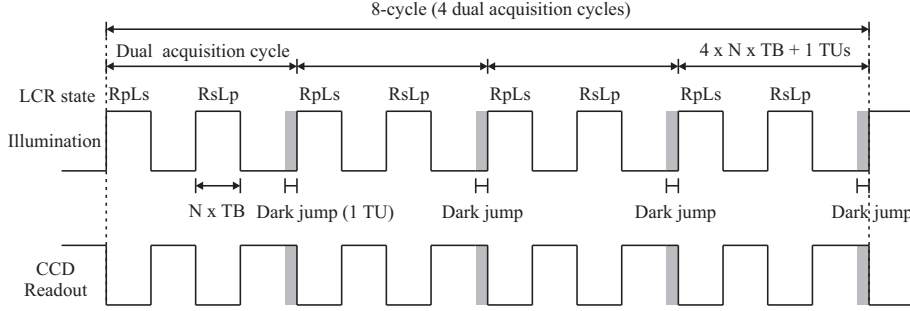


Figure 7.12: Time diagram of the 8-cycles acquisition.

creased by one timing unit TU. With the rotation speed of LR_1 , LR_2 and LR_3 set in a precise way, a rotation in the initial orientation of the plane of polarisation at the start of each exposure window of 45° occurs. An essentially complete compensation of offsets is achieved after 16 dark jumps, which is why the data acquisition is grouped into 8-cycles (8 exposures, 8 readouts and 4 dark jumps), corresponding to four dual acquisition cycles (Fig. 7.12).

7.3.3 Complete Acquisition Cycle

As mentioned in Section 6.3, a complete acquisition cycle is composed of 4 phases, patterned [00], [01], [10] and [11], corresponding to four 8-cycles and hence 16 dark jumps, with the circularity converters moving in and out between these 4 phases (Fig. 7.13). The time needed for CC_1 to move in or out of the beam path is about 115 ms, less than 2 TBs, thus taking place in a single readout window. It is therefore moved with a higher frequency than CC_2 , whose motion is slower, and sometimes exceeds the length of a readout window (setting of an error), except if the window is set to be rather long. The electronics recognises this error, discarding the following data, and continues the acquisition cycle uninterrupted, but keeping all the timing relations and the counting of the number of dark jumps frozen till the start of the next

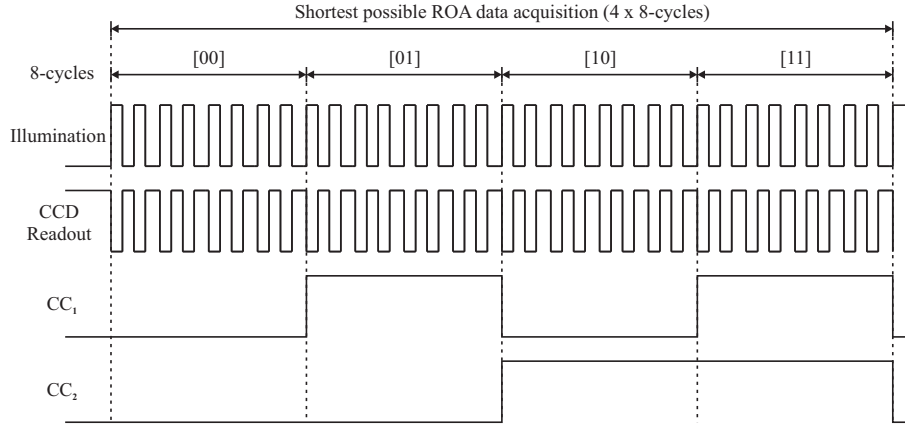


Figure 7.13: Time diagram of a complete acquisition cycle.

valid exposure window, with the goal of locking the orientation of the plane of polarisation produced by the linear rotators.

7.3.4 CCD Readout and Binning

The CCD is composed of a 256 x 1024 pixels surface divided in two 128 pixels halves, and an output register composed of 1024 pixels, located at the lower edge of the chip, used to read the 1024 columns of 256 pixels (Fig. 7.14). The charges of the whole surface along the dispersion direction (1024 pixels wide) are shifted down by one pixel, thus shifting the lower pixel row into the readout register. Its content is then clocked out address by address, amplified, AD converted and numerically stored before it is finally transferred to the acquisition PC. This mode of reading the CCD, the image mode, is quite slow but, in turn, the charge on each single pixel is known. On-chip binning in the vertical direction (along the slit length) can then be performed relative to this video image, in order to reduce readout time and noise. The surface is binned into 16 rows for each half of the CCD, by spreading the energy evenly over the 16 rows. A typical charge distribution on the detector and the corresponding

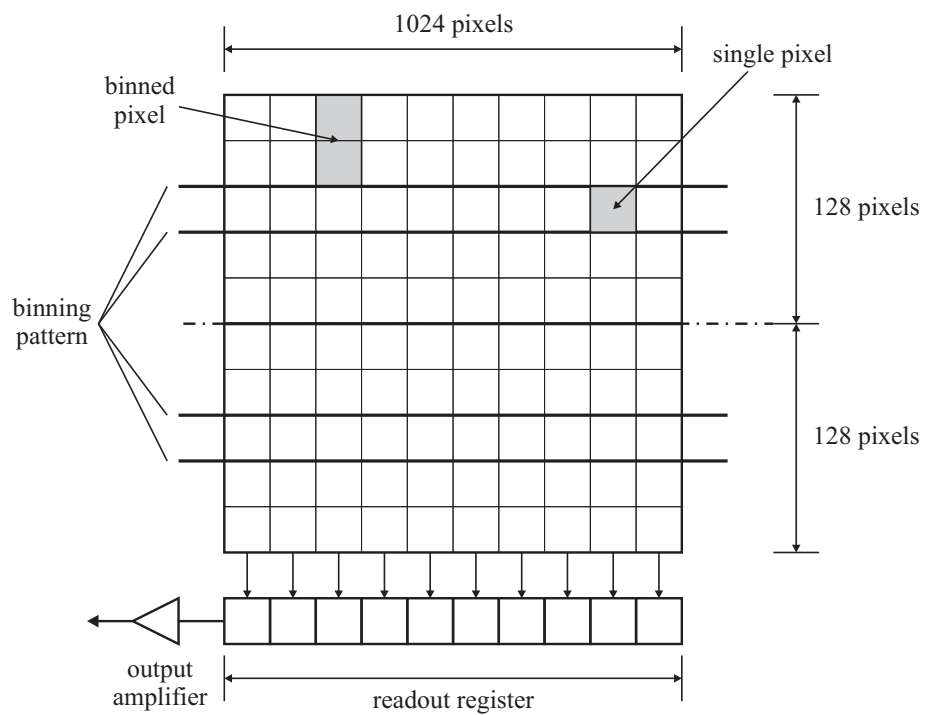


Figure 7.14: Schematic overview of a CCD detector. In image mode, 256 rows of 1024 single pixels are read one after the other, while in binning mode, only 2x16 rows, composed of binned pixels, are read.

binning pattern are illustrated in Fig. 7.15.

The single pixel saturation charge of our CCD camera is around 5.4×10^5 electrons, and the gain setting is 1 ADC count = 10 electrons, so that full scale (16 bits) A/D reading would be about 6.5×10^5 electrons. The relatively small capacity of the read-out register is essentially the same as for the individual pixel, and represents one of the limiting factors in the overall read-out speed. Setting exciting power and illumination time is done during the binning process, where in full image mode, the maximum single pixel charge can be evaluated, and which we try to set below 2.5×10^5 electrons. This value represents about half of the single pixel saturation charge.

7.3.5 The 16 Buffers

During a complete acquisition cycle, data read from the two halves of the CCD are saved in 16 buffers, depending on the correction phase ([00], [01], [10] or [11]), the branch from which the collected scattered radiation arises (A or B) and finally the state of the liquid crystal retarder (0 or 1). These 16 buffers (A to P) are not organised in the same way for our two instruments. A description and a correspondence table for these two different conventions can be found in the Appendices.

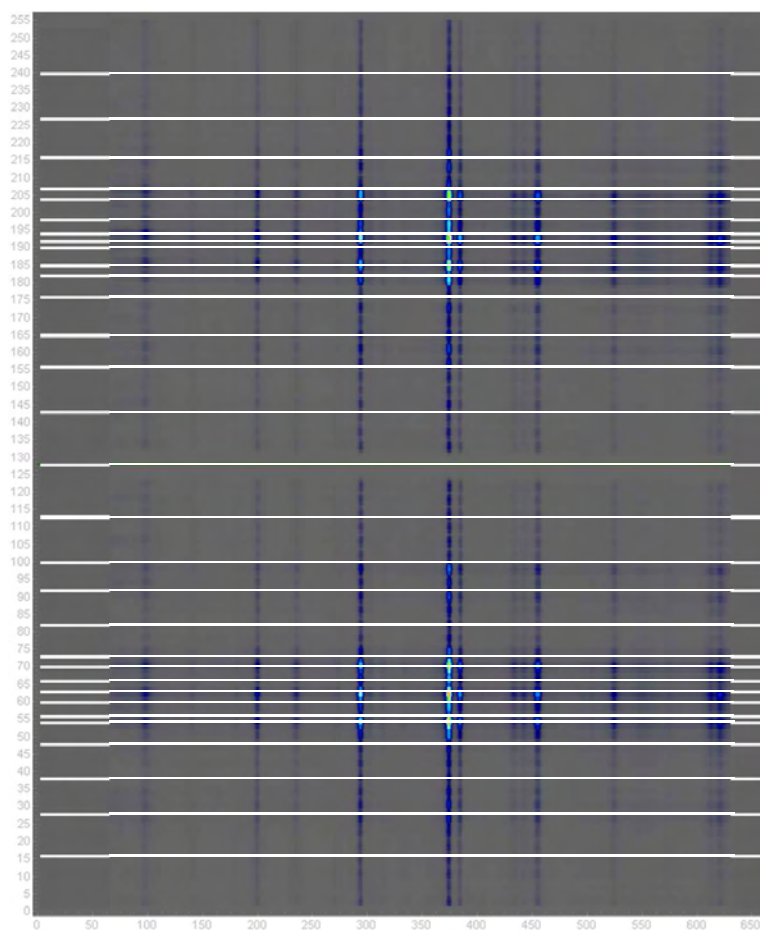


Figure 7.15: Typical binning pattern for toluene. White horizontal lines separate binned rows. The picture is a full resolution CCD video image from column 0 to column 650 ($\Delta\tilde{\nu} \approx -87 - 1672 \text{ cm}^{-1}$).

Chapter 8

Instrumental Performances

In this chapter, an illustration of the performance of our dual-channel SCP back- and forward scattering ROA spectrometer is given, by means of Raman optical activity measurements of commercially available reference substances. The degree of circularity C of the scattered radiation will also be used as a performance demonstration. When measured in SCP backscattering with right circular incident radiation, ${}^RC(\pi)$ is given by [9]

$${}^RC(\pi) = \frac{{}^RI_R(\pi) - {}^RI_L(\pi)}{{}^RI_R(\pi) + {}^RI_L(\pi)} = -{}^RC(0) \quad (8.1)$$

${}^RC(\pi)$ can be measured with a single CCD readout, ${}^RI_R(\pi)$ and ${}^RI_L(\pi)$ being registered in a truly simultaneous fashion.

A collection of experimental spectra measured in backscattering will first be described, followed by some spectra collected for the first time in SCP forward scattering.

8.1 Backscattering SCP Spectra

The substances were used as obtained from the suppliers. Reference compounds were chosen as well as a list of solvents in which Raman optical activity

can be measured. They are all listed in Table 8.1, with their respective quality. Aqueous solutions were prepared by dissolving the corresponding compounds in H₂O and D₂O. The solutions were then filtered through a 0.2 μm pore size filter.

The measurements were performed with different cells, a macro 120 μl cell, a 27 μl high precision cell, and disposable micro capillaries filled to a volume of about 10-12 μl . The laser wavelength was 532 nm in all cases and power indications are for power measured at the sample cell. If not mentioned differently, the standard way to draw spectra is as follows: bottom: Raman; middle: ROA; top: degree of circularity. A Savitzky-Golay third order five points smoothing was applied for all Raman spectra. For the ROA spectra of neat compounds, a similar smoothing was applied, whereas for compounds measured in water or heavy water, a Savitzky-Golay third order nine points smoothing was used.

8.1.1 Degree of Circularity

In order to account for the transmission difference between branch A and B and to improve the signal to noise ratio, measurements of the degree of circularity for CCl₄ were recorded in multiple scans, by switching the liquid crystal retarder between scans and by adding the results.

CCl₄

Figure 8.1 shows backscattering spectra of CCl₄ recorded in the macro cell¹. The value of $^RC(\pi)$ for the fully polarised 464 cm⁻¹ and the depolarised 320

¹The measure of $^RC(\pi)$ for CCl₄ in our 27 μl cell showed a components of the glass windows around 920 cm⁻¹

Table 8.1: List of chemical substances and their respective quality.

| Substance | Supplier | Quality |
|------------------------------------|--------------|---------------------|
| Toluene | Fluka | 99.5% (GC) |
| (-)- α -pinene | Fluka | 99.0% (GC) |
| <i>R</i> -(+)-propylene oxide | Fluka | 99.0% (GC) |
| Neopentane | Linde AG | 99.5% (GC) |
| Neopentane- d_{12} | CDN Isotopes | 99.4% atom D |
| (-)- β -pinene | Fluka | 99.0% (GC) |
| L-Alanine | Fluka | 99.0% (NT) |
| L-Ascorbic acid | Fluka | 99.0% (RT) |
| D-(-)-Isoascorbic acid | Fluka | 99.0% (RT) |
| Deuterium oxide (D ₂ O) | Aldrich | 99.9% atom D |
| Chloroform | Fluka | IR spectrosc. grade |
| Chloroform- d | Aldrich | 99.8% atom D |
| Carbon tetrachloride | Merck | for analysis |
| Acetonitrile | Fluka | UV spectrosc. grade |
| Acetonitrile- d_3 | Aldrich | 99.8% atom D |

Table 8.2: Degree of circularity ${}^RC(\pi)$ and calculated depolarisation ratio for CCl_4 .

| $\tilde{\nu}$ [cm^{-1}] | with CC_2 | | without CC_2 | |
|------------------------------------|--------------------|------------------|-----------------------|------------------|
| | ${}^RC(\pi)$ | ρ_{\perp}^a | ${}^RC(\pi)$ | ρ_{\perp}^a |
| 320 | 0.645 | 0.70 | 0.675 | 0.72 |
| 464 | -0.928 | 0.018 | -0.952 | 0.012 |

^a calculated from measured ${}^RC(\pi)$ with: $\rho_{\perp} = \frac{1+{}^RC(\pi)}{3-{}^RC(\pi)}$ [9]

cm^{-1} band are -0.928 and 0.645 (Table 8.2), respectively. These values are not as good as those given in Ref. [48], but overall satisfactory. A detailed analysis should nevertheless be done to find out the source of this difference. Removing CC_2 for the measurement of the degree of circularity gave values of -0.952 and 0.675. Readjusting the orientation of the quarter wave plate's axis did not improve the results. Better values could perhaps be obtained by rotating the position of the LCR, which has not been tested at all. All the following spectra in this work have been recorded with these settings and with CC_2 in the beam path.

Toluene

Backscattering spectra of neat toluene recorded with a single-shot, 73.4 ms and 20mW illumination time (1.47 mJ) are illustrated in Figure 8.1. The value of 73.4 ms is the shortest illumination time that can be set in our software. Further reduction of pulse energy would still give a satisfactory Raman spectrum.

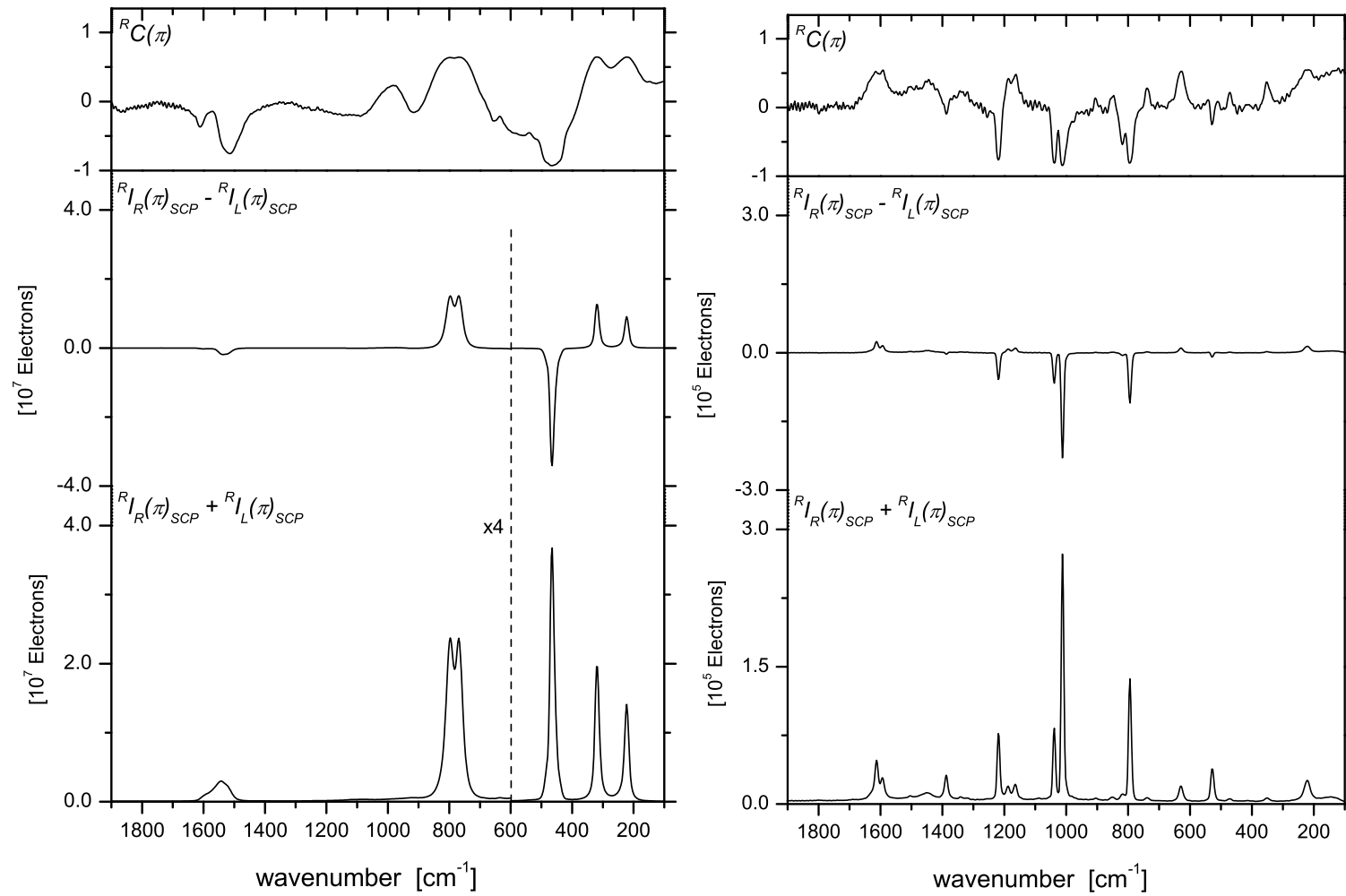


Figure 8.1: Left: Backscattering spectra of neat CCl_4 recorded in the macro cell. Data are blown up by a factor of 4 for wavenumber shifts larger than 600 cm^{-1} . Exciting energy: 530 mJ (5.3 s, 100 mW). Right: Backscattering spectra of neat toluene. Exciting energy: 1.47 mJ (0.0734 s, 20 mW).

8.1.2 Raman Optical Activity

The main feature of this instrument is its ability to measure Raman optical activity of pure chiral compounds, or their solutions (with sufficiently high concentrations) in common solvents like water, with low exciting energy, small sample volume and in a couple of minutes.

Toluene

Figure 8.2 shows the ROA spectrum of neat toluene recorded in our precision cell. After one complete correction cycle (1.4 J exciting energy), an offset free zero ROA spectrum is obtained, even for strongly polarised bands, a situation that stays quite similar after 81 corrections cycles (114 J exciting energy), with low offsets for the high polarised 794 cm^{-1} and 1222 cm^{-1} bands.

(-)- α -pinene

The absolute configuration of (-)- α -pinene, the reference chiral compound for spectroscopic calibration, could be determined in a 32 s single acquisition cycle, recorded with less than $10\text{ }\mu\text{l}$ of substance in a disposable capillary. For comparison, Figure 8.3 shows a high quality ROA spectrum of (-)- α -pinene recorded in our precision cell. The similarity of both spectra is heartening. Even the negative ROA for the CC double bond stretching at 1668 cm^{-1} is reproduced in the 32 s record. Strongly polarised bands have usually been considered in the field of ROA to have a negligible backscattering ROA. From the spectra recorded in the precision cell, this is not so, at least for finite light collection angles. The positive ROA for the 674 cm^{-1} band is actually substantial in the precision measurement, as well as in the 32 seconds capillary

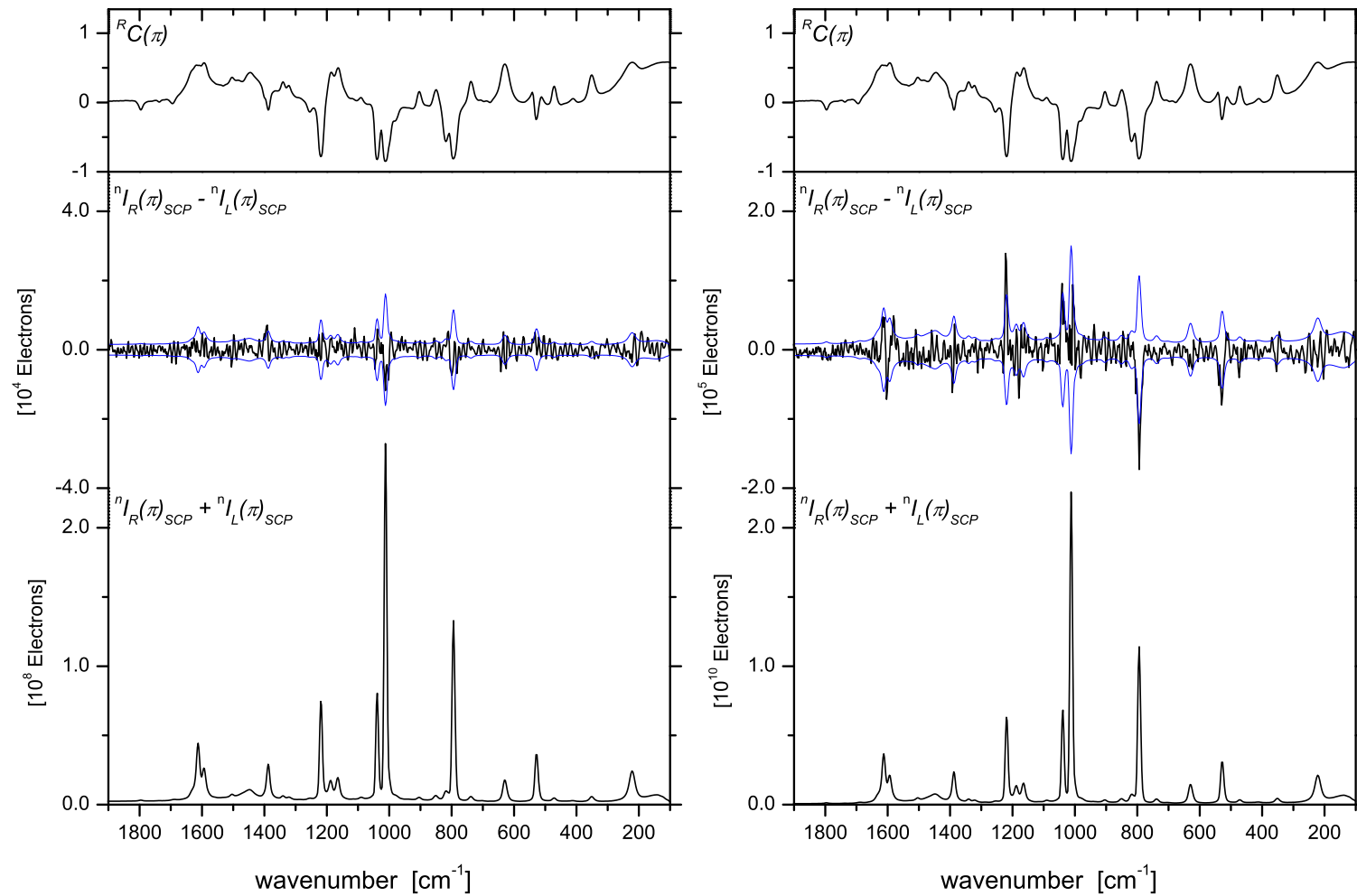


Figure 8.2: Backscattering spectra of neat toluene recorded in the high precision cell. Left: 1 complete correction cycle (32 scans), exciting energy: 1.4 J (14 s, 100 mW). Right: 81 correction cycles (2592 scans), exciting energy: 114 J (19 min, 100 mW). Blue lines indicate the expected r.m.s shot noise (square root of the Raman spectrum).

measurement, where it suffers from noise due to the short exposure time. A longer spectral acquisition of (-)- α -pinene in disposable capillaries (see Appendices) gave spectra of the same quality as those measured in our precision cell, which are exactly similar to those published by Hug in 2003 [49]. We believe that this backscattering positive feature is real, as it is also confirmed by *ab initio* computations. When measured in forward scattering (see Appendices), the 674 cm^{-1} band gives a substantial positive ROA signal, and it could be possible that a small component of forward scattered light, back-reflected by the output cell window, is collected by the backscattering optics. Further investigations will have to be made in this respect, by measuring backscattering spectra with the sample cell inclined, in order to avoid back-reflected forward scattered light to be collected.

(*R*)-(+)-methyloxirane

Figure 8.4 shows the ROA spectrum of the well known (*R*)-(+)-methyloxirane ((*R*)-(+)-propylene oxide). A very satisfactory ROA spectrum could be obtained in a disposable capillary, with about 20 min of illumination time and 200 mW of laser power at the sample, which corresponds to 1184 CCD illumination periods of 1029 ms each. To this, a 360 ms read-out overhead for each CCD illumination has to be added, which increases the total recording time to approximately 27 min. This spectra can be compared to reference spectra measured with our instrument in Zürich [86]. The smallest features of the ROA are well reproduced, like the extended negative band slightly below 200 cm^{-1} due to the methyl torsional mode. Polarised bands are somewhat overestimated but their sign is correctly reproduced. The Raman spectrum shows no contribution arising from the glass wall of the capillaries and the overtones

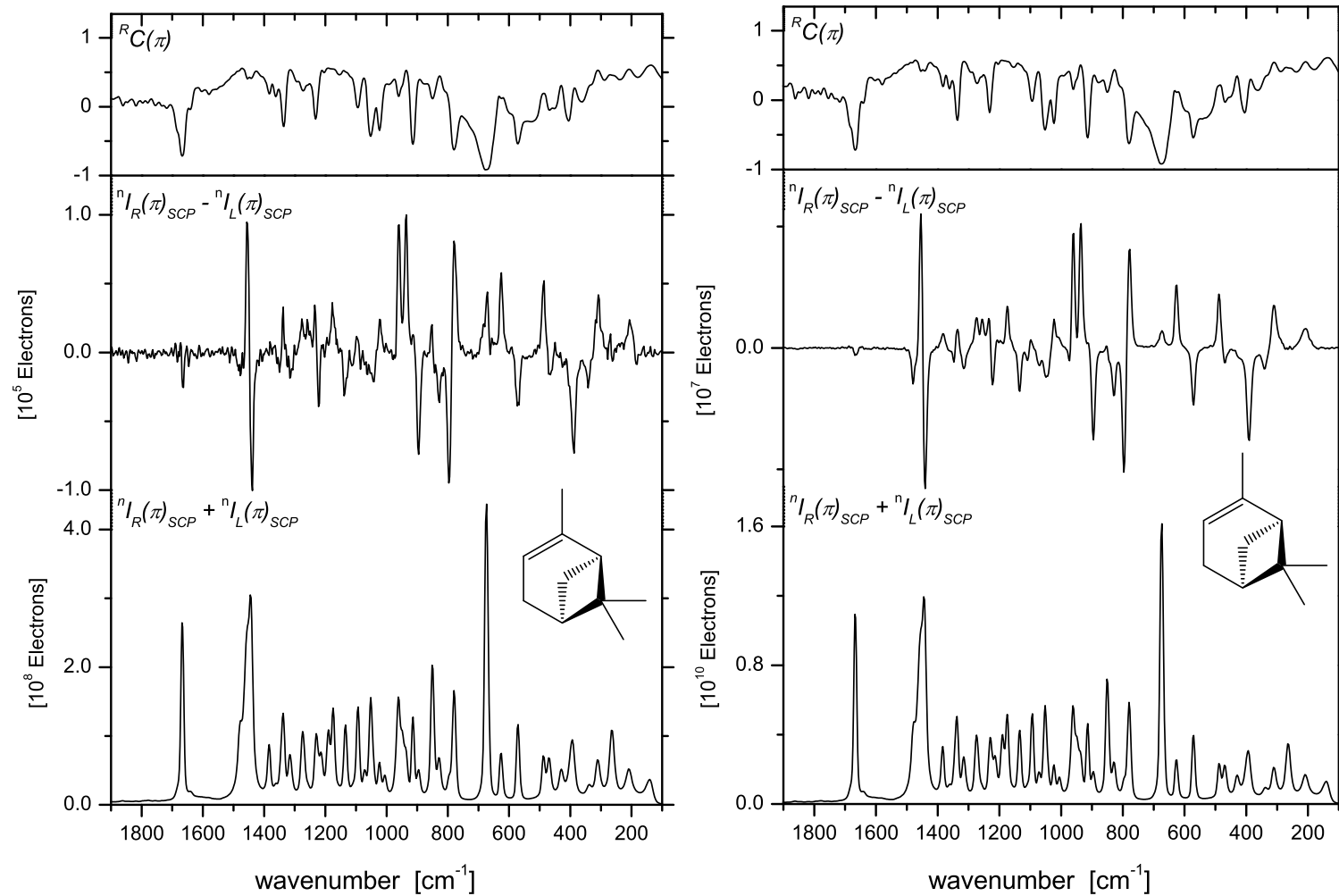


Figure 8.3: Backscattering spectra of (-)- α -pinene. Left: disposable capillary, 1 complete correction cycle (32 scans), exciting energy: 9.6 J (32 s, 300 mW). Right: high precision cell, 57 correction cycles (1824 scans), exciting energy: 360 J (20 min, 300 mW).

of the fundamental frequency at 754 cm^{-1} found at 1480 cm^{-1} and identified in Ref [54] is visible in our capillary measurement.

L-alanine

ROA can be measured in different solvents (Figure 8.5), from which water is the most suitable for applications in biochemistry. Figure 8.6 shows Raman and ROA spectra of water and heavy water, both poor Raman scatterers, which provide almost featureless backgrounds. Figure 8.7 presents spectra of 1.5 M aqueous solutions of the zwitterionic state of L-alanine, the simplest chiral amino acid. Spectra of very good quality were obtained in our precision cell in less than three-quarter of an hour, compared to the 3 hours of Barron in 1991 [87] and the 123.2 hours needed in 1995 in a dual circular polarisation experimental setups [88]. The Raman and ROA spectra are very sensitive to the nature of the solvent, especially in the $700 - 1200\text{ cm}^{-1}$ region. We do not subtract the Raman water background from the recorded L-alanine solution spectra, but draw them with a striped pattern on the same axis, giving a better impression of which features arise from the amino acid itself. Both spectra are in very good agreement with previously reported ROA spectra.

Neopentane

Neopentane is a compound that will be treated in detail in Chapter 11. It has been measured in disposable capillaries and in our precision cell at a temperature of 0°C . The Raman spectrum is of excellent quality with both cells, whereas in the ROA spectrum, a substantial offset for the strongly polarised and narrow breathing band at 742 cm^{-1} occurs in the capillaries. A similar offset is visible in the precision cell but much weaker. The bandwidth of

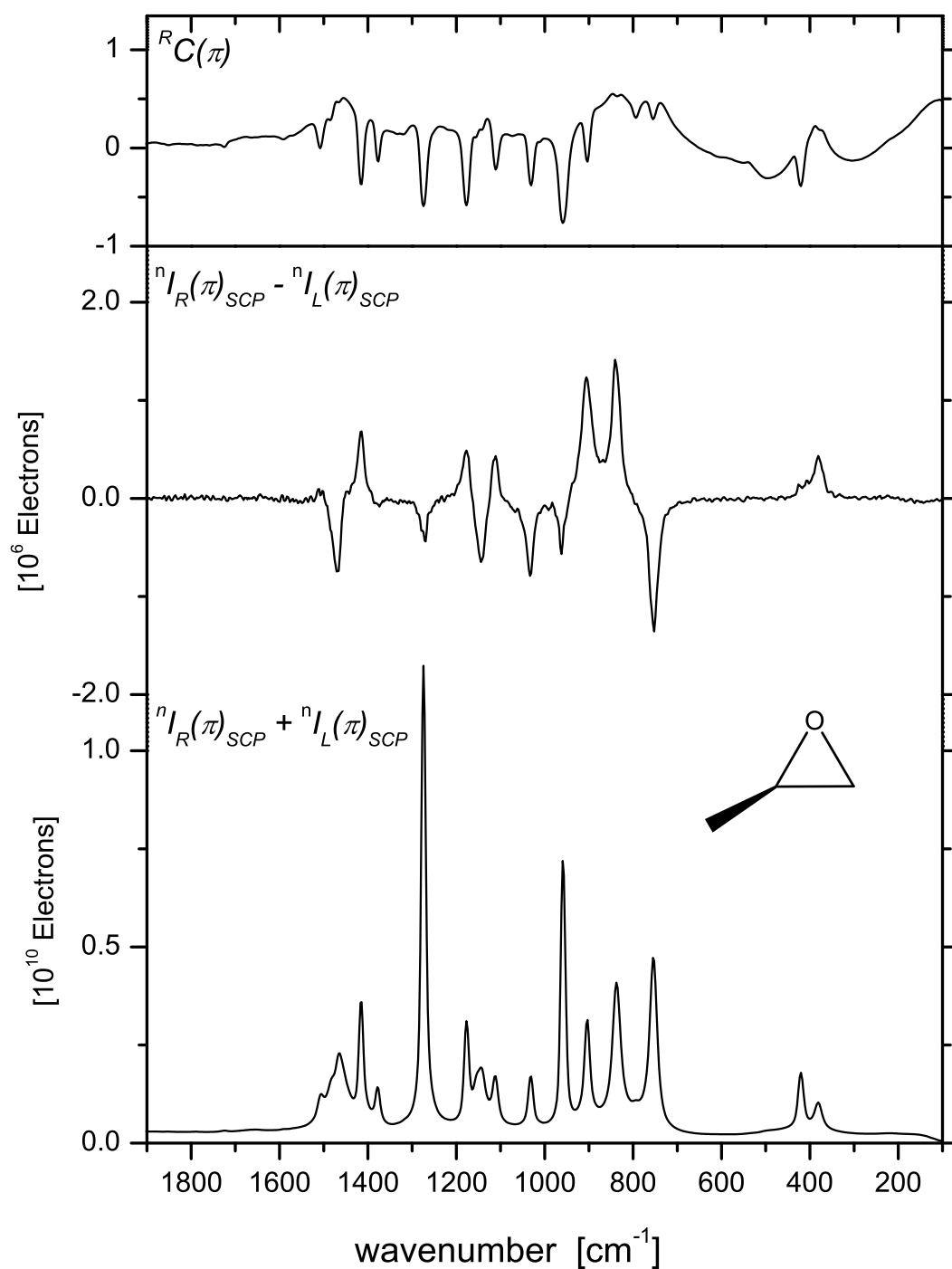


Figure 8.4: Backscattering spectra of (*R*)-(+)-propylene oxide recorded in a disposable capillary. 37 correction cycles (1184 scans), exciting energy: 240 J (20 min, 200 mW).

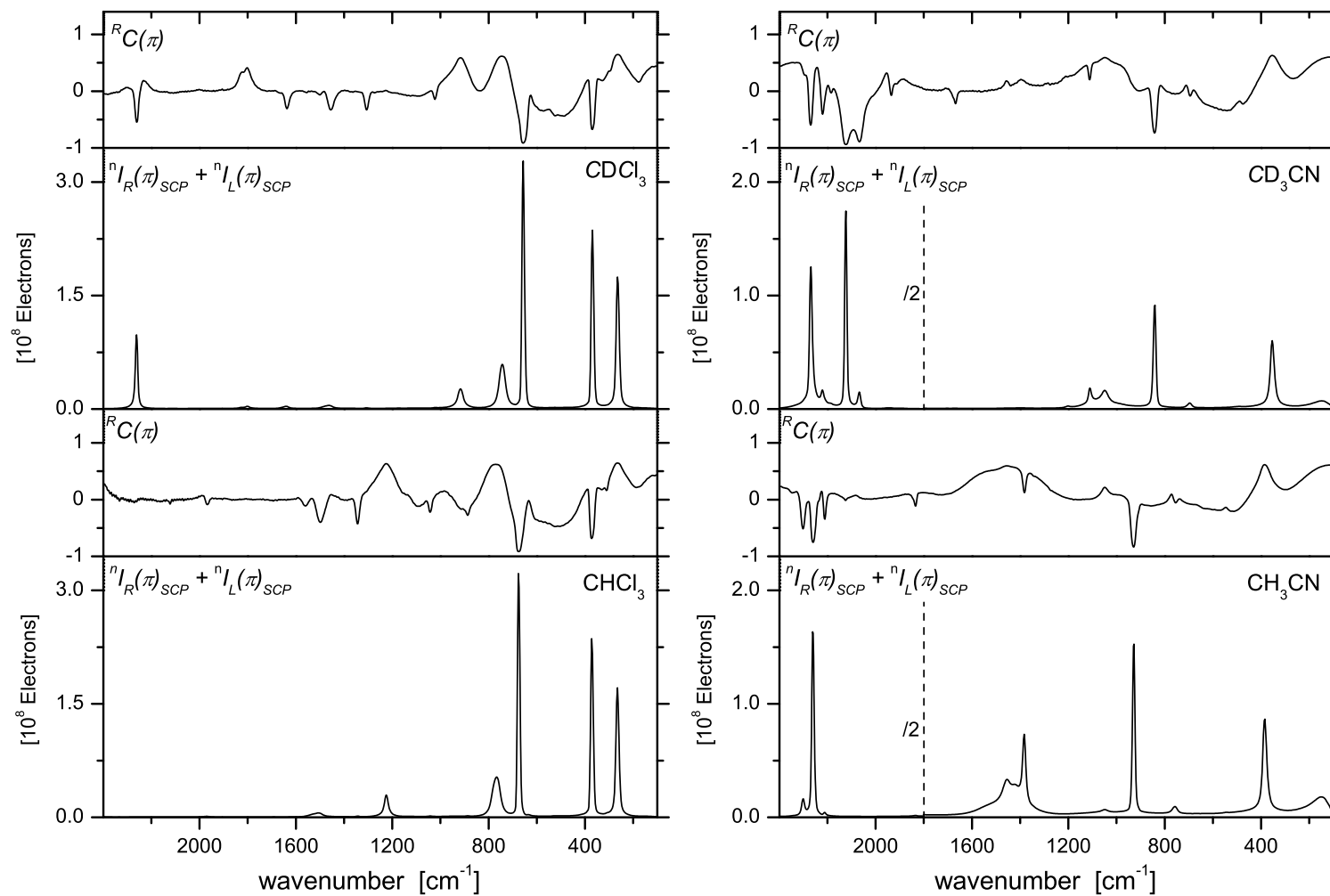


Figure 8.5: Left: backscattering spectra of chloroform (bottom) and chloroform- d (top). Right: backscattering spectra of acetonitrile (bottom) and acetonitrile- d_3 . For all spectra: 32 scans (200 mW).

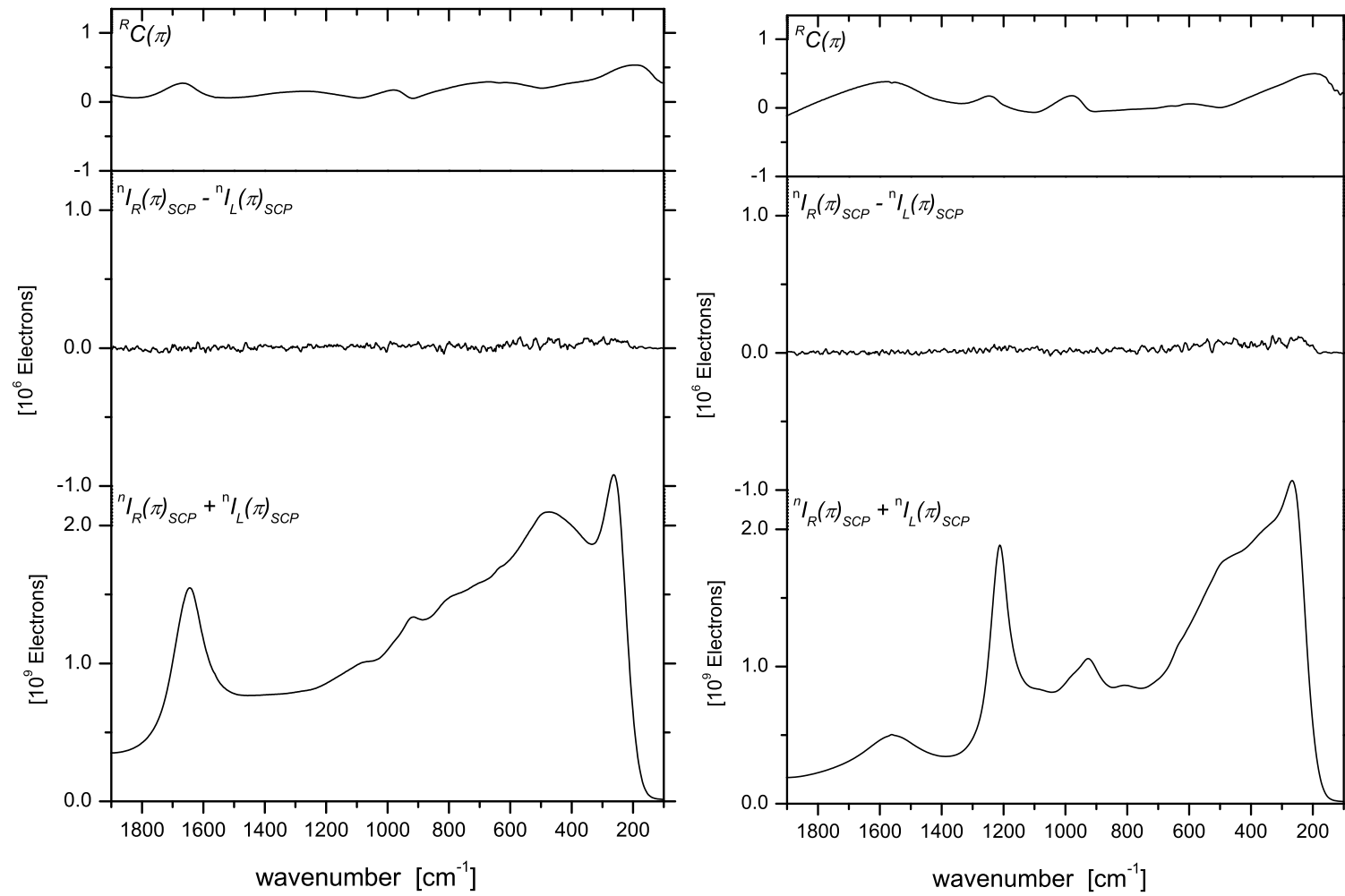


Figure 8.6: Left: backscattering spectra of water. Right: backscattering spectra of heavy water (D_2O). For both sets of spectra: 37 correction cycles (1184 scans), exciting energy: 1.92 kJ (40 min, 800 mW).

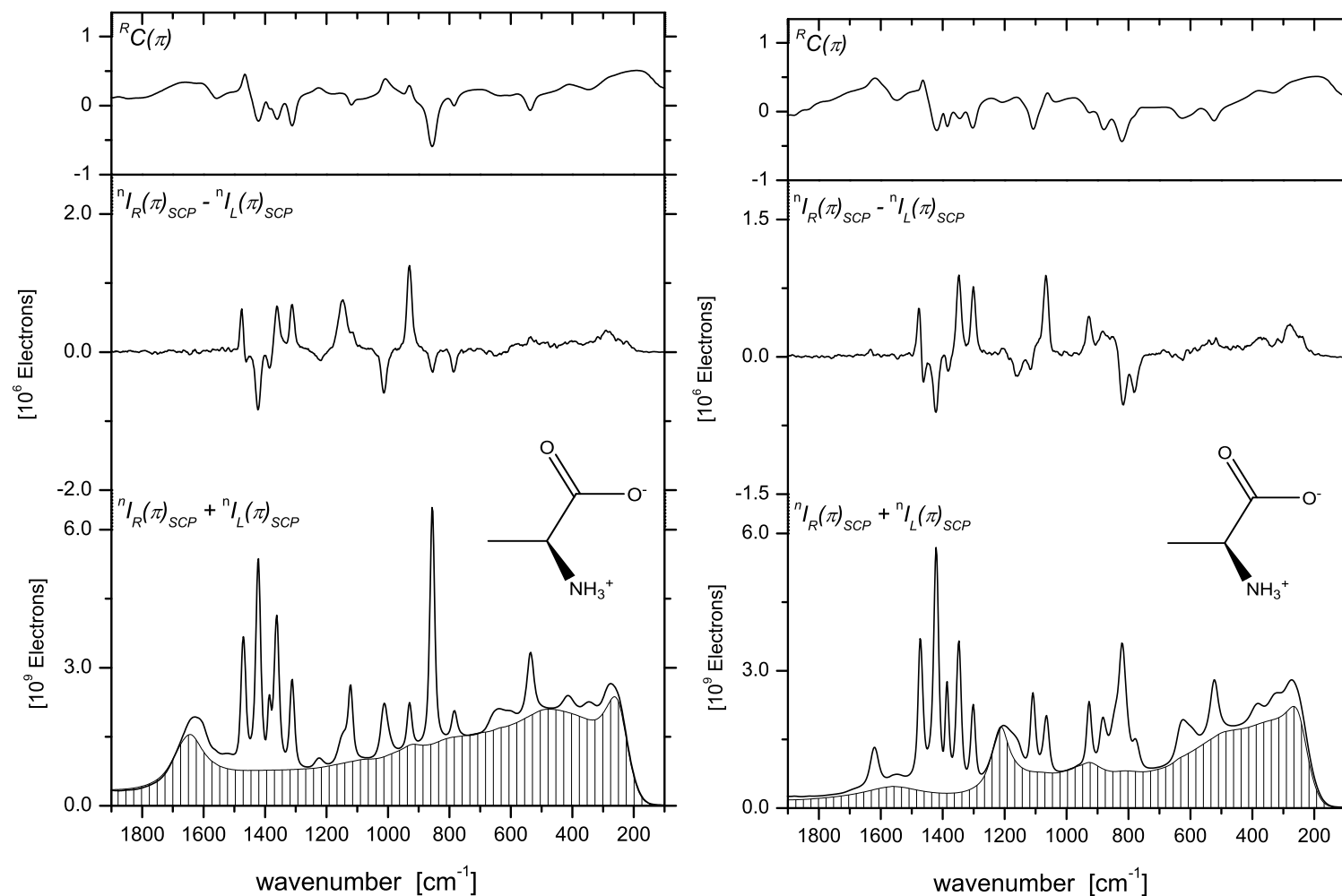


Figure 8.7: Left: backscattering spectra of a 1.5 M L-Alanine water solution recorded in the high precision cell. Right: backscattering spectra of a 1.5 M L-Alanine heavy water solution recorded in the high precision cell. The Raman spectra of pure H₂O and D₂O are shown (striped pattern). For both sets of spectra: 37 correction cycles (1184 scans), exciting energy: 1.92 kJ (40 min, 800 mW).

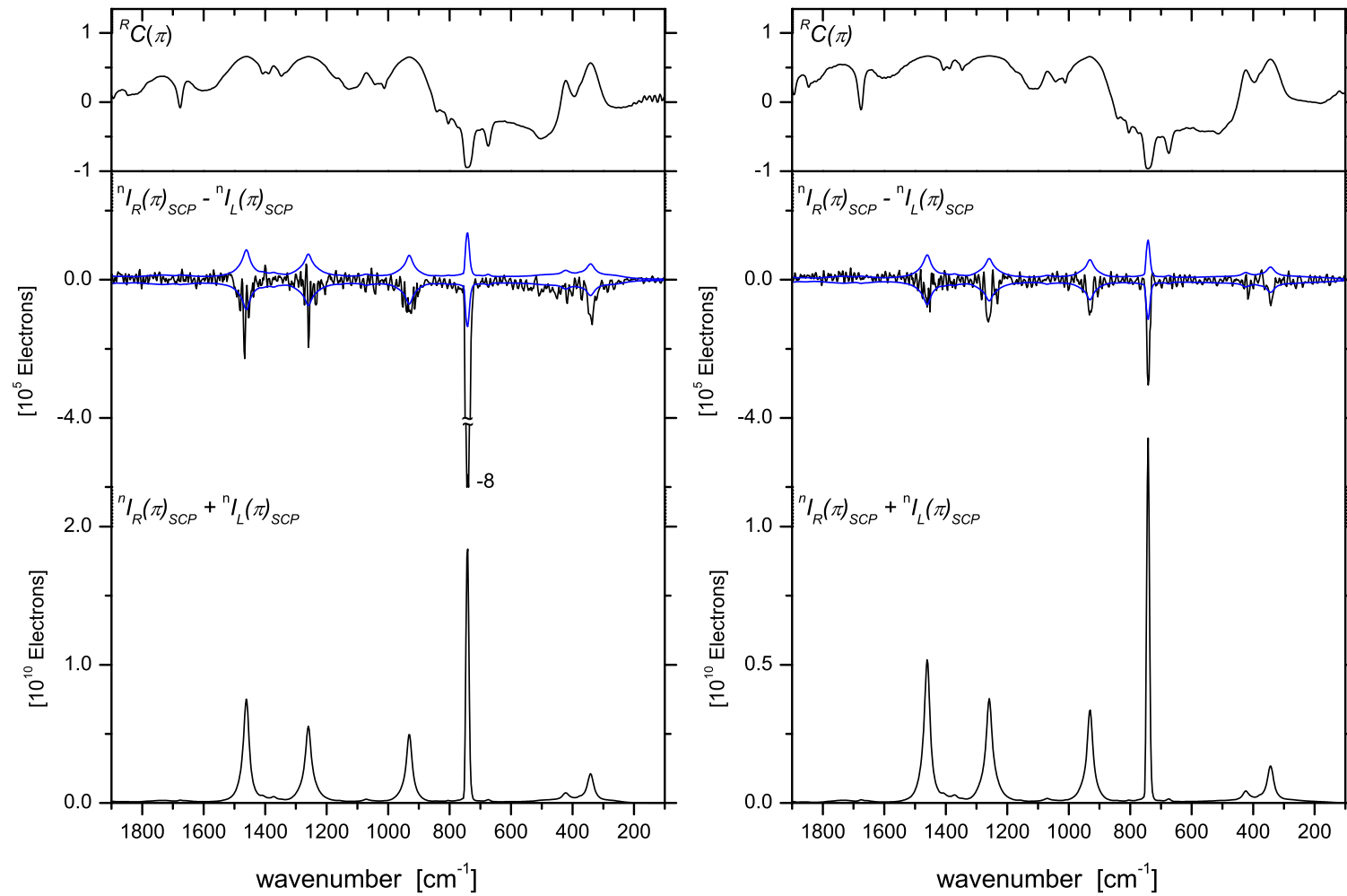


Figure 8.8: Backscattering spectra of neat liquid neopentane recorded at 0°C. Left: disposable capillaries. Right: precision cell. For both records: exciting energy: 240 J (20 min, 200 mW).

that breathing mode has been determined to be around 9 cm^{-1} , a value at the limit of our 7 cm^{-1} instrumental resolution. The rest of the spectrum is of acceptable quality, and we hope to be able to measure, once the synthesis of it becomes possible, (*R*)-[$^2\text{H}_1, ^2\text{H}_2, ^2\text{H}_3$]-neopentane, chiral by selective isotopic substitution. Depending on the quantity available after synthesis and purification, the use of the precision sample cell will be favoured.

8.2 Forward Scattering SCP Spectra

8.2.1 Degree of Circularity

As mentioned earlier, forward SCP scattering has been implemented for the first time during this work. During the implementation process of the forward scattering geometry, an improvement in the cabling of our instrument was realised, with the goal to reduce interferences due to electrical ground loops. We had to use the same CCD camera controller as for backscattering, as it turned out that our second controller showed a still unexplained noise problem. In order to get a first guess of the forward scattering reliability, we compare the value of the degree of circularity for the two bands of CCl_4 at 320 and 464 cm^{-1} reported in Table 8.2. The measured $-^R C(0)$ values were of 0.675 and -0.963, corresponding to depolarisation ratios of 0.72 and 0.009, respectively, even better than those measured in backscattering.

8.2.2 Raman Optical Activity

(-)- β -pinene

(-)- β -pinene was chosen to illustrate SCP(0) scattering, as it is one of the two compounds, for which ICP forward ROA spectra have been published

[66]. Figure 8.10 shows the forward and backscattering SCP spectra obtained after the cabling modification. Both spectra are of very good quality. They were recorded in a non-simultaneous fashion, as it turned out that scattered radiation, reflected by the fiber optics heads, can be back-reflected, and thus collected by the 180° opposite lens. The effect of such back-reflections was observed in particular when collecting the backscattered spectra, whereas for forward scattering, these effects were of minor importance, but still evident. In the actual configuration, the focal point of both Gadium lenses is not located exactly at the same point. When measuring, for example, in backscattering, the forward scattered light is thus not perfectly collimated by its optics, and is therefore not well focused on the fiber optic heads. The material surrounding the fiber optics is polished, thus reflecting a high amount of light, which is certainly the source of the observed offsets.

When measuring in one direction, the opposite scattered radiation was therefore dumped in order to avoid undesirable back-reflected radiation. The recorded spectra (see Appendices) show the effect of such back-reflections for ROA spectra of (-)- β -pinene, when measured without preventing the scattered radiation from being back-reflected. For these forward scattering ROA spectra, the undesirable marked bands are all positive, indicating that the ROA spectrum is contaminated by Raman light. For the backward scattering ROA spectra, the amount of Raman light is very important, as indicated by the strong bands at 652 and 1649 cm^{-1} .

The forward- and backscattering ROA spectra of neat (-)- β -pinene are compared to those obtained in 1990 by Barron and al. in Fig. 8.9. The spectra are in good agreement, except for a much higher quality for those obtained with our new instrument. A discrepancy is observed for the highly polarised

band at 652 cm^{-1} for both measurement geometries. *Ab initio* calculations at the DFT/B3LYP/6-311++G** level for the force field and TDHF/rDPS level for the electronic tensors, indicate the origin of that band to be a typical pinane ring deformation coupled with methylene a twist and a symmetric stretch of both methyl groups. A detailed analysis of quasi-atomics contributions (ACP, see Chapter 10) showed that the methylene twist gives rise to most of the isotropic scattering (Fig. 8.12). Our observed features in forward and backscattering ROA for that highly polarised band are therefore in very good agreement with the simulated forward- and backscattering spectra (Fig. 8.11), in contrast to previous published spectra [66], where the ROA of such polarised band were considered to be negligible, and were actually used for baseline adjustments, in order to null offsets.

The large forward ROA couplet at 726 and 773 cm^{-1} ($\Delta = -1.84 \times 10^{-3}$ and 0.73×10^{-3}) measured with our instrument agrees well with the spectra recorded in 1990 [66]. Hecht and Barron correctly suggested [89] that the olefinic methylene twist makes the most significant contribution to the Raman band at 726 cm^{-1} , as confirmed by its corresponding forward scattering ROA ACP (Fig. 8.12). The origin of the 773 cm^{-1} can be ascribed to a coupling between this methylene twist and a typical pinane skeletal mode.

L-Alanine

Figure 8.13 shows the first forward scattering ROA spectra of an amino acid. 1.5 M solutions of L-Alanine in H_2O and D_2O were measured in our precision cell. The SCP(0) ROA spectra seem to be less dependent on the nature of the solvent than the SCP(π) ROA spectra. The most intense band at 856 cm^{-1} in the water solution and 820 cm^{-1} in heavy water has been assigned

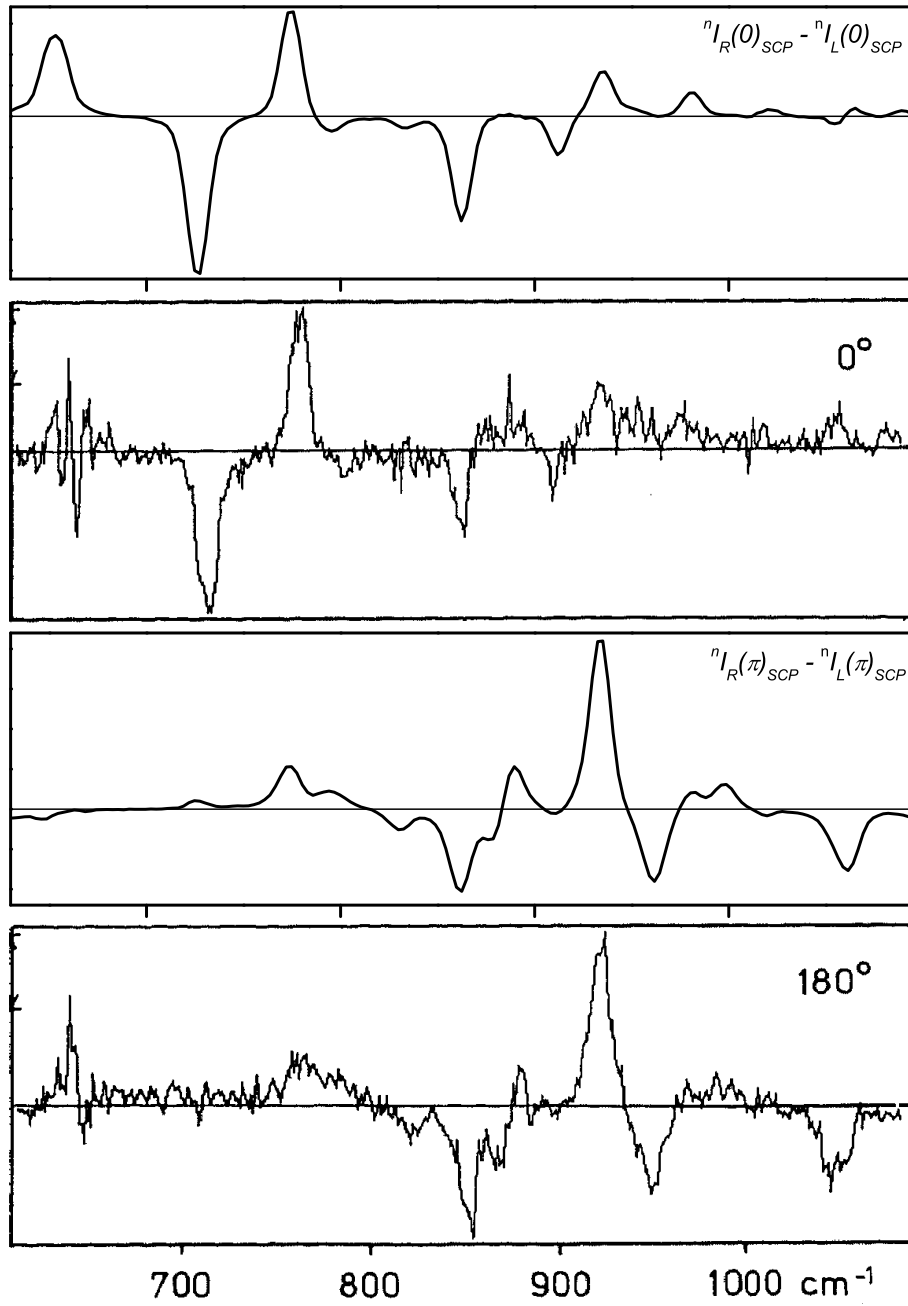


Figure 8.9: Forward- and backscattering spectrum of neat (-)- β -pinene. Old spectra were adapted from Ref. [66]. The excitation parameters were: 488 nm, 600 mW and 1 hours of acquisition time. Experimental parameters for new spectra as in Fig. 8.10. According to our computations (Fig. 8.12), the positive signal observed in forward scattering at $\tilde{\nu}_{15} = 652 \text{ cm}^{-1}$ is not an offset as suggested by Barron and al. [66], but originates from a coupled methylene twist and a typical pinane skeletal motion.

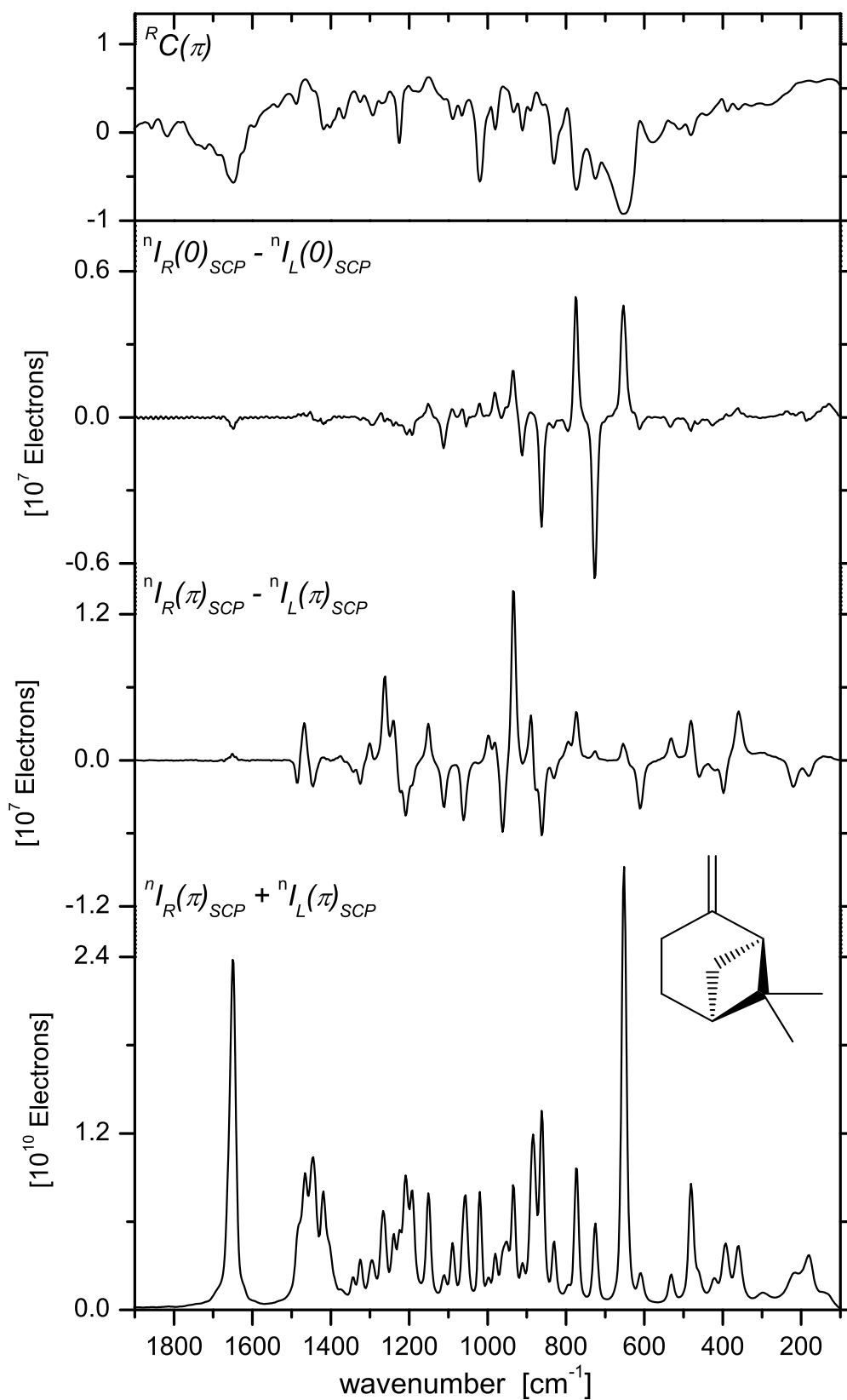


Figure 8.10: Measured forward- and backscattering spectra of neat (-)-β-pinene recorded in the precision cell. Exciting energy: 300 J (20 min, 250 mW). Similar results have been obtained in disposable capillaries (see Appendices).

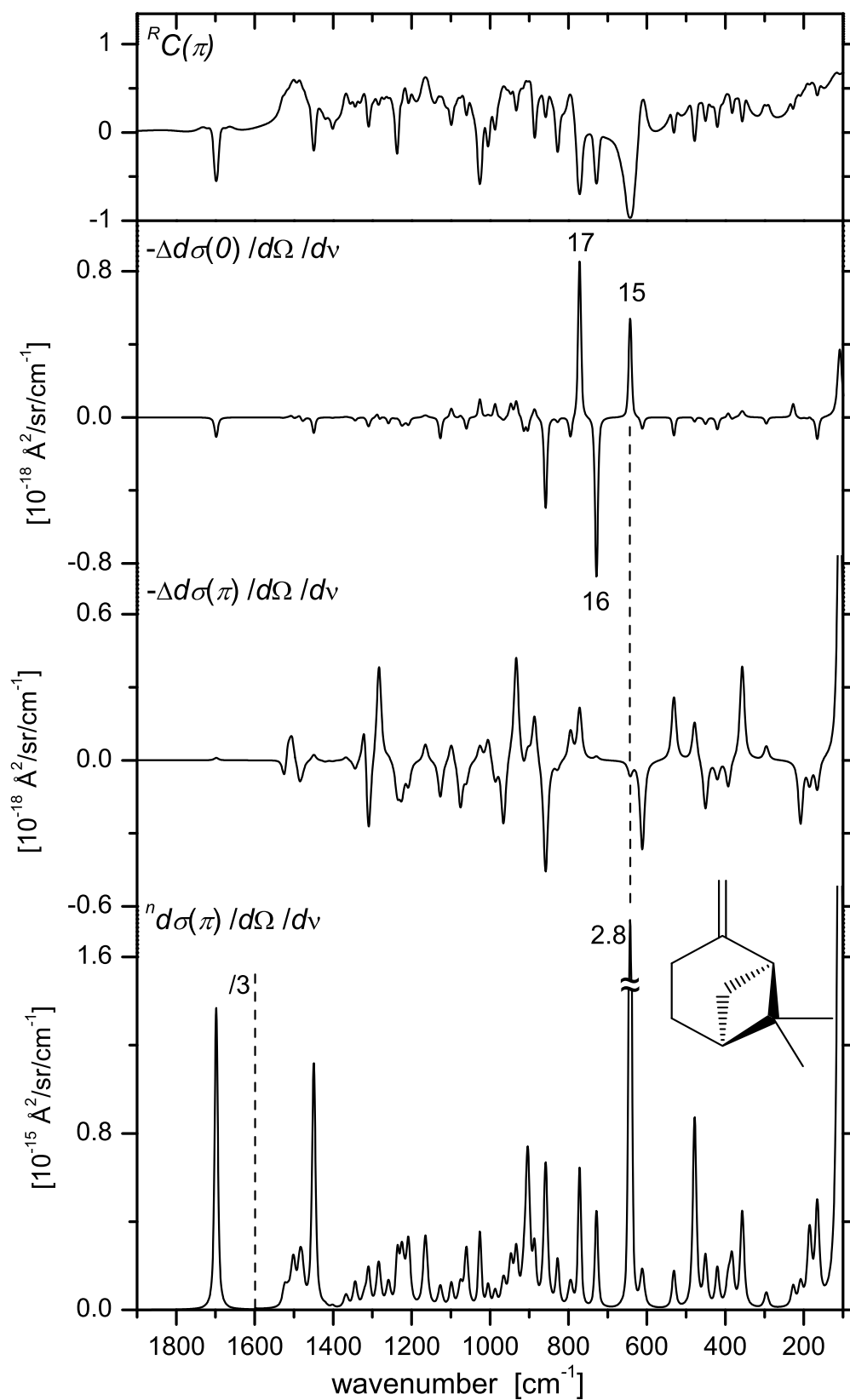


Figure 8.11: Simulated forward- and backscattering spectra of (-)-β-pinene. Computational details: Force field: DFT/B3LYP/6-311++G^{**}; Electronic tensors: TDHF/rDPS.

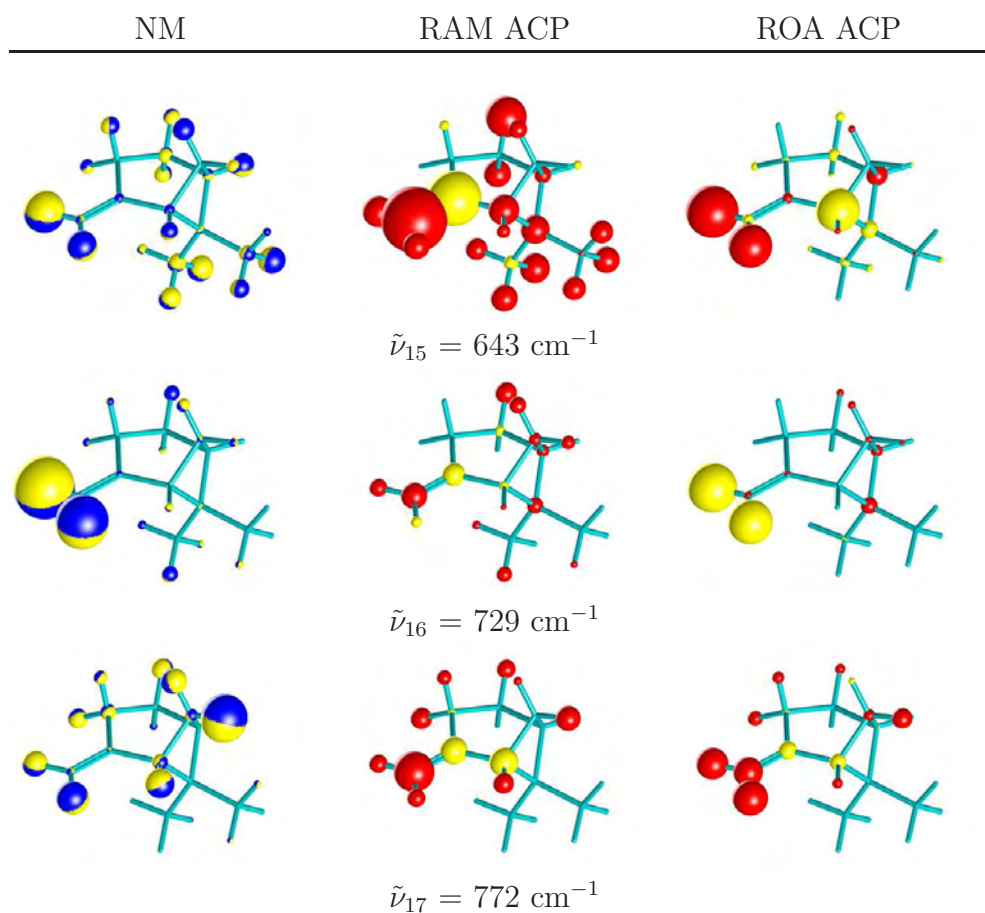


Figure 8.12: Nuclear motions (NM), forward scattering Raman atomic contribution patterns (RAM ACP) and ROA atomic contribution patterns (ROA ACP) of (-)- β -pinene in modes 15, 16 and 17. ROA ACP for mode 15 confirms our measured positive forward scattering ROA (Fig. 8.10), which deviates from old measurements [66]. Computational details: as in Fig. 8.11. Pictures generated by VOAView (see Chapter 10 for a detailed description).

to the symmetric C*-N stretching mode by Diem et al. [90]. From *ab initio* calculation [91], this vibration can be best assigned to the CO₂⁻ symmetric deformation which is extensively coupled with other normal modes, like the C-N and C_α-C stretching modes.

The other intense bands at 1312 in water and 1302 cm⁻¹ in D₂O, respectively, change sign when compared to the backscattering ROA spectra. It had been assigned by Diem et al. [90] to the C_α-H bending mode. However, there must be significant contributions from the NH₃⁺ bending motions, because this band shifts upon deuterating the NH₃⁺ group. The calculated vibration [91] has significant mixing of C_α-H rocking modes and NH₃⁺ bending motions.

L-Ascorbic acid and D-Isoascorbic acid

L-ascorbic acid (AscH₂, 4), best known as vitamin C, has first been isolated by the Hungarian scientist Albert Szent-Györgyi in 1928 [92] and is synthesised by most animals and plants, but not by humans and a small number of animals. This has led a minority of scientists, most notably Linus Pauling, to conclude that failure to produce the chemical by an animal species is a genetic defect, and to hypothesise that if it were replaced in humans to the level found in animals, better health [93] would result.

Vitamin C is absolutely essential for human existence as it is involved in a great number of vital processes. It is needed in collagen production, essential for the skin, bones and teeth. Vitamin C is involved in folic acid metabolism and affects vitamin B₁₂ levels in food. It is required for the synthesis of dopamine, noradrenaline, adrenaline and carnitine. It is also known for its strong antioxidant properties, due to its ability to scavenge oxygen and

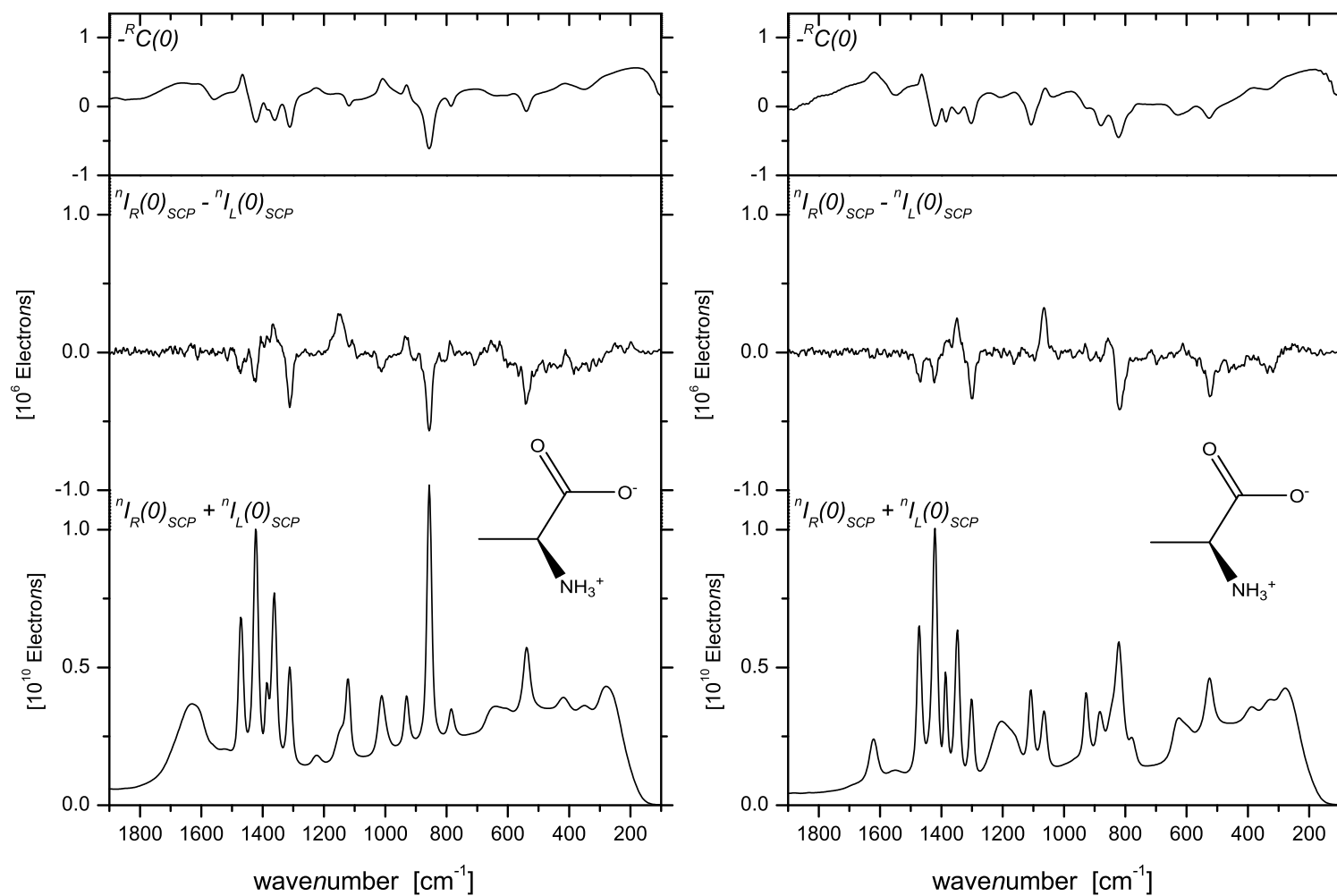
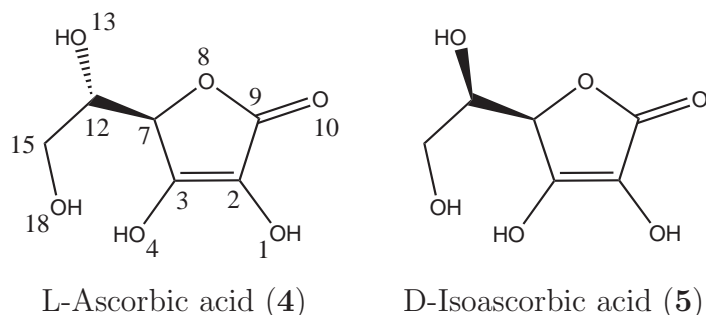
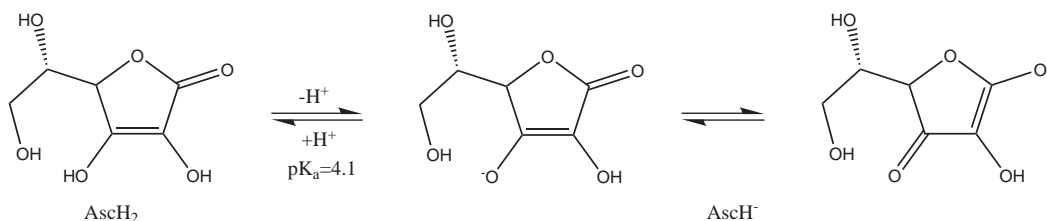


Figure 8.13: Left: forward scattering spectra of a 1.5 M L-Alanine water solution recorded in the high precision cell. Right: forward scattering spectra of a 1.5 M L-Alanine heavy water solution recorded in the high precision cell. For both sets of spectra: 37 correction cycles (1184 scans), exciting energy: 3.84 kJ (80 min, 800 mW).



to protect double bonds. A lack of ascorbic acid in the daily diet leads to a disease called scurvy, a form of avitaminosis. Its epimer, D-isoascorbic acid (**5**), has a smaller biological activity, even though it has similar physical and chemical properties. D-isoascorbic acid is often used as an antioxidant in food industry.

Vitamin C is an acid in aqueous solutions, because the ionisation of the enolic OH linked to C3 ($\text{pK}_a = 4.1$) gives a stabilised delocalised ascorbate anion:



L-ascorbic acid and its epimer are sensitive to oxidation by oxygen in water solution if the pH is alkaline to 7.6, or even at lower pH in the presence of copper as a catalyst [94]. The solutions were therefore prepared by dissolving 300 mg of them in 1 ml of water, resulting in a solution whose pH is around 2. They were filtered (0.2 μm pore size) and measured as soon as possible. The concentration was high and we believe that no oxidation took place in the sample, as no extra Raman band was found around 1600 cm^{-1} , typical for the

ascorbate species [95, 96]. After measurement, the solutions did not show a brown coloration as is the case when oxidation takes place.

Figure 8.14 and 8.15 show the forward- and backscattering solution spectra of **4** in H₂O and D₂O. As has been mentioned before, the forward ROA scattering spectra do not seem to be very sensitive to the change of solvent. The only distinguishable differences arise in the region 1600-1800 cm⁻¹. The intense Raman band around 1700 cm⁻¹ and its neighbour around 1765 cm⁻¹ are assigned to a C=C stretch coupled with an in phase C=O stretch and a C=O stretch coupled with an out of phase C=C stretch, respectively.

ROA spectra measured in backscattering are more sensitive to the influence of solvent molecules, especially in the region 1000-1400 cm⁻¹. This behaviour is expected, as the vibrations in this part of the spectrum mainly involve motions of the hydroxyl groups, which play an important role in the binding interactions with solvent molecules.

Pilot calculations were performed on L-ascorbic acid. Starting from the crystal structure taken from Ref. [97], the molecular structure and vibrational frequencies were calculated at the DFT/B3LYP/6-311++G** level of theory, without inclusion of solvent contributions (this will be the subject of future work). Both hydroxyl groups attached to the five membered ring are found to lie in the same plane as the ring itself, with the hydrogen atoms orientated in such a way that intra-molecular H-bonds with O(1) and O(10) can be formed. However, our ROA computation on that X-ray optimised structure did not account for the experimental spectra. Following other works [98, 99, 100], a conformational analysis was carried out [101]. In order to reduce the number of possible conformers, the ring part of **4** was kept frozen, while the conformation

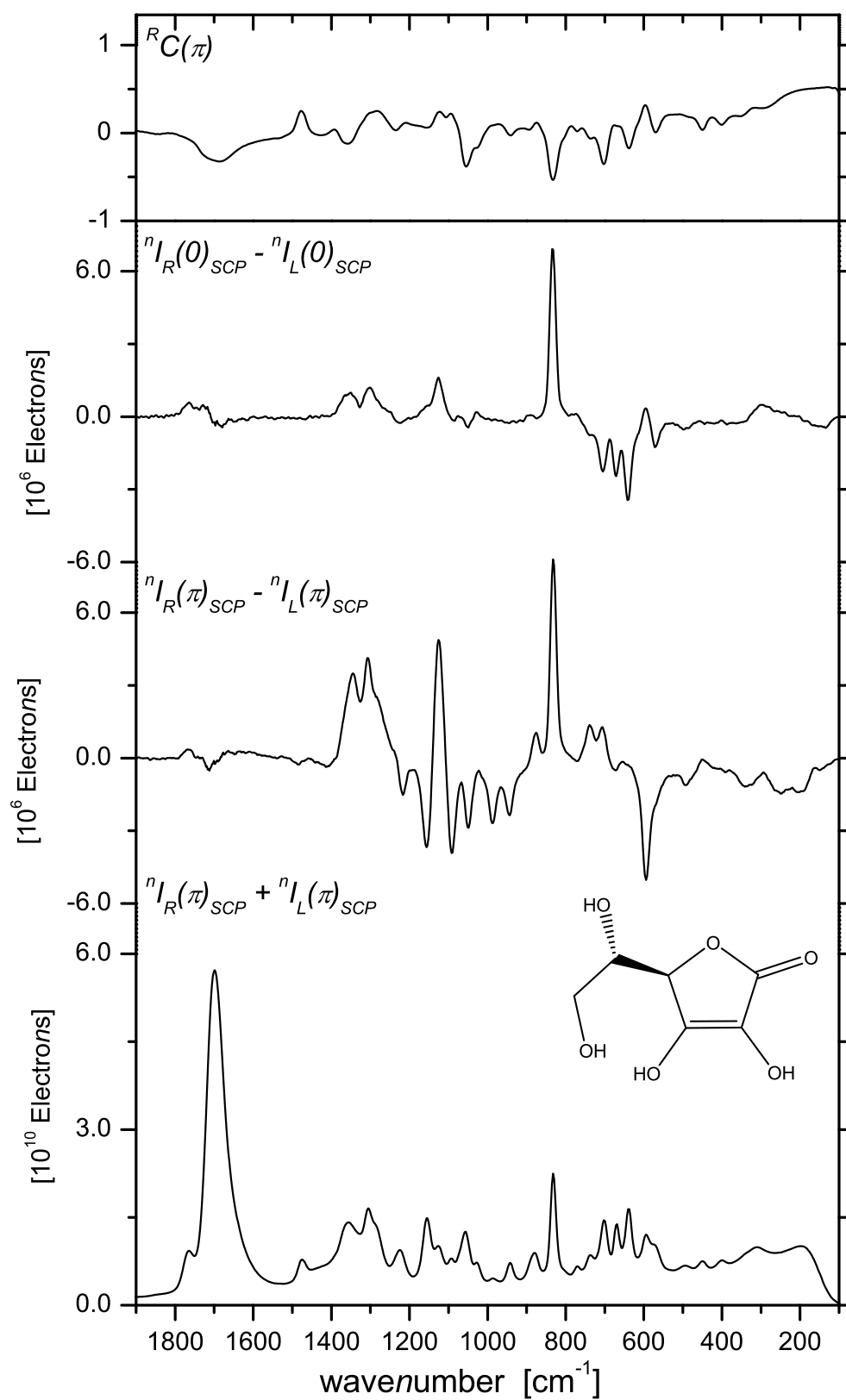


Figure 8.14: Forward- and backscattering spectra of L-Ascorbic acid in H_2O .
Exciting energy: 2.88 kJ (60 min, 800 mW).

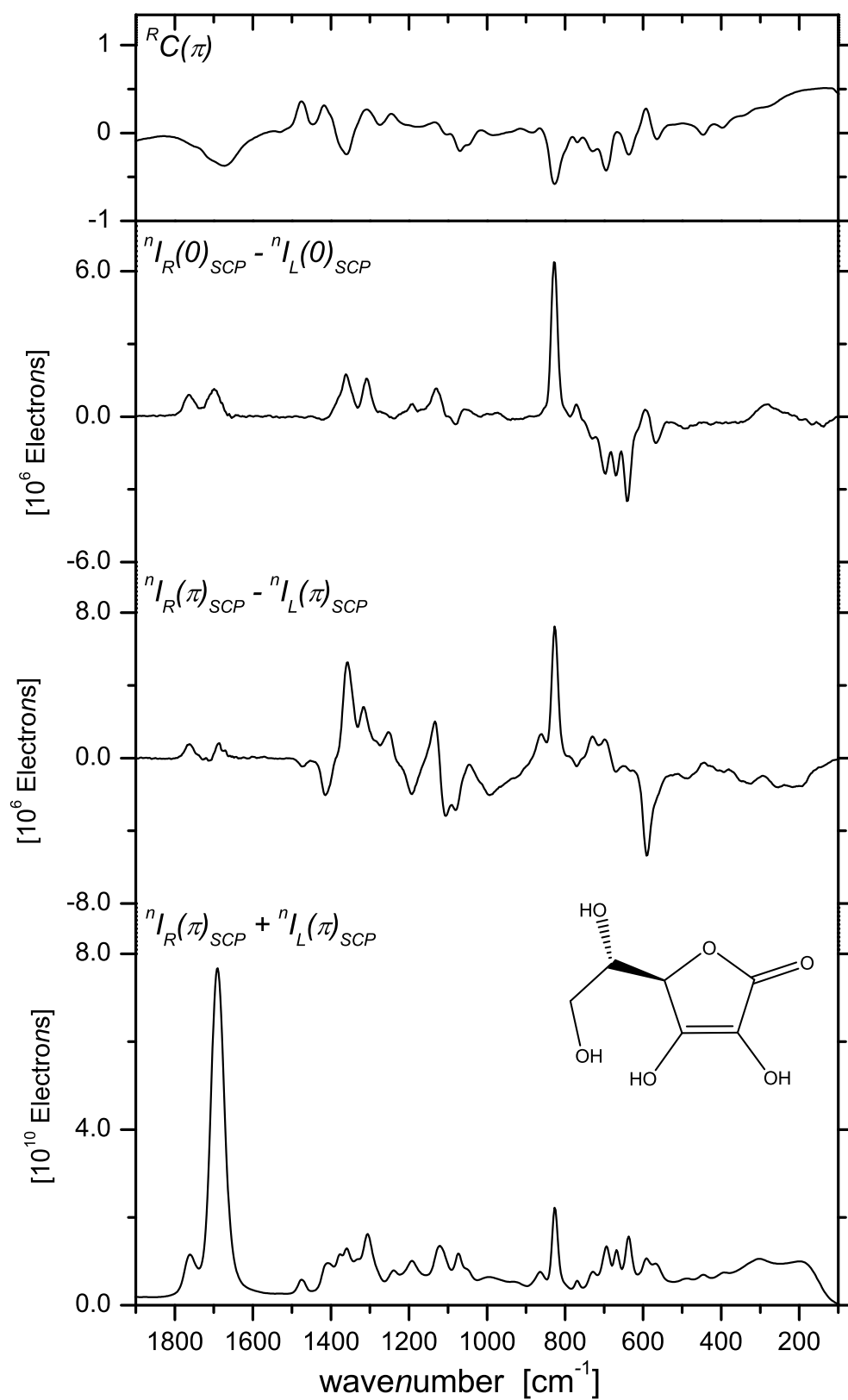


Figure 8.15: Forward- and backscattering spectra of L-Ascorbic acid in D₂O. Exciting energy: 2.88 kJ (60 min, 800 mW).

of the side chain was optimised. The six lowest energy conformers were taken into account, and a least square curve fitting of their respective forward ROA spectra to the experimental spectrum was carried out [101]. The resulting combination spectra are illustrated in Fig. 8.16. The similarity between simulation and experiment is more than acceptable, even if interactions with the solvent molecules were not considered. This confirms that forward scattering could be a promising tool for the study of solvated chiral entities like proteins and viruses.

According to our computation, the very strong positive ROA band around 830 cm^{-1} was found to be due to a distorted ring breathing mode, with a high contribution of the carbon atom on which the side chain is attached (C(7)), as illustrated in Figure 8.17.

D-Isoascorbic acid was also measured on our instrument, with the same concentration and conditions used for L-ascorbic acid. The corresponding spectra in water are illustrated in Figure 8.18. Both ROA spectra reflect the tiny structural difference between L-ascorbic acid and its epimer, i.e. the different orientation of the hydroxyl group at C(12). By comparing them for both compounds, it is interesting to see that in forward scattering, the main changes occur in the region from 600 to 800 cm^{-1} , whereas in backscattering, they appear between 1000 and 1400 cm^{-1} . The vibrations in the 600 - 800 cm^{-1} range are principally motions of atoms which belong to the five membered ring, and are hence quite delocalised over the entire molecule. Intramolecular H-bonds are affected by such vibrations, and because the configurational difference between **4** and **5** is localised on a hydroxyl group, the forward ROA scattering spectra reflect this tiny configurational difference. On the other hand, vibrations in the 1000 - 1400 cm^{-1} range are localised on specific entities, like the hydroxyl

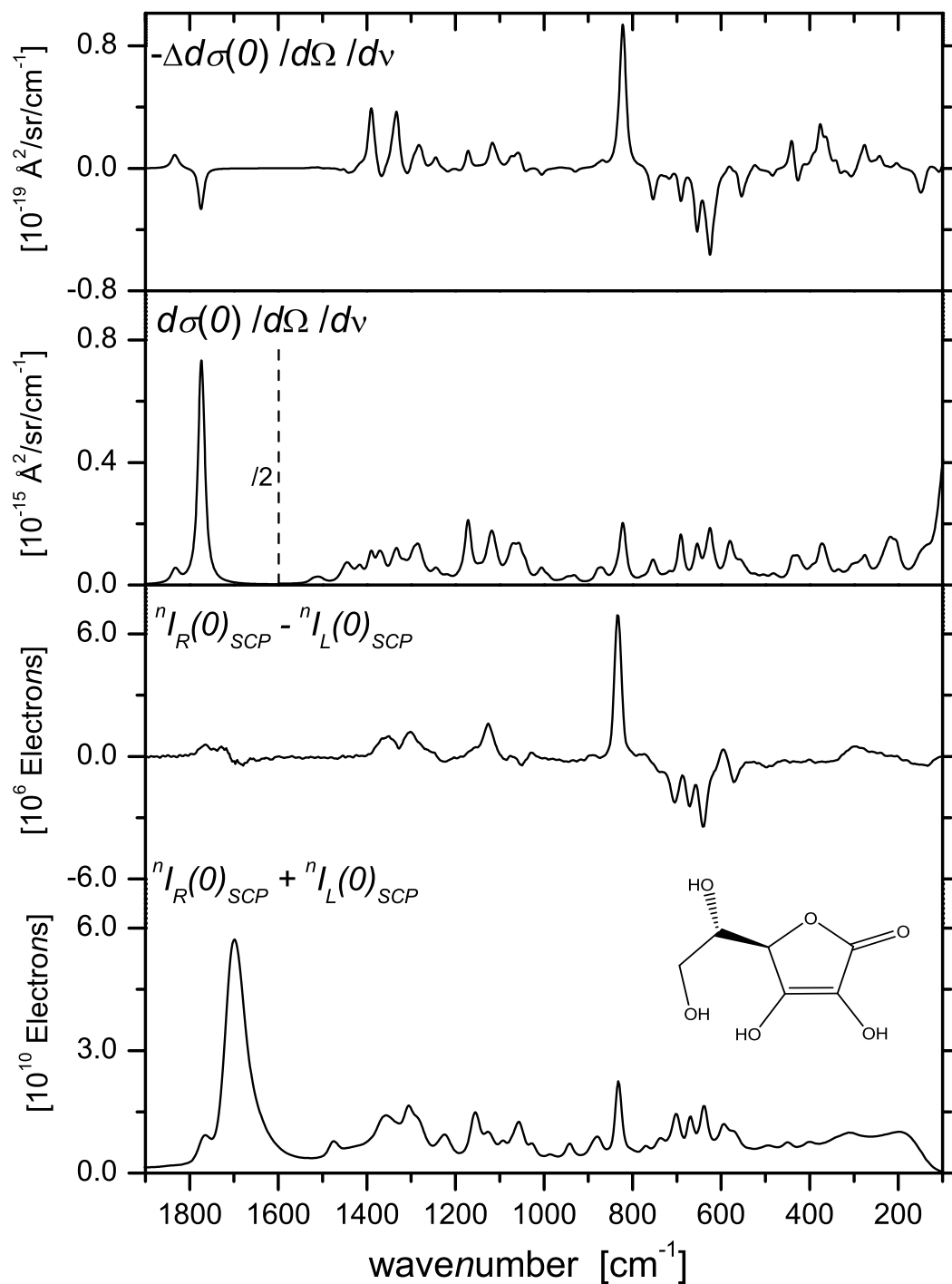


Figure 8.16: Simulated (top) and experimental (bottom) forward scattering spectra of L-Ascorbic acid. The simulated spectra have been obtained by a combination of spectra from six different conformers [101]. Computational details: force field DFT/B3LYP/6-311++G**, electronic tensors: TDHF/rDPS. Isotropic bandwidth: 10.5 cm^{-1} , anisotropic bandwidth: 20 cm^{-1} .

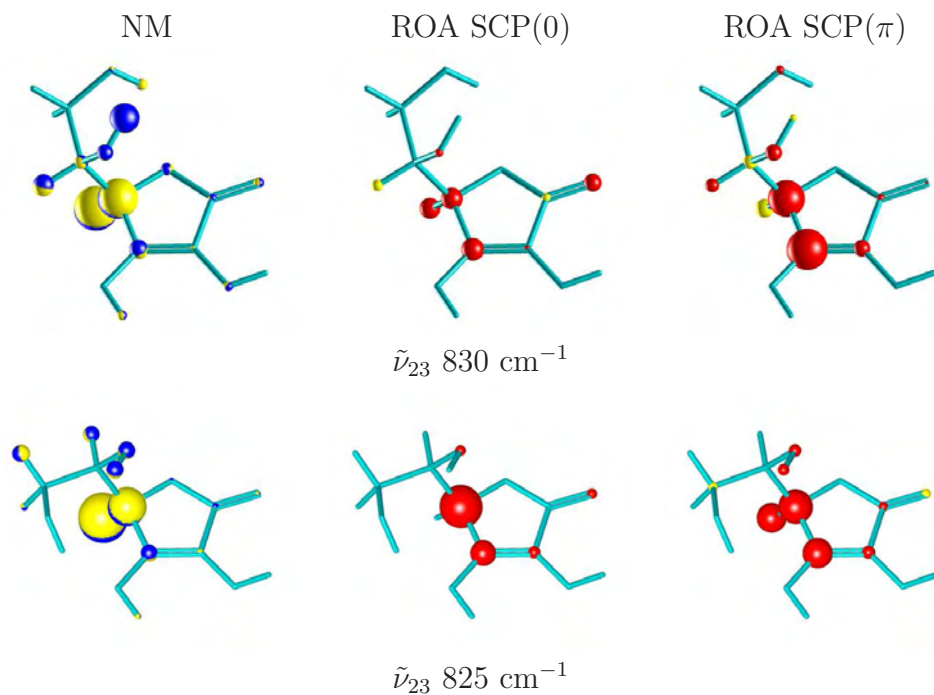


Figure 8.17: Nuclear motion (NM), forward scattering ROA ACP (middle) and backscattering ROA ACP (right) for mode 23 of L-ascorbic acid (top) and D-isoascorbic acid (bottom). Computational details as in Figure 8.16

groups themselves. Thus their motions influence interactions they have with solvent molecules, which are also different for both epimers, and a change in the backscattering ROA spectrum is observed. Forward- and backscattering will therefore be complementary when studying solvated systems.

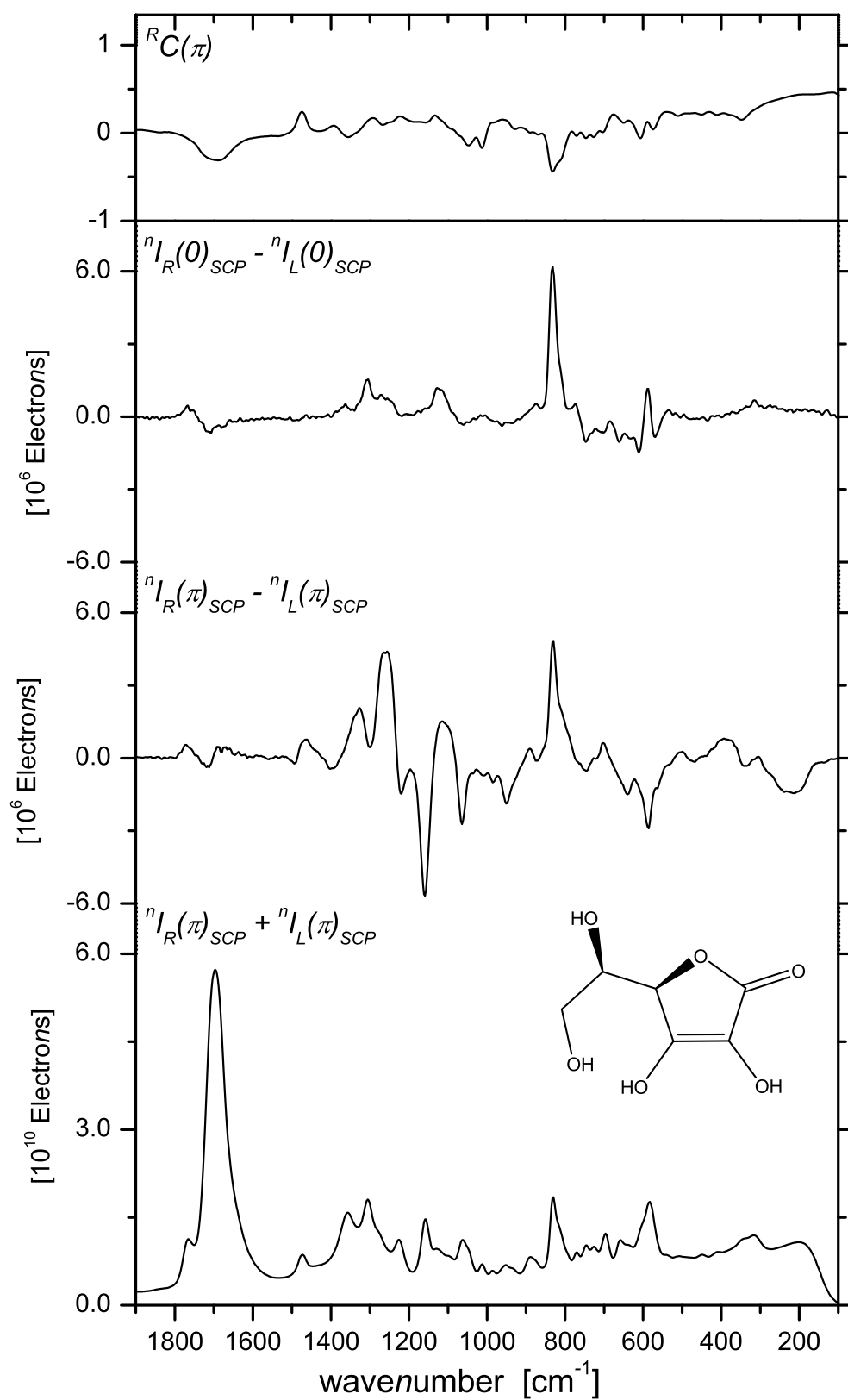


Figure 8.18: Forward- and backscattering spectra of D-Isoascorbic acid in H_2O . Exciting energy: 2.88 kJ (60 min, 800 mW).

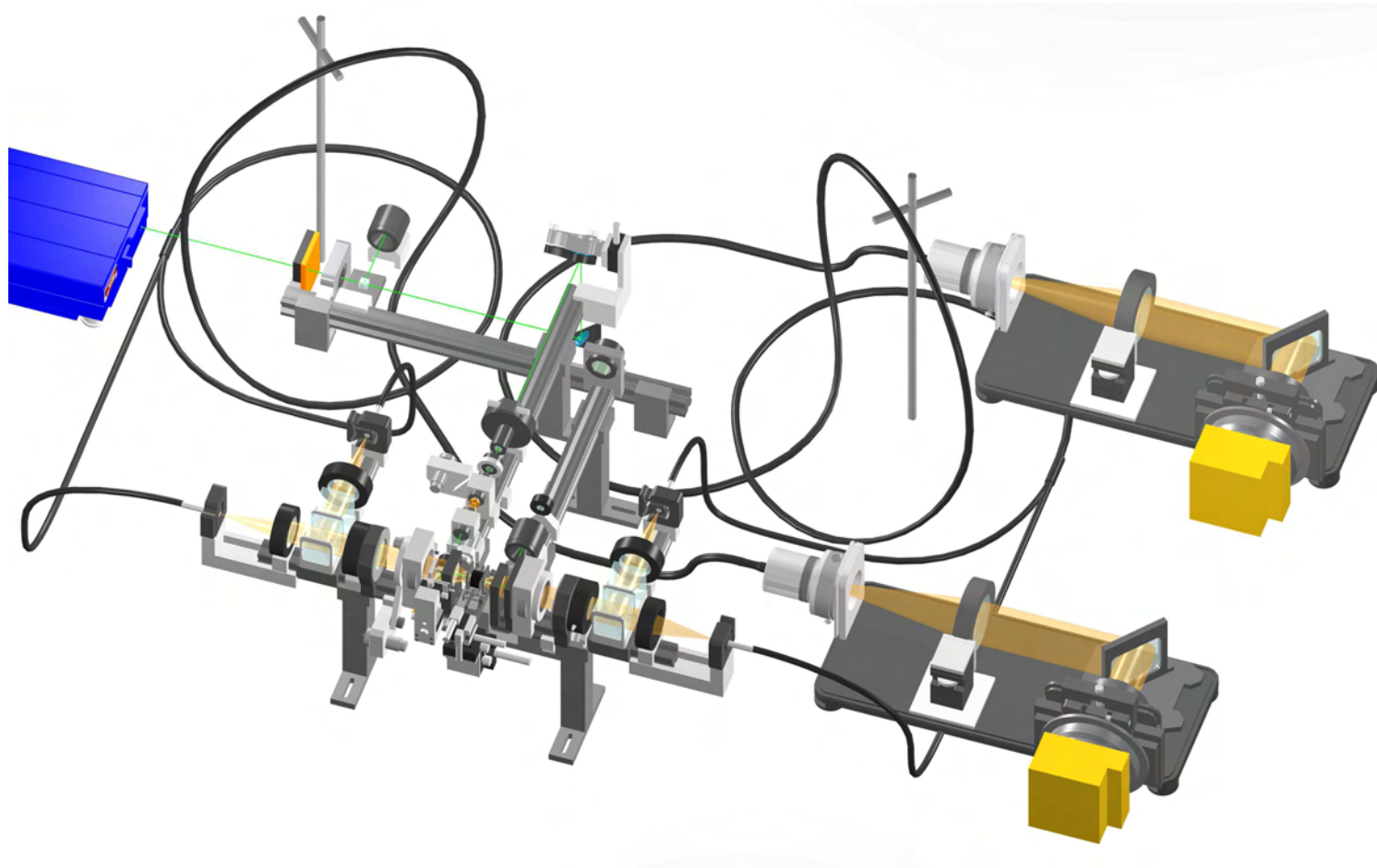


Figure 8.19: 3-dimensional representation of our dual-channel forward and backward ROA SCP instrument in Fribourg.

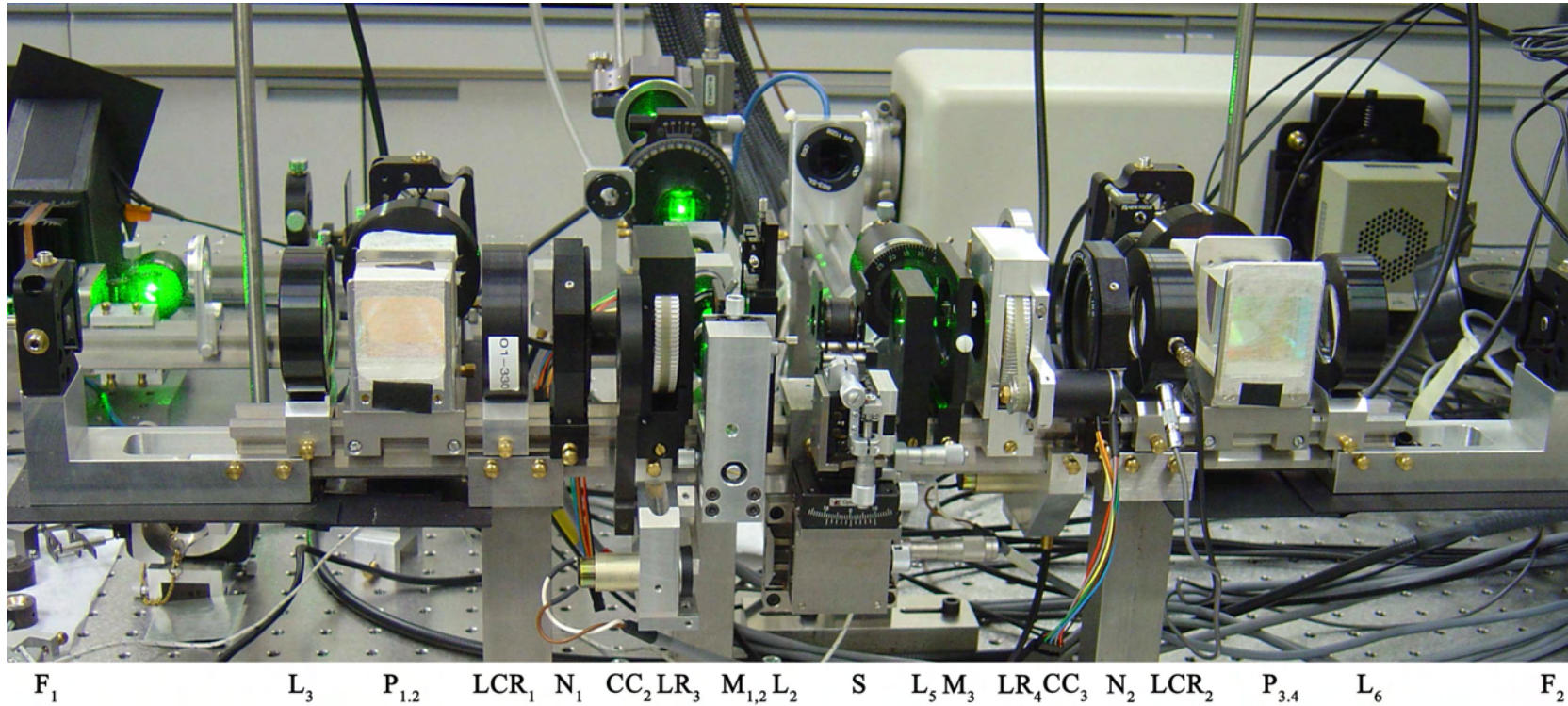


Figure 8.20: Picture of our instrument in Fribourg. The left part collects backscattered radiation and the right part forward scattered radiation. S: sample, L: lens, M: mirror, LR: linear rotator, CC: circularity converter, N: notch, LCR: liquid crystal retarder, P: polarising cube, F: fiber optics.

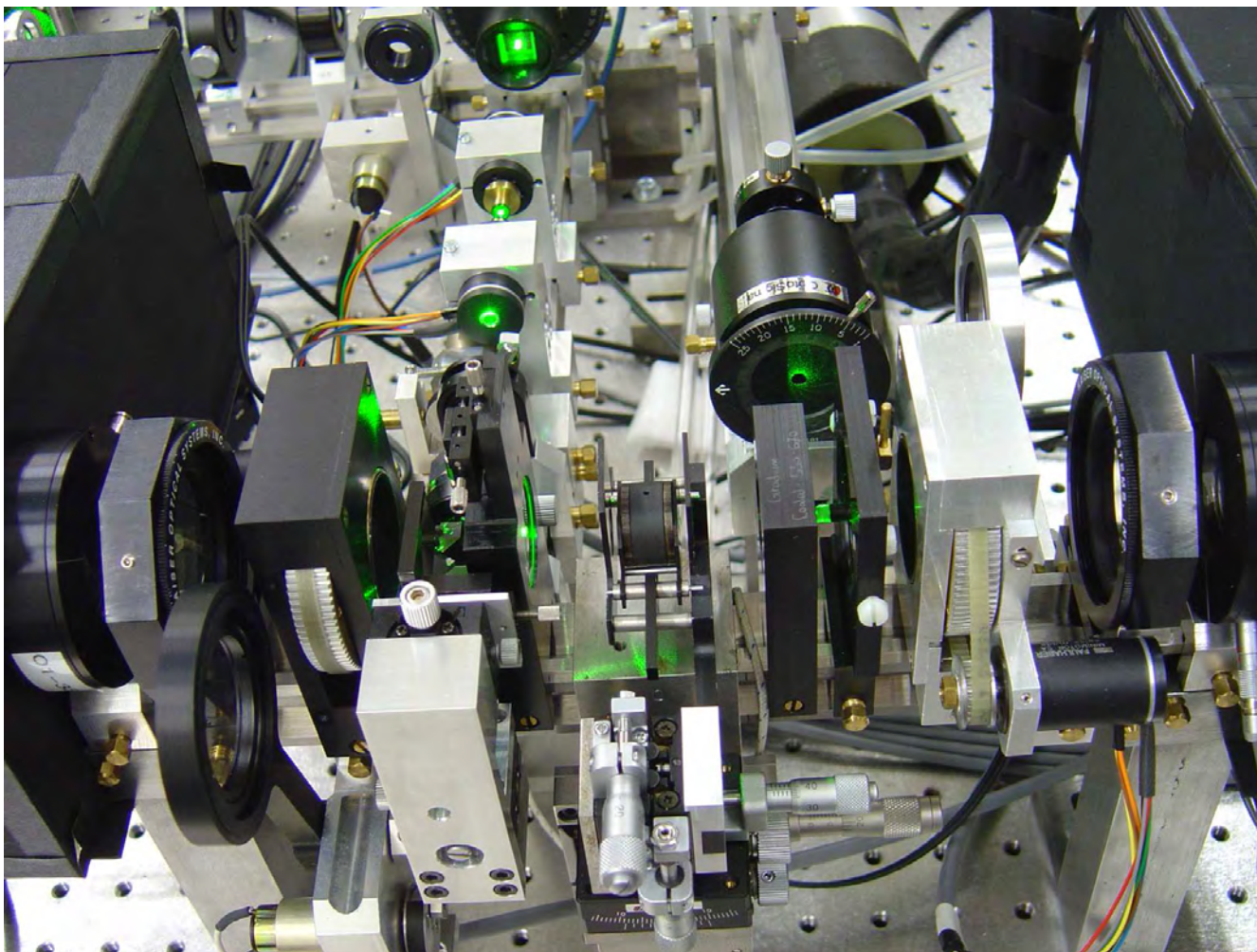


Figure 8.21: Picture of our collection optics. One both side of the cell: Gradium lens, deflection mirrors, linear rotator, circularity converter, notch filter, liquid crystal retarder.

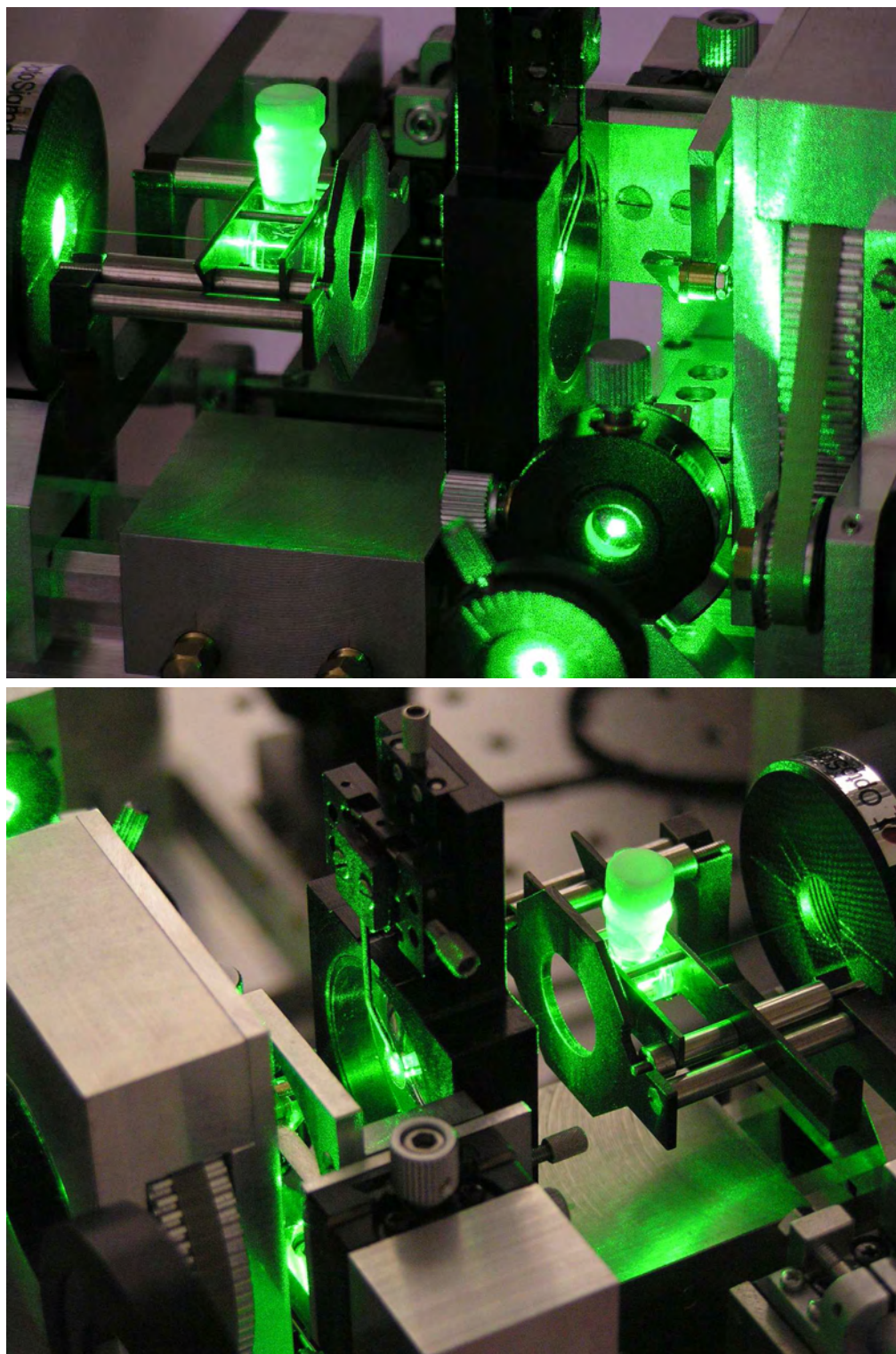


Figure 8.22: Picture illustrating our macro cell illuminated with our 532 nm exciting light. Top: incident laser light is first focused and then deflected by two polarisation neutral prisms. Bottom: backscattered radiation is collected by a Gradium plano-convex lens with a 1.5 mm hole for incident light.

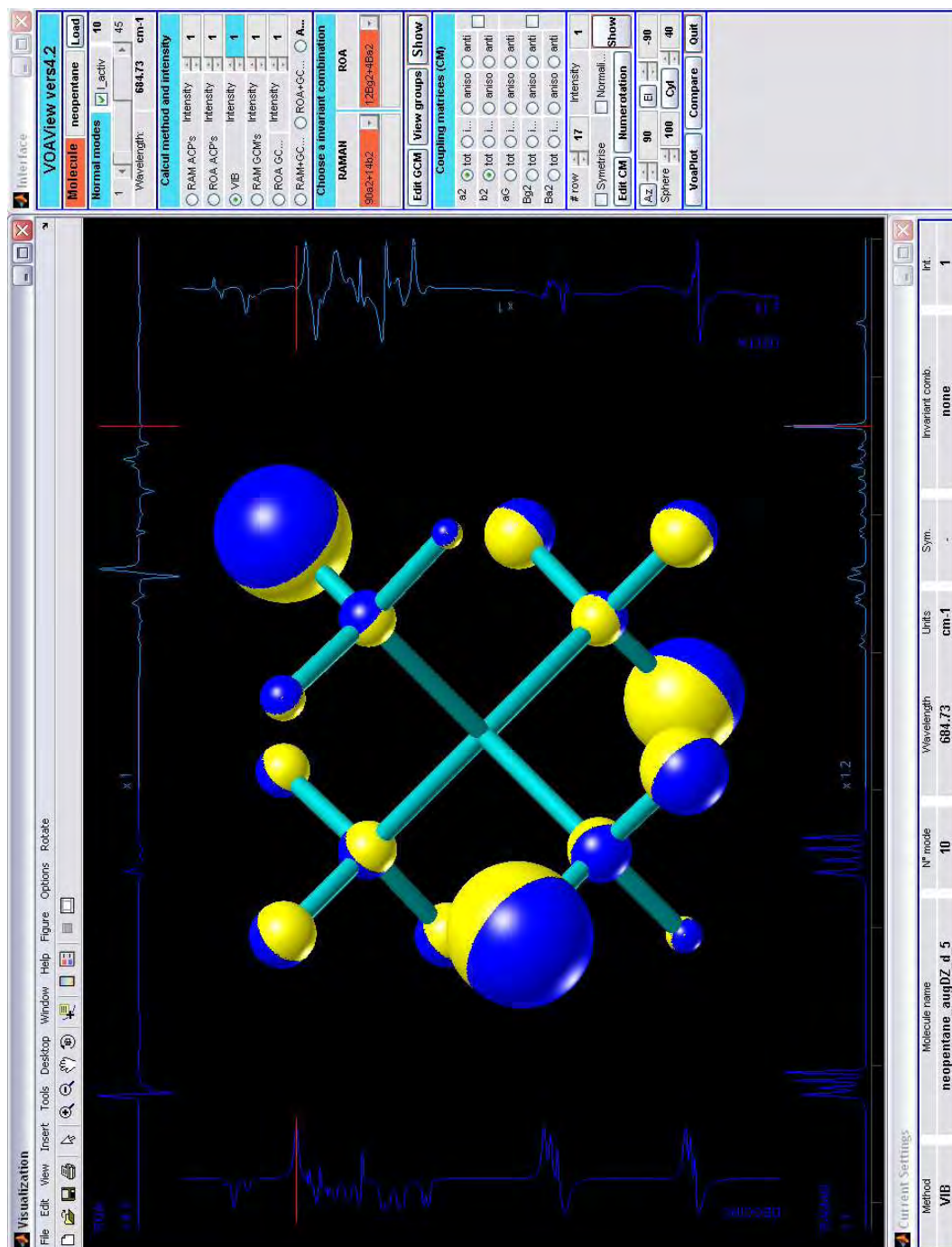


Figure 8.23: Front face of VOAView's GUI.

Part IV

Computation

Chapter 9

Computational Approach

9.1 Raman Optical Activity

The simulation of Raman optical activity spectra by *ab initio* methods is done by evaluating the general expression given in Eqs. (4.20) and (4.21), for which the five independent Raman and ROA invariants defined in Eq. (4.6) have to be calculated. Computation of these latter invariants needs the following:

- i) the cartesian harmonic force field, which yields the cartesian displacement matrix \mathbf{L}^x and the harmonic vibrational frequencies ω_p ,
- ii) the cartesian gradients of the polarisability tensors $\boldsymbol{\alpha}$, \mathbf{G}' and \mathbf{A} .

At first sight, a logical approach would be to calculate i) and ii) on the same level of theory. This has been tested, and will be presented further in this work, but our basic approach is somewhat different: for computational restrictions described later, the cartesian harmonic force field is calculated by density functional theory (DFT) methods, while the cartesian gradients of the polarisability tensors, evaluated at the DFT geometry, are calculated by means of Hartree-Fock linear response theory [102, 103].

9.1.1 Harmonic Force Field

The harmonic force field, represented by the molecular hessian matrix \mathbf{f} , is obtained by evaluating the potential energy V of the harmonic oscillator, given by a Taylor expansion around the equilibrium geometry as:

$$V = V_0 + \sum_i^{3N} \left(\frac{\partial V}{\partial q_i} \right)_0 q_i + \frac{1}{2} \sum_{i,j}^{3N} \left(\frac{\partial^2 V}{\partial q_i \partial q_j} \right)_0 q_i q_j \quad (9.1)$$

where q_i and q_j are the mass weighted cartesian displacements of atoms i and j . As the molecular geometry has first been optimised (indicated by the subscript 0), the system is in a minimum of energy, and the first derivative of the potential energy is zero. Setting $V_0 = 0$, only the right part of Eq. (9.1) is considered, in which one identifies the mass weighted cartesian hessian matrix \mathbf{f} , whose components ij are:

$$f_{ij} = \left(\frac{\partial^2 V}{\partial q_i \partial q_j} \right)_0 \quad (9.2)$$

A subsequent vibrational analysis is done by a program developed during this work and described in chapter 10. It yields the cartesian displacement vectors $L_{\alpha,p}^x$ and the corresponding vibrational frequencies ω_p .

Computational Parameters

Optimisation of the molecular geometry and calculation of the harmonic force field was done by DFT methods with the Gaussian03 [27] program (Revision C.01). DFT has been chosen as it treats explicitly electronic correlation, which is essential to get a good equilibrium geometry and acceptable vibrational frequencies. Our calculation uses the hybrid functionals B3PW91 and B3LYP [104, 105] with the standard 6-311G** or 6-311++G** [106], as well as aug-

cc-pVDZ or aug-cc-pVTZ [24] basis sets, for reasons that will become clear in the next section.

9.1.2 Gradient of Electronic Tensors

Analytical derivatives of the dynamic polarisability tensors α , \mathbf{G}' and \mathbf{A} are still not simultaneously available in the field of vibrational optical activity¹. They have to be evaluated by means of numerical differentiation, where the derivatives are obtained by evaluating the electronic polarisability tensors for $6N+1$ distorted geometries, N being the number of atoms, moving each atoms α along the $\pm x$, $\pm y$ and $\pm z$ axis. The derivative of α along x , for example, is given by

$$\begin{aligned}\frac{\partial \alpha^e}{\partial x} &\approx \frac{[\alpha^e(\mathbf{R} + \Delta x^\alpha) - \alpha^e(\mathbf{R})] + [\alpha^e(\mathbf{R}) - \alpha^e(\mathbf{R} - \Delta x^\alpha)]}{2\Delta x^\alpha} \\ &\approx \frac{\alpha^e(\mathbf{R} + \Delta x^\alpha) - \alpha^e(\mathbf{R} - \Delta x^\alpha)}{2\Delta x^\alpha}\end{aligned}\quad (9.3)$$

where \mathbf{R} is the equilibrium position.

DALTON Computational Parameters

The derivatives of the dynamic electronic polarisability tensors of the type given in Eq. (9.3) were calculated by Hartree-Fock linear response theory and London orbitals, as implemented in the DALTON [110] program (Release 1.1). The wavelength of the incident radiation was set to 532 nm, corresponding to our experimental conditions, and a displacement Δx of 10^{-3} bohr was used for the numerical differentiation. A typical DALTON input file can be found in the Appendices.

¹Analytical derivatives of α and \mathbf{A} [107, 108] are implemented in the GAMESS quantum chemistry package [109].

Calculating these electronic tensors for $6N + 1$ distorted geometries is a process that requires a lot of CPU time and disk space. Such calculations are only reasonably feasible for molecules with less than about 50 atoms with current technology. In order to reduce the computational time, Zuber et al. [86] developed reduced size basis sets, which were used in this work, called DPS (diffuse polarization function and shell augmented) and rDPS (reduced diffuse polarization function and shell augmented). They are spectacularly efficient, and calculated spectra comparable to those simulated with the reference basis set, aug-cc-pVDZ, also used in this work, can be obtained.

Evaluation of these gradients is now possible at the DFT level in Release 2.0 of DALTON [26]. It has been shown that the benefit of a density functional theory approach for the electronic tensors is not evident [52]. It is beyond the scope of this work to test this new version of DALTON.

Gaussian03 Computational Parameters

With the revision C.01, Gaussian03 offers now the possibility of calculating ROA spectra. Unfortunately, the level of theory for the evaluation of the requested electronic tensors cannot be chosen differently from the level used for the calculation of the harmonic force field. The large aug-cc-pVDZ reference basis set was therefore chosen for the calculation of both the force field and the Raman and ROA electronic tensors with Gaussian03, despite its time consuming requirements. Aug-cc-pVDZ calculations provide acceptable harmonic frequencies, thanks to the polarisation functions, and good electronic tensors, thanks to the presence of diffuse functions. A typical Gaussian03 input file can be found in the Appendices.

Chapter 10

VOAView: a Graphical User Interface

As mentioned earlier in this work, it is one thing to measure and simulate ROA spectra, but it is another to understand them. The actual difficulties of such interpretations could explain why researchers still hesitate to invest time in ROA spectroscopy.

A graphical user interface (GUI) has been developed with the goal to facilitate the interpretation of the plethora of information contained in both calculated and measured VOA data. It is written in Matlab® [111], as some original routines were written in this language [112]. Nowadays, an open-source language would be more adapted for the scientific community. It is the work of others to take this GUI as a reference for future open-source developments.

The GUI developed in this work has been given the name **VOAView**, for vibrational optical activity visualisation. It handles Raman (RAM), Raman optical activity (ROA), infrared (IR) and vibrational circular dichroism (VCD) data calculated within the DALTON and Gaussian03 programs, but also measured data from our two spectrometers by an extension called **VOAPlot** included

in the VOAView package.

10.1 Installing and Launching VOAView

VOAView, in its actual 4.2 version, still needs Matlab® to be installed, in order to run. Upon request, a fully stand-alone version of VOAView could be prepared, but this is not the scope of the present work. The description of VOAView's features will be mostly based on the following hardware configuration: Microsoft Windows XP operating system, version 7.0.4 of Matlab® and no hardware graphical acceleration (software OpenGL). VOAView has also been tested with a *n*VIDIA GeForceFX 5600XT graphical acceleration card with good results. The authors do not take responsibility for any bugs arising with different computer configurations. VOAView should also work on Linux operating systems. Please contact the authors for more information.

The minimum requirements for VOAView to run correctly is a personal computer with the following configuration:

- Microsoft Windows (XP recommended), Linux,
- Pentium III or later, AMD Athlon or XP,
- 256 MB RAM (512 recommended),
- Matlab® 6 or later,
- Hardware graphical accelerator recommended but not essential.

VOAView is distributed in two ways: an installation package or a simple copy of VOAView's folder, consisting of all the requested M-files (Matlab® files). By choosing the first way, a double-click on the installation package creates the folder `C:\VOAView` and a shortcut (batch file) on the desktop. A double-click on this shortcut launches Matlab, adds `C:\VOAView` and its sub-

folders to Matlab's path, and executes the command `>> voaview` which starts the graphical user interface. If for some reason this procedure fails, the manual installation will solve the problem. It suffices to copy VOAVIEW's folder on the computer and to add its path (with the subfolders option enabled) to Matlab's path (Menu **File**->**Set Path...**). Starting VOAVIEW is then accomplished by launching Matlab® and by typing the command `>> voaview`.

VOAVIEW's installation directory contains a folder **vers4.2**, where 4.2 is the actual version. The root directory **VOAVIEW\vers4.2** will be denoted \$, and is divided in the following subfolders:

| Folder | Content |
|-------------|-------------------------------------------------------------------------------------|
| \$\Bin: | icons and batch files. |
| \$\Common: | common M-files used by VOAVIEW and VOAPLOT. |
| \$\Compile: | M-files and their compiled coded for previous version of Matlab. |
| \$\Def: | default files and different definition files (coefficients, atomic parameters, ...) |
| \$\Ext: | external M-files, like parsers and other functions. |
| \$\Manuals: | pdf manuals. |
| \$\VOAVIEW: | specific M-files used by VOAVIEW. |
| \$\VOAPLOT: | specific M-files used by VOAPLOT. |

10.2 Main Features of VOAVIEW

VOAVIEW is a program, the graphical user interface of which is illustrated in the central section of this work (Fig. 8.23), that has been developed to make it more comfortable for researchers in the field of vibrational optical activity to handle and interpret calculated data. All the graphical tools implemented in VOAVIEW were developed in our laboratory, some of them were described

in detail in Ref. [54].

The main features of VOAVIEW are the following:

- i) representation of three dimensional molecular structures, which can be freely and rapidly rotated, including multiple and hydrogen bonds,
- ii) new pictorial representation of the vibrational normal modes by means of bicoloured spheres,
- iii) new visualisation methods for a better understanding of Raman, ROA, IR and VCD generation,
- iv) groups of atoms simply defined by click on atoms,
- v) simultaneous display of two sets of data for comparison purposes,
- vi) simultaneous display of graphical tools and simulated spectra.

Concrete examples will be used in order to describe VOAVIEW. The goal of the present description is not to interpret the chosen Raman and ROA data, but rather to illustrate the features offered within the program for the visualisation and the decomposition of molecular quantities. It has to be mentioned that the same features are also available for IR and VCD calculations, for which a brief description can be found in section 10.5.

10.2.1 Input File

VOAVIEW uses a simple proprietary ascii input file format (*.voa), which consists of an array of data in three columns, whose elements are described in the Appendices. The folder \$Ext contains parsers that can be used to convert Gaussian03 output (*.out) or formcheck (*.fchk) files, and DALTON 1.1 output (*.out) files, into VOAVIEW's file format. A description of each parser

can be found in the Appendices, as well as a description of the way DALTON and Gaussian03 organise the tensor's gradients in their respective output files.

10.2.2 Vibrational Analysis

During the parsing process, the hessian matrix \mathbf{f} (Eq. 9.2) of molecular force constants is extracted from the Gaussian03 formatted checkpoint file. The different available parsers transfer this hessian matrix to a vibrational analysis algorithm implemented in VOAView (`vibana.m`), based on the vibrational analysis modules in Gaussian [113, 114]. The 3 translational and 3 rotational modes (2 for linear molecules) are identified and removed, resulting in the $3N - 6$ or $3N - 5$ vibrational normal modes, the associated frequencies $\tilde{\nu}_p$, and the cartesian displacement vectors $L_{\alpha,p}^x$, which are all saved in VOAView's input file (`*.voa`).

Two other input files can be created upon request: an input file (`*.mkl`) for the Molekel molecular graphics package [115, 116], and an input file (`*.mol`) for the Molden molecular and electronic structure program [117, 118].

10.2.3 Molecular Structure

VOAView draws the molecular equilibrium structure extracted from Gaussian03 and saved in the input file in cartesian coordinates (units: Å). An internal algorithm determines the connectivity, the presence of multiple or hydrogen bonds, and the resulting molecular structure is drawn as stick, ball-and-stick or space-fill models (Fig. 10.1). Display of multiple and hydrogen bond can be deactivated and an external connectivity matrix can be loaded if necessary. All the displayed structures can be exported as high quality pictures in multiple

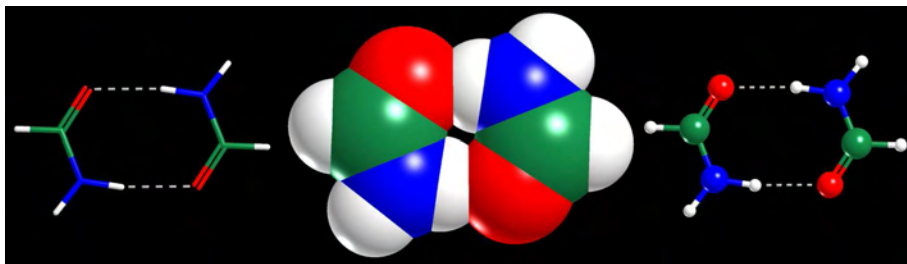


Figure 10.1: Molecular structure of the formamide dimer, drawn as stick, space-fill and ball-and-stick models.

standard formats (`eps`, `tiff`, `jpeg`, `png`, `gif`, and more). The parameters that define the shape of bonds and spheres can be adjusted at the bottom of the right panel.

10.2.4 Vibrational Normal Modes

The graphical representation of vibrational motion in polyatomic non-planar molecules has been a major headache in the past. Unless one makes use of stereoscopic projection, which is inconvenient, it is difficult to simultaneously convey a good impression of the direction and the extent of nuclear motions. Simple arrows are normally used for a graphical representation of vibrational motions, but the resulting pictures are often difficult to appreciate. An effective solution of the problem is to separate the two aspects [54]. The size, an isotropic quantity, can be represented by spheres centered on atoms, with their radius chosen proportional to the magnitude of the nuclear excursion $|L_{\alpha,p}^x|$. The direction of motion can be added by the appropriate shading of bicoloured spheres. Moreover, as can be seen from Eqs. (4.6), (4.7) and (4.20), if one divides $|L_{\alpha,p}^x|$ by $\Delta\tilde{\nu}_p$, the surface of the spheres is proportional to the importance a nuclear motion has in generating Raman scattering.

VOAView represents nuclear motion (NM) in this novel way, by drawing

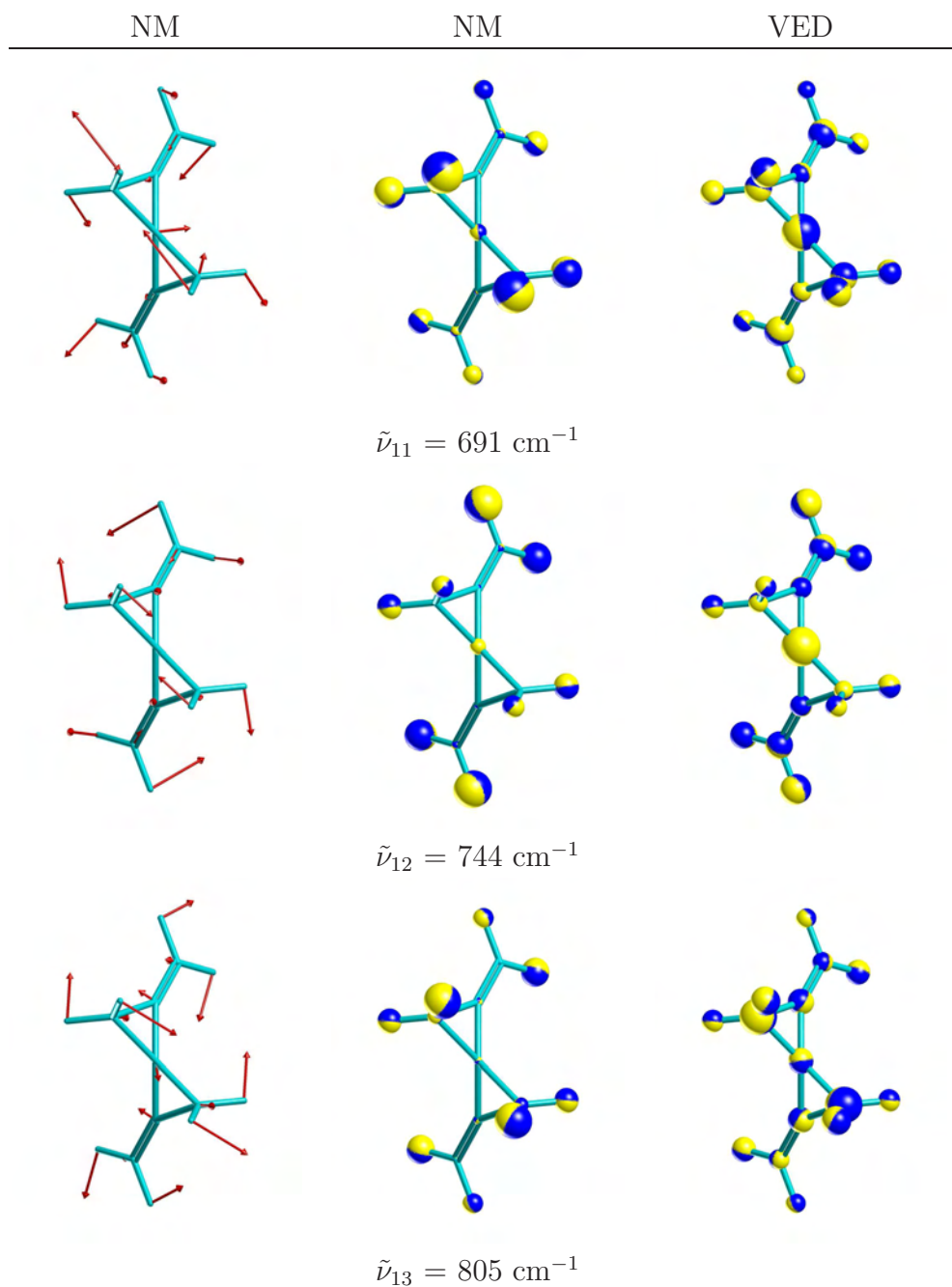


Figure 10.2: Vibrational normal modes 11, 12 and 13 of (M)-(-)-1,4-dimethylenespiropentane. Nuclear motion (NM) is represented by arrows (left) and by bicoloured spheres with a surface area proportional to $|L_{\alpha,p}^{xG}|/\sqrt{\Delta\tilde{\nu}_p}$ (middle). Vibrational energy distribution (VED) are represented by bicoloured spheres with a volume proportional to $m_\alpha(L_{\alpha,p}^x)^2$ (right). Computational details: force field B3LYP/aug-cc-pVTZ.

bicoloured spheres on atoms, with their surface proportional to $(L_{\alpha,p}^x)^2/\Delta\tilde{\nu}_p$, thus having a diameter proportional to $|L_{\alpha,p}^x|/\sqrt{\Delta\tilde{\nu}_p}$. The standard way of normalising \mathbf{L}^x in vibrational spectroscopy is defined as

$$\sum_{\alpha i,p} m_{\alpha} (L_{\alpha i,p}^x)^2 = 1 \quad (10.1)$$

A disadvantage of this normalisation is the strong dependence of the zero point amplitude on the mass of the nuclei in motion, thus attenuating in some cases the nuclear motion of light atoms when heavy atoms also move. Drawing spheres proportional to $|L_{\alpha,p}^x|/\sqrt{\Delta\tilde{\nu}_p}$ has also a disadvantage: the division by $\Delta\tilde{\nu}_p$ has an inflating effect on low-frequency vibrational modes. Both disadvantages imply a frequent readjustment of the scaling factor to meet the screen size. This can be avoided by disabling the frequency division (**Menu Options**->**VIB**->**Norm Coord...**).

VOAView offers the possibility to display vibrational motions according to Gaussian's normalisation (default)

$$\sum_{\alpha i,p} (L_{\alpha i,p}^{xG})^2 = 1 \quad (10.2)$$

When drawing spheres with a diameter proportional to $|L_{\alpha,p}^{xG}|$, the sum of the surfaces of all spheres is equal to 1 and the scale hardly ever needs to be readjusted. A disadvantage is the absence of a physical meaning of this representation.

A remedy for the problem of the mass dependence may be obtained when one is interested in the persistence of certain patterns of nuclear motion on similar fragments of different molecules [23], where the energy of vibrational motions is a more important criterion. The fraction of vibrational energy of a

nucleus α in mode p is proportional to $m_\alpha(L_{\alpha,p}^x)^2$ [119]

$$\frac{E_{\alpha,p}}{E_p} = m_\alpha L_{\alpha,p}^x \cdot L_{\alpha,p}^x \quad (10.3)$$

In representations of the distribution of vibrational energy (VED), a scalar quantity, the volume of the spheres is chosen to be proportional to the contribution made by individual nuclei to the total energy of a vibrational mode.

An illustration of these novel ways of drawing nuclear motion (NM), and vibrational energy distribution (VED), is found in Fig. 10.1. As an example, we represent three vibrational modes of an interesting compound, (M)-(-)-1,4-dimethylenespiropentane [120], the ROA of which has recently been measured [121]. It is evident that in keeping the molecule's orientation fixed, the motion of some atoms (especially carbon atoms, like the central spiro atom in mode 12) cannot be identified with the sole use of arrows.

10.2.5 Scattering Cross Sections

Drawing spectra according to the scattering cross sections defined in Eqs. (4.20) and (4.21) is the best way for a first comparison between theory and experiment. This is featured by VOAPlot and described later.

Where one is more interested in understanding the source of Raman and ROA scattering generation, the graphical representation of the decomposition of scattering cross sections (GCM and ACP), and related molecular quantities (PIT), as defined in Ref. [54], are more powerful methods.

10.2.6 Group Coupling Matrices (GCM)

The molecular invariants defined in Eq. (4.6) are scalar quantities, the linear combinations of which, multiplied by the corresponding frequency factors, define the scattering cross sections. In a similar way, one can multiply the scalar quantities $J_{\alpha\beta,p}$, defined in Eq. (4.5), by the integral over wave functions $\langle f_v|Q_p|i_v\rangle^2$ and the corresponding frequency factor K_p , and arrange them as square $N \times N$ matrices, where N is the number of atoms. The amount of mono- and dinuclear numerical information contained in these kind of matrices, called group coupling matrices (GCM), renders the direct inspection of these data unwieldy for medium-size molecules, but their conversion into pictorial representations make them easier to analyse. Circles, whose surface area are chosen proportional to the $\alpha\beta$ components of $J_{\alpha\beta,p}$ multiplied by $\langle f_v|Q_p|i_v\rangle^2 K_p$, are drawn into similar square $N \times N$ matrices. Positive components are indicated by dark (black or red), and negative components by light (white or yellow) shadings. Drawing linear combinations of $J_{\alpha\beta,p}$, representing scattering cross sections when multiplied by $\langle f_v|Q_p|i_v\rangle^2 K_p$, is of interest, and is given by

$$d\sigma_{\alpha\beta,p} = \langle f_v|Q_p|i_v\rangle^2 K_p [c_1 a_{\alpha\beta,p}^2 + c_2 \beta_{\alpha\beta,p}^2] d\Omega \quad (10.4)$$

$$- \Delta d\sigma_{\alpha\beta,p} = \langle f_v|Q_p|i_v\rangle^2 \frac{K_p}{c_0} [c_3 a_{G'\alpha\beta,p}' + c_4 \beta_{G'\alpha\beta,p}^2 + c_5 \beta_{A\alpha\beta,p}^2] d\Omega \quad (10.5)$$

Where a normal mode spreads over molecular fragments, it is preferable to lump together contributions from individual atoms of particular fragments into individual group contributions. This is obtained by separately adding intragroup mono- and dinuclear terms, and intergroup dinuclear terms of $J_{\alpha\beta,p}$. The resulting pictorial representations are square $N_{Gr} \times N_{Gr}$ matrices, where

N_{Gr} is the number of groups of atoms defined in the molecule. If the matrix elements result from the contraction of two different molecular tensors, then the matrix is not symmetric, but in sums found in Eq.(4.6), only the symmetric part of such matrices contributes. The off diagonals halves of the GCM can therefore be added, and the resulting matrix displayed in upper triangular form (Fig. 10.3).

Figure 10.3 shows these kind of GCM for the vibrational modes 30 and 31 of (M)-(-)-1,4-dimethylenespiropentane. The numbering of the three groups, as defined in Fig. 10.4, goes from left to right and from the top to the bottom of the upper triangular matrix.

Defining Groups of Atoms

Defining groups of atoms has been simplified in VOAView. Choosing **Edit GCM** on the right panel opens a new window where the definition of groups is simply made by clicks on atoms. Once defined, the resulting groups are displayed in various colours and can be saved for a further session of VOAView. Figure 10.4 shows the three groups defined in (M)-(-)-1,4-dimethylenespiropentane.

10.2.7 Atomic Contribution Patterns (ACP)

A pictorial representation, where quantities attributable to individual atoms are drawn directly onto the molecular structure, is sometimes preferable. This is achieved by what are called atomic contribution patterns (ACP), where allocation of a fraction of the dinuclear terms to the contributing atoms is achieved by means of appropriately chosen weighting coefficients $r(\alpha)$ [54].

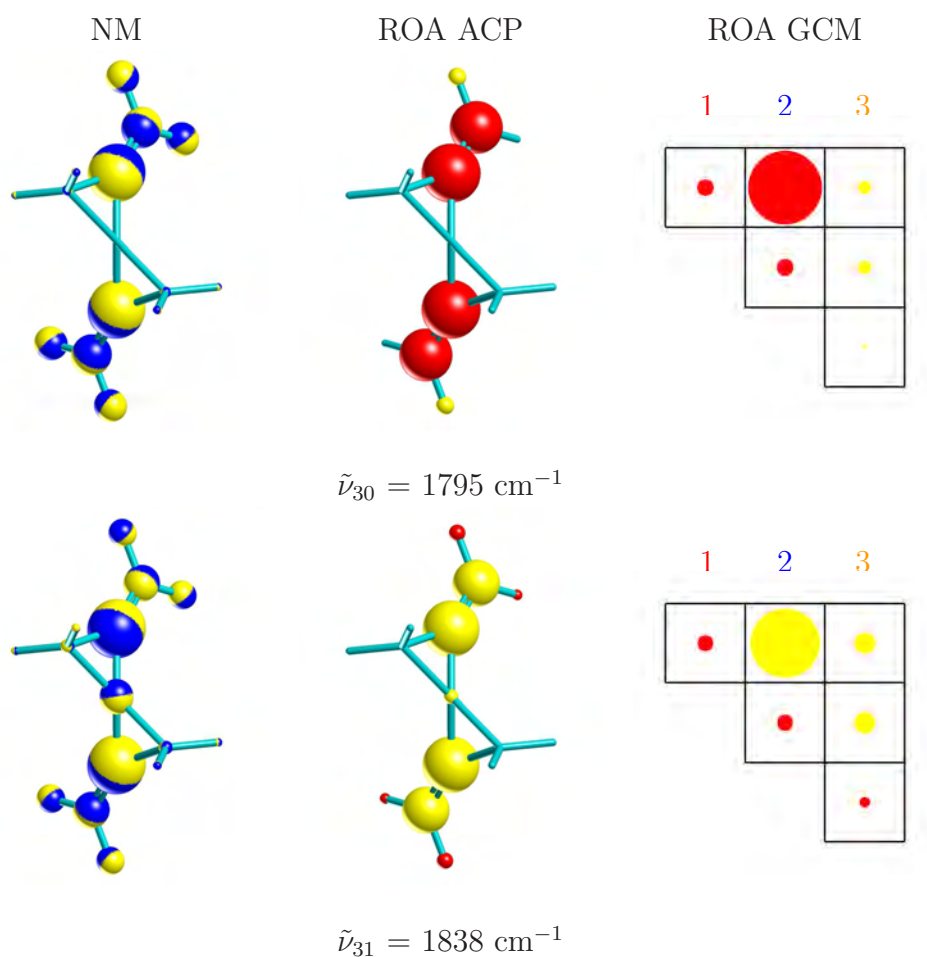


Figure 10.3: Nuclear motions (NM), ROA atomic contribution patterns (ACP) and group coupling matrices (GCM) of (M)-(-)-1,4-dimethylenespiropentane for modes 30 and 31. Groups in GCM are defined as illustrated in Fig. 10.4. Computational details: force field as in Fig. 10.2, , electronic tensors: HF/aug-cc-pVDZ

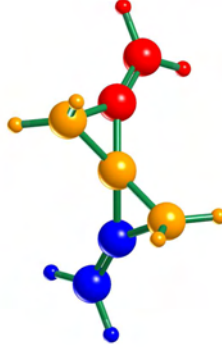


Figure 10.4: Definition of 3 groups of atoms in (M)-(-)-1,4-dimethylenespiropentane: **Group 1:** C=CH₂, **Group 2:** C=CH₂, **Group 3:** rest of the molecule.

The resulting quasi-atomic contributions $J(\alpha)_p$ is given by

$$J(\alpha)_p = \sum_{\beta} [J_{\alpha\beta,p} r(\alpha)_{\alpha\beta,p} + J_{\beta\alpha,p} r(\alpha)_{\beta\alpha,p}] \quad (10.6)$$

where $J(\alpha)_p$ is the quasi-atomic contribution of one of the five molecular invariants \mathfrak{J} . Drawing linear combinations of them multiplied by the frequency factor K_p represents scattering cross section as

$$d\sigma(\alpha)_p = \langle f_v | Q_p | i_v \rangle^2 K_p [c_1 a^2(\alpha)_p + c_2 \beta^2(\alpha)_p] d\Omega \quad (10.7)$$

$$-\Delta d\sigma(\alpha)_p = \langle f_v | Q_p | i_v \rangle^2 \frac{K_p}{c_0} [c_3 a G'(\alpha)_p + c_4 \beta_{G'}^2(\alpha)_p + c_5 \beta_A^2(\alpha)_p] d\Omega \quad (10.8)$$

VOAView draws these quasi-atomic contributions as spheres on atoms (Fig. 10.3). The surface area of each sphere is directly proportional to $d\sigma(\alpha)_p$ or $-\Delta d\sigma(\alpha)_p$. The linear combination coefficients in Eqs. (10.7) and (10.8) can be chosen on the right panel, in order to analyse specific measurement geometries or to identify the individual contributions to a particular invariant. Positive and negative contributions are indicated by dark (red), and light (yellow) shadings, respectively.

For the vibrational modes 30 and 31 of (M)-(-)-1,4-dimethylenespiropentane, i.e., the symmetric and anti-symmetric C=C stretching motion, the ACP in Figure 10.3 indicate the strong contribution of each double bond to the corresponding simulated negative/positive ROA couplet centered at 1816 cm^{-1} (see Fig. 10.7). It can be seen from the simulated spectra illustrated in Fig. 10.7, that our computation overestimates the size of that couplet. Similar results have been published by Ruud and al. [122]. From the GCM, it becomes evident that the main source of that still overestimated couplet, does not arise from the stretching motion itself, but from the coupling between the motion of both methylene entities.

10.2.8 Further Options

A certain amount of options have been implemented in VOAView, but it is not the scope of this work to illustrate all of them. It can be useful to see, for example, simultaneously the computed spectra generated by VOAPlot and the corresponding nuclear motion or atomic contribution patterns. This is illustrated in the central section of this work, with a full picture of VOAView's graphical interface. The spectra were loaded by selecting **Menu Figure->Show Spectra->...** It can also be of interest to compare data obtained with different computational parameters. Figure 10.5 shows the comparison of two sets of data for (M)-(-)-1,4-dimethylenespiropentane. It can be seen that for modes of vibration 13, the ROA contribution for the external methylene hydrogens have opposite signs for data calculated with the rDPS and its parent 3-21++G basis sets, thus yielding different ROA spectra.

Other options will be discovered by using VOAView, among which one can cite the possibility to save molecular orientations and definitions of groups of

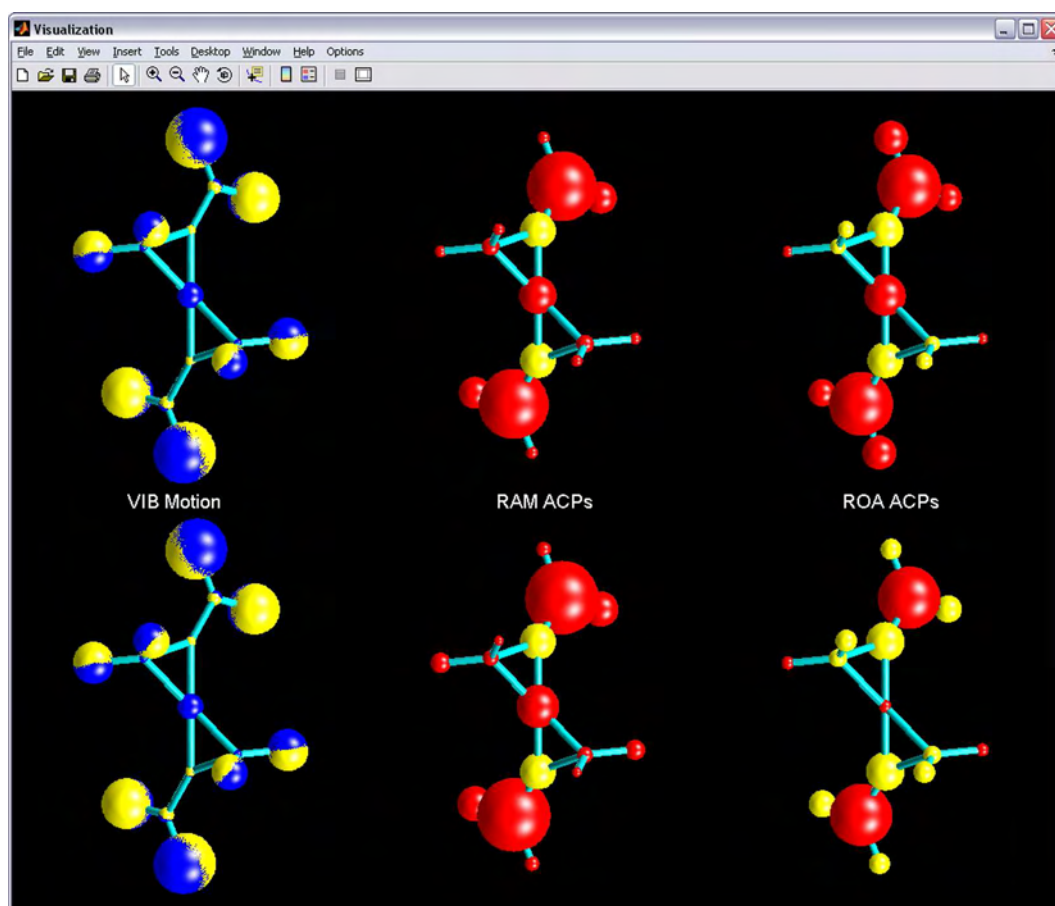


Figure 10.5: VOAView's comparison mode for vibrational mode 13 of (M)-(-)-1,4-dimethylenespiropentane. The force field for the two sets of data were obtained through B3LYP/aug-cc-pVTZ. The electronic tensors were computed by HF/rDPS [86] (top) and HF/3-21++G (bottom).

atoms.

10.2.9 Output File

In order to speed up the drawing process, the evaluation of the reduced invariants defined in Eq. (4.5), their decomposition into an isotropic, anisotropic and anti-symmetric part and the determination of the weighting coefficient in Eq. (10.6) are made the first time a molecule is treated by VOAView. The resulting data are then saved in different files, which will be used for a further session of VOAView. The Appendices contains a description of how data are organised within these output files.

10.3 Main Features of VOAPlot

VOAPlot was first developed for experimental purposes, that is, for reading and analysing spectral data arising from our two ROA instruments. VOAPlot reads the 16 buffers files from both instruments, adds data from different measurement slices and applies a Savitzsky-Golay smoothing upon request.

As the basic purposes of an *ab initio* calculation of vibrational optical activity is the assignment of the unknown absolute configuration of a molecule and the study of its solution conformations, by comparison of measured and computed data, VOAPlot has then been developed for a better representation of simulated VOA spectra.

10.4 Simulating a Voigt Profile

The careful simulation of ROA spectra is critical because terms that occur in the expressions of the scattering cross sections lead to bands with a differing width. Bandwidths for isotropic Raman scattering are generally smaller than for anisotropic scattering, because isotropic scattering depends on the vibrational correlation function only, while for anisotropic Raman scattering, the orientational correlation function also comes into play. The aim of VOAPlot is to account for this generally observed difference in bandwidth between isotropic and anisotropic scattering, and to explicitly include instrumental bandwidth into the simulated spectra [119]. During his diploma work [123], Mehdi Bounouar made a first effort in this respect, and he began to implement such considerations into a Matlab routine. This part of the thesis is a continuation of his work, where by re-implementing the same basic idea, well simulated VOA spectra have finally been obtained.

To keep the problem tractable, the following simplifying assumptions have been made: i) the instrument profile is Gaussian; ii) the band shape of isotropic scattering is a Lorentz profile; and iii) reorientation leads to a Lorentz profile. The band shape of anisotropic scattering, which under these assumptions is the convolution of two Lorentz curves, is therefore also a Lorentz curve.

The convolution of an instrument's Gauss profile with a Lorentz profile leads to a Voigt profile. Voigt profiles must be numerically calculated. A different approach has been undertaken, namely to take advantage of the fact that the convolution of two Gauss functions is also a Gauss function. The whole approach has thus been divided into the following four steps:

- i) simulation of a Lorentz functions by a linear combination of Gaussian functions,
- ii) generation of the Voigt profile by the convolution of the simulated Lorentz functions with the instrument's Gaussian line shape,
- iii) separate calculation of the simulated Voigt profile for the isotropic and anisotropic contributions for each vibrational bands,
- iv) addition of all curves to yield the final Raman and ROA spectra.

In the first step, a Lorentz function $L(x)$ was represented by a linear combination of Gauss functions $G(x) = \exp(-x^2/2a)$

$$L(x) = \frac{k^2}{x^2 + k^2} \quad (10.9)$$

$$L(x) \approx \sum_i c_i e^{-x^2/2a_i^2} \quad (10.10)$$

where the full width at half maximum (FWHM) and area F for the simulated Lorentz function and the individual Gaussian functions is given in Table 10.1.

Table 10.1: FWHM and area F for the simulated Lorentz function, the individual Gaussian functions in the linear combination (Eq. 10.10) and the convolution of two Gaussian functions (Eq. 10.13).

| Functions | FWHM | Area F |
|-----------|------------------------------|--------------------------------|
| $L(x)$ | $2k$ | $k\pi$ |
| $G(x)_i$ | $2\sqrt{2 \ln 2} a_i$ | $\sqrt{2\pi} a_i$ |
| $C(x)$ | $2\sqrt{2 \ln 2(a^2 + b^2)}$ | $\sqrt{2\pi} \sqrt{a^2 + b^2}$ |

FWHM: full width at half maximum; F : area under curves.

Table 10.2: Parameters of the fit of a Lorentz curve (FWHM= 1, $F_L = \pi/2$) by a linear combination of N_G Gauss curves.

| N_G | $1 - r^2$ | $\Delta F[\%]$ | | Coefficient i | | | | | | | |
|-------|----------------------|----------------|-------|----------------------|----------------------|----------------------|----------------------|----------------------|----------------------|----------------------|----------------------|
| | | | | 1 | 2 | 3 | 4 | 5 | 6 | 7 | 8 |
| 8 | $2.20 \cdot 10^{-7}$ | 0.34 | c_i | $1.40 \cdot 10^{-1}$ | $3.71 \cdot 10^{-1}$ | $2.93 \cdot 10^{-1}$ | $1.34 \cdot 10^{-1}$ | $4.58 \cdot 10^{-2}$ | $1.25 \cdot 10^{-2}$ | $2.63 \cdot 10^{-3}$ | $3.43 \cdot 10^{-4}$ |
| | | | a_i | $2.01 \cdot 10^{-1}$ | $3.31 \cdot 10^{-1}$ | $5.61 \cdot 10^{-1}$ | $9.99 \cdot 10^{-1}$ | $1.90 \cdot 10^{+0}$ | $3.99 \cdot 10^{+0}$ | $9.84 \cdot 10^{+0}$ | $3.43 \cdot 10^{+1}$ |
| 7 | $7.84 \cdot 10^{-7}$ | 0.53 | c_i | $1.83 \cdot 10^{-1}$ | $4.05 \cdot 10^{-1}$ | $2.70 \cdot 10^{-1}$ | $1.05 \cdot 10^{-1}$ | $2.98 \cdot 10^{-2}$ | $6.32 \cdot 10^{-3}$ | $8.26 \cdot 10^{-4}$ | |
| | | | a_i | $2.12 \cdot 10^{-1}$ | $3.62 \cdot 10^{-1}$ | $6.45 \cdot 10^{-1}$ | $1.23 \cdot 10^{+0}$ | $2.58 \cdot 10^{+0}$ | $6.34 \cdot 10^{+0}$ | $2.21 \cdot 10^{+1}$ | |
| 6 | $3.01 \cdot 10^{-6}$ | 0.86 | c_i | $2.41 \cdot 10^{-1}$ | $4.32 \cdot 10^{-1}$ | $2.34 \cdot 10^{-1}$ | $7.37 \cdot 10^{-2}$ | $1.60 \cdot 10^{-2}$ | $2.10 \cdot 10^{-3}$ | | |
| | | | a_i | $2.26 \cdot 10^{-1}$ | $4.04 \cdot 10^{-1}$ | $7.69 \cdot 10^{-1}$ | $1.61 \cdot 10^{+0}$ | $3.97 \cdot 10^{+0}$ | $1.38 \cdot 10^{+1}$ | | |
| 5 | $1.28 \cdot 10^{-5}$ | 1.44 | c_i | $3.20 \cdot 10^{-1}$ | $4.44 \cdot 10^{-1}$ | $1.85 \cdot 10^{-1}$ | $4.34 \cdot 10^{-2}$ | $5.76 \cdot 10^{-3}$ | | | |
| | | | a_i | $2.43 \cdot 10^{-1}$ | $4.65 \cdot 10^{-1}$ | $9.75 \cdot 10^{-1}$ | $2.40 \cdot 10^{+0}$ | $8.36 \cdot 10^{+0}$ | | | |
| 4 | $6.12 \cdot 10^{-5}$ | 2.50 | c_i | $4.26 \cdot 10^{-1}$ | $4.27 \cdot 10^{-1}$ | $1.25 \cdot 10^{-1}$ | $1.73 \cdot 10^{-2}$ | | | | |
| | | | a_i | $2.68 \cdot 10^{-1}$ | $5.63 \cdot 10^{-1}$ | $1.38 \cdot 10^{+0}$ | $4.82 \cdot 10^{+0}$ | | | | |
| 3 | $3.47 \cdot 10^{-4}$ | 4.65 | c_i | $5.69 \cdot 10^{-1}$ | $3.63 \cdot 10^{-1}$ | $5.85 \cdot 10^{-2}$ | | | | | |
| | | | a_i | $3.05 \cdot 10^{-1}$ | $7.48 \cdot 10^{-1}$ | $2.60 \cdot 10^{+0}$ | | | | | |

ΔF : error on the area for the best least-square fit of a linear combination of Gauss curves to the shape of a Lorentz curve; r : correlation coefficient between the two curves; N_G : number of Gauss curves used in the fit; c_i : coefficient in the linear combination(10.10), a_i : standard deviation of the individual Gauss curves.

The coefficients c_i and the standard deviations a_i were determined by fitting Gauss functions to the shape of a Lorentz function with $2k = 1$ (i.e., $F_L = \pi/2$). As can be seen from Table 10.2, 6 Gauss functions suffice amply for representing the shape of a Lorentz curve for VOA spectral purposes, with the area of the approximate curve having an error of less than 1% as compared with the exact Lorentz curve. Any Lorentz curve with a FWHM of $2k$ can then be obtained as

$$L(x) \approx \sum_{i=1}^6 c_i e^{-x^2/2(2ka_i)^2} \quad (10.11)$$

By putting in equality the area of the Lorentz curve ($k\pi$) and the area of the sum of Gaussian curves ($\sum_{i=1}^6 c_i 2k\sqrt{2\pi}a_i$), one ends with the following relation:

$$\sum_{i=1}^6 c_i a_i \approx \frac{1}{2} \sqrt{\frac{\pi}{2}} \quad (10.12)$$

It has to be mentioned that this first step, i.e., the fit of a Lorentz curve by a linear combination of Gauss curves, is made only once, the resulting linear combination coefficients c_i and standard deviation a_i being used to represent any further Lorentz curve. This approach can be compared to the Gaussian type orbital (GTO) basis sets approach used in our quantum chemical calculations.

In the second step, the linear combination of Gauss functions is convoluted with the Gaussian line shape function of the instrument. For the convolution of two Gauss functions one has

$$\begin{aligned} C(x) &= G_a(x) \otimes G_b(x) \\ &= e^{-x^2/2a^2} \otimes e^{-x^2/2b^2} \\ &= e^{-x^2/2(a^2+b^2)} \end{aligned} \quad (10.13)$$

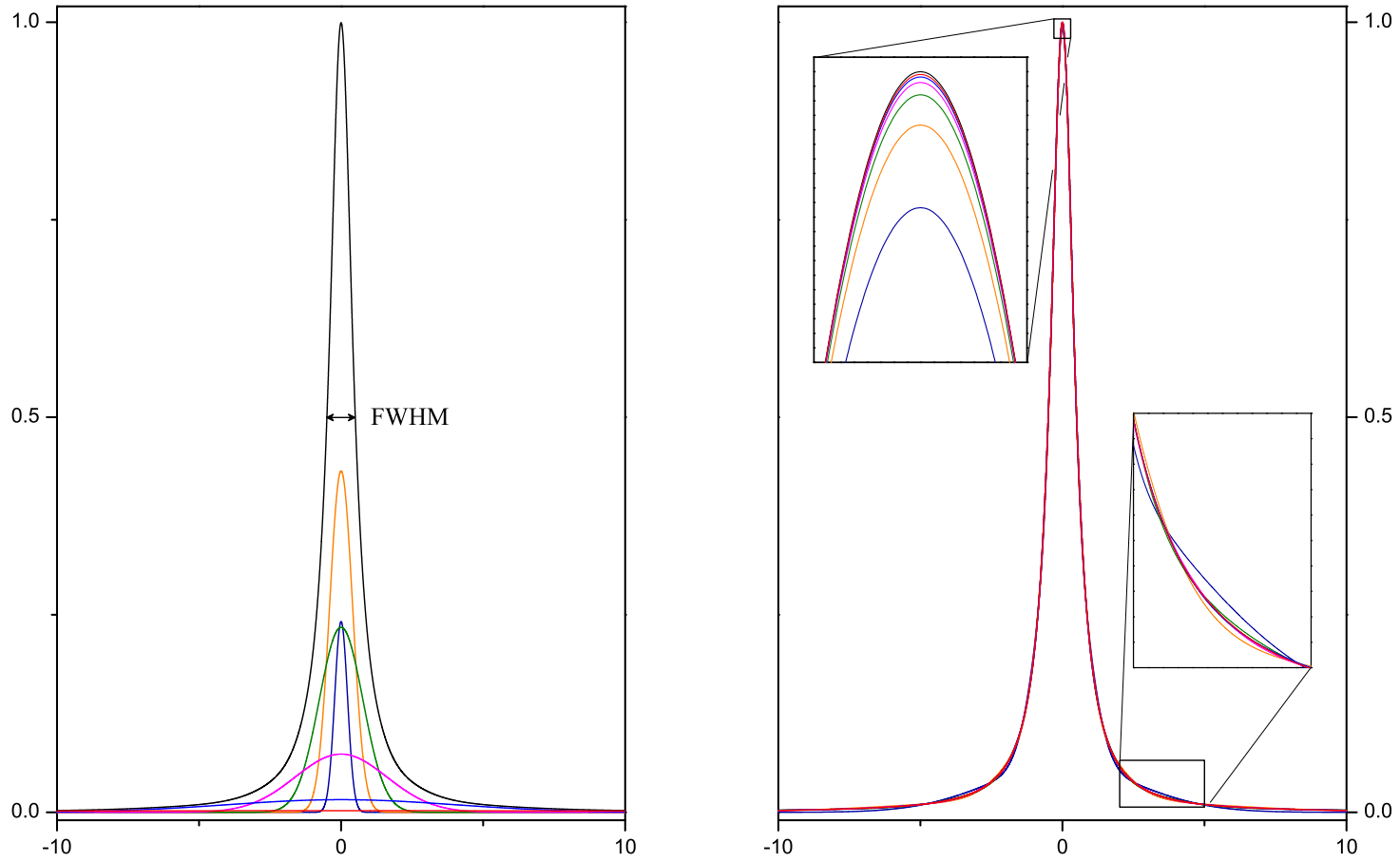


Figure 10.6: Left: Linear combination of 6 Gaussian functions according to the parameters in Table 10.2; the resulting approximate Lorentz curve of FWHM=1 is drawn in black. Right: Fit of N_G Gauss curves to the Lorentz curves (in black). The combination of 6 Gauss curves is drawn in magenta.

which is a Gauss function with an FWHM and an area given in Table 10.1. The convolution of the approximate Lorentz function, Eq. (10.11), with the instrument Gauss line shape of standard deviation b , is thus obtained by the sum of the convolution of each Gaussian functions in the linear combination with the instrument Gauss profile, yielding an approximate Voigt profile $V(x)$ given by

$$V(x) = \sum_{i=1}^6 c_i e^{-x^2/2[(2ka_i)^2+b^2]} \quad (10.14)$$

the area of which is

$$\begin{aligned} F_V &= \sum_{i=1}^6 c_i \sqrt{2\pi} \sqrt{(2ka_i)^2 + b^2} \\ &= \sum_{i=1}^6 c_i a_i \sqrt{2\pi} \sqrt{4k^2 + \left(\frac{b}{a_i}\right)^2} \end{aligned} \quad (10.15)$$

Introducing relation (10.12) into (10.15) gives the final area of the approximate Voigt profile as

$$F_V \approx \frac{\pi}{2} \sum_{i=1}^6 \sqrt{4k^2 + \left(\frac{b}{a_i}\right)^2} \quad (10.16)$$

and the final normalised approximate Voigt profile is given by

$$V_N(x) = \frac{2}{\pi} \sum_{i=1}^6 \frac{1}{\left[4k^2 + \left(\frac{b}{a_i}\right)^2\right]^{\frac{1}{2}}} c_i e^{-x^2/2[(2ka_i)^2+b^2]} \quad (10.17)$$

$$F_{V_N} = \int_{-\infty}^{+\infty} V_N(x) dx \approx 1 \quad (10.18)$$

The final Raman and ROA spectra are obtained in the third step, by calculating Eq. (10.17) separately for the isotropic and anisotropic contributions

for each vibrational bands, with the areas corresponding to the *ab initio* calculated values of the isotropic and anisotropic part of the differential scattering cross sections, according to Eqs. (4.20) and (4.21). The curves are then added to yield the complete and final Raman and ROA spectra. The curves represent differential scattering cross sections per steradian, per inverse centimeter [$\text{\AA}^2 \text{sr}^{-1} \text{cm}$].

The different spectra presented in this work, according to Eq. (10.17), were calculated using bandwidths measured for the ROA instrument in Zürich [48], where the Gaussian profile was found to be 6.7 cm^{-1} (i.e. $b = 6.7/2\sqrt{2 \ln 2}$). The isotropic bandwidth $2k_{iso}$ was chosen as 3.5 cm^{-1} and the anisotropic width $2k_{anis}$ was chosen as 10 cm^{-1} [119, 123]. The choice of the isotropic and anisotropic linewidth is important for a correct simulation of Raman and ROA spectra¹, and especially for a good representation of the degree of circularity C , which, when measured in backscattering with right circular incident radiation, is defined in Eq. (8.1).

Taking the linear combination coefficients c_i and standard deviations a_i from Table 10.2, and the bandwidths b , $2k_{iso}$ and $2k_{anis}$ defined previously, a complete set of Raman, ROA and degree of circularity spectra (from 0 to 3600 cm^{-1}) is obtained in less than 0.3 s for a compound like (M)-(-)-1,4-dimethylenespiropentane. The resulting spectra are illustrated in Fig. 10.7, in combination with the experimental data.

¹For ROA backscattering, the isotropic linewidth is not important, as isotropic scattering makes no contribution (see Table 4.1).

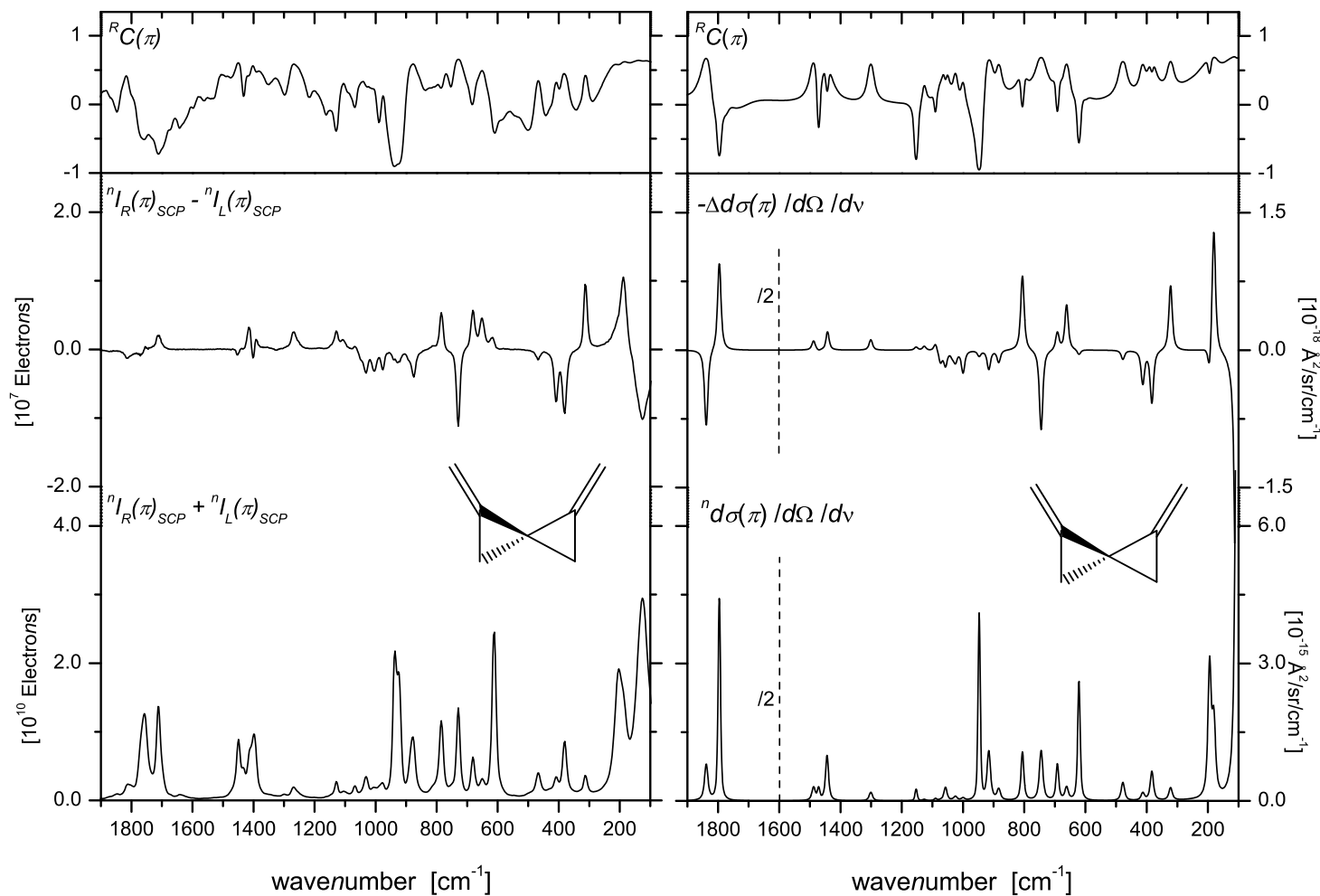


Figure 10.7: Left: SCP backscattering spectra of (M)-(-)-1,4-dimethylenespiropentane measured on the Zürich instrument; 532nm excitation, 38 min exposure time and 120 mW power at sample. Right: simulated SCP(π) spectra. Top: degree of circularity, middle: ROA spectra, bottom: Raman spectra. Instrument profile width: 6.7 cm^{-1} , isotropic width: 3.5 cm^{-1} and anisotropic width: 10 cm^{-1} . Computational details same as in Fig. 10.3.

10.5 Infrared (IR) and Vibrational Circular Dichroism (VCD)

It has been shown elsewhere [54] that the electric dipole strength D , relevant for infrared (IR) absorption, as well as the rotational strength R , relevant for circular difference absorption, i.e., vibrational circular dichroism (VCD), can be expressed in the same way as all molecular Raman and ROA invariants, as a sum of terms that represents the contraction of a pair of nuclear cartesian displacement vectors with a diatomic electronic second-rank tensor.

10.5.1 Expressions for VOAView

For a pictorial representation in VOAView, as for Raman and ROA, the reduced dipole strength D_p and the reduced rotational strength R_p can be introduced, whose $\alpha\beta$ components are given by

$$D_{\alpha\beta,p} = \mathbf{L}_{\alpha,p}^x \cdot \mathbf{V}(D)_{\alpha\beta} \cdot \mathbf{L}_{\alpha,p}^x \quad (10.19)$$

$$R_{\alpha\beta,p} = \mathbf{L}_{\alpha,p}^x \cdot \mathbf{V}(R)_{\alpha\beta} \cdot \mathbf{L}_{\alpha,p}^x \quad (10.20)$$

They are related to the ordinary dipole strength D and rotational strength R as

$$D(f_v \leftarrow i_v) = \langle f_v | Q_p | i_v \rangle^2 \sum_{\alpha,\beta} D_{\alpha\beta,p} \quad (10.21)$$

$$R(f_v \leftarrow i_v) = \langle f_v | Q_p | i_v \rangle \langle i_v | \hat{P}_p | f_v \rangle \sum_{\alpha,\beta} R_{\alpha\beta,p} \quad (10.22)$$

where in D the integral over wave functions (Eq. 4.7), and in R , the integral of the moment operator \hat{P} , for a fundamental transition, have been used:

$$\langle f_v | \hat{P}_p | i_v \rangle = i \sqrt{\frac{\hbar \Delta \omega_p}{2}} \quad (10.23)$$

The elements of the electronic second-rank tensors in Eqs. (10.19) and (10.20), or dyadics $\mathbf{V}_{\alpha\beta}$, have the form

$$V(D)_{\alpha i, \beta j} = \text{Re} \left[\sum_{\mu} \left(\frac{\partial \mu_{\mu}}{\partial x_i^{\alpha}} \right)_0 \left(\frac{\partial \mu_{\mu}}{\partial x_j^{\beta}} \right)_0 \right] = \text{Re} \left[\sum_{\mu} P_{i\mu}^{\alpha} P_{j\mu}^{\beta} \right] \quad (10.24)$$

$$V(R)_{\alpha i, \beta j} = \text{Re} \left[\sum_{\mu} \left(\frac{\partial \mu_{\mu}}{\partial x_i^{\alpha}} \right)_0 \left(\frac{\partial m_{\mu}}{\partial \dot{x}_j^{\beta}} \right)_0 \right] = \text{Re} \left[\sum_{\mu} P_{i\mu}^{\alpha} M_{j\mu}^{\beta} \right] \quad (10.25)$$

where $\boldsymbol{\mu}$ stands for the electric and \boldsymbol{m} for the magnetic dipole moment of the molecule, and $P_{i\mu}^{\alpha}$ and $M_{i\mu}^{\alpha}$ are components of what is known in the VCD literature as atomic polar tensors (APTs) and atomic axial tensors (AATs), respectively. The AATs are defined according to Nafie [124, 125]².

10.5.2 Expressions for VOAPlot

VOAPlot calculates and draws infrared and vibrational circular dichroism spectra, as the molar decadic extinction coefficient and the difference of the extinction coefficients, respectively, for left and right circular radiation, given by [127, 128]

$$\epsilon_p(\tilde{\nu}) = \frac{20\pi^2 N_A}{3\epsilon_0 h c \ln(10)} \tilde{\nu} \langle f_v | Q_p | i_v \rangle^2 D_p f(\tilde{\nu}_p, \tilde{\nu}) \quad (10.26)$$

$$\Delta\epsilon_p(\tilde{\nu}) = \frac{80\pi^2 N_A}{3\epsilon_0 h c^2 \ln(10)} \tilde{\nu} \text{Im}[\langle f_v | Q_p | i_v \rangle \times \langle i_v | \hat{P}_p | f_v \rangle] R_p f(\tilde{\nu}_p, \tilde{\nu}) \quad (10.27)$$

The normalised band shape $f(\tilde{\nu}_p, \tilde{\nu})$ can be assumed to be Lorentzian or Voigt.

²This definition differs by a factor of $i/2\hbar$ from the one used by Stephens and coworkers [126] and in the DALTON and Gaussian03 programs.

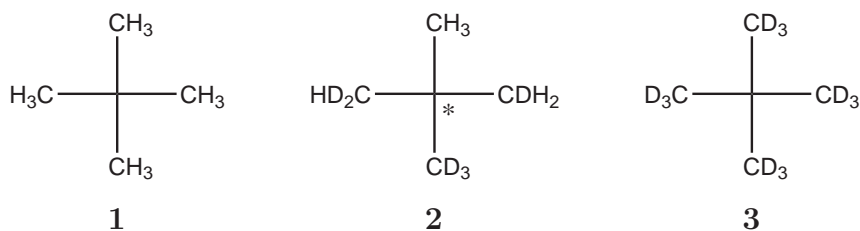
Part V

Applications

Chapter 11

Neopentane and Neopentane- d_{12}

2,2-dimethylpropane (tetramethylmethane or simply neopentane, **1**), is a hydrocarbon molecule present initially in fuels, and therefore found in the atmosphere because of incomplete combustion (exhausts gas). It can have a strong direct adverse influence on the environment.



A selective isotopic substitution of **1** gives rise to an interesting molecule, [$^2\text{H}_1, ^2\text{H}_2, ^2\text{H}_3$]-neopentane (**2**), the *R* enantiomer of which is the subject of a detailed theoretical analysis (see Chapter 12), which assesses the measurability of its vibrational optical activity (VOA). (*R*)-**2** represents the lightest stable molecule whose chirality can be traced to an asymmetrically substituted carbon atom, and the only gaseous or liquid compound in which the asymmetry of a carbon atom is due exclusively to the differing masses of its four substituents. The theoretical work on this reference compound has recently been published in a special issues of the *International Journal of Quantum Chemistry*. This

paper will be used in the next chapter as an introduction to the analysis of (*R*)-[$^2\text{H}_1, ^2\text{H}_2, ^2\text{H}_3$]-neopentane.

From an experimental point of view, the synthesis of (*R*)-**2** seems to be feasible. Chemists are still at work and we hope to get the desired enantiopure (*R*)-[$^2\text{H}_1, ^2\text{H}_2, ^2\text{H}_3$]-neopentane in a near future. In the mean time, the Raman spectrum of the parent achiral neopentane, as well as its fully deuterated form **3**, have been measured.

11.1 Geometry and Conformation

Neopentane has only one stable conformer, a staggered conformation (τ (H6-C2-C1-C3) = 180°) with T_d symmetry (Figure 11.1); the eclipsed conformation (τ (H6-C2-C1-C3) = 120°), with C_{3v} symmetry, is higher in energy and does therefore not need to be taken into account in our simulation. The calculated relative energy barrier between the two states is given in Table 11.1. The methyl group rotation barrier has also been obtained experimentally by several different methods: 4.29 kcal/mol, derived from combination bands of gas phase IR spectra [129]; 4.3 kcal/mol, derived from low frequency modes of molecular crystals [130]; and 4.4 kcal/mol, from thermodynamic measurements [131]. Our calculated DFT mean value of about 3.81 kcal/mol is lower, but in quite good agreement with experimental values, even if DFT is not the suited method when low frequency torsional motions play a important role [132]. The calculated values were obtained by rotating the methyl group by steps of 10° followed by a fully relaxed geometry optimisation (opt). It seems that the methyl group rotation barrier is not very sensitive to the conformation of the rest of the molecule. A mean value of 3.96 kcal/mol has been obtained by just

rotating the methyl group, keeping the remaining atoms fixed.

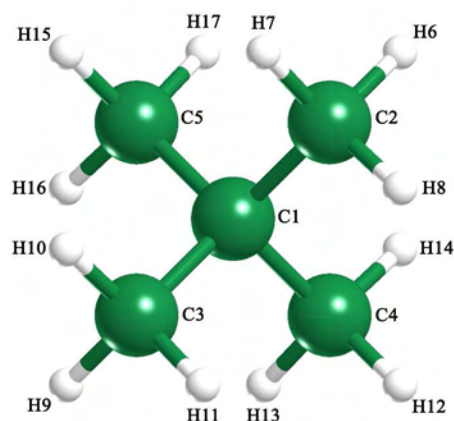


Figure 11.1: Stable staggered T_d geometry of neopentane.

The equilibrium geometry of neopentane **1** and neopentane- d_{12} **3** have been considered to be identical, even if it is known that C-D bond lengths are slightly shorter than C-H bonds, because of their lower zero-point energy (Fig. 11.2). Due to the Born-Oppenheimer approximation used in most quantum chemical packages, the computed geometry of isotopically substituted compounds will be identical to their parent species.

11.2 Vibrational Frequencies

Neopentane and neopentane- d_{12} have 45 normal modes of vibration, distributed in 19 different symmetry species: $3A_1 + A_2 + 4E + 4T_1 + 7T_2$. The A_1 and E vibrations are only Raman active, the T_2 modes are both Raman and IR active, and the A_2 and T_1 modes are forbidden in both Raman and IR.

Pictures of the vibrational motion calculated at the DFT/B3PW91/6-311++G** level for **1** and **3** can be found in Fig. 11.3 and 11.4. A vibrational

Table 11.1: Calculated symmetry barriers for the methyl group rotation in neopentane.

| Theoretical Level | Rotation barrier [kcal/mol] | |
|-------------------------------|-----------------------------|--------------------|
| | relaxed ^a | fixed ^b |
| HF/6-31G ^{*c} | 4.25 | 4.52 |
| MP2/6-31G ^{*d} | 4.41 | - |
| MP2/6-311++G ^{**} | 4.08 | 4.47 |
| B3LYP/6-311++G ^{**} | 3.71 | 3.87 |
| B3PW91/6-311++G ^{**} | 3.76 | 3.94 |
| B3LYP/aug-cc-pVDZ | 3.88 | 4.05 |
| B3PW91/aug-cc-pVDZ | 3.92 | 4.00 |

^a methyl rotation followed by a fully relaxed geometry optimisation.

^b methyl rotation keeping the remaining atoms fixed.

^c from Ref. [133] and confirmed in this work.

^d from Ref. [133].

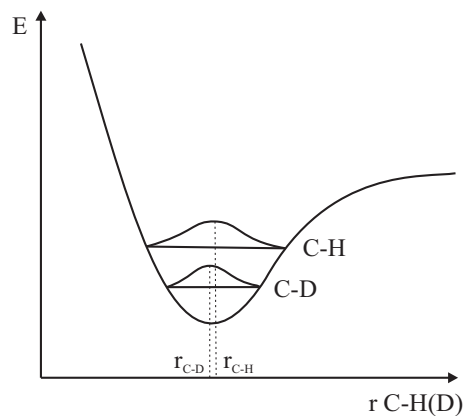


Figure 11.2: The C-D bond has a lower zero-point energy than the C-H bond, and hence a slightly shorter bond length, which is not reproduced by most quantum chemical packages. Drawing not to scale.

Table 11.2: Vibrational inversion occurring for modes of symmetry T_2 between neopentane and neopentane- d_{12} .

| Neopentane | | Neopentane- d_{12} | Symmetry |
|------------|-------------------|----------------------|----------|
| 15 | \leftrightarrow | 16 | T_2 |
| 16 | \leftrightarrow | 17 | T_2 |
| 17 | \leftrightarrow | 15 | T_2 |

correlation has been done by looking at these pictures, where it came out that the numbering of symmetry species for the vibrations of both compounds is mainly identical. There are only three inversions, occurring in the T_2 group, and resumed in Table 11.2. The motion of the central carbon atom in symmetry species 17 in **1** and 15 in **3** is somewhat bigger in the perdeuterated compound in order to fulfill the Sayvetz conditions. This manual correlation has been confirmed by results obtained with a theoretical method [53] and a program recently developed in our group [134].

Different computational levels have been tested for the frequency calculations. With the actual high T_d symmetry, the degree of freedom is quite small and we did not find any vibrational inversion between the sequence computed with the B3LYP and B3PW91 functionals, and the 6-311++G** and aug-cc-pVDZ basis sets. Results presented for **1** and **3** will mainly be concerned with a geometry and frequency calculation at the DFT/B3PW91/6-311++G** level, whereas the geometry and frequencies obtained with the same functional but with the aug-cc-pVDZ basis set have been used for the ROA computation of R -[$^2H_1, ^2H_2, ^2H_3$]-neopentane, in order to be able to compare the results obtained with DALTON and Gaussian03 (Chapter 12).

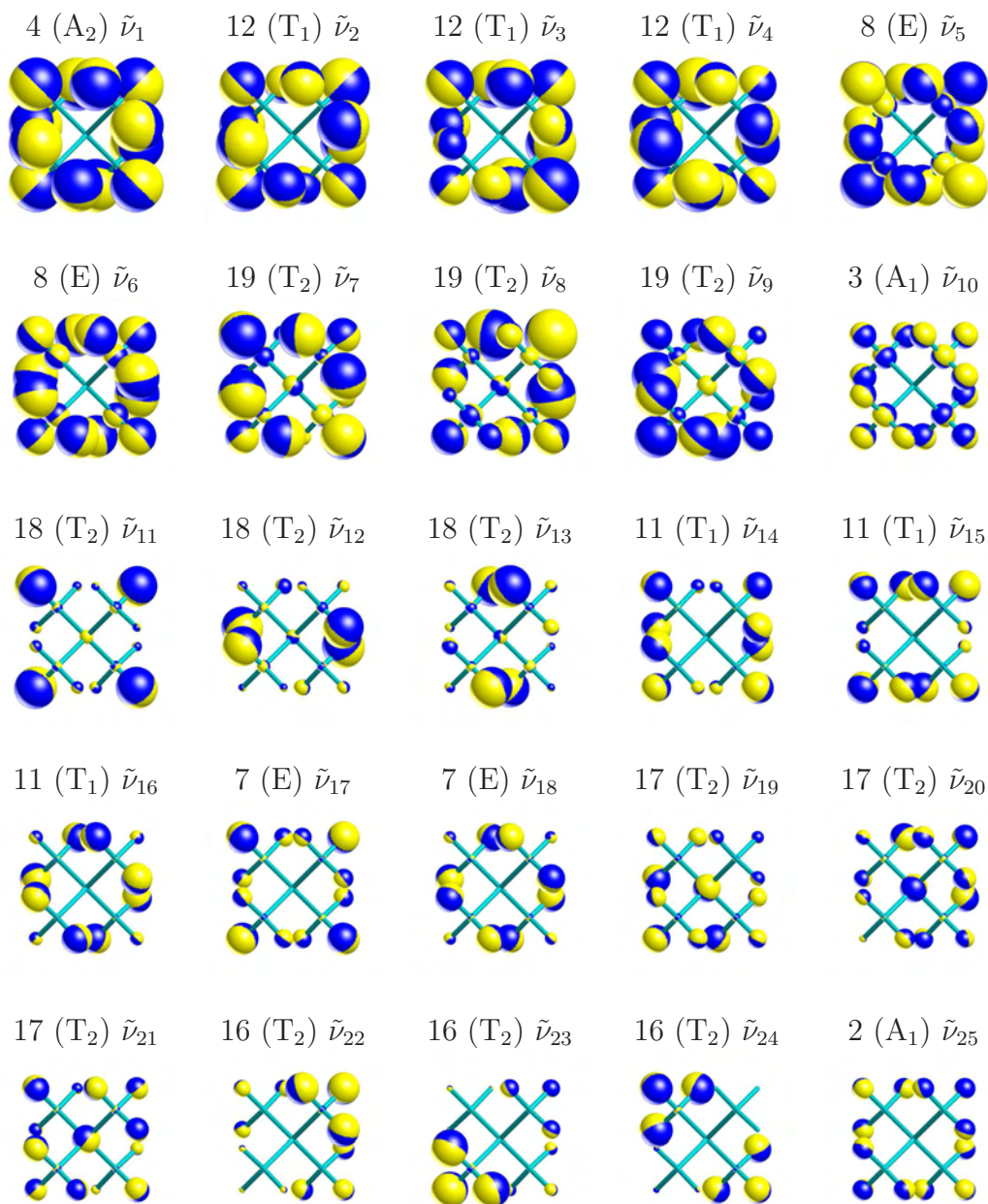


Figure 11.3: Representation of the vibrational motion in neopentane, calculated at the DFT/B3PW91/6-311++G** level. Pictures were obtained with VOAView and are represented according to Gaussian's normalisation, divided by $\sqrt{\Delta\omega}$. Numbering is made according to the 19 symmetry species, from A_1 to T_2 , with decreasing wavenumbers.

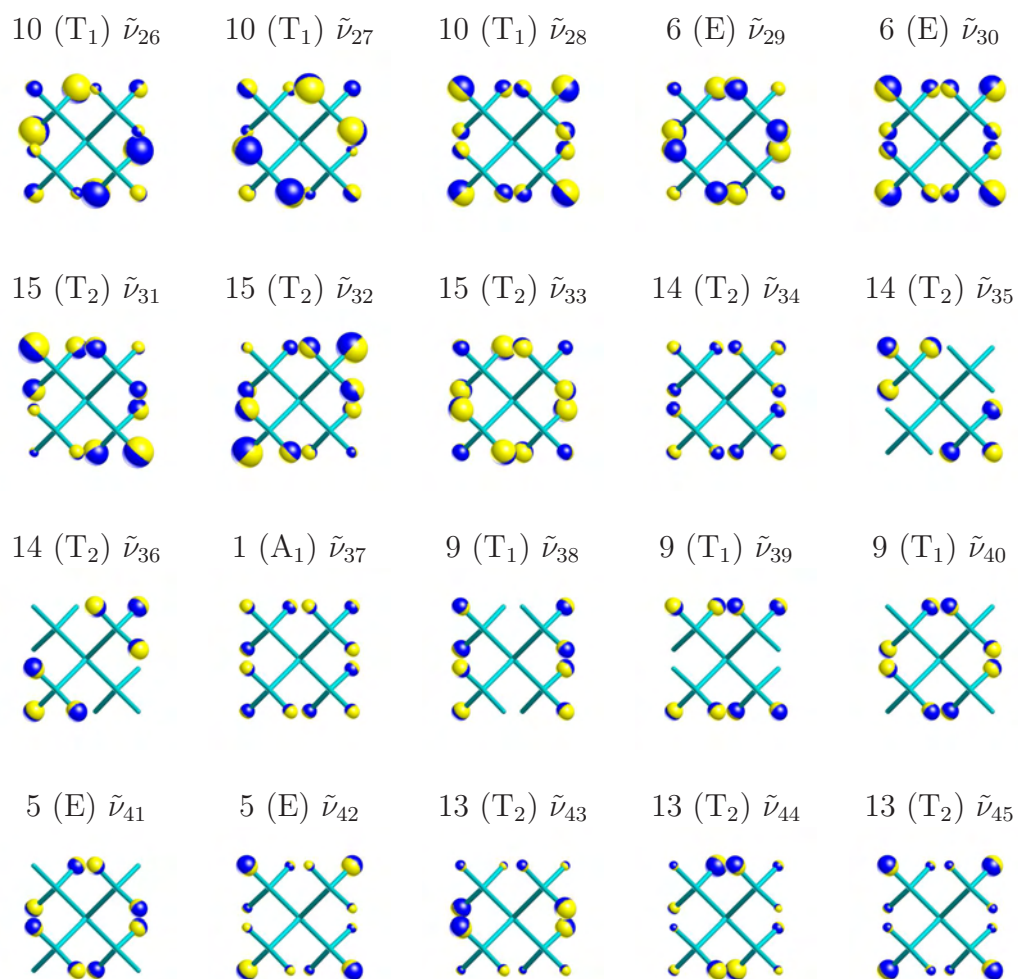


Figure 11.3: continued.

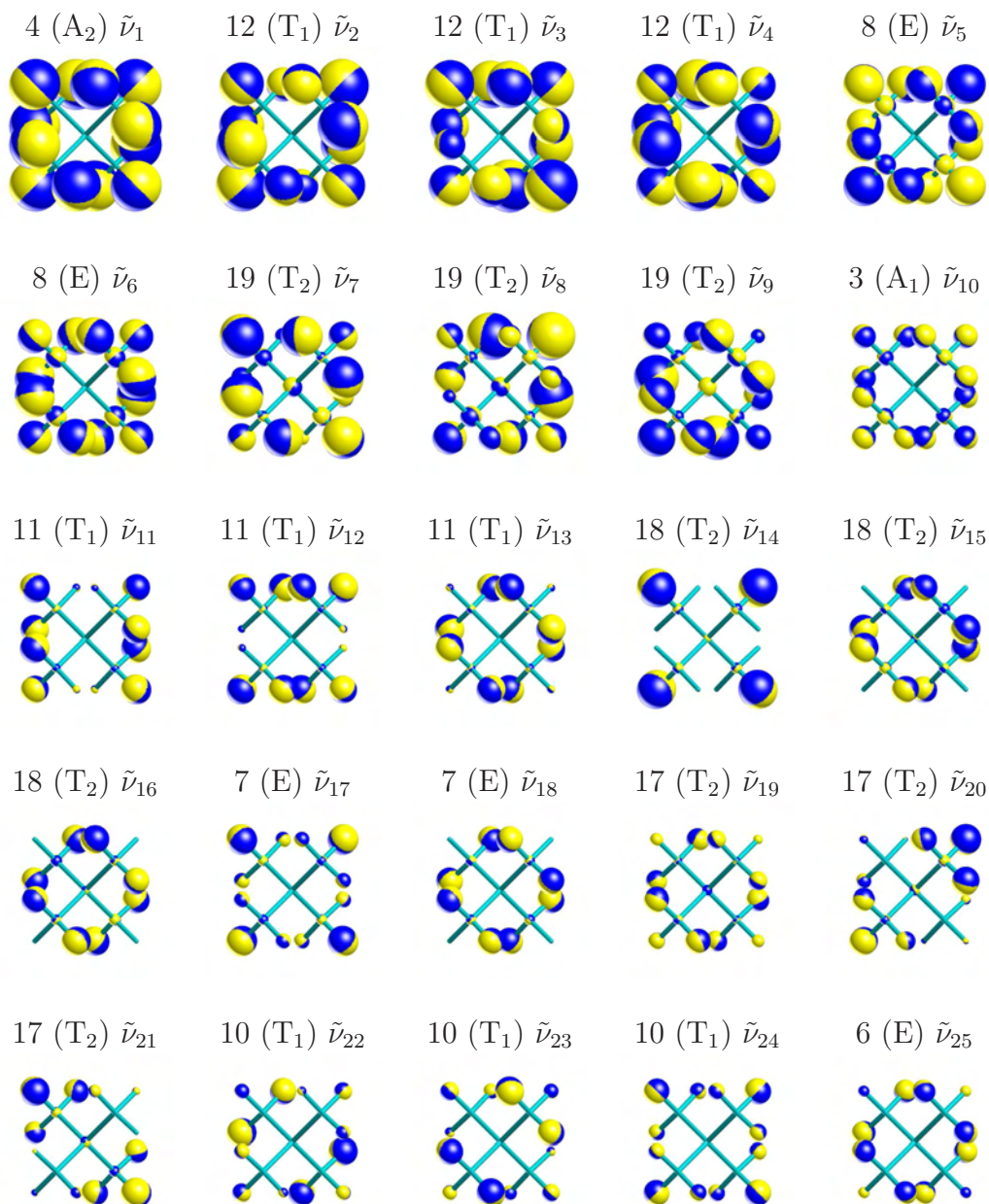


Figure 11.4: Representation of the vibrational motion in neopentane- d_{12} , calculated at the DFT/B3PW91/6-311++G** level. Pictures were obtained with VOAView and are represented according to Gaussian's normalisation, divided by $\sqrt{\Delta\omega}$. Numbering is made according to the 19 symmetry species, from A_1 to T_2 , with decreasing wavenumbers.

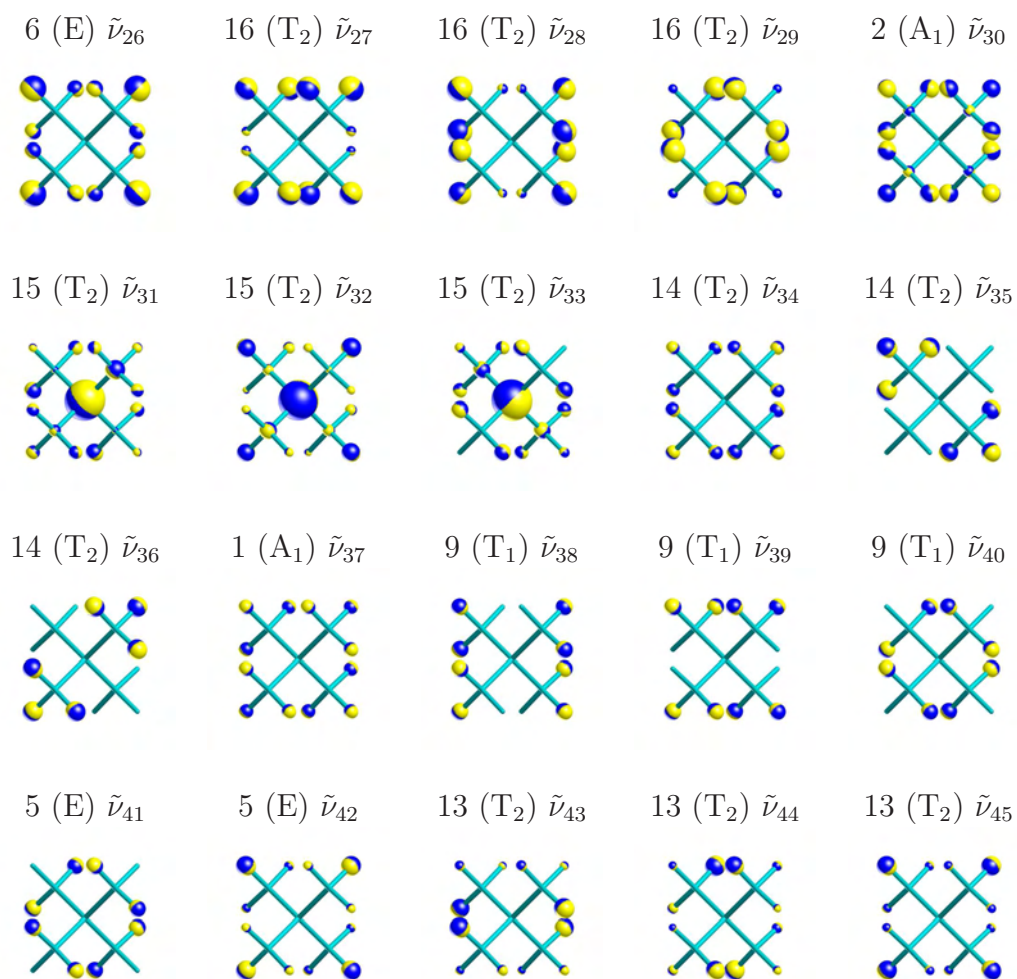


Figure 11.3: continued.

11.3 Raman Spectra

The Raman spectra of neat liquid neopentane and neopentane- d_{12} have been measured at 0°C with an arrangement for controlling the temperature of our Raman optical activity measuring cells (Chapter 7). Figures 11.5 and 11.6 show the corresponding experimental and simulated Raman spectra together with their degree of circularity, and Fig. 11.7 presents simulated line spectra for both compounds. Tables 11.3 and 11.4 resume the recorded Raman fundamentals in comparison with other experimental values, as well as unscaled *ab initio* predicted frequencies.

11.3.1 Assignment for Neopentane

Figure 11.8 shows again the Raman and degree of circularity spectra of neat neopentane. The recorded fundamentals are marked with numbers and symmetry symbols.

There are three predicted A_1 modes. The first one is a CH_3 symmetric stretch observed at 2918 cm^{-1} and the third one consists of a CC stretch vibration (breathing mode) at 742 cm^{-1} . The latter value seems to be higher than other experimental values. One will have to check the calibration procedure for further measurements. The A_1 mode corresponding to the all in-phase CH_3 symmetric bending (umbrella mode) has apparently not been observed in previous experiment. We believe that the recorded band at 1409 cm^{-1} is its first observation in a liquid Raman spectrum, indicated by a degree of circularity different from that for depolarised bands. The A_2 torsional band is optically inactive and has therefore not been observed.

From the four doubly degenerated E modes, three of them have been

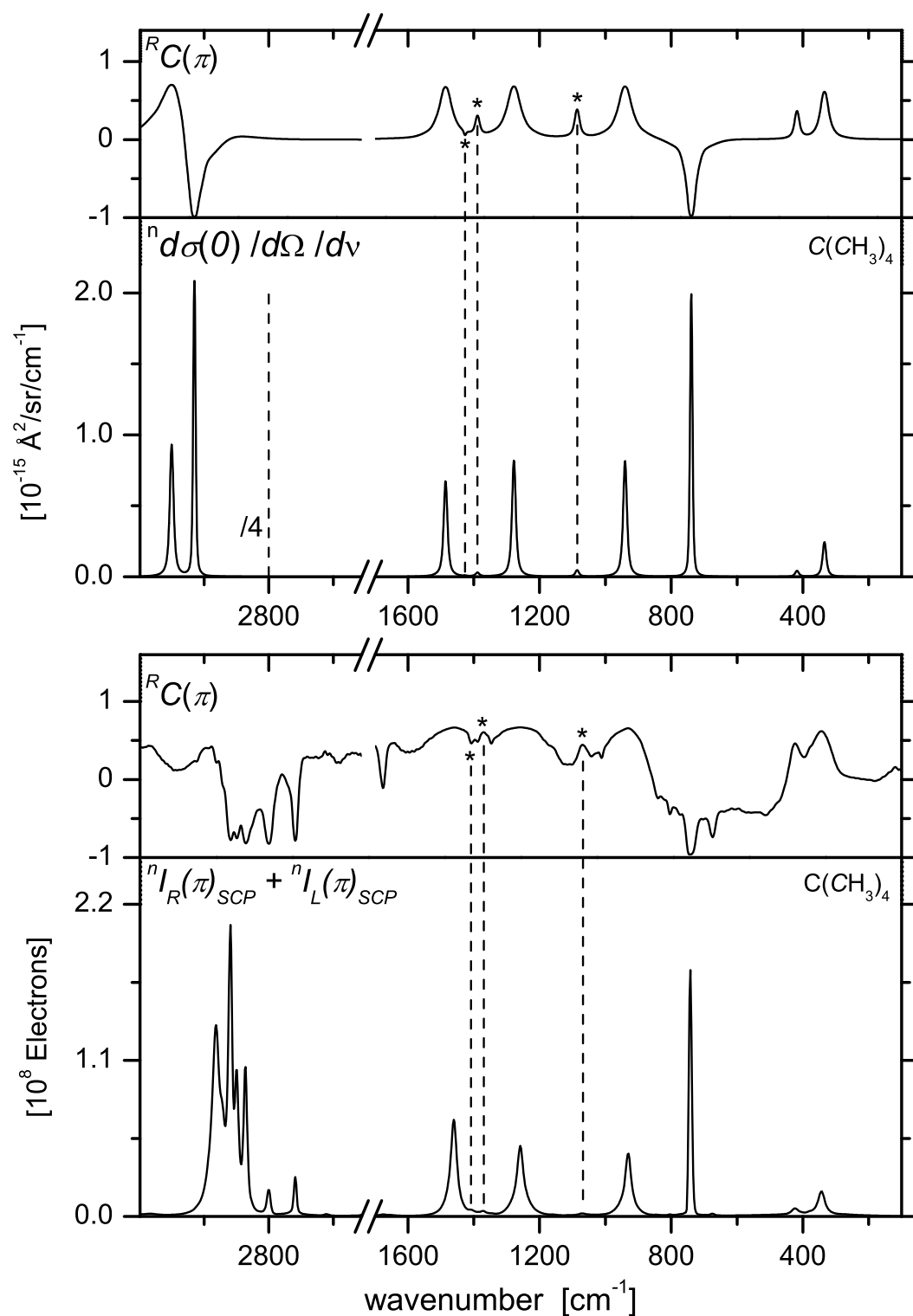


Figure 11.5: Backscattering Raman and degree of circularity spectra of neopentane. Bottom: experimental spectra recorded in a disposable capillary with 200 mW exciting laser power at sample. Top: simulated spectra. Computational details: FF: B3LYP/6-311++G**, ET: TDHF/aug-cc-pVDZ. C-H stretch intensities divided by 4.

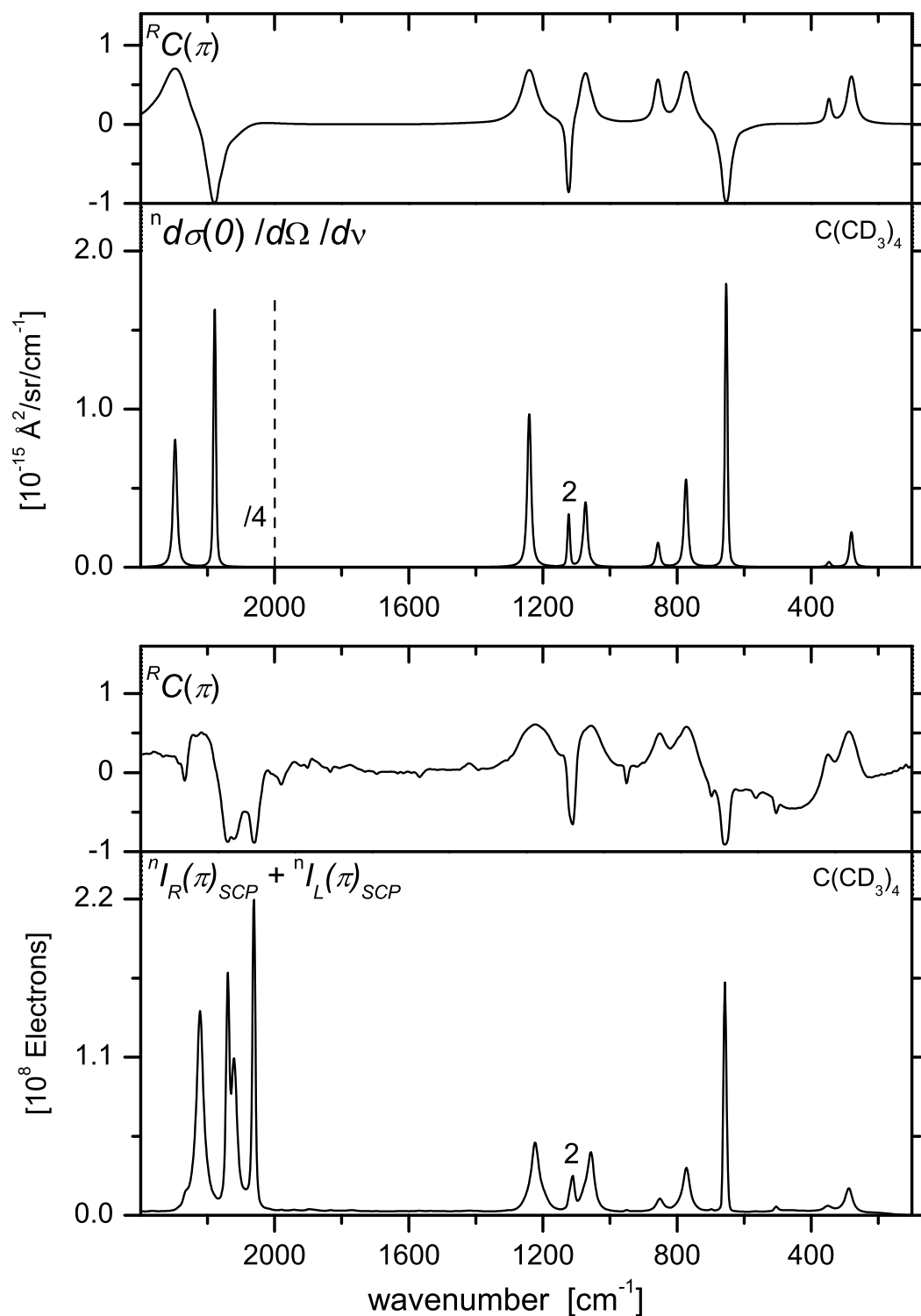


Figure 11.6: Backscattering Raman and degree of circularity spectra of neopentane- d_{12} . Bottom: experimental spectra recorded in a disposable capillary with 200 mW exciting laser power at sample. Top: simulated spectra. Computational details as in Fig. 11.5. Vibrational mode 2 (A_1), corresponding to the symmetric umbrella motion, gives a significant Raman band, whereas it is inactive in the undeuterated neopentane. C-D stretch intensities divided by 4.

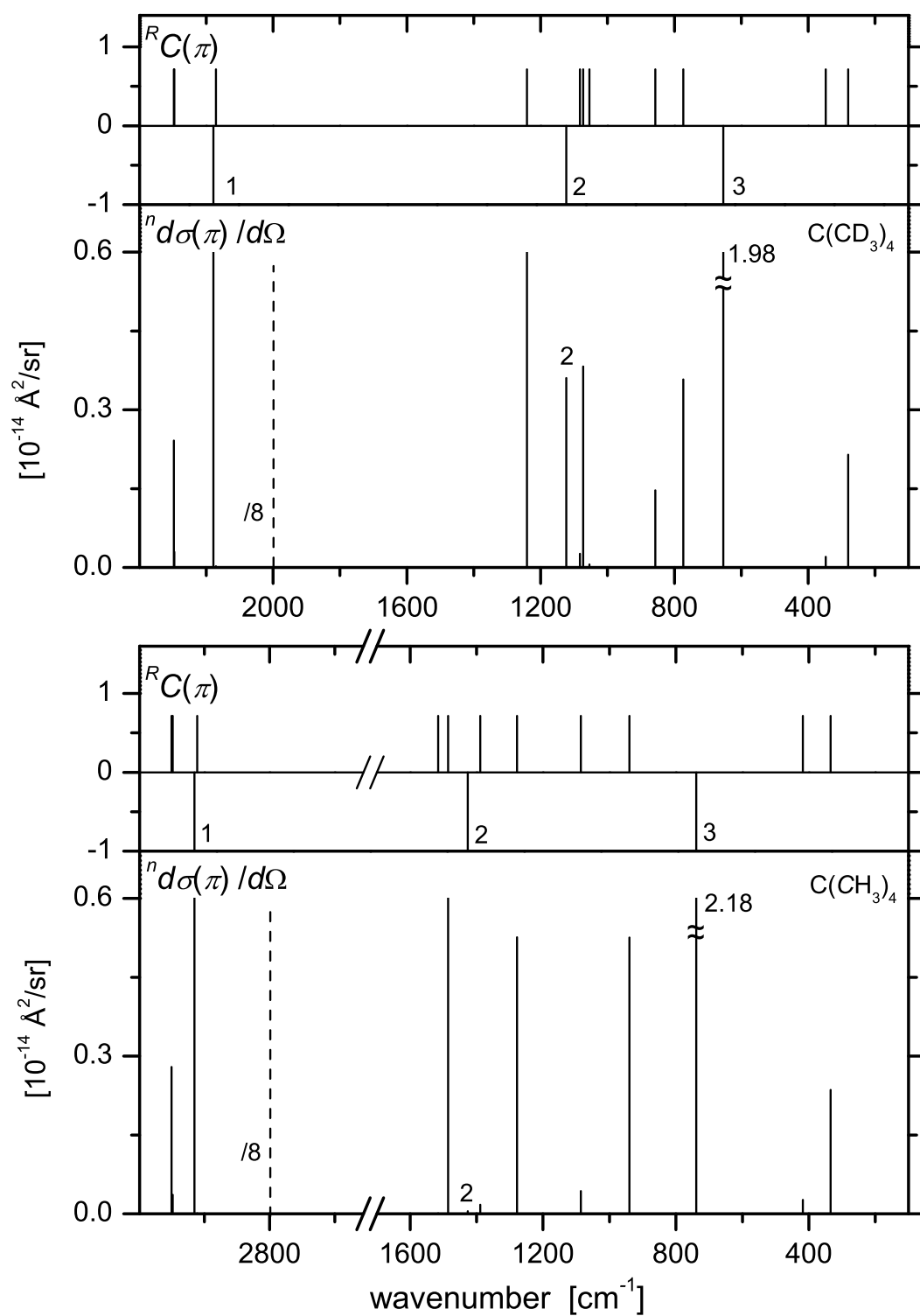


Figure 11.7: Simulated line spectra of neopentane and neopentane- d_{12} . Computational details as in Fig. 11.5. C-H and C-D stretch intensities divided by 8. An interesting behaviour is the substantial scattering observed for vibrational mode 2 (A_1) in the perdeuterated compound.

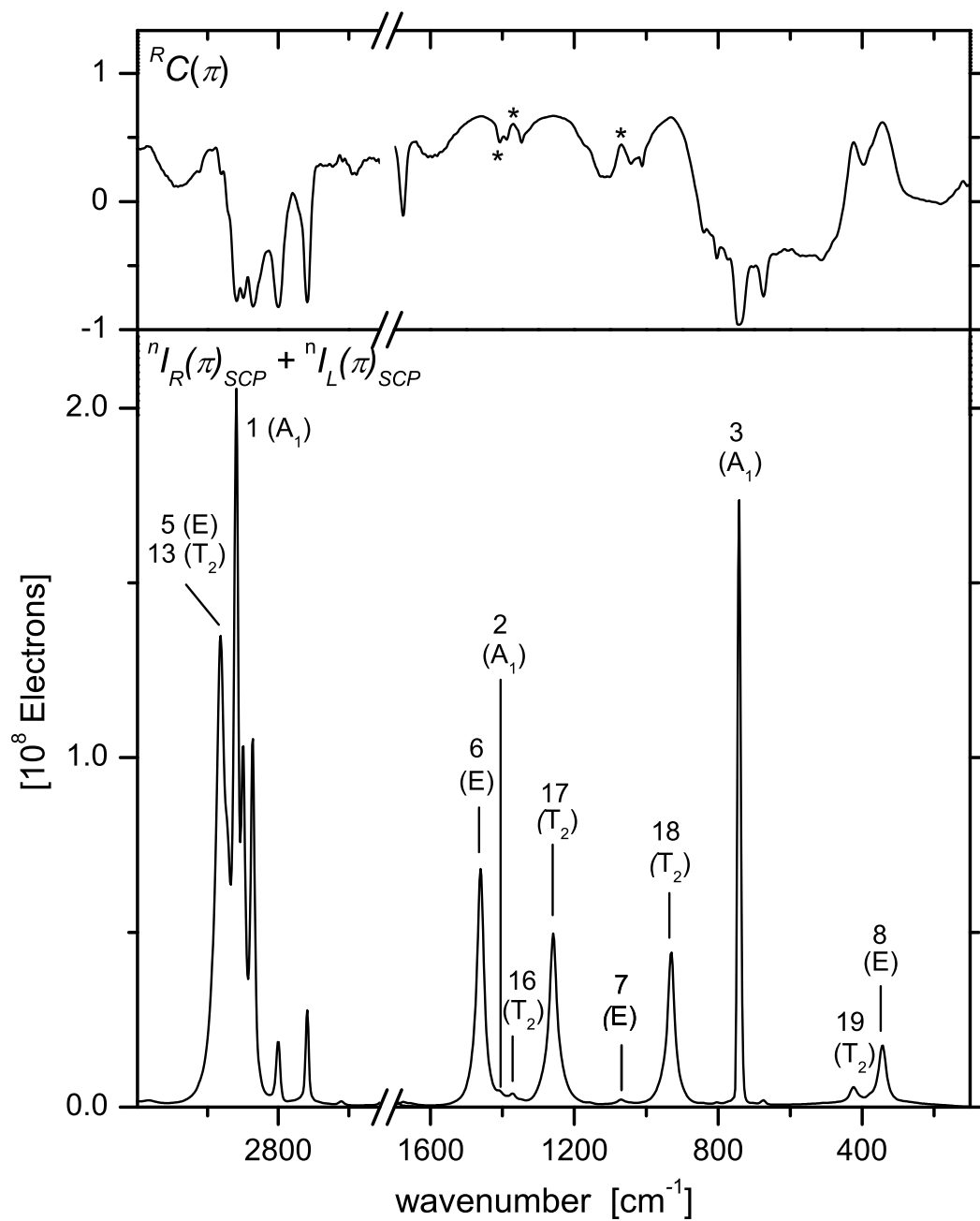


Figure 11.8: Backscattering Raman and degree of circularity spectra of neopentane. Experimental details as in Fig. 11.5.

Table 11.3: Comparison of experimental and theoretical vibrational frequencies for neopentane.

| No. | Mode | Type | Sym. | Gas Raman ^a | Liq. Raman ^b | Liq. Raman ^c | This Work ^d | Harm. calc. ^e |
|-----|-------|----------------------------|----------------|---------------------------|----------------------------|----------------------------|---------------------------|-----------------------------|
| 4 | 1 | $\tau(\text{CH}_3)$ | A ₂ | | | | | 243 |
| 12 | 2-4 | $\tau(\text{CH}_3)$ | T ₁ | | | | | 312 |
| 8 | 5-6 | $\gamma(\text{CCC})$ | E | 334 | 335 | 334 | 342 | 334 |
| 19 | 7-9 | $\gamma(\text{CCC})$ | T ₂ | | 414 | 415 | 423 | 418 |
| 3 | 10 | $\nu_s(\text{CC})$ | A ₁ | 733 | 733 | 733 | 742 | 739 |
| 18 | 11-13 | $\rho(\text{CH}_3)$ | T ₂ | 927 | 925 | 931 | 930 | 940 |
| 11 | 14-16 | $\rho(\text{CH}_3)$ | T ₁ | | | | | 957 |
| 7 | 17-18 | $\rho(\text{CH}_3)$ | E | | | | 1069 | 1086 |
| 17 | 19-21 | $\nu_{as}(\text{CC})$ | T ₂ | 1258 | 1252 | 1256 | 1259 | 1278 |
| 16 | 22-24 | $\gamma_s(\text{CH}_3)$ | T ₂ | | | | 1373 | 1389 |
| 2 | 25 | $\gamma_s(\text{CH}_3)$ | A ₁ | | | | 1409 | 1427 |
| 10 | 26-28 | $\delta_{as}(\text{CH}_3)$ | T ₁ | | | | | 1477 |
| 6 | 29-30 | $\delta_s(\text{CH}_3)$ | E | 1458 | 1455 | 1467 | 1461 | 1486 |
| 15 | 31-33 | $\delta_s(\text{CH}_3)$ | T ₂ | | | | | 1516 |
| 14 | 34-36 | $\nu_s(\text{CH}_3)$ | T ₂ | | 2864 | 2874 | (2871) | 3023 |
| 1 | 37 | $\nu_s(\text{CH}_3)$ | A ₁ | 2922 | 2911 | 2923 | 2918 | 3030 |
| 9 | 38-40 | $\nu_{as}(\text{CH}_3)$ | T ₁ | | | | | 3096 |
| 5 | 41-42 | $\nu_{as}(\text{CH}_3)$ | E | 2962 | 2955 | 2963 | (2963) | 3098 |
| 13 | 43-45 | $\nu_{as}(\text{CH}_3)$ | T ₂ | 2962 | 2955 | | 2963 | 3101 |

Notation: τ : torsion, γ : bending, ν : stretching, ρ : rocking, δ : deformation.

s : symmetric, as : antisymmetric. Frequencies in cm^{-1} .

^a from Ref. [135]. ^b from Ref. [136]. ^c from Ref. [137].

^d 0°C liquid, laser: 532nm, resolution 7 cm^{-1} .

^e Unscaled. Computational details: DFT/B3PW91/6-311++G**.

recorded. The first one, an antisymmetric CH_3 stretch vibration seems to be lost in the broad band at 2963 cm^{-1} , assigned to the T_2 mode. The 1461 cm^{-1} band has been assigned to a symmetric methyl deformation. The observed band at 1069 cm^{-1} corresponds to CH_3 rocking motion, which is also observed for the first time in a liquid Raman spectrum. Finally, the (CCC) bending motion band is found at 342 cm^{-1} , a value that could be corrected by a renewed calibration procedure if compared to the 335 cm^{-1} found in other works.

As mentioned before, we assign the 2963 cm^{-1} band to the first T_2 antisymmetric CH_3 stretch. The second T_2 has been assigned in other works to the 2871 cm^{-1} observed band. This region is difficult to assign because of combination bands and fermi resonances. The third triply degenerated T_2 mode is not observed. We assign, for the first time in liquid Raman spectrum, the band at 1373 cm^{-1} to the out-of-phase symmetric methyl bending (methyl umbrella), indicated again by its degree of circularity. The remaining T_2 modes are assigned unambiguously to the 1259 cm^{-1} , 930 cm^{-1} and 423 cm^{-1} bands, where the last value suffers again from a deviation of about 9 cm^{-1} from other experimental values.

11.3.2 Assignment for Neopentane- d_{12} .

Figure 11.9 shows the Raman and degree of circularity spectra of neat neopentane- d_{12} . The recorded fundamentals are marked with numbers and symmetry symbols.

The assignment of Raman bands for neopentane- d_{12} is very similar to that of the undeuterated compound and will therefore not be repeated here. An

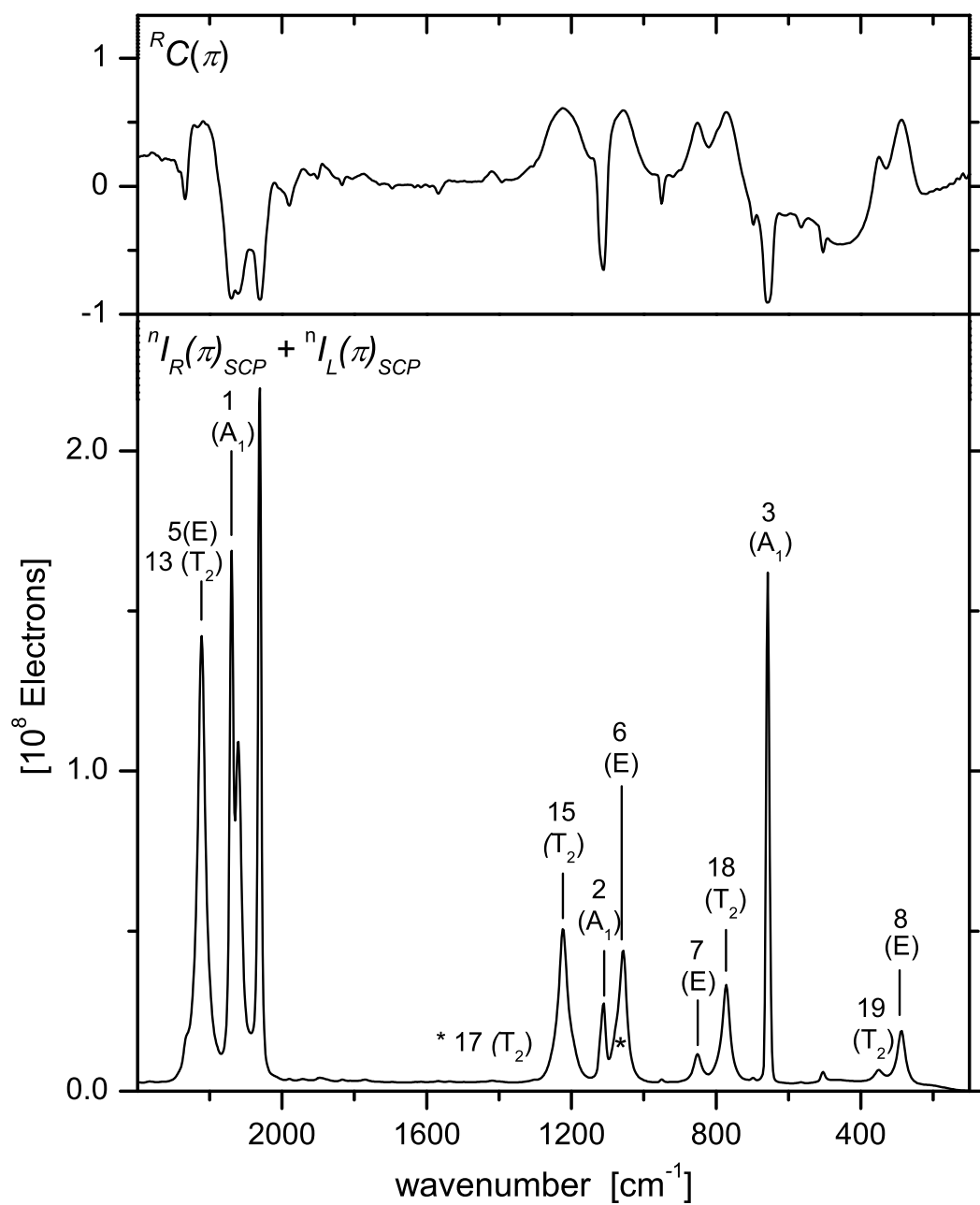


Figure 11.9: Backscattering Raman and degree of circularity spectra of neopentane- d_{12} . Experimental details as in Fig. 11.5.

Table 11.4: Comparison of experimental and theoretical vibrational frequencies for neopentane- d_{12} .

| No. | Mode | Type | Sym. | Gas IR ^a | Liq. Raman ^a | Liq. Raman ^b | This Work ^c | Harm. calc. ^d |
|-----|-------|----------------------------|----------------|------------------------|----------------------------|----------------------------|---------------------------|-----------------------------|
| 4 | 1 | $\tau(\text{CD}_3)$ | A ₂ | | | | | 172 |
| 12 | 2-4 | $\tau(\text{CD}_3)$ | T ₁ | | | | | 222 |
| 8 | 5-6 | $\gamma(\text{CCC})$ | E | | 276 | 282 | 286 | 280 |
| 19 | 7-9 | $\gamma(\text{CCC})$ | T ₂ | | 342 | 346 | 350 | 347 |
| 3 | 10 | $\nu_s(\text{CC})$ | A ₁ | | 648 | 650 | 657 | 653 |
| 11 | 11-13 | $\rho(\text{CD}_3)$ | T ₁ | | | | | 727 |
| 18 | 14-16 | $\rho(\text{CD}_3)$ | T ₂ | 765 | 764 | 765 | 771 | 774 |
| 7 | 17-18 | $\rho(\text{CD}_3)$ | E | | | 844 | 851 | 857 |
| 17 | 19-21 | $\gamma_s(\text{CD}_3)$ | T ₂ | 1037 | 1048 | 1072 | 1056 | 1054 |
| 10 | 22-24 | $\delta_{as}(\text{CD}_3)$ | T ₁ | | | | | 1066 |
| 6 | 25-26 | $\delta_s(\text{CD}_3)$ | E | | | | 1057 | 1073 |
| 16 | 27-29 | $\delta_s(\text{CD}_3)$ | T ₂ | 1066 | | | 1076 | 1082 |
| 2 | 30 | $\gamma_s(\text{CD}_3)$ | A ₁ | | 1104 | 1108 | 1113 | 1123 |
| 15 | 31-33 | $\nu_{as}(\text{CC})$ | T ₂ | 1218 | 1212 | 1217 | 1224 | 1241 |
| 14 | 34-36 | $\nu_s(\text{CD}_3)$ | T ₂ | 2058 | | | 2120 | 2171 |
| 1 | 37 | $\nu_s(\text{CD}_3)$ | A ₁ | | 2128 | 2100 | 2139 | 2178 |
| 9 | 38-40 | $\nu_{as}(\text{CD}_3)$ | T ₁ | | | | | 2293 |
| 5 | 41-42 | $\nu_{as}(\text{CD}_3)$ | E | | 2211 | 2219 | (2222) | 2295 |
| 13 | 43-45 | $\nu_{as}(\text{CD}_3)$ | T ₂ | 2218 | | | 2222 | 2297 |

Notation: τ : torsion, γ : bending, ν : stretching, ρ : rocking, δ : deformation.

s : symmetric, as : antisymmetric. Frequencies in cm^{-1} .

^a from Ref. [138]. ^b from Ref. [139].

^c 0°C liquid, laser: 532nm, resolution 7 cm^{-1} .

^d Unscaled. Computational details: DFT/B3PW91/6-311++G**.

interesting feature is the intensity increase for the totally symmetric A_1 umbrella mode [119]. In **1**, this vibrational mode is almost inactive, whereas in **3**, it's corresponding Raman band is quite substantial. The two other vibrational modes where a similar motion of the methyl group contributes (T_2 modes 16 and 17 in **1** and T_2 modes 17 and 15 in **3**, respectively), do not show a similar Raman activity increase in the fully deuterated compound. In order to account for this interesting behaviour, different tools have been developed during this thesis.

Looking at the difference of the distance between nuclei [119] for the two turning point of nuclear motion, is useful when trying to sort vibrational modes. Fig. 11.10 shows a plot for **1** and **3**, where the sum of distance changes for the whole molecules is drawn for each vibrational mode. Because of the T_d symmetry, only the three A_1 modes show a sum of distance changes different from zero. Vibrational modes 1 and 3 give similar values for both compounds, whereas for the umbrella mode 2, the sum of distance changes is about three times bigger for the undeuterated neopentane than for neopentane.

Fig. 11.10 shows the vibrational energy of the particular kind of atoms in both compounds. It is obtained by summing the contributions of the particular nuclei in the fraction of vibrational energy $E_{\alpha,p}$ which a nucleus α contributes to a normal mode p , defined in [119]:

$$\frac{E_{\alpha,p}}{E_p} = m_{\alpha} \mathbf{L}_{\alpha,p}^x \cdot \mathbf{L}_{\alpha,p}^x \quad (11.1)$$

The vibrational energy of the carbon and hydrogen atoms in neopentane for the umbrella mode 2 is quite different, with a factor of about 4 between them, whereas for neopentane- d_{12} , a similar value is obtained for carbon and deuterium atoms. A somewhat analogous impression is given by looking at

the vibrational energy distribution (VED) in Fig. 11.11. It is evident that the carbon atoms have to move with a bigger amplitude in the deuterated compound, in order to fulfill the Sayvetz conditions. All these considerations, in terms of distance changes and fraction of vibrational energy, are properties of individual nuclei, and one would think that the Raman spectrum of this umbrella mode should be stronger for the undeuterated compound. As has been seen previously, the opposite is true in the experimental spectra.

In order to elucidate the origin of the Raman activity of that interesting symmetric umbrella mode, a detailed expertise of the importance of inter-atomic contributions is necessary. Group coupling matrices (see Chapter 10, Section 10.2) are used here in this respect. Fig. 11.12 shows the ACP and two different GCM for both compounds. The ACP reflects very well the stronger scattering observed in the experimental spectra of **3**.

In a first try, we decided to look at group coupling matrices for the individual methyl groups, of local symmetry C_3 , where columns and rows correspond to the H or D, and the C atoms. In neopentane, a cancellation between positive mononuclear and negative dinuclear terms for individual CH_3 groups is observed. The cancellation is less pronounced for the CD_3 groups, despite its identical electronic structure, mainly because coupling terms between deuterium atoms are positive. Additionally, mononuclear contributions by carbon atoms also make a larger contributions in **3**. The result is a slightly stronger overall scattering by individual CD_3 groups. This effect cannot be observed for the two other modes mentioned previously, where the umbrella motion of individual methyl groups is mixed with modes of other symmetry.

Dinuclear terms in individual methyl groups do not account for the observed

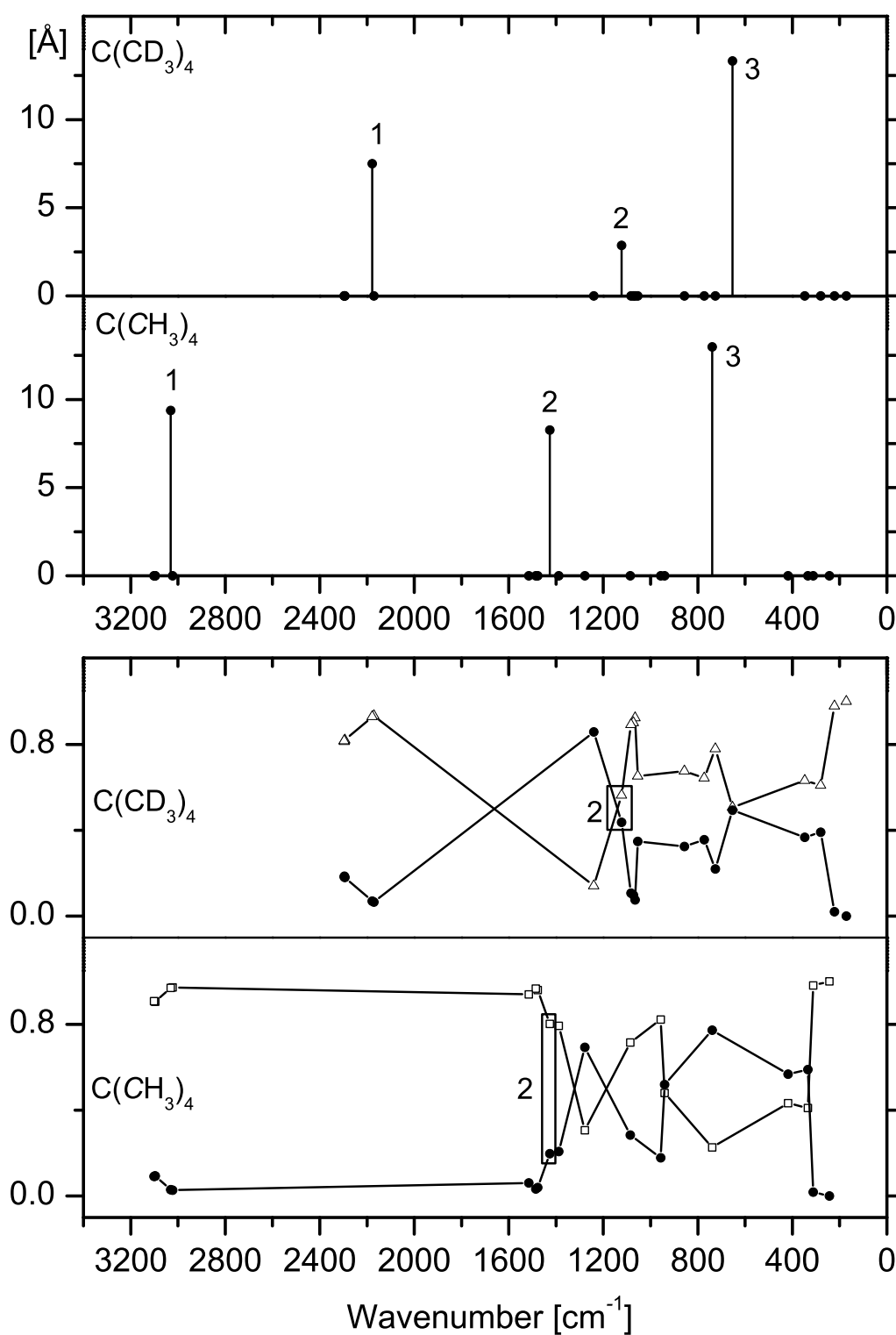


Figure 11.10: Top: variation of the sum of internuclear distances with vibrational motion. Bottom: vibrational energy distribution diagrams calculated according to Eq. 11.1. \bullet : carbon, \square : hydrogen, \triangle : deuterium atoms.

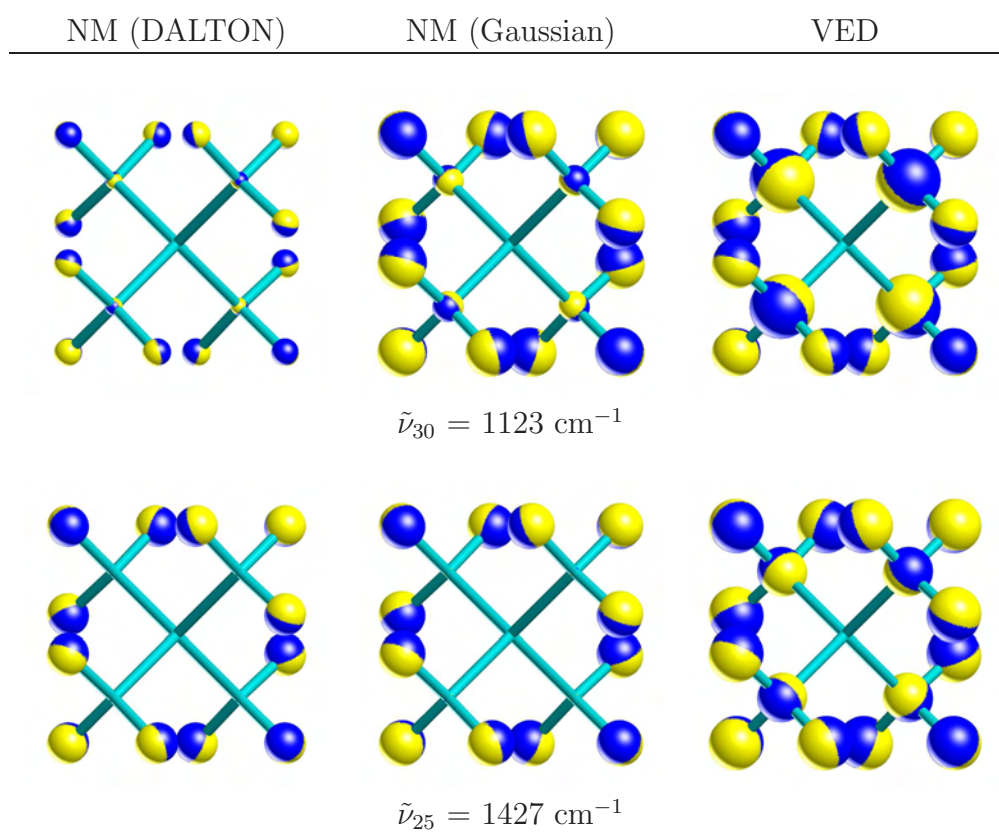


Figure 11.11: Nuclear motion (NM) and vibrational energy distribution (VED) for mode 2 (A_1) of **1** (bottom) and **3** (top). Computational details as in Fig. 11.5.

behaviour of the fully symmetric umbrella mode. The right part of Fig. 11.12 shows GCMs where columns and rows correspond to the three H or D atoms from each of the four methyl groups. The resulting pictorial representation is self-explanatory. First, mono-group terms are slightly stronger in the fully deuterated compound, and secondly, the coupling terms between individual D_3 groups are positive and substantial, whereas coupling terms between H_3 groups are negative. The origin of the stronger scattering by CD_3 groups in neopentane is thus largely the result of the coupled motion of the four individual entities.

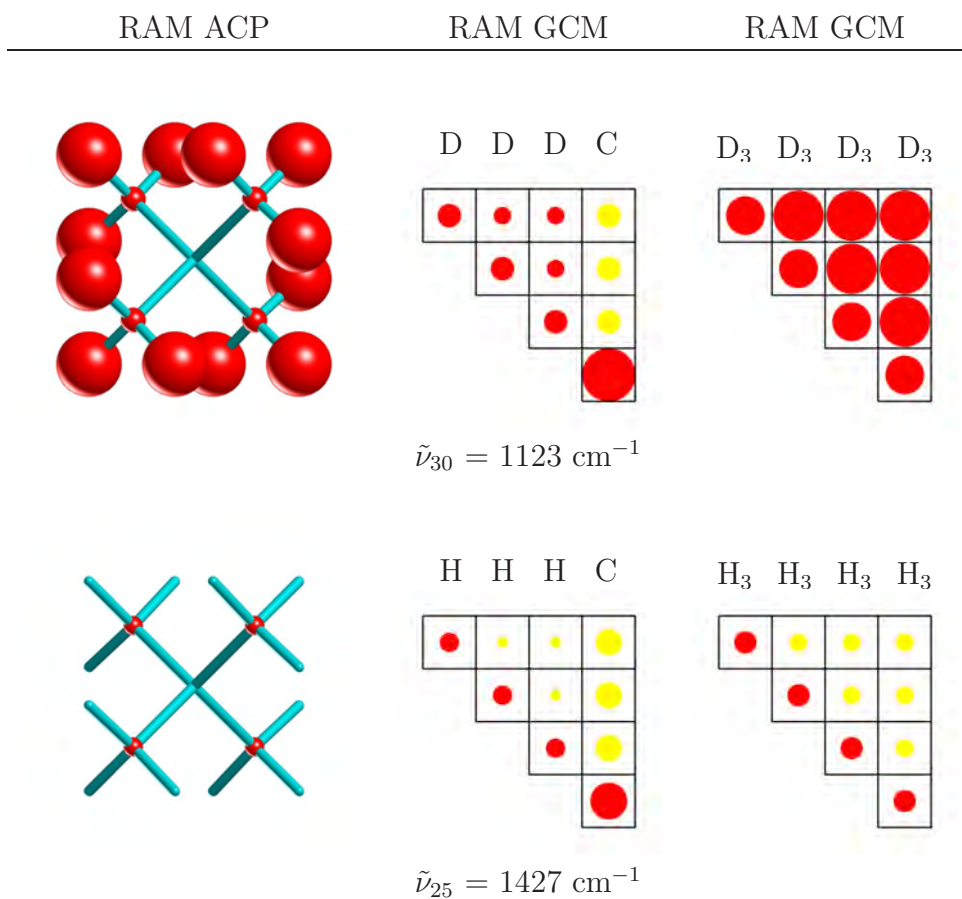


Figure 11.12: Raman atomic contribution patterns (RAM ACP) and Raman group coupling matrices (ROA GCM) for the umbrella mode 2 (A_1) of **1** (bottom) and **3** (top). Computational details as in Fig. 11.5. RAM ACP for **1** have been multiplied by a factor of 2. Groups in GCM are indicated on top of columns.

Chapter 12

(R) -[$^2\text{H}_1$, $^2\text{H}_2$, $^2\text{H}_3$]-Neopentane

12.1 Introduction: Publication in *Int. J. Quantum Chem.*

(R) -[$^2\text{H}_1$, $^2\text{H}_2$, $^2\text{H}_3$]-neopentane (**2**), as has been mentioned in the previous chapter, is a very interesting molecule, which owes its chirality exclusively to an asymmetric distribution of its masses, the electronic distribution being completely symmetric (T_d). Being able to measure the ROA and VCD of this compound would assess the power and experimental limits of vibrational optical activity spectroscopy. According to organic chemists, the synthesis of **2** seems feasible. While waiting on the compound itself, a theoretical work has been done, which assesses its VOA measurability.

The results of that work have recently been published in a special issue of the *International Journal of Quantum Chemistry* dedicated to vibrational spectroscopy. This paper, illustrated in the next pages, demonstrates the benefits of realistic band shapes of the Voigt type to best simulate VOA spectra, as well as the power of graphical tools developed during this thesis to analyse computed data.

Is the Vibrational Optical Activity of (R)-[²H₁, ²H₂, ²H₃]-Neopentane Measurable?

WERNER HUG, JACQUES HAESLER

Department of Chemistry, University of Fribourg, Ch. du Musée 9, CH-1700 Fribourg, Switzerland

Received 17 November 2004; accepted 14 February 2005

Published online 11 April 2005 in Wiley InterScience (www.interscience.wiley.com).

DOI 10.1002/qua.20600

ABSTRACT: The compound, (R)-[²H₁, ²H₂, ²H₃]-neopentane, with its *T_d* symmetric electron distribution, is the archetype of molecules that owe their chirality exclusively to an asymmetric distribution of the masses of their nuclei. It has nine rotamers, which fall into two classes, one where the interchange of hydrogen and deuterium nuclei leads to an identical rotamer, and one where it interconverts different rotamers. Ab initio computations show that individual rotamers have Raman optical activity (ROA) and vibrational circular dichroism (VCD) of the same size as ordinary chiral molecules. Dilution and cancelation for the experimentally accessible equilibrium mixture reduces ROA and VCD, but the simulation of spectra with realistic band shapes of the Voigt type shows that both remain measurable in the 700–1,400-cm⁻¹ range, where ROA and VCD have a close to mirror image appearance. In the CH- and CD-stretch region, in contrast, the sign pattern of ROA and VCD is identical. This curious behavior appears to be a consequence of the differing influence of inertial contributions in the two spectral regions. If summed over all vibrations, ROA and VCD cancel neatly, as one expects from the *T_d* symmetric electron distribution. © 2005 Wiley Periodicals, Inc. *Int J Quantum Chem* 104: 695–715, 2005

Key words: vibrational optical activity; neopentane; Voigt line shape; inertial contributions

Introduction

Vibrational optical activity (VOA) depends on the chirality of a molecule's electron distribution as well as the chirality of the mass distribution of its nuclei. Measurements [1, 2] and theoretical

considerations [3] have shown that the dissymmetry of nuclear motion is generally more important for generating VOA than the dissymmetry of the electron distribution, with the exception of resonance ROA [4]. A convincing demonstration of this fact is the observation that electronically achiral molecules, rendered chiral by isotope substitution only, can show VOA of the same size as the VOA one measures and calculates for molecules with an overall chiral structure.

Correspondence to: W. Hug; e-mail: w.hug@gmx.net
Contract grant sponsor: Swiss National Science Foundation.
Contract grant numbers: 2000-066679; 200020-103750.

HUG AND HAESLER

Carbon atoms, substituted fourfold with physically distinguishable groups, have historically been considered the prime source of molecular chirality. Compounds derived from methane with three or four of its hydrogen atoms replaced by differing groups have often been discussed as chiral model compounds, and sometimes synthesized for studying their chiroptical properties [5]. With electronic optical activity, until recently the only physical method available for distinguishing enantiomers by spectroscopic means, one of the objectives of such work has been to test the limit to which similar, but not identical, substituents lead to measurable electronic optical rotatory dispersion or circular dichroism (CD) [6]. It does not appear, however, that [$^2\text{H}_1$, $^2\text{H}_2$, $^2\text{H}_3$]-neopentane has ever been discussed in such a context. One of the reasons may have been that its two enantiomers were judged a priori as not physically or chemically distinguishable.

With the advent of vibrational optical activity, ROA and VCD now exist as new spectroscopic techniques that should potentially be able to distinguish the R and S form of [$^2\text{H}_1$, $^2\text{H}_2$, $^2\text{H}_3$]-neopentane. Assessing the measurability of the ROA and VCD spectrum of this molecule has therefore been one of the reasons we have undertaken a theoretical study of its VOA. There are other aspects, however, which make the study of this interesting molecule worthwhile. It certainly represents the lightest stable molecule whose chirality can be traced to an asymmetrically substituted carbon atom and, in the absence of four stable isotopic species of hydrogen, fluorine, chlorine, and bromine, it is also the only gaseous or liquid compound in which the asymmetry of a carbon atom is due exclusively to the differing masses of its four substituents.

From the point of view of vibrational spectroscopy, comparison of the vibrations of [$^2\text{H}_1$, $^2\text{H}_2$, $^2\text{H}_3$]-neopentane with those of the nondeuterated and the fully deuterated form of the molecule is of interest. One can hope to gain a better understanding of the vibrational spectrum of the nonsymmetric molecule by relating it to those of the two symmetric ones. Understanding of how VOA is generated in small molecules, and in particular the knowledge of what structural elements lead to vibrational motion, producing large or negligible vibrational optical activity, is still quite limited. Analysis of the computed VOA of the title compound, which has a comparatively simple and fully symmetric electronic structure, can be expected to yield new insights into this important aspect of VOA.

Theoretical Expressions

VOA of molecular origin is measured for samples of randomly oriented molecules (an exception is the measurement of mulls in VCD, where the samples consist of randomly oriented crystallites embedded in a viscous solvent). Theoretical expressions for circular difference scattering (ROA) [7] and circular difference absorption (VCD) [8] therefore represent rotational averages over all orientations of a molecule. The situation for ROA is complicated by the fact that one has the option to measure it with different polarization schemes, by using different scattering geometries, and in resonance with electronic transitions. The formulae given below refer to the off-resonance situation, and the Placzek polarizability theory [9] is expected to apply for a molecule like [$^2\text{H}_1$, $^2\text{H}_2$, $^2\text{H}_3$]-neopentane. With respect to scattering geometries, only forward [10] and backward [1, 11] scattering have been considered, as little additional insight can be expected from either polarized or depolarized right-angle scattering. Numerical results are only reported for backward scattering, as the size of forward scattering turned out to be far too small to be measured.

For ROA, rotational averaging of the scattering tensor leads to combinations of tensor products that were first derived by Barron and Buckingham [12], and later shown by Long [13] to be expressible as linear combinations of invariants resulting from the double contraction of second-rank tensors. For VCD, the analogous quantity is the well-known rotational strength, the contraction of the magnetic and electric transition moment. A complication arises in VCD through the need to go beyond the Born–Oppenheimer approximation, by considering nuclear velocity as well, rather than nuclear excursion exclusively [14].

As has been shown explicitly elsewhere [15], all molecular Raman and ROA invariants can be conveniently expressed as the sum of terms that represent the contraction of a pair of nuclear displacement vectors with a diatomic electronic second-rank tensor. The same holds true for the electric dipole strength relevant for infrared (IR) absorption, and the rotational strength, which is relevant for VCD. The formulae for VCD can be obtained in a precisely analogous way as described for ROA, except that nuclear displacement has to be substituted by nuclear velocity for magnetic moments [16].

VIBRATIONAL OPTICAL ACTIVITY OF (R)-[²H₁, ²H₂, ²H₃]-NEOPENTANE

The differential Raman scattering cross section for forward or backward scattering into an infinitesimally small element of the solid angle is given by Ref. [13]:

$$d\sigma_p(0, \pi) = K_p \langle m_p | Q_p | n_p \rangle^2 [90a_p^2 + 14\beta_p^2] d\Omega, \quad (1)$$

where n_p and m_p are the vibrational quantum numbers of the initial and final state, respectively, for vibration p . For Raman optical activity, the differential scattering cross section for forward scattering differs from that for backward scattering [3]:

$$-\Delta d\sigma_p(0) = \frac{4K_p}{c} \langle m_p | Q_p | n_p \rangle^2 [90a_p G'_p + 2\beta_{Gp}^2 - 2\beta_{Ap}^2] d\Omega \quad (2)$$

$$-\Delta d\sigma_p(\pi) = \frac{4K_p}{c} \langle m_p | Q_p | n_p \rangle^2 [12\beta_{Gp}^2 + 4\beta_{Ap}^2] d\Omega, \quad (3)$$

where Ω is the solid angle, and K_p is a constant that depends on the frequency ω_0 of the exciting light and the frequency ω_p of the scattered light, where p is the vibrational mode for which a transition between different states occurs:

$$K_p = \frac{1}{90} \left(\frac{\mu_0}{4\pi} \right)^2 \omega_p^3 \omega_0. \quad (4)$$

A minus sign has been included for difference expressions (2) and (3) because the sign convention in ROA for presenting data is opposite to that used in optical activity in general [17]. $-\Delta d\sigma$ corresponds to the ROA convention to represent the data measured or calculated for right circular light minus the data for left circular light, with $\Delta d\sigma$ defined in agreement with the standard convention left minus right used for molecular quantities in optical activity.

a^2 and β^2 , without the index p , signify the isotropic and anisotropic invariant, respectively, of the molecular electric dipole–electric dipole polarizability tensor α , aG' , and β_G^2 the corresponding invariants of the cross product of this tensor with the electric dipole–magnetic dipole polarizability tensor G' , and β_A^2 the anisotropic invariant of it with the tensor A obtained by contracting the electric dipole–electric quadrupole tensor with the antisymmetric unit tensor of Levi–Civita. For a vibration p , the reduced invariants J_p , which do not

include integration over vibrational wave functions, can be written in the general form

$$J_p = \sum_{\alpha, \beta} \mathbf{L}_{\alpha, p}^x \cdot \mathbf{V}_{\alpha \beta} \cdot \mathbf{L}_{\beta, p}^x. \quad (5)$$

They are related to the Raman and ROA invariants I , which in general are used for convenience without the index p of the vibration to which they pertain, as

$$I(1 \leftarrow 0) = \langle 1 | Q_p | 0 \rangle^2 J_p = \frac{\hbar}{2\Delta\omega_p} J_p. \quad (6)$$

In Eq. (6), the value of the integral over wave functions for a fundamental transition has been inserted

$$\langle 1 | Q_p | 0 \rangle = \left(\frac{\hbar}{2\Delta\omega_p} \right)^{1/2}, \quad (7)$$

with Q_p the vibrational coordinate.

$\mathbf{L}_{\alpha, p}^x$, the Cartesian displacement vector of nucleus α with mass m_α in normal mode p , is normalized so that

$$\sum_{\alpha, i} m_\alpha (L_{\alpha i, p}^x)^2 = 1. \quad (8)$$

The elements of the electronic second-rank tensors, or dyadics, $\mathbf{V}_{\alpha \beta}$, have the form:

$$V(a^2)_{\alpha i, \beta j} = \frac{1}{9} \sum_{\mu, \nu} \left(\frac{\partial \alpha_{\mu \mu}^e}{\partial x_i^\alpha} \right)_0 \left(\frac{\partial \alpha_{\nu \nu}^e}{\partial x_j^\beta} \right)_0 \quad (9a)$$

$$V(\beta^2)_{\alpha i, \beta j} = \frac{1}{2} \sum_{\mu, \nu} \left[3 \left(\frac{\partial \alpha_{\mu \nu}^e}{\partial x_i^\alpha} \right)_0 \left(\frac{\partial \alpha_{\mu \nu}^e}{\partial x_j^\beta} \right)_0 - \left(\frac{\partial \alpha_{\mu \mu}^e}{\partial x_i^\alpha} \right)_0 \left(\frac{\partial \alpha_{\nu \nu}^e}{\partial x_j^\beta} \right)_0 \right] \quad (9b)$$

$$V(aG')_{\alpha i, \beta j} = \frac{1}{9} \sum_{\mu, \nu} \left(\frac{\partial \alpha_{\mu \mu}^e}{\partial x_i^\alpha} \right)_0 \left(\frac{\partial G'_{\nu \nu}^e}{\partial x_j^\beta} \right)_0 \quad (9c)$$

$$V(\beta_G^2)_{\alpha i, \beta j} = \frac{1}{2} \sum_{\mu, \nu} \left[3 \left(\frac{\partial \alpha_{\mu \nu}^e}{\partial x_i^\alpha} \right)_0 \left(\frac{\partial G'_{\mu \nu}^e}{\partial x_j^\beta} \right)_0 - \left(\frac{\partial \alpha_{\mu \mu}^e}{\partial x_i^\alpha} \right)_0 \left(\frac{\partial G'_{\nu \nu}^e}{\partial x_j^\beta} \right)_0 \right] \quad (9d)$$

HUG AND HAESLER

$$V(\beta^2 \mathcal{A})_{\alpha i, \beta j} = \frac{\omega_0}{2} \sum_{\mu, \nu} \left(\frac{\partial \alpha_{\mu\nu}^e}{\partial x_i^\alpha} \right)_0 \left(\frac{\partial \mathcal{A}_{\mu\nu}^e}{\partial x_j^\beta} \right)_0. \quad (9e)$$

Indices i and j refer to the Cartesian coordinates of nuclei α and β , and indices μ and ν to the Cartesian coordinate system in which the molecular tensors are defined.

The molar decadic extinction coefficient for vibrational absorption, and the difference of the extinction coefficients for left and right circular light, are given by [18]

$$\varepsilon_p(\tilde{\nu}) = \frac{20\pi^2 N_A}{3\varepsilon_0 h c \ln(10)} \tilde{\nu} \langle m_p | Q_p | n_p \rangle^2 D_p f(\tilde{\nu}_p, \tilde{\nu}) \quad (10)$$

$$\Delta\varepsilon_p(\tilde{\nu}) = \frac{80\pi^2 N_A}{3\varepsilon_0 h c^2 \ln(10)} \tilde{\nu} \operatorname{Im}\{\langle n_p | Q_p | m_p \rangle \times \langle m_p | \hat{P}_p | n_p \rangle\} R_p f(\tilde{\nu}_p, \tilde{\nu}), \quad (11)$$

where N_A is Avogadro's number, and $\tilde{\nu}_p$ the vibrational frequency in cm^{-1} .

The expressions for the reduced dipole strength D_p and the reduced rotational strength R_p are

$$D_p = \sum_{\alpha, \beta} \mathbf{L}_{\alpha, p}^x \cdot \mathbf{V}(D)_{\alpha\beta} \cdot \mathbf{L}_{\beta, p}^x \quad (12)$$

$$R_p = \sum_{\alpha, \beta} \mathbf{L}_{\alpha, p}^x \cdot \mathbf{V}(R)_{\alpha\beta} \cdot \mathbf{L}_{\beta, p}^x. \quad (13)$$

They are related to the ordinary dipole strength D and rotational strength R as

$$D(1 \leftarrow 0) = \langle 1 | Q_p | 0 \rangle^2 D_p = \frac{\hbar}{2\Delta\omega_p} D_p \quad (14)$$

$$R(1 \leftarrow 0) = \operatorname{Im}\{\langle 0 | Q_p | 1 \rangle \langle 1 | \hat{P}_p | 0 \rangle\} R_p = \frac{\hbar}{2} R_p, \quad (15)$$

where in R the integral of the moment operator \hat{P} for a fundamental transition has been used:

$$\langle 1 | \hat{P}_p | 0 \rangle = i \left(\frac{\hbar \Delta\omega_p}{2} \right)^{1/2}. \quad (16)$$

The elements of the dyadics $\mathbf{V}_{\alpha\beta}$ have the form

$$V(D)_{\alpha i, \beta j} = \operatorname{Re} \left\{ \sum_{\mu} \left(\frac{\partial \mu_{\mu}}{\partial x_i^\alpha} \right)_0 \left(\frac{\partial \mu_{\mu}}{\partial x_j^\beta} \right)_0 \right\} = \operatorname{Re} \left\{ \sum_{\mu} P_{i\mu}^\alpha P_{j\mu}^\beta \right\} \quad (17)$$

$$V(R)_{\alpha i, \beta j} = \operatorname{Re} \left\{ \sum_{\mu} \left(\frac{\partial \mu_{\mu}}{\partial x_i^\alpha} \right)_0 \left(\frac{\partial m_{\mu}}{\partial x_j^\beta} \right)_0 \right\} = \operatorname{Re} \left\{ \sum_{\mu} P_{i\mu}^\alpha M_{j\mu}^\beta \right\}, \quad (18)$$

where μ stands for the electric and \mathbf{m} for the magnetic dipole moment of the molecule, and $P_{i\mu}^\alpha$ and $M_{j\mu}^\beta$ are components of what is known in the VCD literature as atomic polar tensors (APT) and atomic axial tensors (AATs), respectively. The AATs are defined according to Nafie [14]. This definition differs by a factor of $i/2\hbar$ from the one used by Stephens and coworkers [19] and in the DALTON and GAUSSIAN programs.

Computational Approach

The Cartesian harmonic force field, AATs and APTs, were all calculated at the density functional theory (DFT) level, using direct, analytical derivatives methods implemented within the GAUSSIAN program [20] and described elsewhere [19]. Our calculation uses the hybrid functionals B3PW91 and B3LYP [21] with the standard 6-311++G** [22] and aug-cc-pVDZ [23] basis sets, all available in GAUSSIAN.

Hartree-Fock linear response theory [24] and London orbitals, as implemented in the DALTON program [25], were used to compute the Raman and ROA tensors of Eqs. (9a)–(9d). They were calculated at the DFT geometry with the aug-cc-pVDZ basis set for the frequency of the exciting light, in our case 532 nm. As analytical gradients for ROA tensors are presently not available in any program, we decided to use the DALTON program, as it provides a gauge origin invariant implementation of dynamic molecular property tensors.

The displacement vectors $\mathbf{L}_{\alpha, p}^x$ of Eqs. (5), (12), and (13) were calculated with the force field from GAUSSIAN by a MATLAB [26] program developed in our laboratory. The elements of all the dyadics $\mathbf{V}_{\alpha\beta}$ [Eqs. (9a)–(9e), (17), and (18)] were also calculated by this program with gradients from DALTON for Raman and ROA and from GAUSSIAN for vibrational absorption and VCD. They were then combined with the vectors $\mathbf{L}_{\alpha, p}^x$ into the Raman and

VIBRATIONAL OPTICAL ACTIVITY OF (*R*)-[²H₁, ²H₂, ²H₃]-NEOPENTANE

ROA invariants [Eqs. (5) and (6)] and into the dipole and rotational strength [Eqs. (14) and (15)].

Representation of Computed Data

SPECTRA

The purpose of an *ab initio* calculation of VOA can be as practical as the assignment of the unknown absolute configuration of a molecule or the study of its solution conformations, by comparison of measured and computed data. Assigning absolute configurations in this way is generally cheaper than by chemical means, and far more reliable than by electronic CD or optical rotatory dispersion. In other cases, one might want to gain a better understanding of measured data with the aim of drawing conclusions of a general nature.

With the increasing precision with which *ab initio* calculations can be done, it has also become convenient sometimes to run a calculation, ahead of any measurement, to assess what measurable spectral features of interest one might expect for a particular molecular structure. This then allows for an informed decision as to whether undertaking a difficult and lengthy chiral synthesis may be of interest. In a case like [²H₁, ²H₂, ²H₃]-neopentane, where one expects partial cancelation of VOA of opposite sign due to the close spacing of vibrational modes, the realistic simulation of experimental spectra, ahead of an arduous synthesis, is particularly important.

The careful simulation of ROA spectra is more critical than that of VCD spectra. One reason is that [²H₁, ²H₂, ²H₃]-neopentane is a good Raman scatterer but a weak IR absorber. Thus, the ratio of ROA to Raman intensity is expected to be smaller than the ratio of VCD to vibrational absorption. A second reason why ROA spectra merit more careful simulation than VCD spectra resides with the fact that the various terms that occur in the expressions of the scattering cross sections [Eqs. (1)–(3)] lead to bands with a differing width.

Bandwidths for isotropic Raman scattering are generally smaller than for anisotropic scattering because isotropic scattering depends on the vibrational correlation function only, while for anisotropic Raman scattering, and equally well for vibrational absorption, the orientational correlation function also comes into play. Over the past decade, rapid laser spectroscopy has made substantial contributions to the understanding of linewidths of

liquid phase spectra. The classical line-broadening mechanisms, such as the Doppler effect, radiation broadening, collisions between molecules, their interaction, and their reorientation, have had to be supplanted by mechanisms such as intermolecular vibrational redistribution (IVR) [27] and vibrational dephasing by shear fluctuations [28]. A simulation of ROA spectra based on such detailed mechanisms contributing to linewidth is not possible here, notably because their importance can only be assessed by analyzing experimental data. Our aim has therefore been pragmatic, namely to account for the generally observed difference in bandwidth between isotropic and anisotropic scattering, and to explicitly include instrumental bandwidth into the simulated spectra.

To keep the problem tractable, we have made the following simplifying assumptions: (i) the instrument profile is Gaussian; (ii) the band shape of isotropic scattering is a Lorentz profile; and (iii) reorientation leads to a Lorentz profile. The band shape of anisotropic scattering, which under these assumptions is the convolution of two Lorentz curves, is therefore also a Lorentz curve.

The width of the instrument profile (full width at half-maximum [FWHM]) can be measured. For our present ROA instrument [29], the input slit is formed by fiber optics. Thus, its width, which largely determines the resolution of the instrument, is fixed. The average value of the FWHM for the spectral range of interest was found to be 6.7 cm⁻¹. Because of the discrete nature of the CCD detector, we cannot verify that the instrument profile is truly Gaussian but, by assuming a profile, we can determine its width with reasonable precision.

The isotropic bandwidth was chosen as 3.5 cm⁻¹. This value allows us to account for the shape of the sharp, polarized Raman bands, such as the 996-cm⁻¹ line of benzene, which are often observed for symmetric molecules. One must keep in mind, however, that strongly polarized bands can also have larger widths. For ROA backscattering, the choice of the isotropic linewidth is not important as isotropic scattering makes no contribution. The anisotropic width was chosen as 10 cm⁻¹.

For simulating Fourier transform VCD spectra, a 8-cm⁻¹ FWHM Lorentzian line shape has often been used in the past [18]. In addition to spectra simulated with this assumption, we also present spectra obtained by the convolution of an 8-cm⁻¹ Lorentz curve with the 10-cm⁻¹ Gauss curve one expects for a scanning VCD spectrometer [30].

HUG AND HAESLER

TABLE I
Parameters of the fit of Gauss curves to a Lorentz curve.

| N_G | | 1 | 2 | 3 | 4 | 5 | 6 | 7 | 8 |
|-------|-------|-----------------------|-----------------------|-----------------------|-----------------------|-----------------------|-----------------------|-----------------------|-----------------------|
| 8 | c_i | 1.40×10^{-1} | 3.71×10^{-1} | 2.93×10^{-1} | 1.34×10^{-1} | 4.58×10^{-2} | 1.25×10^{-2} | 2.63×10^{-3} | 3.43×10^{-4} |
| | a_i | 2.01×10^{-1} | 3.31×10^{-1} | 5.61×10^{-1} | 9.99×10^{-1} | $1.90 \times 10^{+0}$ | $3.99 \times 10^{+0}$ | $9.84 \times 10^{+0}$ | $3.43 \times 10^{+1}$ |
| 7 | c_i | 1.83×10^{-1} | 4.05×10^{-1} | 2.70×10^{-1} | 1.05×10^{-1} | 2.98×10^{-2} | 6.32×10^{-3} | 8.26×10^{-4} | |
| | a_i | 2.12×10^{-1} | 3.62×10^{-1} | 6.45×10^{-1} | $1.23 \times 10^{+0}$ | $2.58 \times 10^{+0}$ | $6.34 \times 10^{+0}$ | $2.21 \times 10^{+1}$ | |
| 6 | c_i | 2.41×10^{-1} | 4.32×10^{-1} | 2.34×10^{-1} | 7.37×10^{-2} | 1.60×10^{-2} | 2.10×10^{-3} | | |
| | a_i | 2.26×10^{-1} | 4.04×10^{-1} | 7.69×10^{-1} | $1.61 \times 10^{+0}$ | $3.97 \times 10^{+0}$ | $1.38 \times 10^{+1}$ | | |
| 5 | c_i | 3.20×10^{-1} | 4.44×10^{-1} | 1.85×10^{-1} | 4.34×10^{-2} | 5.76×10^{-3} | | | |
| | a_i | 2.43×10^{-1} | 4.65×10^{-1} | 9.75×10^{-1} | $2.40 \times 10^{+0}$ | $8.36 \times 10^{+0}$ | | | |
| 4 | c_i | 4.26×10^{-1} | 4.27×10^{-1} | 1.25×10^{-1} | 1.73×10^{-2} | | | | |
| | a_i | 2.68×10^{-1} | 5.63×10^{-1} | $1.38 \times 10^{+0}$ | $4.82 \times 10^{+0}$ | | | | |
| 3 | c_i | 5.69×10^{-1} | 3.63×10^{-1} | 5.85×10^{-2} | | | | | |
| | a_i | 3.05×10^{-1} | 7.48×10^{-1} | $2.60 \times 10^{+0}$ | | | | | |

 a_i , standard deviations of the individual Gauss curves; c_i , coefficients of the individual Gauss curves in the linear combinations.

The convolution of an instrument's Gauss profile with a Lorentz profile leads to a Voigt profile. Voigt profiles must be numerically calculated. We have decided on a different approach, namely to take advantage of the fact that the convolution of two Gauss functions is also a Gauss function.

In a first step, we have represented a Lorentz function $L(x)$ by a linear combination of Gauss functions:

$$L(x) = \frac{k^2}{x^2 + k^2} \quad (19)$$

$$L(x) \approx \sum_i c_i e^{-x^2/2a_i^2}, \quad (20)$$

where $2k$ is the FWHM of the Lorentz function with the area $F_L = k\pi$. The FWHM of the individual Gauss functions in Eq. (20) is given by $2(2 \ln 2)^{1/2}a_i$, and the area by $(2\pi)^{1/2}a_i$.

The coefficients c_i and the standard deviations a_i (Table I) were determined by fitting Gauss functions to the shape of a Lorentz function with $2k = 1$ (i.e., $F_L = \pi/2$). As can be seen from Table II, 6 Gauss functions suffice amply for representing the shape of a Lorentz curve for our spectral purposes, with the area of the approximate curve having an error of less than 1% as compared with the exact Lorentz curve. Any Lorentz curve with a FWHM of $2k$ can then be obtained as

$$L(x) \approx \sum_{i=1}^6 c_i e^{-x^2/2(ka_i)^2}. \quad (21)$$

In a second step, the linear combination of Gauss functions is convoluted with the Gaussian line shape function of the instrument. For the convolution of two Gauss functions one has

$$C(x) = G_a(x) \otimes G_b(x) = e^{-x^2/2a^2} \otimes e^{-x^2/2b^2} = e^{-x^2/[2(a^2+b^2)]}, \quad (22)$$

which is a Gauss function with an FWHM of $2[2 \ln 2(a^2 + b^2)]^{1/2}$ and an area of $(2\pi)^{1/2}a[1 + (b^2/a^2)]^{1/2}$.

TABLE II
Fit of Gauss curves to a Lorentz curve.

| N_G | 1 - r^2 | ΔF [%] |
|-------|-----------------------|----------------|
| 3 | 3.47×10^{-4} | 4.65 |
| 4 | 6.12×10^{-5} | 2.50 |
| 5 | 1.28×10^{-5} | 1.44 |
| 6 | 3.01×10^{-6} | 0.86 |
| 7 | 7.84×10^{-7} | 0.53 |
| 8 | 2.20×10^{-7} | 0.34 |

ΔF , error of the area for the best least-squares fit of a linear combination of Gauss curves to the shape of a Lorentz curve. r , correlation coefficient between the two curves; N_G , number of Gauss curves used in the fit.

VIBRATIONAL OPTICAL ACTIVITY OF (R)-[²H₁, ²H₂, ²H₃]-NEOPENTANE

Hence, the convolution of the approximate Lorentz function, Eq. (21), with the instrument Gauss line shape of standard deviation b yields

$$V(x) = \frac{2}{\pi} \sum_{i=1}^6 \frac{1}{\left[4k^2 + \left(\frac{b^2}{a_i^2}\right)\right]^{1/2}} c_i e^{-x^2 / \{2[(2ka_i)^2 + b^2]\}}. \quad (23)$$

The normalized area F_V of the approximate Voigt function (23) is

$$F_V = \int_{-\infty}^{+\infty} V(x) dx = \frac{2}{\pi} (2\pi)^{1/2} \sum_{i=1}^6 c_i a_i \approx 1. \quad (24)$$

The spectra were obtained by calculating Eq. (23) separately for the isotropic and anisotropic contributions for each vibrational band, with the areas F_V corresponding to the ab initio calculated values of the isotropic and anisotropic part of the differential scattering cross sections according to Eqs. (1), (2), and (3). The curves were then added to yield the final Raman and ROA spectra. The curves therefore represent differential scattering cross sections per steradian, and per cm^{-1} .

VIBRATIONAL MOTION, GCMS, AND ACPs

The graphic representation of vibrational motion in polyatomic non-planar molecules has been a major headache in the past, as evidenced by classical works on vibrational spectroscopy [31–33]. Except by the use of stereoscopic projections, which is inconvenient, it is difficult to simultaneously convey a good impression of the direction and the size of nuclear motion. An effective solution of the problem is to separate the two aspects [15]. The size, an isotropic quantity, can be represented by spheres centered on a molecule's nuclei, with their radius chosen proportional to the magnitude $|\mathbf{L}_{\alpha,p}^x|$ of the nuclear excursion. The direction of motion can be added by the appropriate shading of the spheres. Moreover, the surface of the spheres is then proportional to the importance of nuclear motion in generating Raman scattering and vibrational absorption.

When one is interested in the persistence of certain pattern of nuclear motion on similar fragments of different molecules [34], the energy of vibrational motion is a more important criterion. As discussed

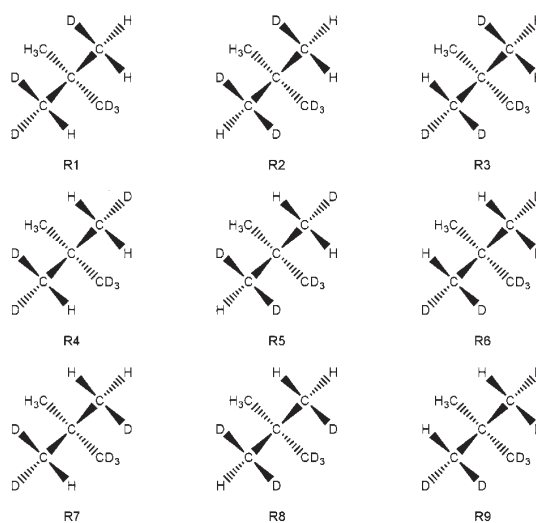


FIGURE 1. The nine rotamers of (R)-[²H₁, ²H₂, ²H₃]-neopentane. Rotamers R1, R5, and R9 on the diagonal are invariant with respect to the interchange of H and D nuclei; the others are related pairwise according to Table III.

further in the section on categorizing vibrational modes, the energy of vibration of a nucleus α in mode p is proportional to $m_\alpha (\mathbf{L}_{\alpha,p}^x)^2$. In representations of the distribution of vibrational energy, we have chosen the volume of spheres proportional to the contribution made by individual nuclei to the energy of a vibrational mode.

The decomposition of Raman and ROA invariants [Eq. (5)] and dipole and rotational strengths [Eqs. (12) and (13)] into mononuclear and dinuclear terms leads naturally to what we call the group coupling matrices (GCMs), which give insight into how scattering cross sections and absorption cross sections are generated within a molecule. The idea is explained in more detail in Ref. [15]. The atomic contribution patterns (ACPs) are obtained from the GCMs by splitting dinuclear terms in a meaningful way between atoms [3].

Computed Spectra

CH- AND CD-STRETCH REGION

[²H₁, ²H₂, ²H₃]-neopentane has nine different conformers, which are represented in Figure 1. These rotamers have identical statistical weight,

HUG AND HAESLER

TABLE III
Rotamers interconverted by the interchange of H and D nuclei.

| Group 1 | Group 2 |
|---------|-------------------------|
| R1 | R2 \leftrightarrow R4 |
| R5 | R3 \leftrightarrow R7 |
| R9 | R6 \leftrightarrow R8 |

and their computed energy is so close that the experimental spectrum of liquid [$^2\text{H}_1$, $^2\text{H}_2$, $^2\text{H}_3$]-neopentane is expected to correspond to the superposition of the spectra of the individual rotamers in equal proportions.

The nine rotamers can be divided into two groups, one where the interchange of hydrogen and deuterium atoms leads to the same rotamer, and a second where it leads to a different rotamer (Table III). As an even number of nuclei is interchanged, the absolute configuration is not modified. The property that the interchange of isotopic nuclei leads to the same enantiomer of a molecule is not unique to [$^2\text{H}_1$, $^2\text{H}_2$, $^2\text{H}_3$]-neopentane. It also pertains to a compound like 1,3-dideuterionallene. Likewise, other chiral molecules with two distinct groups of conformers, one that does have this property and another where it is absent, can be thought of, but stereochemists do not seem to have discussed this aspect of molecules chiral by isotope substitution. [$^2\text{H}_1$, $^2\text{H}_2$, $^2\text{H}_3$]-neopentane can certainly be considered the prototype and the smallest of the molecules where this is possible.

Naively, one might think that the three rotamers 1, 5, and 9, where hydrogen and deuterium nuclei occupy equivalent sites, must lead to identical VOA, except for size, for vibrations where either the H nuclei, or the D nuclei, move in the same coupled motion, independent of the other nuclei of the molecule. Vibrations that satisfy this criterion are the CH- and the CD-stretch vibrations. The expected similarity of the VOA of the two spectral regions is not borne out for the antisymmetric stretch vibrations of rotamers 1 and 5, as can be seen from the line spectra in Figure 2. Rather, upon more careful inspection, it turns out that pairs of antisymmetric CH- and CD-stretch vibrations with the same nuclear motion for H and D nuclei, i.e., 45 and 39, and 43 and 37, represent textbook examples for a situation where inertial contributions, rather than coupling of nuclear motion, determine VOA spectra.

The existence of inertial contributions can best be appreciated by first assuming that all hydrogen and deuterium nuclei do actually move in precisely the same way, with an interchanged role, in high- and low-energy sister vibrations. It is then obvious that the Sayvetz conditions cannot, in general, be satisfied simultaneously for both vibrations, because of the differing mass of the H and D nuclei. Thus, even if the motion of the two types of nuclei looks similar, except for the smaller size of the amplitudes of the D atoms, sister vibrations must differ. For rotamers 1 and 5, the calculations show that this difference is sufficiently pronounced as to lead to an opposite sign for ROA as well as VCD.

The same is true for all rotamers of group 2 without exception, where the VOA of sister vibrations has to be compared for pairs of rotamers

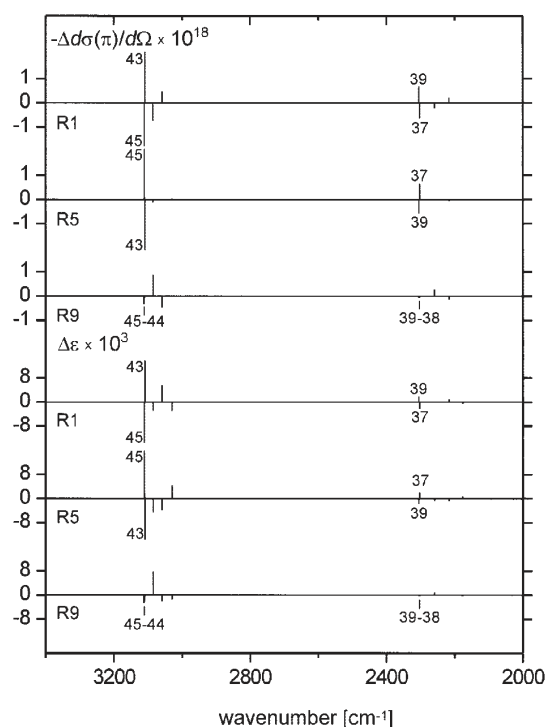


FIGURE 2. ROA backscattering and VCD line spectra of the CH- and CD-stretch region of the rotamers of (R)-[$^2\text{H}_1$, $^2\text{H}_2$, $^2\text{H}_3$]-neopentane invariant to H/D interchange. Vertical scales: ROA: [$\text{\AA}^2 \text{sr}^{-1}$], VCD: [$10^3 \text{cm}^2 \text{mol}^{-1}$]. Force field for all spectra: DFT with B3PW91 hybrid functional and aug-cc-pVDZ basis set. VCD electronic tensors: same as force field. ROA electronic tensors: TDHF with aug-cc-pVDZ basis set.

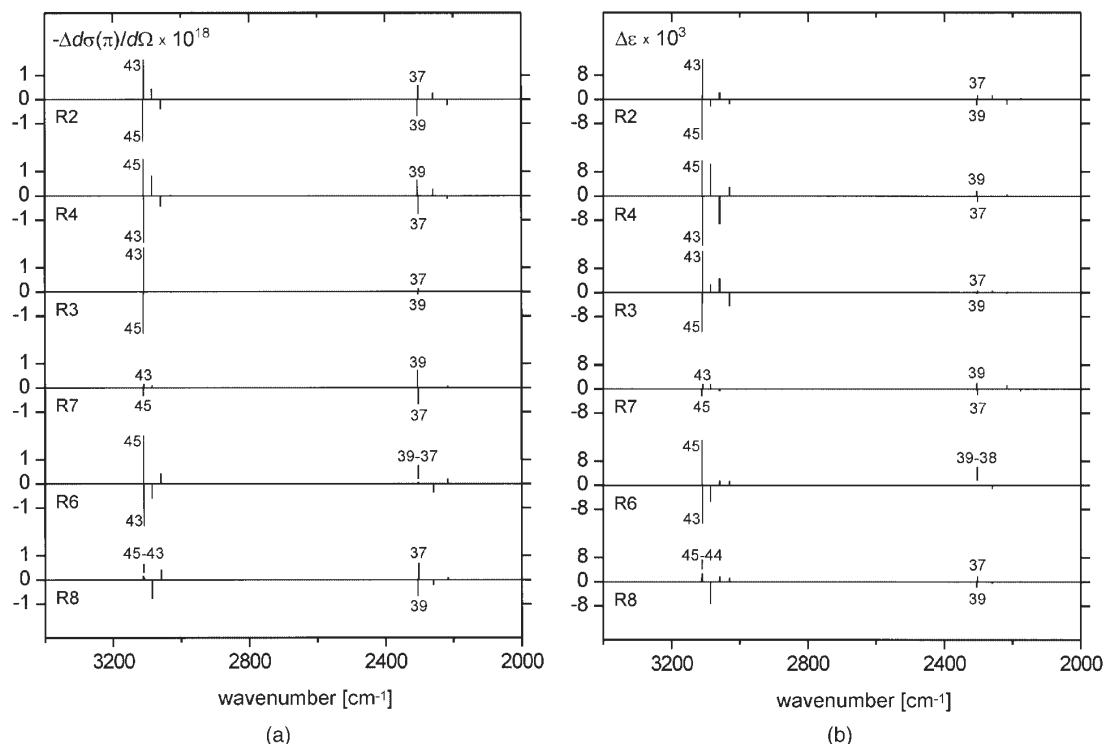
VIBRATIONAL OPTICAL ACTIVITY OF (R)-[²H₁, ²H₂, ²H₃]-NEOPENTANE

FIGURE 3. (a) ROA backscattering line spectra of the CH- and CD-stretch region of the rotamers of (R)-[²H₁, ²H₂, ²H₃]-neopentane not invariant to H/D interchange. Pairs of interconverted rotamers are grouped. Vertical scale: [$\text{\AA}^2 \text{sr}^{-1}$]. Computational parameters: as in Fig. 2. (b) VCD line spectra of the CH- and CD-stretch region of the rotamers of (R)-[²H₁, ²H₂, ²H₃]-neopentane not invariant to H/D interchange. Pairs of interconverted rotamers are grouped. Vertical scale: [$10^3 \text{ cm}^2 \text{ mol}^{-1}$]. Computational parameters: as in Fig. 2.

according to Table III; i.e., one has to compare the VOA of the antisymmetric CH-stretch vibration 45 of rotamer 2 with the VOA of the antisymmetric CD-stretch vibration 39 of rotamer 4, and vice versa. The ROA line spectra, grouped for pairs of rotamers, are shown in Figure 3(a) and the VCD spectra in Figure 3(b). The vibrations 45 and 39, and 43 and 37, are invariably coupled antisymmetric vibrations spread over two methyl groups in the way shown in Figure 4 for rotamer 5. The antisymmetric stretch vibrations 44 and 38, which are not discussed further, are located on a single methyl group and show small VOA.

The group coupling matrices for sister vibrations show identical sign pattern, as one would expect for vibrations with such a similar appearance. The exception are matrix elements with the nucleus at position e in Figure 4, which is occupied by hydrogen in mode 45 and 43, and deuterium in 39 and 37,

and which moves in sister vibrations with an opposite phase, relative to other nuclei. This is clearly visible in Figure 4, which, for the sake of clarity, reproduces only a small fragment of the complete atomic GCM. It is not, however, actually the contributions of site e by themselves that determine the sign of 39 relative to 45, and 37 relative to 43. Rather, the relative size of all the major positive and negative matrix elements changes systematically. It is through this that the influence of inertial contributions is manifested.

The relative size of the ROA and VCD for the CH-stretch and CD-stretch region can be understood. ROA and VCD are proportional to the square of $L_{\alpha,p}^x$ according to Eqs. (5) and (13), and for vibrations where the H or D nuclei only move, the square of $L_{\alpha,p}^x$ is inversely proportional to the mass m_α of these nuclei, according to Eq. (8). In reality, the size of $L_{\alpha,p}^x$ will be additionally reduced for the

HUG AND HAESLER

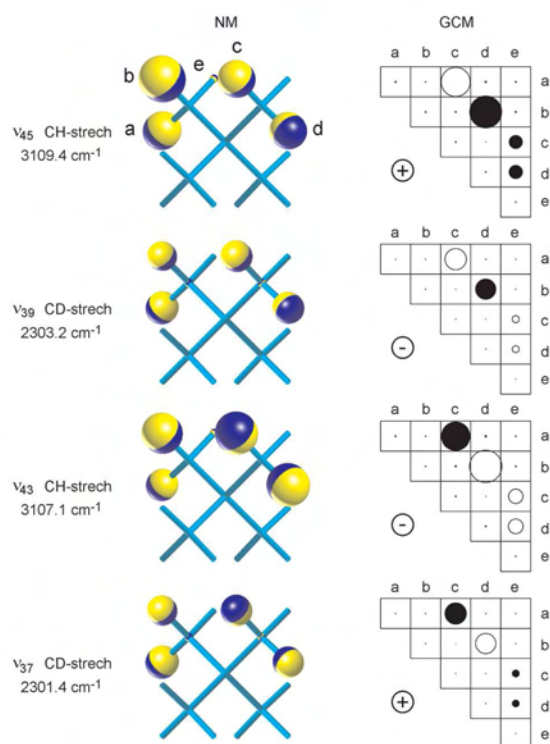


FIGURE 4. Antisymmetric CH- and CD-stretch vibrations 45, 39, and 43, 37 of rotamer 5. For clarity, the group coupling matrices include only the five nuclei that make the largest contributions. Site **e** is the only one for which the relative phase of motion changes upon an interchange of H and D nuclei. Sites **a**, **b**, **c**, **d**, and **e** are occupied by H nuclei for vibrations 45 and 43, and by D nuclei for vibrations 39 and 37. Black circles: positive, open circles: negative. Computational parameters: as in Fig. 2. [Color figure can be viewed in the online issue, which is available at www.interscience.wiley.com.]

CD-stretch region by a larger contribution from carbon nuclei. This favors ROA and VCD in the CH-stretch region. In contrast, ROA, but not VCD, is disfavored in the CH-stretch region by a factor $\Delta\omega_{CD}/\Delta\omega_{CH}$, and by the dependence of K_p , Eq. (4), on the frequency ω_p of the scattered light. The difference in size in the CH-stretch and the CD-stretch region is therefore less pronounced for ROA than for VCD.

The signs of the ROA line spectra show a remarkable similarity to that of the VCD spectra in the CH- and the CD-stretch region, for all nine rotamers. This is of interest for two reasons. For

one, ROA and VCD are defined with differing sign conventions: ROA as proportional to the number of right minus left circularly polarized photons removed by scattering from light traversing a sample, and VCD as proportional to the number of left minus right circularly polarized photons removed by absorption. For another, it has so far been found that there is no relation [35] between ROA and VCD spectra. While this is certainly often true, our results also show that such a relation can exist. The fact that for CH- and CD-stretch vibrations of [$^2\text{H}_1$, $^2\text{H}_2$, $^2\text{H}_3$]-neopentane the ROA and the VCD show the same sign is most likely a consequence of their being determined by inertial contributions, but this will have to be investigated in more detail. As will be seen later, for the lower-energy regions, the sign of ROA and VCD is predominantly opposite.

The diagram in Figure 5 shows the energy of the CH- and CD-stretch vibrations of [$^2\text{H}_1$, $^2\text{H}_2$, $^2\text{H}_3$]-neopentane, relative to that of undeuterated and fully deuterated neopentane. These latter molecules have 12 CH- and CD-stretch vibrations, respectively, with eight modes representing linear combinations of the doubly degenerate antisymmetric stretch vibrations of the four methyl groups, and four modes combinations of symmetric methyl stretch vibrations. In [$^2\text{H}_1$, $^2\text{H}_2$, $^2\text{H}_3$]-neopentane,

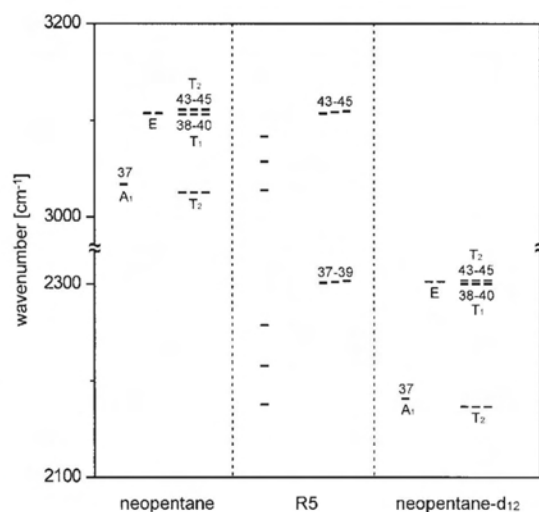


FIGURE 5. Diagrammatic representation of the energy levels of the CH- and the CD-stretch modes of neopentane, rotamer 5 of [$^2\text{H}_1$, $^2\text{H}_2$, $^2\text{H}_3$]-neopentane, and perdeuterated neopentane. Computational parameters: as in Fig. 2.

VIBRATIONAL OPTICAL ACTIVITY OF (*R*)-[²H₁, ²H₂, ²H₃]-NEOPENTANE

the four CH-stretch vibrations of highest energy go back to the antisymmetric CH-stretch vibrations of the undeuterated molecule. Three of them have been discussed in a previous paragraph, and the fourth is a simple CH-stretch motion of the lonely H nucleus of the CHD₂ group. The two symmetric CH-stretch vibrations occur at lower energy and are localized on the CDH₂ and the CH₃ group, respectively. The CD-stretching vibrations follow the same pattern.

According to our calculations with a harmonic force field, the ROA and the VCD of individual rotamers would be measurable in the CH- and CD-stretch region but, as shown in Figures 6 and 7, not for their mixture, because of dilution and extensive cancelation. Direct frequency shifts due to anharmonicity are not likely to have much influence on cancelation, as different rotamers are expected to be similarly affected. Less predictable is the indirect influence that anharmonicity can have on the energy of CH- and CD-stretch vibrations through Fermi resonances. The energy of lower-frequency modes, the overtones and combination frequencies of which are relevant to Fermi resonance, varies from one rotamer to another. This is an aspect of considerable interest, but it is outside the scope of the present work.

LOWER FREQUENCY REGION

At <1,600 cm⁻¹, the ROA and VCD of [²H₁, ²H₂, ²H₃]-neopentane should both be measurable for the mixture of rotamers, as is evident from Figures 6 and 7. The effect of dilution and cancelation can be estimated from comparison of the line and band spectra of the Δ -values for ROA and g -values for VCD. These quantities are defined as

$$\Delta = \frac{I_R - I_L}{I_R + I_L} \quad (25)$$

$$g = \frac{2(\varepsilon_L - \varepsilon_R)}{\varepsilon_L + \varepsilon_R}. \quad (26)$$

The line spectra reflect Δ - and g -values for individual rotamers, while the band spectra correspond to the ratio of the difference to the sum spectra obtained by summing the band spectra of individual rotamers.

Δ and g can be used to judge the measurability of VOA. For ROA, the value of Δ should, with present instrumentation, be $\sim >10^{-5}$ as otherwise measure-

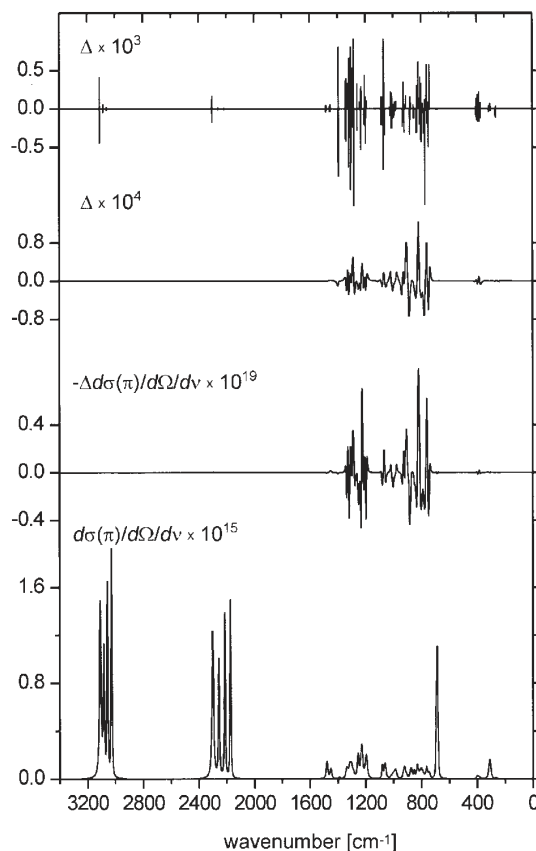


FIGURE 6. Backscattering Raman and ROA spectra of the mixture of the nine rotamers of (*R*)-[²H₁, ²H₂, ²H₃]-neopentane. From bottom to top: Raman, ROA, ratio of ROA to Raman, line spectrum of Δ -values of individual vibrations. Band shapes: isotropic, 3.5 cm⁻¹ FWHM Lorentz convoluted with 6.7 cm⁻¹ FWHM Gauss; anisotropic, 10 cm⁻¹ FWHM Lorentz convoluted with 6.7 cm⁻¹ FWHM Gauss. Units for the representation of scattering cross sections: [Å² sr⁻¹ cm]. Computational parameters: as in Fig. 2.

ments become difficult or impossible. This limitation is due to offsets caused by straylight and multiple reflections between optical elements, which can be present even in a spectrometer with advanced offset compensation [36]. According to Figure 6, more than a dozen of the ROA bands in the 700–1,400-cm⁻¹ range have Δ -values that satisfy this condition easily. The minimum amount of substance required in backscattering, to which Figure 6 applies, is of the order of 2–4 mg, but it can be reduced to <1 mg in right angle scattering [1].

HUG AND HAESLER

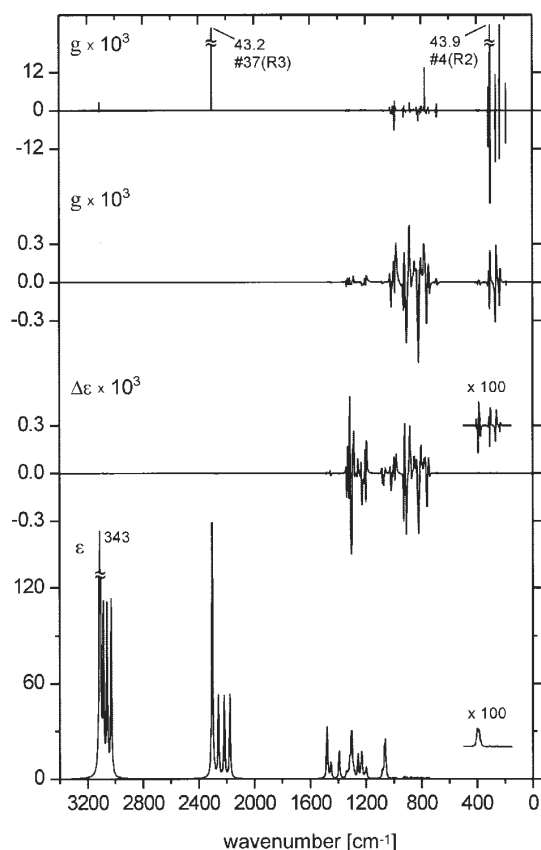


FIGURE 7. Vibrational absorption and VCD spectra of the mixture of the nine rotamers of (R)-[$^2\text{H}_1$, $^2\text{H}_2$, $^2\text{H}_3$]-neopentane. From bottom to top: absorption, VCD, ratio of VCD to absorption, line spectrum of g -values of individual vibrations. A Lorentzian line shape with an FWHM of 8 cm^{-1} was used for all bands. Exceptionally large g -values in the line spectrum are due to modes with negligible absorption. Units of extinction coefficients: [$10^3\text{ cm}^2\text{ mol}^{-1}$]. Computational parameters: as in Fig. 2.

The conditions for the measurability of VCD are similar to ROA. One advantage of VCD over ROA is that weak absorption can be compensated for by a longer path length of the measurement cell. This does, of course, require more substance than the usual 50 mg, already far in excess of what is needed for ROA. In contrast, VCD should be easier to measure as the g -values calculated for the 700–1,000- cm^{-1} region are much larger than the Δ -values for ROA. The reason is not that the VCD as such is large for [$^2\text{H}_1$, $^2\text{H}_2$, $^2\text{H}_3$]-neopentane, but rather that

IR absorption at $<1,000\text{ cm}^{-1}$ is very small for this nonpolar molecule, and exceedingly small at $<400\text{ cm}^{-1}$. This latter spectral region, which is dominated by methyl torsional motion, is, at present, out of reach for VCD.

Two silent modes of individual rotamers, i.e., 37 for R3 at $2,303\text{ cm}^{-1}$ and 4 for R2 at 303 cm^{-1} , show g -values of more than 4%, which is extraordinary for VCD.

Figure 8 shows the influence of instrumental res-

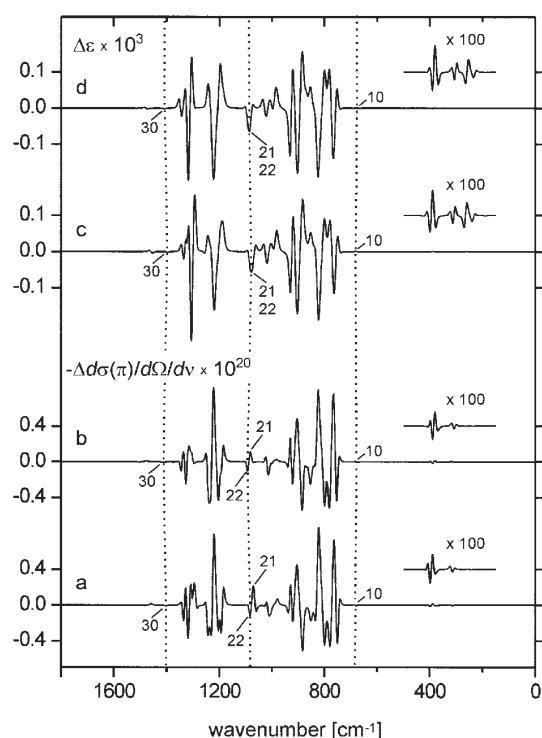


FIGURE 8. Influence of line shape and computational parameters on computed spectra of the mixture of rotamers. ROA spectra **a** and **b**: line shape as in Fig. 6. VCD spectra **c** and **d**: 8 cm^{-1} FWHM Lorentz curve convoluted with 10 cm^{-1} Gauss curve. **a**: DFT/B3LYP/aug-cc-pVDZ force field, TDHF/aug-cc-pVDZ electronic tensors. **b**: DFT/B3LYP/6-311++G** force field, TDHF/aug-cc-pVDZ electronic tensors. **c**: DFT/B3LYP/aug-cc-pVDZ force field and electronic tensors. **d**: DFT/B3LYP/6-311++G** force field and electronic tensors. Broken vertical lines indicate the position of the molecular breathing mode 10, the CD_3 umbrella mode 22, and the CH_3 umbrella mode 30, which delimit the spectral regions of large VOA. Units of scattering cross sections and extinction coefficients: as in Figs. 6 and 7.

VIBRATIONAL OPTICAL ACTIVITY OF (R)-[²H₁, ²H₂, ²H₃]-NEOPENTANE

olution on measured VCD. The pure Lorentzian band shape of an FWHM of 8 cm⁻¹ used in Figure 7 was convoluted as described earlier with the 10-cm⁻¹ FWHM Gaussian resolution curve typical for a scanning VCD instrument. Clearly, the size of the VCD is reduced, and its appearance somewhat modified, but there is no doubt that, given enough substance, the VCD of [²H₁, ²H₂, ²H₃]-neopentane should remain easily measurable.

As a further check of the validity of our assessment of the measurability of the ROA and VCD of [²H₁, ²H₂, ²H₃]-neopentane, we have repeated the calculations with a different functional and a different basis set, namely B3LYP and 6-311++G**. Again, as seen in Figure 8, the measurability of the molecule's VOA is confirmed.

Sorting Vibrational Modes

Traditionally, vibrational modes have been characterized by looking at internal coordinates such as the bending of valence angles, the deformation of torsional angles, and bond stretching. Where a vibration is located primarily on a small molecular fragment, internal coordinates are an immensely practical way of categorizing nuclear motion. In analytical applications of vibrational spectroscopy, in particular, the notion of group vibrations, such as the carbonyl stretching vibration, and the notion of spectral regions, such as amide I and II, are of key importance. The approach is less useful for skeletal modes extending over sizable portions of a molecule, and quite generally for vibrations of the so called fingerprint region. It is typically these spectral regions that are of particular interest in VOA, and both have only become computationally accessible through the advent of ab initio methods.

The classical approach for categorizing molecular vibrations also reaches somewhat its limits for a molecule such as [²H₁, ²H₂, ²H₃]-neopentane, for which four methyl groups are the only distinct molecular fragments. This has been an incentive for us to look for additional means for distinguishing molecular vibrations, and in particular for measures directly adapted to the ab initio computation of normal modes in Cartesian coordinates.

The decomposition of the potential energy of a vibration into components attributable to internal coordinates has been used in the past [37]. We suggest as an alternative measure the decomposition of the total energy of vibration into individual nuclear components. The vibrational energy can be

decomposed in mononuclear terms by looking at the kinetic energy, rather than the potential energy, because the kinetic energy of a normal mode Q_p is the sum of the kinetic energies of the individual nuclei α ,

$$T_p = \frac{1}{2} \dot{Q}_p^2 = \sum_{\alpha} T_{\alpha,p} = \frac{1}{2} \sum_{\alpha} m_{\alpha} \Delta \dot{\mathbf{x}}_{\alpha,p} \cdot \Delta \dot{\mathbf{x}}_{\alpha,p} \\ = \frac{1}{2} \dot{Q}_p^2 \sum_{\alpha} m_{\alpha} \mathbf{L}_{\alpha,p}^x \cdot \mathbf{L}_{\alpha,p}^x \quad (27)$$

where $\Delta \mathbf{x}_{\alpha} = \mathbf{L}_{\alpha,p}^x Q_p$ has been used. According to the virial theorem, $V_p = T_p = E_p/2$. In a normal vibration, all nuclei execute a harmonic motion with the same frequency and phase, which means that the effective potential seen by each nucleus must be harmonic. One can therefore also set $V_{\alpha,p} = T_{\alpha,p}$. This effective potential is the sum of the local potential of the nucleus and the potential produced by the pushing and pulling of all other nuclei. Thus, the fraction of vibrational energy $E_{\alpha,p}$ which nucleus α contributes to normal mode p can be written as:

$$\frac{E_{\alpha,p}}{E_p} = m_{\alpha} \mathbf{L}_{\alpha,p}^x \cdot \mathbf{L}_{\alpha,p}^x \quad (28)$$

By summing the contributions of individual nuclei, one can define the vibrational energy of a molecular fragment, or of a particular kind of nuclei. It is the latter approach that is used in this case.

Another useful means for distinguishing modes is to look at the difference of the distance between nuclei for the two turning points of nuclear motion. The sum of distance changes can be defined for the whole molecule, for molecular fragments, or between molecular fragments, in a completely analogous fashion as discussed for group coupling matrices [15], except that mono-nuclear terms are, of course, inherently zero.

Figure 9 shows the decomposition of the vibrational energy into separate components attributable to carbon, deuterium, and hydrogen atoms for neopentane, and for fully and partially deuterated neopentane, with rotamer 5 chosen as the example. The change of the sum of all distances between nuclei is displayed in Figure 10. The Raman spectra of the symmetric molecules are shown together with the degree of circularity [13, 29] in Figure 11, and the Raman and ROA spectra for the nonsymmetric one in Figure 12.

HUG AND HAESLER

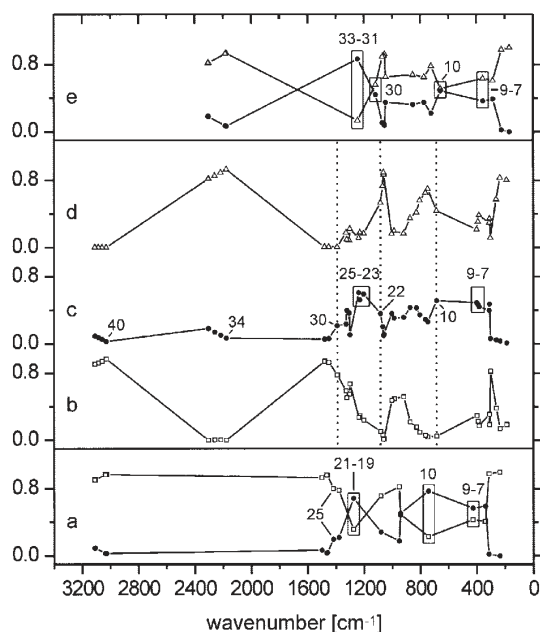


FIGURE 9. Vibrational energy distribution diagrams calculated according to Eq. (28). Bottom: neopentane. Middle: rotamer 5 of $[^2\text{H}_1, ^2\text{H}_2, ^2\text{H}_3]$ -neopentane. Top: perdeuterated neopentane. Vertical broken lines separate the same spectral regions as in Fig. 8. ●, carbon; □, hydrogen; △, deuterium atoms. Computational parameters: as in Fig. 2.

Figure 10 is easiest to interpret. For the two symmetric molecules, the sum of all distances differs from zero only for the three vibrations of A_1 symmetry, i.e., the molecular breathing mode, the totally symmetric umbrella or symmetric CH_3/CD_3 deformation mode, and the totally symmetric CH_3/CD_3 stretching mode. Raman scattering for these A_1 symmetric vibrations is fully polarized, which means a degree of circularity of -1 in Figure 11. In contrast to the stretching and breathing motions, the Raman scattering intensity of the A_1 umbrella mode is weak, however, and for neopentane it would not be identifiable separately in the experimental Raman spectrum.

The small Raman scattering intensity is a general, and so far not well understood, characteristic of the CH_3 umbrella mode. The reason is cancellation between positive mononuclear and negative dinuclear terms on individual CH_3 groups, as can be seen from the GCMs in Figure 13. The cancellation is less pronounced for the CD_3 group, despite

its identical electronic structure. Additionally, mononuclear contributions by carbon atoms also make a larger contribution. CD_3 groups therefore lead to more scattering than CH_3 groups. For vibrational absorption, the situation is the opposite: absorption by the umbrella mode of individual methyl groups is substantial [33], and most of it is due to the hydrogen and not the carbon atoms, as seen from Figure 13. In contrast, the umbrella motion of CD_3 groups produces less absorption than that of CH_3 groups. In the symmetric molecules, the total absorption intensity vanishes, of course, for the A_1 symmetric mode, because of exact cancellation between methyl groups.

In $[^2\text{H}_1, ^2\text{H}_2, ^2\text{H}_3]$ -neopentane, the isolated umbrella mode 22 of the single CD_3 group shows a fair amount of mixing with other modes, the umbrella mode 30 of the CH_3 group very little. The umbrella mode of the CD_3 group contributes substantially to the negative VCD band just below $1,200\text{ cm}^{-1}$ in the spectra for the mixture of rotamers in Figure 8. It

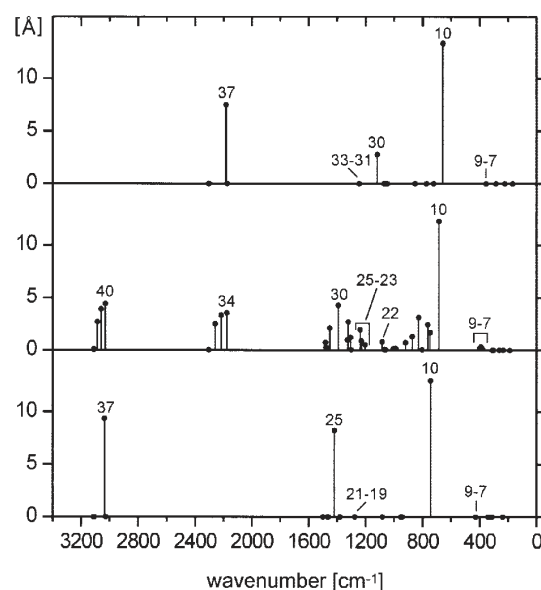


FIGURE 10. Variation of the sum of internuclear distances with vibrational motion. The magnitude of the difference of the sums of all internuclear distances is shown for the two classical turning points of nuclear motion, with zero point vibrational amplitudes. Bottom: neopentane. Middle: rotamer 5 of $[^2\text{H}_1, ^2\text{H}_2, ^2\text{H}_3]$ -neopentane. Top: perdeuterated neopentane. Only modes of symmetry species A_1 produce a change for the two symmetric molecules. Force field: as in Fig. 2.

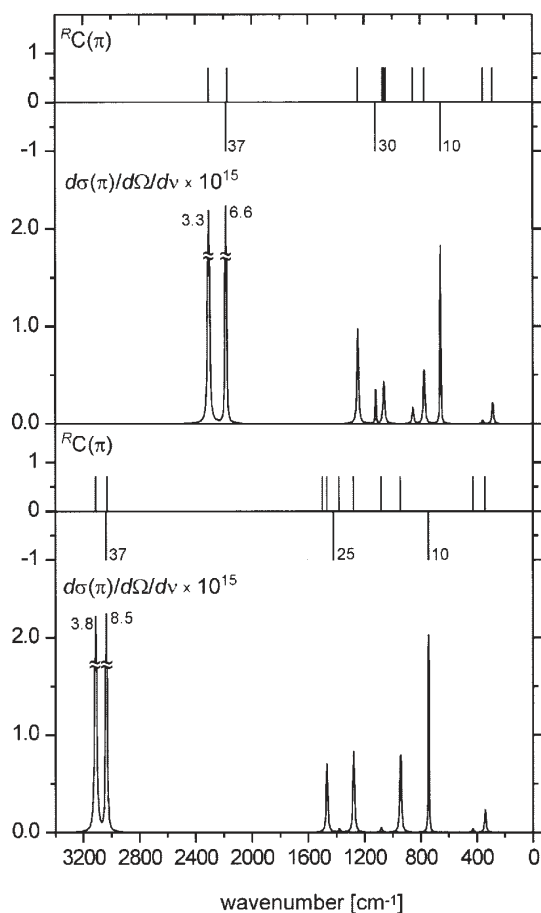
VIBRATIONAL OPTICAL ACTIVITY OF (*R*)-[²H₁, ²H₂, ²H₃]-NEOPENTANE

FIGURE 11. Backscattering Raman spectrum of neopentane (bottom half) and perdeuterated neopentane (top half). The line spectra indicate the degree of circularity. Vibrations of species A_1 have $C(\pi) = -1$, vibrations of species T_2 and E have $C(\pi) = 5/7$, vibrations of species T_1 and A_2 are silent. Bandwidths and units of scattering cross sections: as in Fig. 6. Computational parameters: as in Fig. 2.

can be easily identified in the energy decomposition diagram (Fig. 9) by its low H, high D, and substantial C energy content. In contrast, the VCD signal of the umbrella vibration 30 of the CH_3 group is negligible.

The degree of mixing, in the partially deuterated molecule, of the A_1 symmetric modes of neopentane and of fully deuterated neopentane with modes of other symmetry species, is evidenced by the nonzero value of the sum of the internuclear

distances of most modes. Notable exceptions are the lowest-energy torsional vibrations, and the three highest-energy vibrations of the antisymmetric CH- and CD-stretch type. If compared with their parent vibrations of the symmetric molecules, even these modes appear strongly modified, however, less by the character of the motion of the H and D atoms on individual methyl groups than by the change of coupling between methyl groups. In the torsional modes, which are the four lowest-energy modes of the molecule, the CD_3 , CD_2H , CDH_2 , and CH_3 group execute their motions largely independently from each other. Their motion cannot be completely independent, however, notably because of the Sayvetz conditions. This is visible from the energy decomposition diagram in Figure 9, which shows that the D energy content of the second to lowest torsional motion is actually slightly higher than in the lowest one.

The spectral region with substantial VOA in Figure 8 is bound at the lower end by the molecular

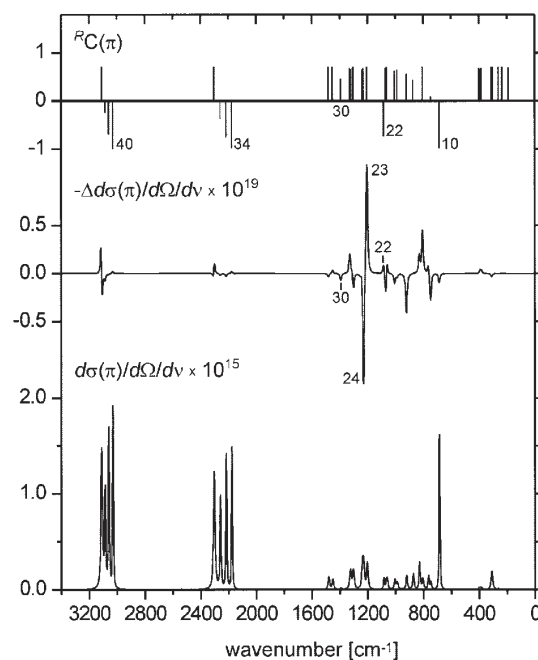


FIGURE 12. Backscattering Raman and ROA spectra of rotamer 5 of (*R*)-[²H₁, ²H₂, ²H₃]-neopentane. The line spectrum indicates the degree of circularity of individual Raman bands. Bandwidths and units of scattering cross sections: as in Fig. 6. Computational parameters: as in Fig. 2.

HUG AND HAESLER

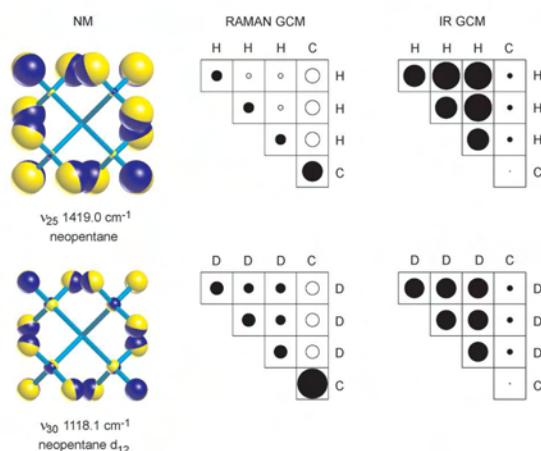


FIGURE 13. Umbrella mode of species A_1 of neopentane and perdeuterated neopentane. Columns and rows of the group coupling matrices correspond to the H or D, and the C atoms of individual methyl groups. For neopentane, the total vibrational absorption intensity of the A_1 mode vanishes due to canceling terms between methyl groups. Black circles, positive; open circles, negative. Computational parameters: as in Fig. 2. [Color figure can be viewed in the online issue, which is available at www.interscience.wiley.com.]

breathing mode 10 at 685 cm^{-1} , and at the higher end by the CH_3 umbrella mode 30 at $1,391\text{ cm}^{-1}$. There is little ROA and VCD outside these bounds, contrary perhaps to what one might expect for the CCC bending and twisting motions at energy of $<685\text{ cm}^{-1}$. The observation agrees with our experience for other molecules chiral by deuterium substitution.

Moreover, from Figures 8 and 12, it is evident that the main region of VOA activity falls into a lower- and a higher-energy section, to the right and left, respectively, of the CD_3 umbrella mode 22, found at $1,084\text{ cm}^{-1}$ in rotamer 5. In the lower-energy section, $685\text{--}1,084\text{ cm}^{-1}$, the rocking motion of whole methyl groups, and their deformation motions, dominate, with the energy distribution gradually shifting from D to H with increasing total energy. In the higher-energy section, $1,084\text{--}1,391\text{ cm}^{-1}$, CC-stretching motion comes into play. The three CC-stretching vibrations 23–25, identified by numbering in Figure 14, have a high carbon content and produce substantial ROA in all rotamers. Figure 15 displays the nuclear motion of vibration 23 and 24, which are responsible for the large couplet in the ROA spectrum of rotamer 5 in Figure 12. The

parent vibrations in the symmetric molecules are the T_2 symmetric modes 19–21 in neopentane and 31–33 in perdeuterated neopentane. This triplet of vibrations can be easily identified for the three molecules in the energy level diagram of Figure 14.

Comparison of the ROA and the VCD spectra of Figure 8 shows that they are close to mirror images of each other. This is contrary to what we found for the CH- and CD-stretch region dominated by inertial contributions, and is one of the unexpected features of the VOA of $[^2\text{H}_1, ^2\text{H}_2, ^2\text{H}_3]$ -neopentane. The mirror image aspect, which is far too pronounced to represent a statistical fluke, is more easily visible for the mixture of rotamers than for individual rotamers. A detailed analysis will have to show why this is so, as well as what conclusions

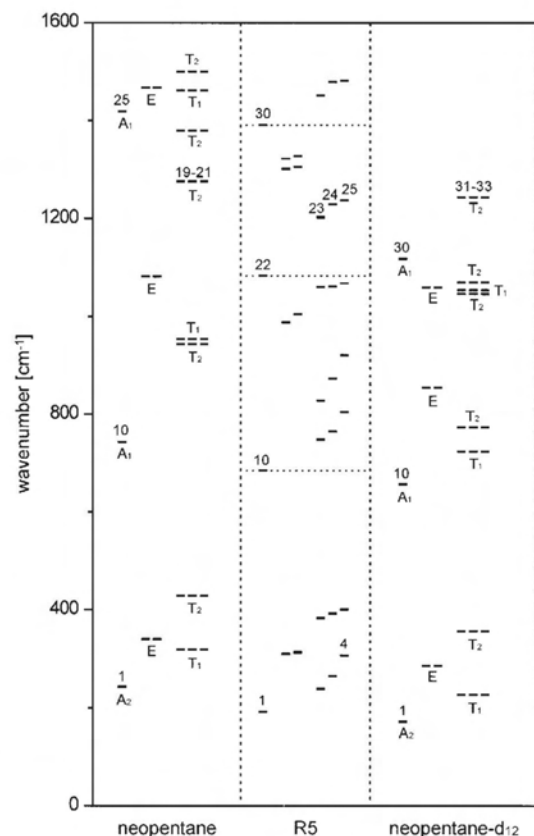


FIGURE 14. Diagrammatic representation of the energy levels of the lower frequency modes of neopentane, rotamer 5 of $[^2\text{H}_1, ^2\text{H}_2, ^2\text{H}_3]$ -neopentane, and perdeuterated neopentane. Computational parameters: as in Fig. 2.

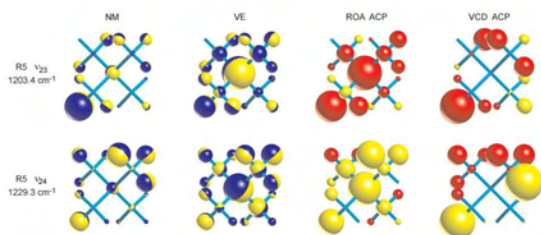
VIBRATIONAL OPTICAL ACTIVITY OF (R)-[²H₁, ²H₂, ²H₃]-NEOPENTANE

FIGURE 15. Representation of the displacements (NM) and the vibrational energies (VE) of individual nuclei in modes 23 and 24 of rotamer 5 of (R)-[²H₁, ²H₂, ²H₃]-neopentane, with the ROA and VCD atomic contribution pattern generated by these vibrations. Red circles, positive; yellow circles, negative. Computational parameters: as in Fig. 2. [Color figure can be viewed in the online issue, which is available at www.interscience.wiley.com.]

can be drawn from it for the VOA of other molecules.

Summed VOA Intensities

A striking aspect of all VOA spectra is the fact that positive and negative contributions appear to cancel over an entire spectrum. This is particularly visible in ROA spectra because they can be measured over a more extended spectral range than VCD spectra. In electronic optical activity, according to a well-known sum rule, the value of the rotational strengths summed over all transitions between the ground state and electronically excited states vanishes [38]. In VOA, the analogous sum over the excited states of a particular vibrational mode is of little interest, as it is the VOA for fundamental transitions, summed over all vibrational modes, that can be measured. Cuony and Hug [39] showed that a general rule for the value of the ROA summed over vibrational modes does not exist, even though this sum (if it is extended to include all normal modes, which also means those with zero vibrational frequency corresponding to translational and rotational motion) does vanish for certain molecules that owe their chirality to isotope substitution. For VCD, Buckingham [16] has more recently discussed the balancing of summed positive and negative VCD contributions for fundamental vibrational transitions by using the argument that nondegenerate vibrational levels cannot support a time-odd property, such as a magnetic moment.

The significance of the small but definite nonzero size of the sum of total vibrational ROA intensity, obtained by adding the ROA of individual vibrational modes multiplied by appropriate frequency factors, has only recently been understood [3]. It is a measure of the chirality of the electron distribution, as seen by the nuclei when they move in the various normal modes of a molecule. [²H₁, ²H₂, ²H₃]-neopentane, with its *T_d* symmetric electron distribution, is the perfect molecule for numerically testing this as it can be argued that its summed vibrational ROA should be negligible.

Summing individual terms in Eq. (5) over all normal modes, including those with zero frequency, yields an expression independent of the normal coordinates $L_{\alpha,p}^x$:

$$\begin{aligned} \sum_p^{NM} L_{\alpha,p}^x \cdot V_{\alpha\beta} \cdot L_{\beta,p}^x &= \sum_p^{NM} \sum_{i,j} V_{\alpha i, \beta j} L_{\alpha i, p}^x L_{\beta j, p}^x \\ &= \sum_{i,j} V_{\alpha i, \beta j} m_{\alpha}^{-1} \delta_{\alpha i, \beta j} = \sum_i V_{\alpha i, \alpha i} m_{\alpha}^{-1} \delta_{\alpha\alpha} = V_{\alpha} m_{\alpha}^{-1} \delta_{\alpha\alpha} \end{aligned} \quad (29)$$

where NM means summation over all normal modes, and where

$$V_{\alpha} = \sum_i V_{\alpha i, \alpha i} \quad (30)$$

V_{α} is a purely electronic quantity. For Raman and vibrational absorption, it is a true scalar, but for ROA and VCD, as an invariant combination of the elements of a true and of a pseudo-second-rank tensor, it is a pseudo-scalar. Consequently, for a nucleus located in a mirror plane of a molecule's electron distribution, V_{α} vanishes, and for two nuclei α and β located at enantiotopic sites, $V_{\beta} = -V_{\alpha}$ [39]. Thus, for ROA and VCD the sum (29) vanishes for a molecule such as [²H₁, ²H₂, ²H₃]-neopentane, where all nuclei are located in mirror planes of the electron distribution. In molecules with a less symmetric electron distribution, (29) will not, in general, vanish for ROA, but it does vanish for VCD unless the molecule supports a permanent magnetic dipole moment [16].

Translational motion does not lead to ROA. Equation (29) therefore represents a rovibrational sum. It is possible to subtract the rotational contribution and to obtain a measure for the vibrational part alone, which then can be directly compared with the sum of measured vibrational ROA inten-

HUG AND HAESLER

sities, provided individual measured bands are multiplied by appropriate frequency factors. For this purpose, it is best to define a fractional, dimensionless measure [3], as it is difficult to measure absolute Raman scattering cross sections. For ROA backscattering, one can write for the fractional contribution of a molecule's chiral electron distribution to rovibrational Raman scattering:

$$\delta(\text{rovib}) = \frac{\sum_{\alpha} [12V(\beta_G^2)_{\alpha} + 4V(\beta_A^2)_{\alpha}] m_{\alpha}^{-1}}{\sum_{\alpha} [12V(\beta_G^2)_{\alpha} + 4V(\beta_A^2)_{\alpha}] m_{\alpha}^{-1}}, \quad (31)$$

where the summations are over all nuclei.

It has been shown that rotational ROA is small in comparison with vibrational ROA [40]. It will therefore make a negligible contribution only to the sum of absolute values that occur in the denominator of (31), where all terms are taken positive, and we can set

$$\sum_{\alpha} [12V(\beta_G^2)_{\alpha} + 4V(\beta_A^2)_{\alpha}] m_{\alpha}^{-1} \approx \sum_p^{\text{vib}} [12\beta_{Gp}^2 + 4\beta_{Ap}^2], \quad (32)$$

where the summation is over the vibrational modes of the molecule. In the numerator, we cannot neglect rotational contributions, however, because, in contrast to vibrational ROA, all rotational terms have the same sign [40]. Their fractional contribution in (31) can be formally written as

$$\begin{aligned} \delta(\text{rot}) &= \frac{\sum_p^{\text{rot}} (12\beta_{Gp}^2 + 4\beta_{Ap}^2)}{\sum_p^{\text{vib}} [12\beta_{Gp}^2 + 4\beta_{Ap}^2]} \\ &= \frac{\sum_{\alpha} [12V(\beta_G^2)_{\alpha} + 4V(\beta_A^2)_{\alpha}] m_{\alpha}^{-1} - \sum_p^{\text{vib}} (12\beta_{Gp}^2 + 4\beta_{Ap}^2)}{\sum_p^{\text{vib}} [12\beta_{Gp}^2 + 4\beta_{Ap}^2]}. \end{aligned} \quad (33)$$

Rotational ROA is determined by the anisotropy of purely electronic tensors. We can therefore consider it an expression of electronic chirality. Subtracting (33) from (31) then yields a measure of the influence of the chiral distribution of a molecule's electrons on vibrational ROA alone:

$$\delta(\text{vib}) = \frac{\sum_p^{\text{vib}} (12\beta_{Gp}^2 + 4\beta_{Ap}^2)}{\sum_p^{\text{vib}} [12\beta_{Gp}^2 + 4\beta_{Ap}^2]}. \quad (34)$$

Analogous expressions pertain to other scattering geometries.

Comparison with the experiment can be made by multiplying the measured ROA difference intensities, expressed as the difference ΔN_p of scattered photons for right and left circularly polarized light by vibration p , multiplied by appropriate frequency and Boltzmann factors:

$$\delta(\text{vib}) = \frac{\sum_p \Delta N_p \Delta \omega_p [1 - \exp(-\hbar \Delta \omega_p / kT)] / \omega_p^3}{\sum_p |\Delta N_p| \Delta \omega_p [1 - \exp(-\hbar \Delta \omega_p / kT)] / \omega_p^3}. \quad (35)$$

In choosing the frequency factors in (35), it has been assumed that the spectral linewidth of individual vibrational bands is narrow enough so that they can be characterized by a single discrete vibrational frequency $\Delta \omega_p$.

For [$^2\text{H}_1$, $^2\text{H}_2$, $^2\text{H}_3$]-neopentane, $\delta(\text{vib}) = -\delta(\text{rot})$ as $\delta(\text{rovib})$ vanishes according to (29). According to [40], $\delta(\text{rot})$ is expected to vanish as electronic tensors for a T_d symmetric electron distribution have no anisotropic part. The calculated values of $\delta(\text{vib})$ are negligible, as expected, and the deviation from zero below the computational precision.

Of particular interest is the cumulative sum which one obtains by the stepwise adding of the VOA intensities of individual vibrations, starting with the vibration of the lowest and progressing to vibrations of higher energy. Normalized by the full denominator of Eq. (34), it is represented graphically for ROA and VCD in Figure 16. The value at the left-hand side of Figure 16 represents the value of $\delta(\text{vib})$, Eq. (34), i.e., the sum over all vibrations. The cumulative sum tends to return to a zero value after relatively small spectral sections, and in particular after the low frequency region of major VOA discussed earlier, as well as the CD- and the CH-stretch region.

The spectral ranges over which cancelation occurs are similar for ROA and VCD, and similar for all rotamers. Clearly, nuclear motion is strongly coupled within such regions of vibrational energy, but largely independent for the different regions. This brings to mind a venerable technique of the pre-computer age for simplifying otherwise untractable problems of a vibrational analysis, namely by the selection of spectral regions of interest through putting certain force constants in internal coordinates either to zero or to infinity [37].

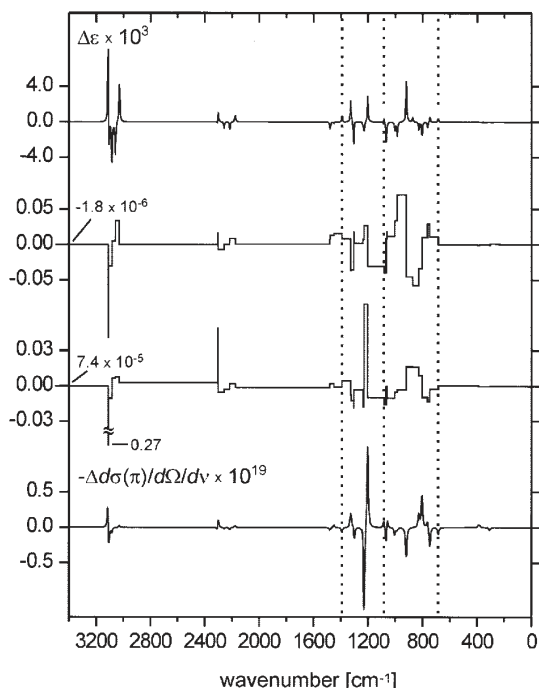
VIBRATIONAL OPTICAL ACTIVITY OF (R)-[²H₁, ²H₂, ²H₃]-NEOPENTANE

FIGURE 16. Cumulated normalized sums of the VCD (top half) and the ROA (bottom half) according to Eqs. (34) and (35), for rotamer 5 of (R)-[²H₁, ²H₂, ²H₃]-neopentane. Summation starts with vibration 1 at the right-hand side. The value of the cumulated sum goes from positive to negative approximately between the two spectral regions of major VOA indicated in Figs. 8 and 9, and returns to zero between the lower-frequency region, the CD-stretch, and the CH-stretch region. Actual ROA and VCD spectra are included for comparison. Computational parameters: as in Fig. 2.

Conclusions

There can be little doubt that [²H₁, ²H₂, ²H₃]-neopentane is one of the most spectacular, and perhaps indeed the most spectacular, chiral molecule in the field of vibrational optical activity. At the outset, it might look like a very special case, with little relevance to the molecules stereochemists encounter in their everyday work. Upon closer inspection, it becomes clear, however, that the molecule is a treasure trove for the separate study of many aspects of the generation of vibrational optical activity which are confounded in most chiral molecules.

One of these aspects we had not expected to encounter is the apparent importance of inertial contributions for the VOA of the CH- and CD-stretch vibrations. They lead to ROA and VCD of the same sign, despite the opposite sign convention of the two methods. Another unexpected result is the roughly mirror image appearance of VCD and ROA in the region of lower vibrational energies. Both findings are independent of the computational approach used and merit further investigation.

For the CH- and CD-stretch region, the similarity of ROA and VCD manifests itself for vibrations of individual rotamers, and the conclusion that inertial contributions are decisive is supported by the opposite signs which the CH- and CD-stretch vibrations produce for sister vibrations in rotamers which are related through the interchange of H and D nuclei. For the lower-energy region, the mirror image appearance of ROA and VCD is best visible for the mixture of the nine rotamers of the molecule, where it is clear cut. For vibrations of individual rotamers it can be absent, as Figure 15 demonstrates for the prominent vibrations 23 and 24 of rotamer 5.

A result that we expected, and looking for which provided the original incentive for our theoretical investigation of [²H₁, ²H₂, ²H₃]-neopentane, is that the total ROA, summed for all vibrations according to Eqs. (34) and (35), is negligible. This is not only the case for the ROA of all vibrations, but to fair approximation also for individual spectral regions, namely the CH-stretch, the CD-stretch, and the lower-frequency region. The results are very similar for VCD. In view of Eq. (29), this makes it evident that the vibrational motions of these three energy regions are largely independent of each other. This is a result that we expect to hold approximately for most chiral molecules.

Another important goal of this study has been to computationally assess the measurability of the ROA and the VCD of the enantiomers of [²H₁, ²H₂, ²H₃]-neopentane. If measurable, the molecule is of enough intellectual interest so that it will be synthesized by stereochemists. According to some inquiries we made to this end, the synthesis, while not trivial, appears feasible. We have therefore been as careful as possible in judging the measurability of the VOA of the compound, including the use of realistic band shapes of the Voigt type to simulate expected spectra. The ROA, while not generous for the mixture of rotamers due to canceling, should nevertheless be measurable in the 700–1,400-cm⁻¹ region, with only a few milligrams of substance.

HUG AND HAESLER

The g -values for VCD are far larger than the Δ -values for ROA, and VCD should therefore easily be measurable in the 700–1,100-cm⁻¹ region and beyond, including with scanning instruments of low spectral resolution [30]. This prediction assumes that enough substance becomes available, as the vibrational absorption of the nonpolar compound with its T_d symmetric electron distribution is small.

The physical properties of [²H₁, ²H₂, ²H₃]-neopentane are not expected to present an obstacle to a measurement. The boiling point of neopentane itself is 9.5°C, so it can be handled as a liquid under slight pressure or with refrigeration.

Some questions have only been touched upon, such as why the signs of the ROA and VCD of [²H₁, ²H₂, ²H₃]-neopentane are related in such a peculiar way. Other aspects of the molecule's VOA, and of its vibrational spectrum in general, have not even been mentioned in this article, e.g., the relative sign pattern of quadrupole and magnetic dipole contributions. One aspect that needs closer scrutiny is the influence the many approximations that enter VCD and ROA calculations can have on numerical results. The methods we use are well tested, but [²H₁, ²H₂, ²H₃]-neopentane is also a molecule particularly well suited to assess some of the limits of present VOA calculations. Questions of this kind remain the subject of future work. Nevertheless, we hope we have been able to show that modern *ab initio* computations, combined with innovative graphic methods, can make a decisive contribution to the understanding of vibrational spectra.

ACKNOWLEDGMENTS

Some of the pilot calculations of [²H₁, ²H₂, ²H₃]-neopentane, and tests on the realistic representation of its spectra, were done by Mehdi Bounouar in the frame of his diploma work with one of the authors (W.H.). Some of the original MATLAB routines for visualising ACPs and GCMs were written by Gérard Zuber.

References

- Hug, W. In *Raman Spectroscopy, Linear and Nonlinear*; Lascomb, J.; Huang, P., Eds.; Wiley-Heyden: Chichester, 1982; p 3.
- (a) Barron, L. D. *J Chem Soc Chem Commun* 1977, 305; (b) Barron, L. D.; Numan, H.; Wynberg, H. *J Chem Soc Chem Commun* 1978, 259; (c) Holzwarth, G.; Hsu, E. C.; Mosher, H. S.; Faulkner, T. R.; Moscovitz, A. *J Am Chem Soc* 1974, 96, 251; (d) Stephens, P. J.; Clark, R. In *Optical Activity and Chiral Discrimination*; Mason, S. F., Ed.; D. Riedel: Dordrecht, 1979; (e) Polavarapu, P. L.; Nafie, L. A.; Benner, S. A.; Morton, T. H. *J Am Chem Soc* 1981, 103, 5349.
- Hug, W. In *Handbook of Vibrational Spectroscopy*; Chalmers, J. M.; Griffiths, P. R., Eds.; John Wiley & Sons: Chichester, 2002; Vol 1, p 745.
- Nafie, L. A. *Chem Phys* 1996, 205, 309.
- Constante, J.; Hecht, L.; Polavarapu, P. L.; Collet, A.; Barron, L. D. *Angew Chem Int Ed* 1997, 36, 885.
- Wynberg, H. *Acc Chem Res* 1971 4, 65.
- Barron, L. D. *Molecular Light Scattering and Optical Activity*, 2nd ed.; Cambridge University Press: Cambridge, 2004.
- Freedman, T. B.; Nafie, L. A. In *Modern Nonlinear Optics*; Evans, M.; Kielich, S., Eds.; Wiley: New York, 1994; Part 3, p 207.
- Placzek, G. *Handbuch der Radiologie*; Marx, E., Ed.; Akademische Verlagsgesellschaft: Leipzig, 1934; Vol VI, p 205.
- Barron, L. D.; Hecht, L.; Gargaro, A. R.; Hug, W. *J Raman Spectrosc* 1990, 21, 375.
- (a) Barron, L. D.; Hecht, L.; Hug, W.; MacIntosh, M. J. *J Am Chem Soc* 1989, 111, 8731; (b) Hecht, L.; Barron, L. D.; Hug, W. *Chem Phys Lett* 1989, 158, 341.
- Barron, L. D.; Buckingham, A. D. *Mol Phys* 1971, 20, 1111.
- Long, D. A. *Raman Spectroscopy*; McGraw-Hill: New York, 1977; p 130.
- (a) Nafie, L. A. *J Chem Phys* 1983, 79, 4950; (b) Nafie, L. A. *J Chem Phys* 1992, 96, 5687.
- Hug, W. *Chem Phys* 2001, 264, 53.
- Buckingham, A. D. *Faraday Discuss* 1994, 99, 1.
- (a) Hug, W.; Surbeck, H. *Chem Phys Lett* 1979, 60, 186; (b) Barron, L. D. *Chem Phys Lett* 1983, 102, 285; (c) Nafie, L. A. *Chem Phys Lett* 1983, 102, 287.
- (a) Devlin, F. J.; Stephens, P. J.; Cheeseman, J. R.; Frisch, M. J. *J Phys Chem* 1997, 101, 6322; (b) Devlin, F. J.; Stephens, P. J.; Cheeseman, J. R.; Frisch, M. J. *J Phys Chem* 1997, 101, 9912.
- Cheeseman, J. R.; Frisch, M. J.; Devlin, F. J.; Stephens, P. J. *J Chem Phys Lett* 1996, 252, 211.
- Frisch, M. J.; Trucks, G. W.; Schlegel, H. B.; Scuseria, G. E.; Robb, M. A.; Cheeseman, J. R.; Montgomery, J. A., Jr.; Vreven, T.; Kudin, K. N.; Burant, J. C.; Millam, J. M.; Iyengar, S. S.; Tomasi, J.; Barone, V.; Mennucci, B.; Cossi, M.; Scalmani, G.; Rega, N.; Petersson, G. A.; Nakatsuji, H.; Hada, M.; Ehara, M.; Toyota, K.; Fukuda, R.; Hasegawa, J.; Ishida, M.; Nakajima, T.; Honda, Y.; Kitao, O.; Nakai, H.; Klene, M.; Li, X.; Knox, J. E.; Hratchian, H. P.; Cross, J. B.; Bakken, V.; Adamo, C.; Jaramillo, J.; Gomperts, R.; Stratmann, R. E.; Yazyev, O.; Austin, A. J.; Cammi, R.; Pomelli, C.; Ochterski, J. W.; Ayala, P. Y.; Morokuma, K.; Voth, G. A.; Salvador, P.; Dannenberg, J. J.; Zakrzewski, V. G.; Dapprich, S.; Daniels, A. D.; Strain, M. C.; Farkas, O.; Malick, D. K.; Rabuck, A. D.; Raghavachari, K.; Foresman, J. B.; Ortiz, J. V.; Cui, Q.; Baboul, A. G.; Clifford, S.; Cioslowski, J.; Stefanov, B. B.; Liu, G.; Liashenko, A.; Piskorz, P.; Komaromi, I.; Martin, R. L.; Fox, D. J.; Keith, T.; Al-Laham, M. A.; Peng, C. Y.; Nanayakkara, A.; Challacombe, M.; Gill, P. M. W.; Johnson, B.; Chen, W.; Wong, M. W.; Gonzalez, C.; and Pople, J. A. *Gaussian 03, Revision C.03*; Gaussian: Wallingford, CT, 2004.
- (a) Becke, A. D. *J Chem Phys* 1993, 98, 5648; (b) Lee, C.; Yang, W.; Parr, R. G. *Phys Rev B* 1988, 37, 785.

VIBRATIONAL OPTICAL ACTIVITY OF (*R*)-[²H₁, ²H₂, ²H₃]-NEOPENTANE

22. Krishnan, R.; Binkley, J. S.; Seeger, R.; Pople, J. A. *J Chem Phys* 1980, 72, 650.
23. Kendal, R. A.; Dunning, T. H.; Harrison, R. J. *J Chem Phys* 1992, 96, 6796.
24. (a) Oddershede, J.; Jørgensen, P.; Yeager, D. L. *Comput Phys Rep* 1984, 2, 33; (b) Jørgensen, P.; Jensen, H. J. Aa.; Olsen, J. *J Chem Phys* 1988, 89, 3654.
25. Helgaker, T.; Jensen, H. J. Aa.; Jørgensen, P.; Olsen, J.; Ruud, K.; Ågren, H.; Auer, A. A.; Bak, K. L.; Bakken, V.; Christiansen, O.; Coriani, S.; Dahle, P.; Dalskov, E. K.; Enevoldsen, T.; Fernandez, B.; Hättig, C.; Hald, K.; Halkier, A.; Heiberg, H.; Hettema, H.; Jonsson, D.; Kirpekar, S.; Kobayashi, R.; Koch, H.; Mikkelsen, K. V.; Norman, P.; Packer, M. J.; Pedersen, T. B.; Ruden, T. A.; Sanchez, A.; Saue, T.; Sauer, S. P. A.; Schimmelpfennig, B.; Sylvester-Hvid, K. O.; Taylor, P. R.; Vahtras, O. DALTON, A Molecular Electronic Structure Program, Release 1.1; 2000, see <http://www.kjemi.uio.no/software/dalton/dalton.html>.
26. MATLAB Version 6.1 Release 12.1; Mathworks: Natick, CA, 2001.
27. Berg, M.; Vanden Bout, D. A. *Acc Chem Res* 1997, 30, 65.
28. Hubble, H. W.; Lai, T.; Berg, M. A. *J Chem Phys* 2001, 114, 3662.
29. Hug, W.; Hangartner, G. J. *Raman Spectrosc* 1999, 30, 841.
30. Keiderling, T. A. In *Biomolecular Structure and Dynamics*; NATO ASI series, Series E: Applied Sciences; Vergoten, G.; Theophanides, T., Eds.; Kluwer Academic: Dordrecht, The Netherlands, 1997; Vol 342, p 299.
31. Herzberg, G. H. *Molecular Spectra and Molecular Structure. II. Infrared and Raman Spectra of Polyatomic Molecules*; Van Nostrand: Princeton, NJ, 1945.
32. Dollish, F. R.; Fateley, W. G. *Characteristic Raman Frequencies of Organic Compounds*; John Wiley & Sons: New York, 1974.
33. Colthup, N. B.; Daly, L. H.; Wiberley, S. E. *Introduction to Infrared and Raman Spectroscopy*; Academic Press: New York, 1975.
34. Zuber, G.; Hug, W. *Helv Chim Acta* 2004, 87, 2208.
35. (a) Nafie, L. A.; Yu, G.-S.; Qu, X.; Freedman, T. B. *Faraday Discuss* 1994, 99, 13; (b) Tam, C. N.; Bouř, P.; Keiderling, T. A. *J Am Chem Soc* 1997, 119, 7061.
36. Hug, W. *Appl Spectrosc* 2003, 57, 1.
37. Wilson, E. B.; Decius, J. C.; Cross, P. C. *Molecular Vibrations*; Dover: New York, 1955.
38. Kauzmann, W. *Quantum Chemistry*; Academic Press: New York, 1957; p 711.
39. Cuony, B.; Hug, W. *Chem Phys Lett* 1981, 84, 131.
40. Barron, L. D.; Johnston, C. J. *J Raman Spectrosc* 1985, 16, 208.

12.2 Geometry and Conformations of (*R*)-[²H₁, ²H₂, ²H₃]-neopentane

(*R*)-[²H₁, ²H₂, ²H₃]-neopentane (**2**) has nine different conformers, which are represented in Figure 12.1.

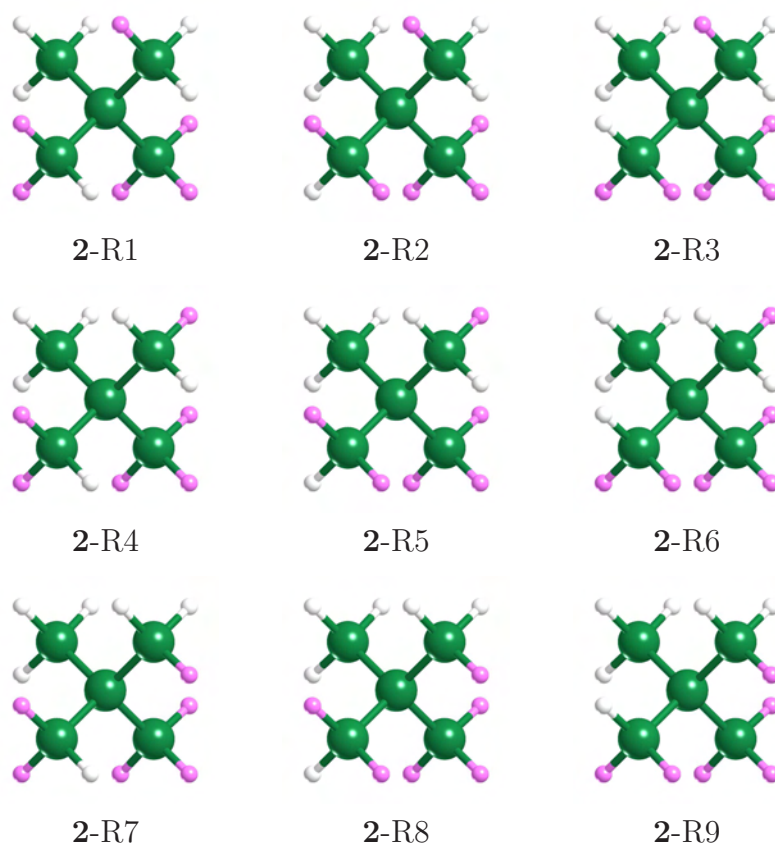


Figure 12.1: The nine rotamers of (*R*)-[²H₁, ²H₂, ²H₃]-neopentane (**2**)

As has been calculated in the previous chapter, the rotation barrier for the methyl group is about 4 kcal/mol. This is sufficient to make the staggered conformation of neopentane be thermodynamically the most and only probable one. Kinetically, even at 0°C, according to Eyring's equation, the reaction rate for the rotation of a methyl group, with a rotation barrier of 4 kcal/mol, is of the order of $k_{obs} = 3.9 \times 10^9 \text{ s}^{-1}$. The 9 rotamers of **2** will therefore interconvert

very rapidly. In order to avoid the calculation of the derivatives of the electronic tensors for all rotamers separately, the 9 species have been considered to have the same geometry as the undeuterated neopentane. Their relative free energy has been calculated to be within 0.008 kcal/mol (DFT/B3LYP/6-311++G**), and it has been concluded that an equiprobable mixture of the 9 rotamers will be a good approximation for the sample's composition.

12.3 Vibrational frequencies

The vibrational frequencies for all 9 rotamers were obtained by an isotopic vibrational analysis of the hessian force constant matrix obtained for the undeuterated neopentane. Different basis sets and functionals have been tested, which gave all similar but not identical frequencies (Table 12.2 and 12.3). We settled on the B3PW91/aug-cc-pVDZ level of theory, in order to be able to compare the ROA computations obtained with DALTON and Gaussian03. The resulting vibrational frequencies are listed in Table 12.1 and the vibrational motions for rotamer R5 are represented in Figure 12.2.

12.4 Simulation of Raman and ROA Spectra

The simulation of the ROA spectra for (*R*)-[²H₁, ²H₂, ²H₃]-neopentane has been realised by calculating the 9 individual rotamers and by adding 1/9 of their respective ROA spectra to get the final spectrum. As mentioned before, the DFT/B3PW91/aug-cc-pVDZ geometry and force field have been chosen for our ROA calculations.

Our actual ROA computations have all been evaluated at the Hartree-Fock (HF) level of theory. In order to assess the potential benefit of a density

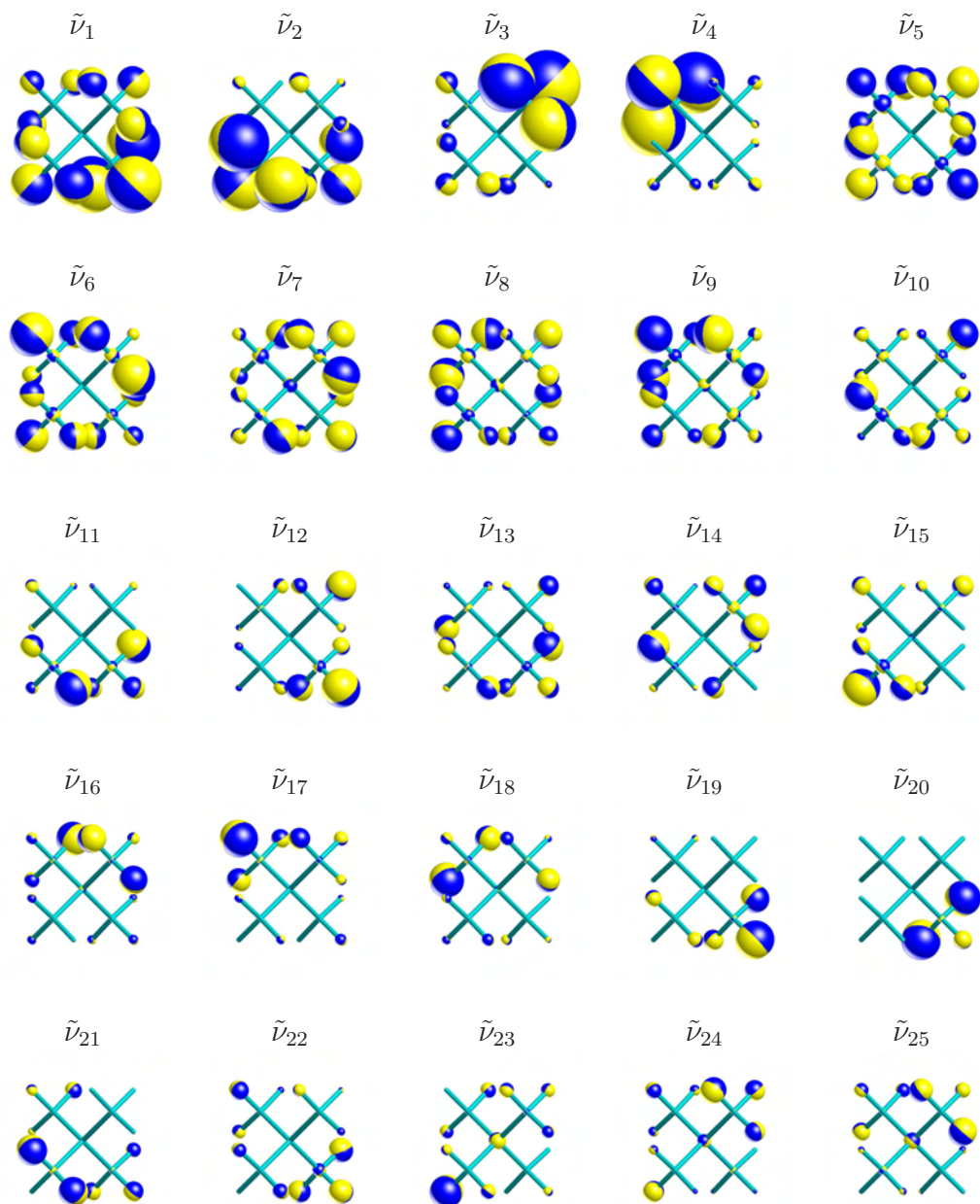


Figure 12.2: Representation of the vibrational motion in rotamer **2-R5**, calculated at the DFT/B3PW91/aug-cc-pVDZ level. Pictures were obtained with VOAView and are represented according to Gaussian's normalisation. Numbering of normal modes is made with increasing wavenumbers.

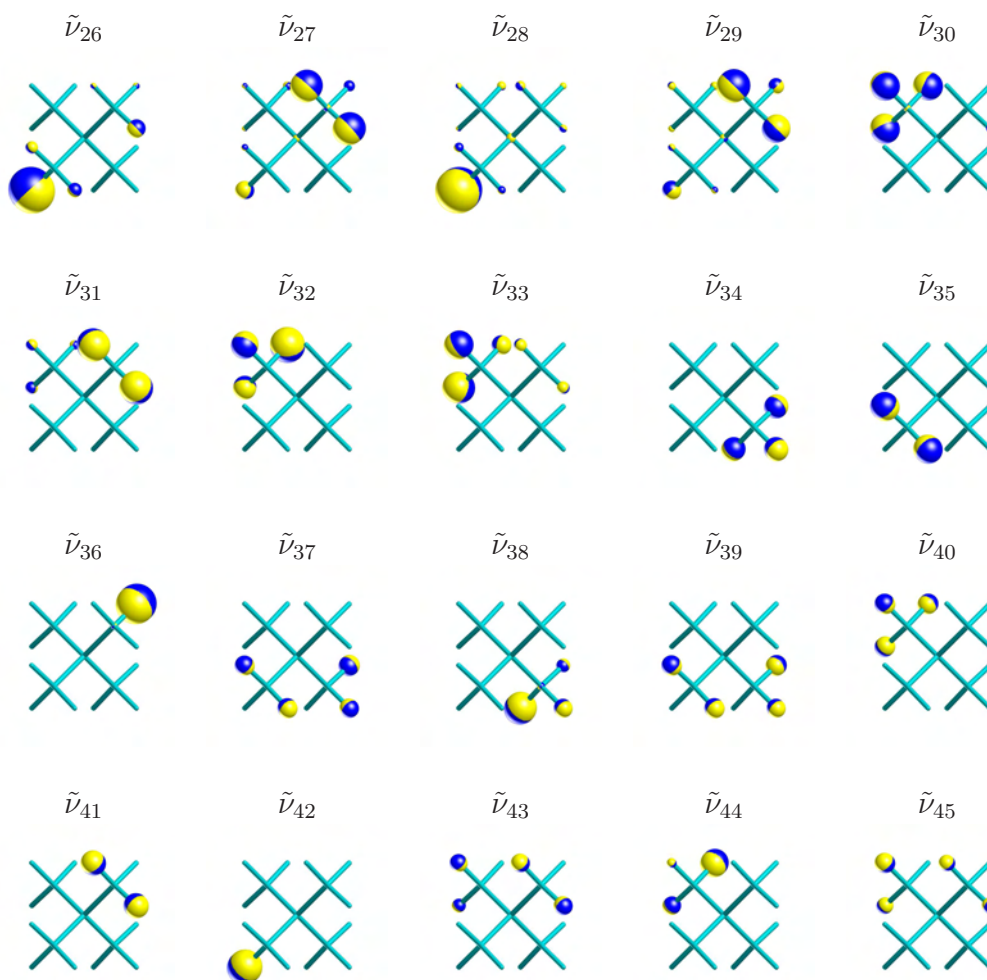


Figure 12.2: continued.

Table 12.1: Vibrational frequencies calculated for the 9 rotamers of **2** with DFT/B3PW91/aug-cc-pVDZ. C-H and C-D stretch are not listed here as they are identical for all 9 rotamers (see Fig. 12.3). Frequencies in cm^{-1} .

| | R1 | R2 | R3 | R4 | R5 | R6 | R7 | R8 | R9 |
|----|--------|--------|--------|--------|--------|--------|--------|--------|--------|
| 1 | 189.1 | 188.6 | 187.4 | 188.3 | 188.2 | 187.1 | 187.7 | 187.7 | 187.0 |
| 2 | 234.7 | 233.7 | 236.8 | 235.7 | 235.6 | 238.5 | 235.0 | 234.6 | 238.3 |
| 3 | 261.1 | 264.4 | 262.9 | 261.9 | 261.8 | 260.8 | 263.7 | 264.2 | 260.3 |
| 4 | 304.7 | 303.0 | 302.7 | 302.1 | 303.3 | 301.6 | 302.2 | 302.6 | 303.1 |
| 5 | 309.0 | 307.8 | 307.7 | 308.8 | 309.5 | 309.3 | 307.5 | 306.8 | 305.9 |
| 6 | 311.5 | 312.7 | 312.6 | 313.9 | 312.1 | 313.1 | 316.0 | 316.2 | 317.2 |
| 7 | 385.8 | 385.4 | 382.5 | 384.0 | 383.1 | 382.8 | 379.1 | 373.5 | 372.6 |
| 8 | 389.4 | 388.0 | 391.0 | 390.5 | 391.2 | 386.5 | 395.9 | 397.6 | 394.3 |
| 9 | 400.0 | 401.3 | 401.3 | 399.9 | 400.3 | 405.4 | 397.7 | 401.9 | 406.6 |
| 10 | 684.4 | 688.2 | 686.0 | 686.5 | 684.7 | 693.1 | 690.4 | 693.4 | 695.7 |
| 11 | 740.1 | 747.8 | 755.8 | 742.0 | 747.4 | 747.6 | 745.0 | 746.0 | 748.0 |
| 12 | 779.2 | 770.5 | 764.0 | 772.1 | 764.2 | 765.3 | 759.2 | 758.5 | 765.6 |
| 13 | 803.4 | 796.9 | 788.6 | 809.1 | 804.7 | 789.1 | 796.0 | 802.6 | 773.2 |
| 14 | 831.3 | 814.2 | 831.2 | 830.7 | 828.3 | 821.4 | 850.9 | 819.3 | 836.2 |
| 15 | 853.6 | 881.4 | 871.7 | 852.1 | 873.2 | 875.3 | 868.2 | 879.6 | 876.6 |
| 16 | 925.2 | 923.0 | 928.5 | 923.3 | 920.3 | 932.8 | 907.0 | 916.6 | 927.1 |
| 17 | 994.8 | 986.8 | 988.6 | 987.6 | 987.4 | 993.0 | 981.3 | 984.9 | 978.4 |
| 18 | 1007.8 | 1009.7 | 1001.4 | 1016.5 | 1004.7 | 998.1 | 1023.4 | 1019.8 | 1018.0 |
| 19 | 1058.5 | 1059.7 | 1061.1 | 1058.4 | 1060.0 | 1061.2 | 1059.2 | 1059.9 | 1061.6 |
| 20 | 1061.5 | 1061.4 | 1061.8 | 1061.5 | 1061.9 | 1062.1 | 1061.9 | 1061.4 | 1062.0 |
| 21 | 1068.2 | 1067.9 | 1067.9 | 1066.9 | 1068.1 | 1067.6 | 1067.7 | 1068.6 | 1068.8 |
| 22 | 1079.0 | 1080.1 | 1081.2 | 1083.1 | 1083.7 | 1084.2 | 1080.5 | 1082.3 | 1083.0 |
| 23 | 1208.8 | 1199.1 | 1198.7 | 1195.4 | 1203.4 | 1197.7 | 1191.8 | 1192.9 | 1199.6 |
| 24 | 1228.5 | 1231.8 | 1225.8 | 1229.3 | 1229.8 | 1226.8 | 1230.4 | 1230.2 | 1228.4 |
| 25 | 1236.0 | 1256.6 | 1257.4 | 1257.1 | 1238.6 | 1256.1 | 1259.4 | 1255.6 | 1236.6 |
| 26 | 1302.5 | 1281.0 | 1292.6 | 1292.1 | 1301.4 | 1289.5 | 1292.0 | 1283.8 | 1300.9 |
| 27 | 1308.3 | 1304.1 | 1304.0 | 1300.8 | 1305.7 | 1301.7 | 1303.9 | 1304.5 | 1306.8 |
| 28 | 1316.2 | 1316.6 | 1317.5 | 1312.5 | 1323.1 | 1312.0 | 1313.9 | 1316.8 | 1315.7 |
| 29 | 1328.4 | 1341.3 | 1334.7 | 1338.9 | 1328.0 | 1343.8 | 1334.7 | 1340.5 | 1335.0 |
| 30 | 1393.0 | 1391.2 | 1391.3 | 1393.4 | 1391.3 | 1391.2 | 1392.6 | 1391.2 | 1391.1 |
| 31 | 1451.5 | 1451.3 | 1451.2 | 1451.4 | 1451.2 | 1451.2 | 1454.7 | 1455.0 | 1454.9 |
| 32 | 1478.4 | 1478.3 | 1478.3 | 1478.4 | 1478.7 | 1478.7 | 1478.4 | 1478.4 | 1478.5 |
| 33 | 1482.0 | 1482.1 | 1482.0 | 1481.7 | 1481.6 | 1481.6 | 1479.1 | 1479.1 | 1479.1 |

Table 12.2: Vibrational frequencies calculated for rotamer **2**-R5 with different basis sets and functionals. C-H and C-D stretch are listed in Table 12.3. Frequencies in cm⁻¹.

| | B3PW91 | | B3LYP | |
|----|------------|-------------|------------|-------------|
| | 6-311++G** | aug-cc-pVDZ | 6-311++G** | aug-cc-pVDZ |
| 1 | 191.8 | 188.2 | 189.3 | 188.8 |
| 2 | 233.8 | 235.6 | 231.3 | 236.4 |
| 3 | 259.8 | 261.8 | 257.2 | 262.8 |
| 4 | 300.7 | 303.3 | 298.1 | 304.6 |
| 5 | 304.6 | 309.5 | 307.0 | 312.4 |
| 6 | 307.4 | 312.1 | 309.1 | 314.8 |
| 7 | 373.9 | 383.1 | 379.7 | 388.8 |
| 8 | 382.0 | 391.2 | 387.6 | 396.8 |
| 9 | 390.8 | 400.3 | 396.3 | 405.7 |
| 10 | 681.6 | 684.7 | 675.0 | 678.7 |
| 11 | 750.1 | 747.4 | 752.8 | 750.3 |
| 12 | 766.3 | 764.2 | 767.5 | 765.7 |
| 13 | 806.2 | 804.7 | 805.0 | 804.3 |
| 14 | 828.7 | 828.3 | 826.3 | 826.1 |
| 15 | 874.4 | 873.2 | 872.9 | 872.1 |
| 16 | 921.9 | 920.3 | 922.2 | 920.9 |
| 17 | 991.2 | 987.4 | 994.8 | 991.2 |
| 18 | 1007.3 | 1004.7 | 1008.2 | 1006.0 |
| 19 | 1071.5 | 1060.0 | 1078.3 | 1064.8 |
| 20 | 1074.1 | 1061.9 | 1081.2 | 1066.9 |
| 21 | 1078.3 | 1068.1 | 1085.2 | 1073.0 |
| 22 | 1090.6 | 1083.7 | 1096.7 | 1088.1 |
| 23 | 1205.4 | 1203.4 | 1198.9 | 1197.5 |
| 24 | 1233.5 | 1229.8 | 1229.1 | 1225.6 |
| 25 | 1239.9 | 1238.6 | 1233.7 | 1233.4 |
| 26 | 1312.0 | 1301.4 | 1318.3 | 1307.0 |
| 27 | 1316.0 | 1305.7 | 1323.7 | 1309.0 |
| 28 | 1327.9 | 1323.1 | 1329.4 | 1322.3 |
| 29 | 1337.8 | 1328.0 | 1340.7 | 1328.3 |
| 30 | 1399.9 | 1391.3 | 1410.0 | 1398.1 |
| 31 | 1466.9 | 1451.2 | 1476.3 | 1457.7 |
| 32 | 1495.0 | 1478.7 | 1502.9 | 1483.8 |
| 33 | 1497.6 | 1481.6 | 1505.3 | 1486.5 |

Table 12.3: C-H and C-D stretch vibrational frequencies calculated for rotamer **2-R5** with different basis sets and functionals. Frequencies in cm^{-1} .

| | B3PW91 | | B3LYP | |
|----|------------|-------------|------------|-------------|
| | 6-311++G** | aug-cc-pVDZ | 6-311++G** | aug-cc-pVDZ |
| 34 | 2172.4 | 2177.0 | 2164.8 | 2169.3 |
| 35 | 2211.5 | 2217.1 | 2201.9 | 2207.7 |
| 36 | 2252.1 | 2259.0 | 2240.1 | 2247.4 |
| 37 | 2294.1 | 2302.6 | 2278.9 | 2288.1 |
| 38 | 2295.0 | 2303.5 | 2279.9 | 2289.1 |
| 39 | 2296.0 | 2304.4 | 2281.0 | 2290.2 |
| 40 | 3024.4 | 3029.6 | 3014.6 | 3020.1 |
| 41 | 3051.5 | 3059.2 | 3037.7 | 3045.9 |
| 42 | 3075.5 | 3085.4 | 3058.1 | 3068.6 |
| 43 | 3097.2 | 3108.9 | 3076.5 | 3089.0 |
| 44 | 3098.4 | 3110.2 | 3078.0 | 3090.5 |
| 45 | 3099.4 | 3111.2 | 3079.2 | 3091.8 |

functional theory approach, computations of the electronic tensors at that DFT level have been evaluated within Gaussian03 rev. C.01¹. A DFT approach for the computation of ROA has first been conducted by Ruud et al. in 2002 [52] within DALTON. They claimed that it represents the most accurate method, but acknowledged that the benefit over a standard HF approach is small. We did not find any published work on the reliability of the code implemented in Gaussian03 for the computation of the different optical activity tensors, and believe that our results are the first ever presented. A comparison of computed ROA spectra obtained with DALTON and Gaussian03, using an identical level of theory (HF), for (*R*)-(+)-propylene oxide, can be found in the Appendices. The results obtained with Gaussian03 are identical to those obtained with DALTON (the reference program), and are thus considered to be reliable.

¹Evaluation of the electronic tensors at the DFT level is also possible in DALTON Release 2.0, but this has not been tested in this work.

A comparison is now made between the DFT and HF level of theory. The computed individual spectra obtained by both approaches for the nine rotamers, as well as their respective sums, are illustrated in Fig. 12.3 and 12.4. As already mentioned by Ruud et al., both level of theory give very similar results, and it seems that a DFT approach does not improve significantly our ROA simulations.

Fig. 12.5 and 12.6 show the simulated Raman, ROA and degree of circularity spectra obtained for the mixture of the 9 rotamers of **2** in the range where the ROA should remain measurable [119]. The Δ -values band spectra are also illustrated, which are defined as

$$\Delta = \frac{I_R - I_L}{I_R + I_L} \quad (12.1)$$

and obtained by simply calculating the ratio of the ROA to the Raman simulated spectra. $|\Delta|$ can be used to judge the measurability of Raman optical activity, and with our present instruments, it should be $>10^{-5}$ [48, 49], as otherwise measurements become difficult or impossible. According to Fig. 12.5 and 12.6, a dozen of ROA bands satisfy this condition.

All the precautions have been taken in order to best assess the ROA measurability of (R)-[²H₁, ²H₂, ²H₃]-neopentane, and we are therefore confident in being able to measure it. In order to get a good signal to noise ratio, one will perhaps have to make use of filters, to get ride of the intense umbrella mode 10 and C-D stretching modes 34 to 39.

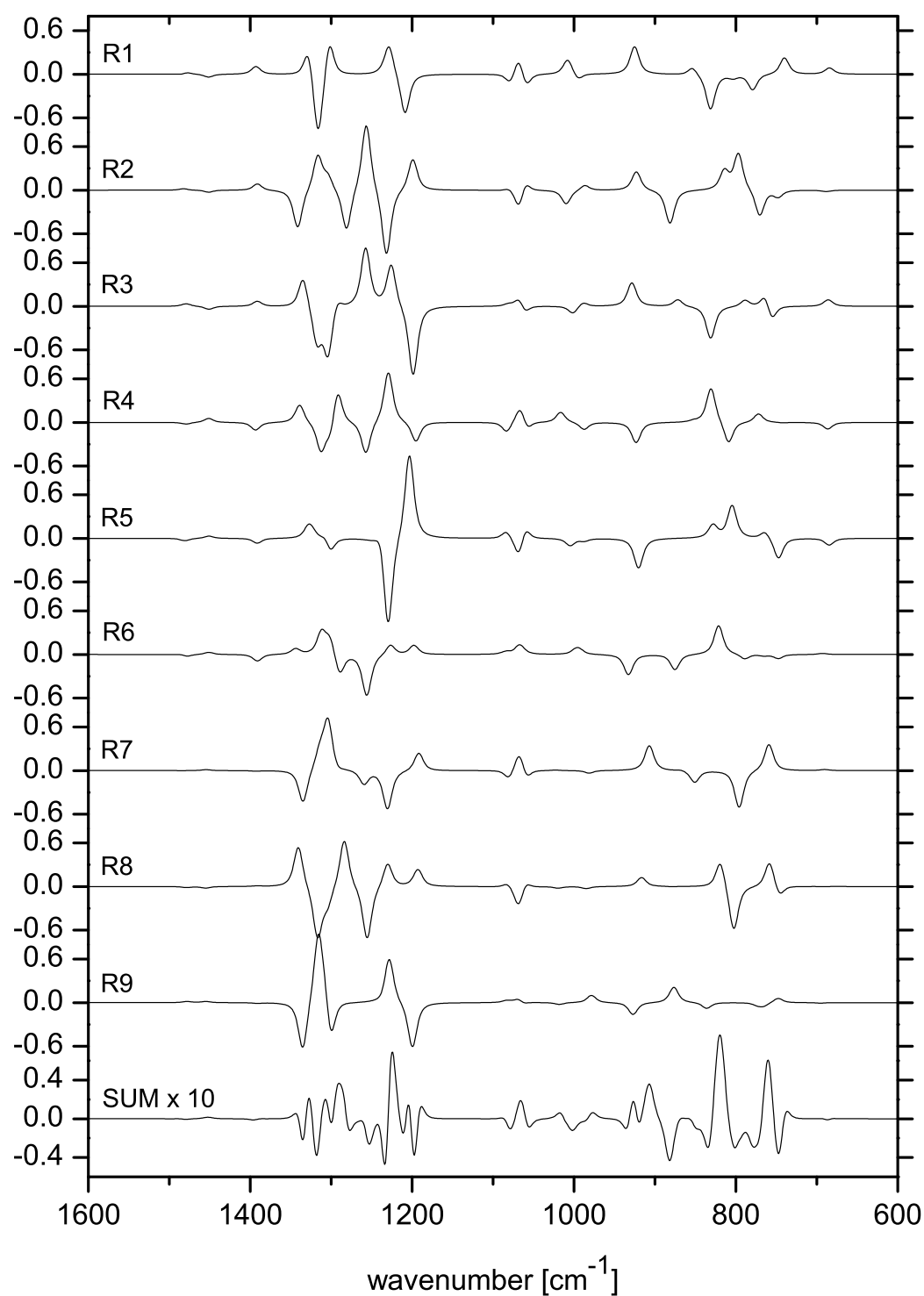


Figure 12.3: Simulated ROA spectra for the 9 rotamers of **2** and 1/9 of the sum of all spectra. Units: [$10^{-19} \text{ \AA}^2 \text{ sr}^{-1} \text{ cm}$]. Computational details: Gaussian03 force field: DFT/B3PW91/aug-cc-pVDZ, DALTON electronic tensor: TDHF/aug-cc-pVDZ.

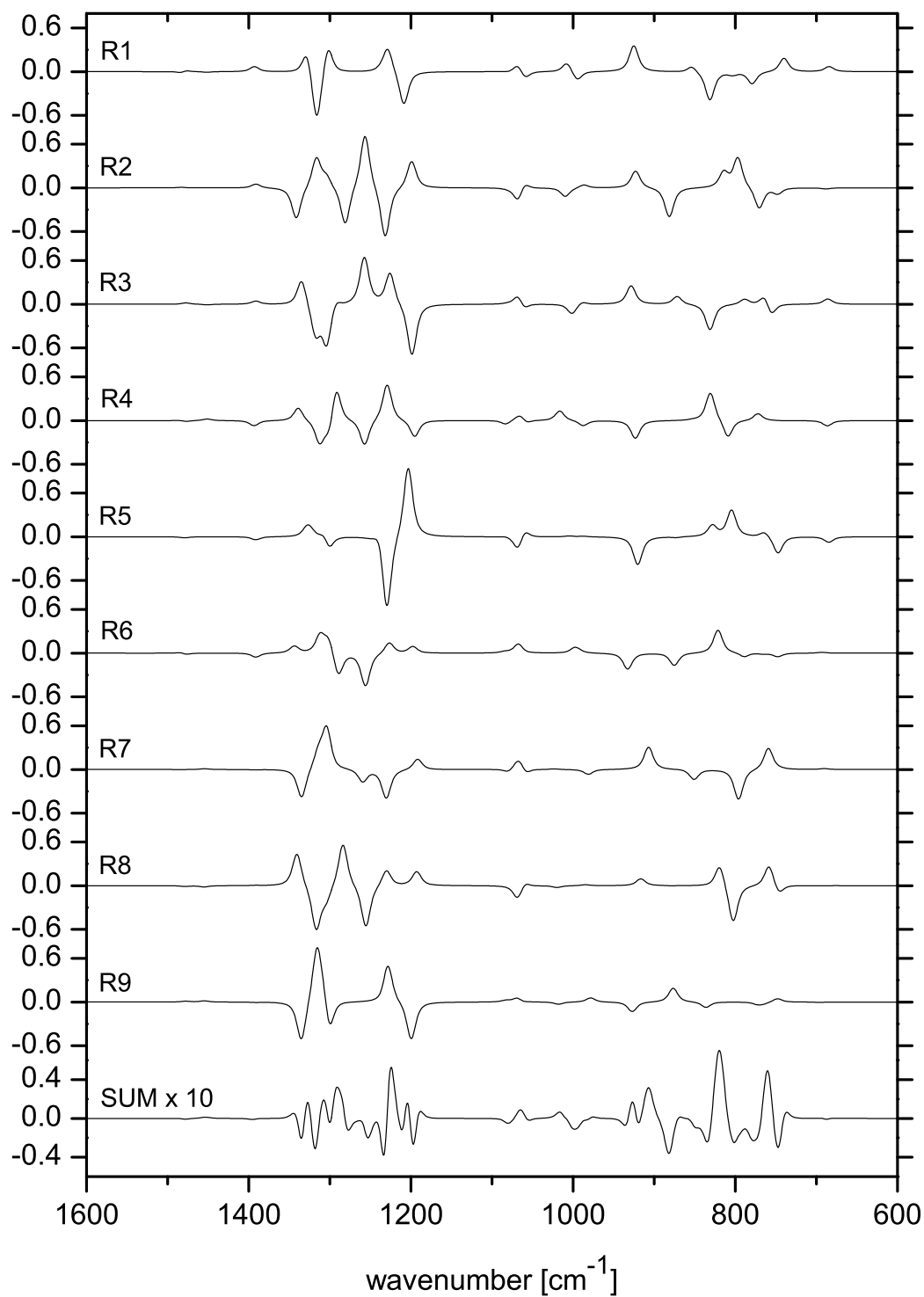


Figure 12.4: Simulated ROA spectra for the 9 rotamers of **2** and 1/9 of the sum of all spectra. Units: [$10^{-19} \text{ \AA}^2 \text{ sr}^{-1} \text{ cm}$]. Computational details: Gaussian03 force field and electronic tensors: DFT/B3PW91/aug-cc-pVDZ.

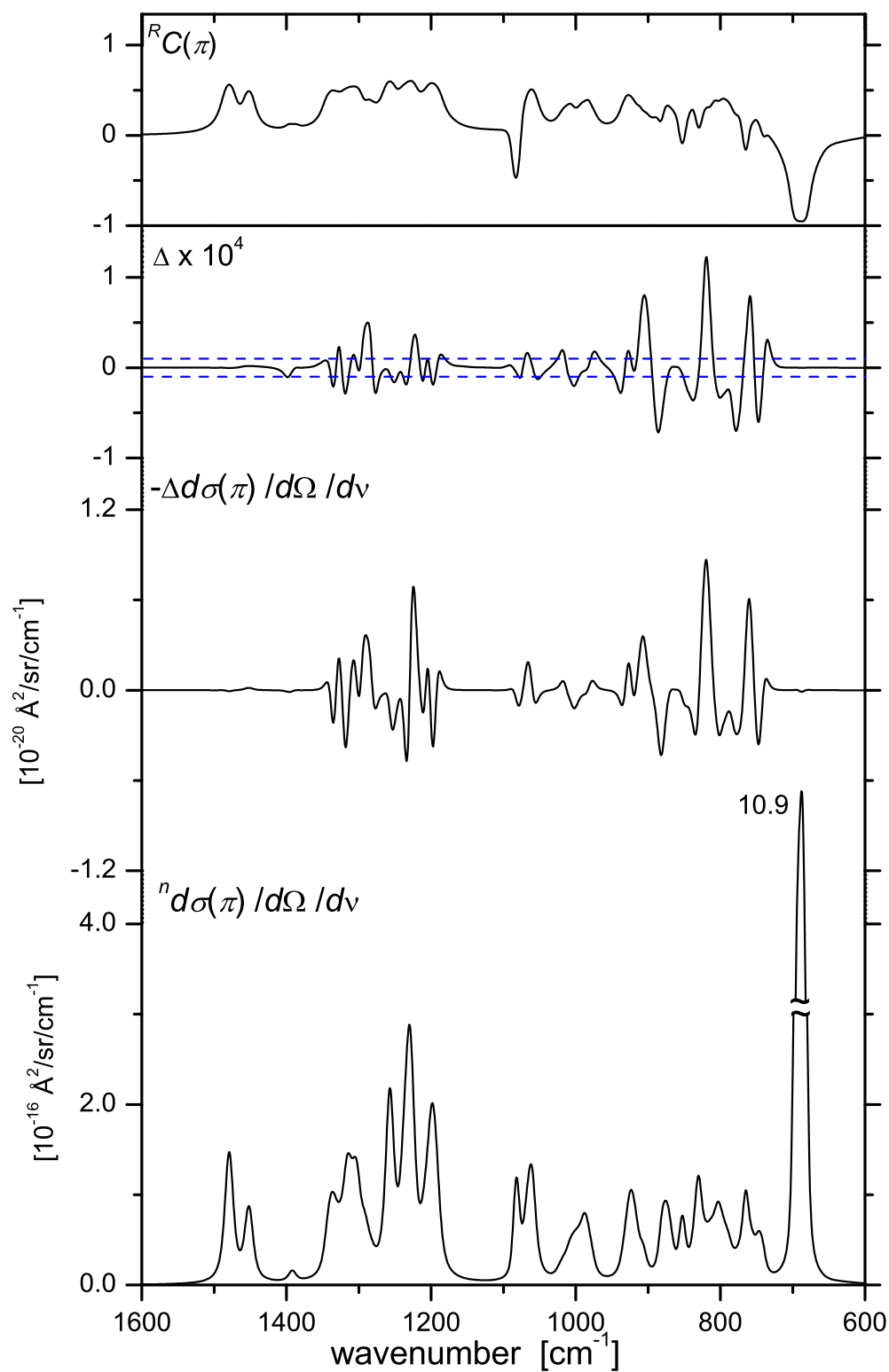


Figure 12.5: DALTON simulated spectra of **2**. Computational details: as in Fig. 12.3. The Δ value has been added for measurability judgement. Doted blue lines indicate our present limits of measurability: $|\Delta| > 10^{-5}$.

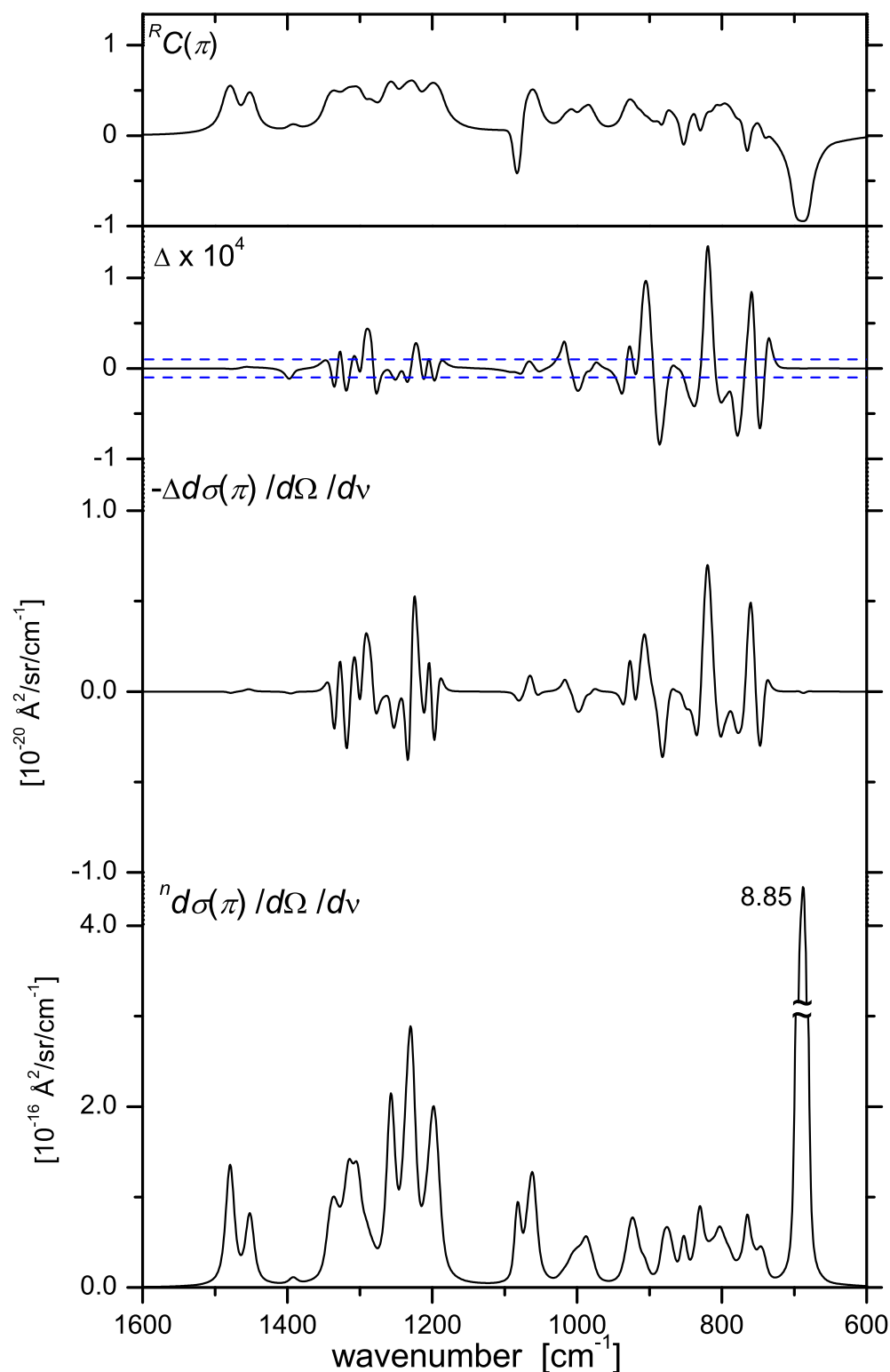


Figure 12.6: Gaussian03 simulated spectra of **2**. Computational details: as in Fig. 12.4. The Δ value has been added for measurability judgement. Doted blue lines indicate our present limits of measurability: $|\Delta| > 10^{-5}$.

Part VI

Appendices

Appendix A

ROA Spectrometer

In this Appendix, a description is given of the way the collected data are saved in the 16 buffers. As our first instrument is located in Zürich, presentation of the 16 buffers for the Fribourg instrument is done in accord with the way it was done for the Zürich instrument, though the buffer's assignment is, for historical reasons, not the same in the two instruments. They are numbered with capital letters, from A to P.

Table A.1: The 16 buffers (A to P) for our instrument in Fribourg.

| Corr. Phase | LCR state | | | |
|-------------|--------------|--------------|--------------|--------------|
| | 0 | 1 | 0 | 1 |
| | ${}^n I_R^A$ | ${}^n I_L^A$ | ${}^n I_L^B$ | ${}^n I_R^B$ |
| [00] | I | B | A | J |
| [01] | K | D | C | L |
| [10] | M | F | E | N |
| [11] | O | H | G | P |

Table A.2: The 16 buffers (A to P) for our instrument in Zürich.

| Corr. Phase | LCR state | | | |
|-------------|-------------|-------------|-------------|-------------|
| | 0 | 1 | 0 | 1 |
| | ${}^nI_R^A$ | ${}^nI_L^A$ | ${}^nI_L^B$ | ${}^nI_R^B$ |
| [00] | A | B | C | D |
| [01] | I | J | K | L |
| [10] | N | M | P | O |
| [11] | F | E | H | G |

Table A.3: Correspondence table for the 16 buffers (A to P) of our instrument in Fribourg and Zürich.

| Symbol | Phase | LCR | Branch | SCPolar. | Buffer | |
|-----------------|-------|-----|--------|----------|--------|----|
| | | | | | FR | ZH |
| ${}^nI_R^A[00]$ | [00] | 0 | A | R | I | A |
| ${}^nI_L^B[00]$ | | | B | L | A | C |
| ${}^nI_R^B[00]$ | | 1 | B | R | J | D |
| ${}^nI_L^A[00]$ | | | A | L | B | B |
| ${}^nI_R^A[01]$ | [01] | 0 | A | R | K | I |
| ${}^nI_L^B[01]$ | | | B | L | C | K |
| ${}^nI_R^B[01]$ | | 1 | B | R | L | L |
| ${}^nI_L^A[01]$ | | | A | L | D | J |
| ${}^nI_R^A[10]$ | [10] | 0 | A | R | M | N |
| ${}^nI_L^B[10]$ | | | B | L | E | P |
| ${}^nI_R^B[10]$ | | 1 | B | R | N | O |
| ${}^nI_L^A[10]$ | | | A | L | F | M |
| ${}^nI_R^A[11]$ | [11] | 0 | A | R | O | F |
| ${}^nI_L^B[11]$ | | | B | L | G | H |
| ${}^nI_R^B[11]$ | | 1 | B | R | P | G |
| ${}^nI_L^A[11]$ | | | A | L | H | E |

Appendix B

Additional Spectra

In this Appendix, additional spectra are illustrated without any comments. They were shifted in the Appendix in order not to overload the Chapters which refer to them.

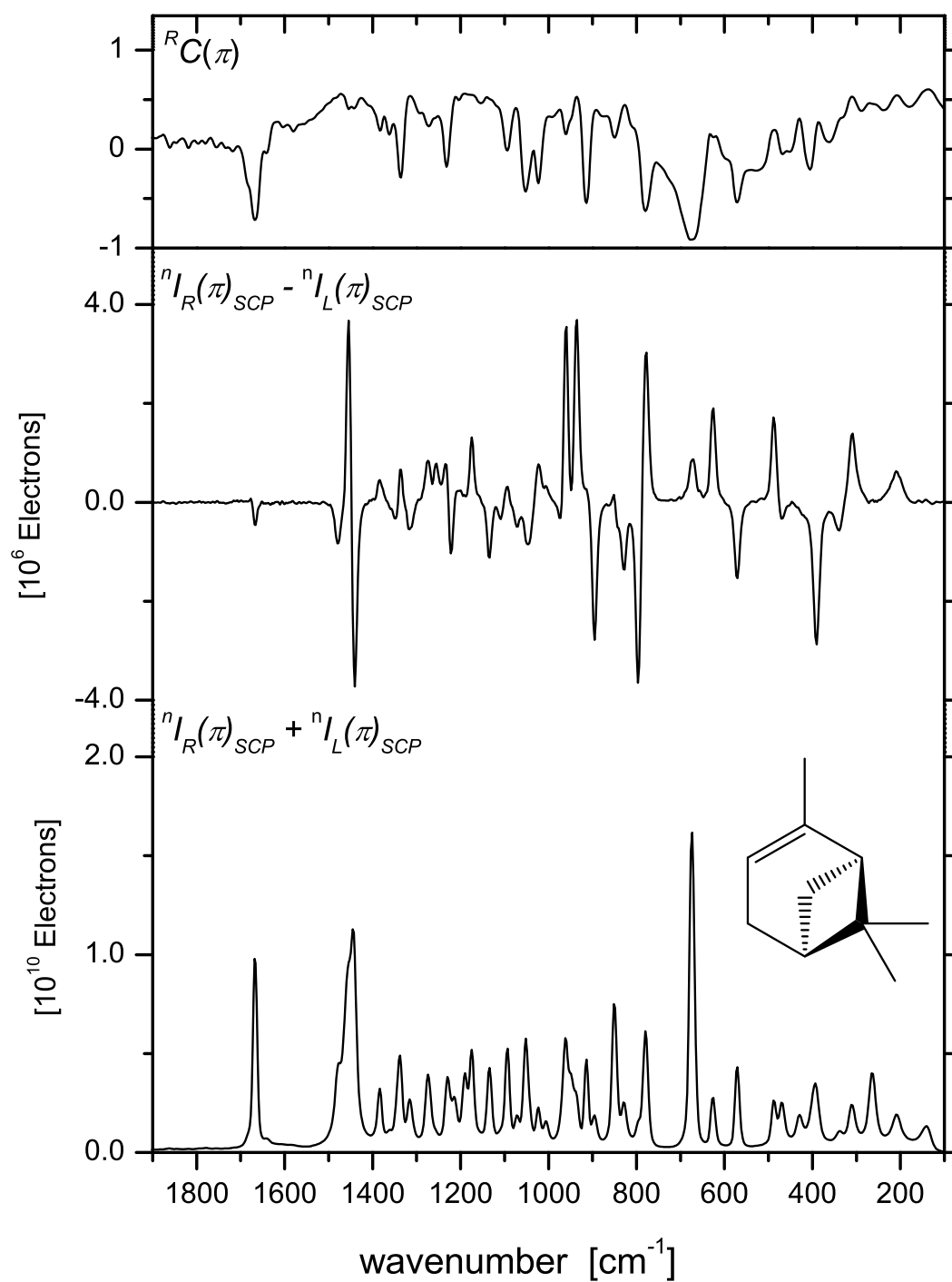


Figure B.1: Backscattering SCP ROA spectra of neat (-)- α -pinene measured in a disposable capillary. Experimental parameters: exciting energy: 360 J (20 min, 300 mW).

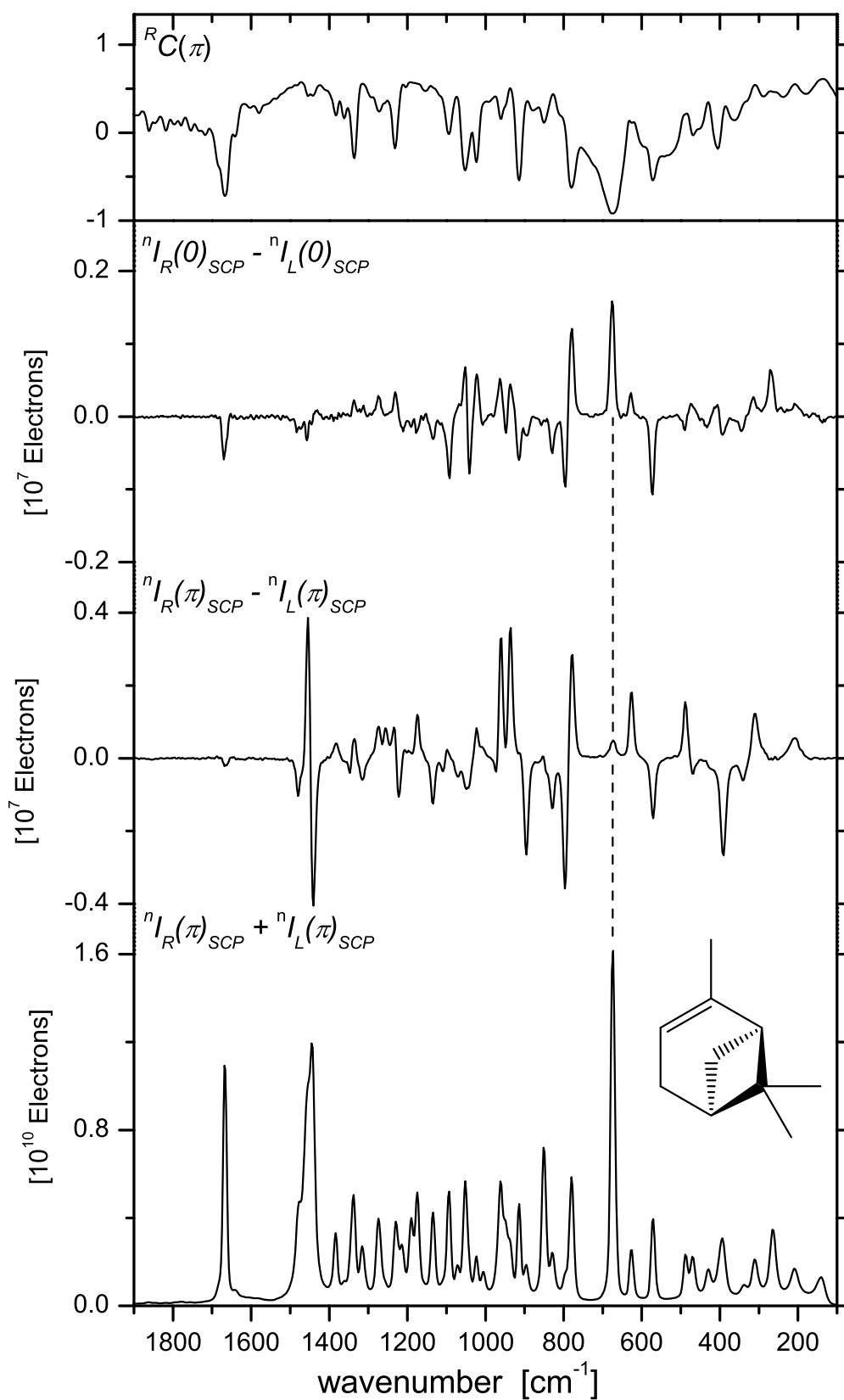


Figure B.2: Forward (top) and backscattering (bottom) SCP ROA spectra of neat (-)- α -pinene measured in our precision cell. Experimental parameters as in Fig. B.1.

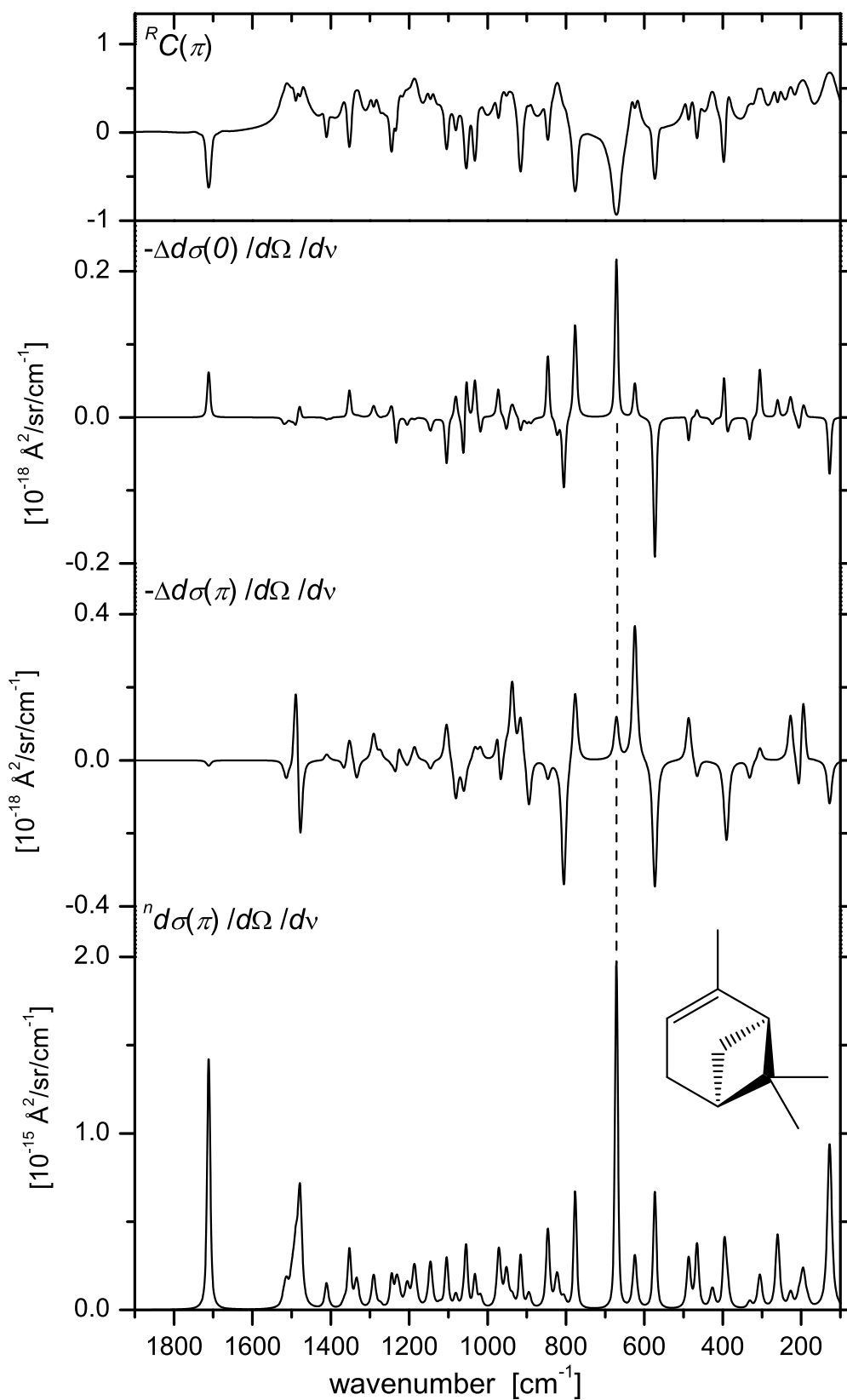


Figure B.3: Simulated forward (top) and backscattering (bottom) SCP ROA spectra of (-)- α -pinene. Computational parameters: force field: B3LYP/6-311++G**, electronic tensors: TDHF/rDPS.

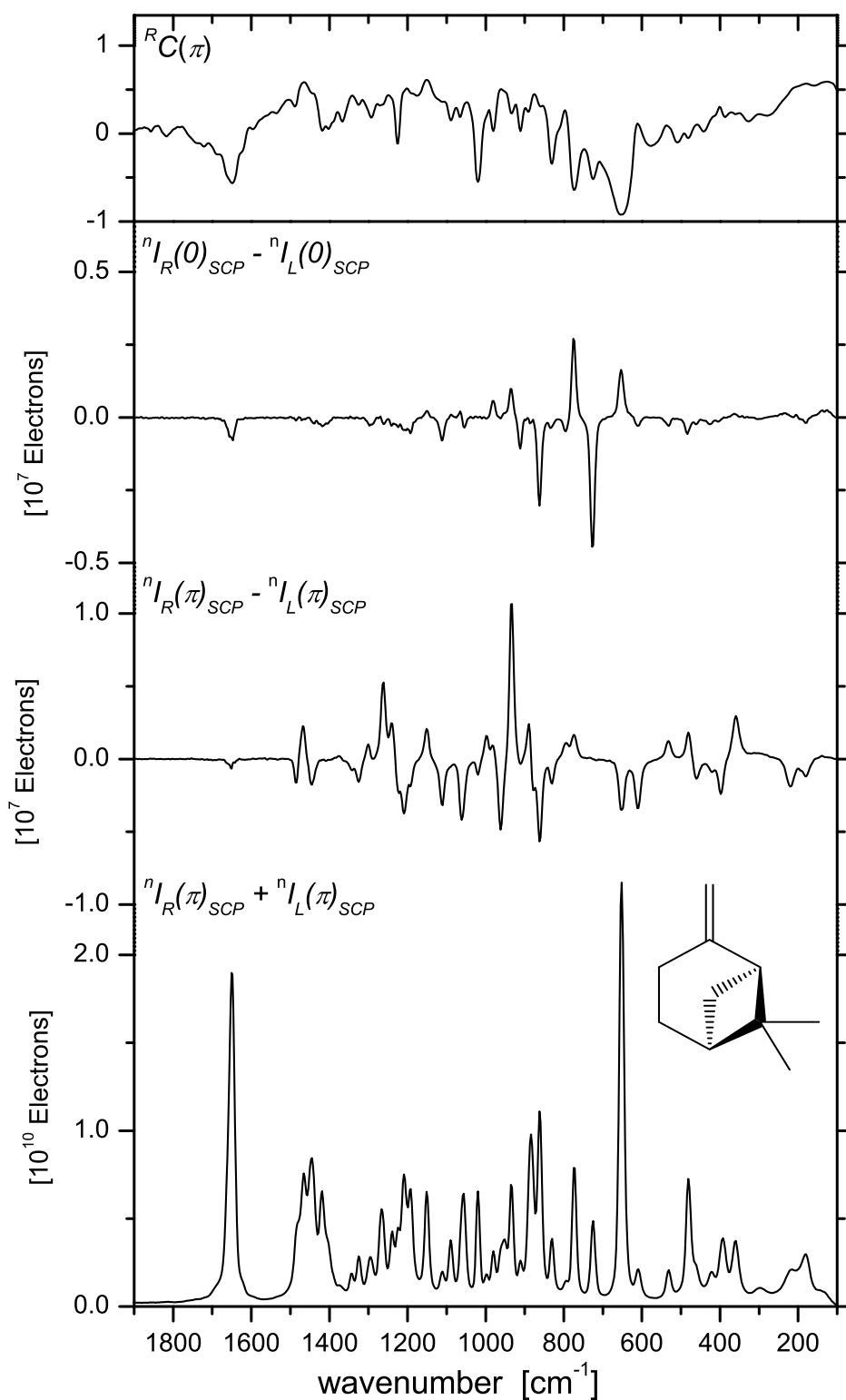


Figure B.4: Forward (top) and backscattering (bottom) SCP ROA spectra of neat (-)-β-pinene measured in disposable capillaries. Experimental parameters: exciting energy: 300 J (20 min, 250 mW).

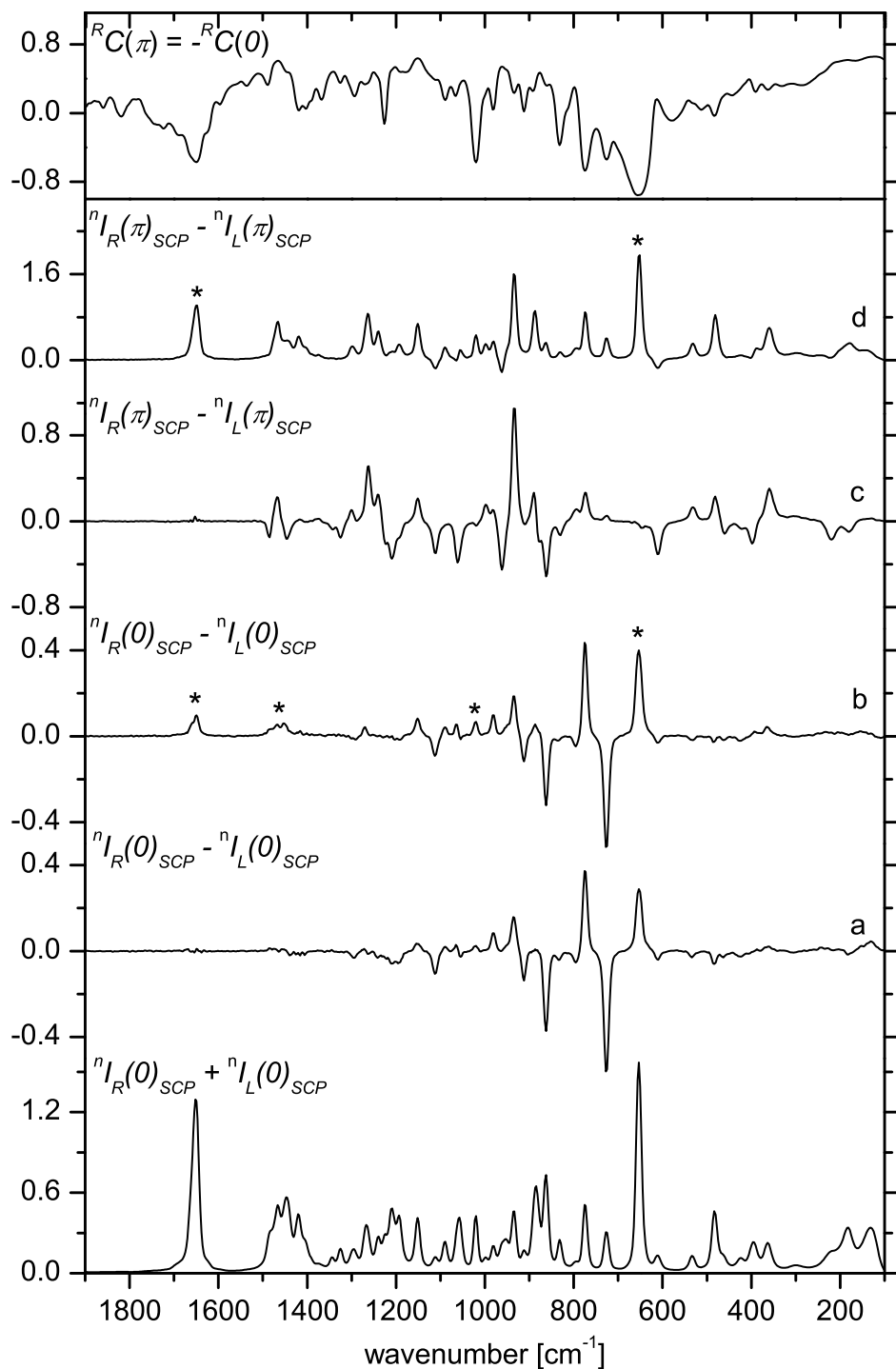


Figure B.5: Influence of back-reflected radiation on ROA spectra of neat (-)- β -pinene. a,c : forward- and backscattering SCP ROA with opposite scattered light dumped. b,d: forward- and backscattering ROA spectra without back-reflection prevention. Experimental parameters as in Fig. 8.10.

Appendix C

VOAView

In this Appendix, a description of the three parsers available in VOAView and the main input and output files is given.

| Parser | Description/Dependencies |
|-------------------------------|-------------------------------------------------------------------------------------------------------------------------------------------------------------------------------------------------------------------------------------------------------------------------------------------------------------------------------------------------------------------------------------------------------------------------------------------------------------------------------------------------------------------------------------------------------------------|
| <code>dal2mol.m</code> : | <ul style="list-style-type: none">- extracts cartesian derivatives of α, G' and A or APTs and AATs, from Dalton ROA and VCD output file (*.out), respectively,- reads equilibrium geometry and molecular hessian from Gaussian formcheck file (*.fchk)- internal vibrational analysis,- saves VOAView input file and other optional files. Dependencies: <code>extgauss2vib.m</code> , <code>get_tensgrad.m</code> , <code>vibana.m</code> , <code>mol_dat.m</code> . |
| <code>gauss2mol.m</code> : | <ul style="list-style-type: none">- extracts cartesian derivatives of α, G' and A or APTs and AATs, from Gaussian Raman, ROA and IR, VCD formcheck file (*.fchk), respectively,- reads equilibrium geometry and molecular hessian,- internal vibrational analysis. Dependencies: <code>extgauss2vib.m</code> , <code>vibana.m</code> , <code>mol_dat.m</code> . |
| <code>allgauss2mol.m</code> : | <ul style="list-style-type: none">- reads equilibrium geometry, cartesian displacement vectors, vibrational frequencies, Raman and ROA molecular invariants or dipole and rotational strength from Gaussian output file (*.out). Dependencies: <code>extgauss2mol_G.m</code> , <code>mol_dat.m</code> . |

VOAView's input file `*.voa`, which consists of a simple 3 columns array of data organised as illustrated below, where the `*` is the generic file name. `Natom` is the number of atom and `Nfreq` is the number of vibrational modes.

| | 1 | 2 | 3 | |
|----------------------------|-------------------------------------------------------------------------------------------------------------------------------------------------------------------------------------------------------------------------------|-------|---|-------------|
| 1 | Natom | NFreq | 0 | 1 |
| 2 | Atomic Masses | 0 | 0 | Natom |
| Natom+2 | Cartesian Coordinates [Å] $r_{\alpha x}$ $r_{\alpha y}$ $r_{\alpha z}$ | | | Natom |
| 2*Natom+2 | Wave- numbers [cm ⁻¹] | 0 | 0 | NFreq |
| 2*Natom+2+Nfreq | Cartesian displacements vectors [a.u] $L_{\alpha x,p}^x$ $L_{\alpha y,p}^x$ $L_{\alpha z,p}^x$ | | | Natom*NFreq |
| 2*Natom+2+(Natom+1)*Nfreq | Gradients of α [a.u] $\frac{\partial \alpha_{\mu\nu}^e}{\partial x_x^\alpha}$ $\frac{\partial \alpha_{\mu\nu}^e}{\partial x_y^\alpha}$ $\frac{\partial \alpha_{\mu\nu}^e}{\partial x_z^\alpha}$ | | | 9*Natom |
| 11*Natom+2+(Natom+1)*Nfreq | Gradients of G' [a.u] $\frac{\partial G_{\mu\nu}^{'e}}{\partial x_x^\alpha}$ $\frac{\partial G_{\mu\nu}^{'e}}{\partial x_y^\alpha}$ $\frac{\partial G_{\mu\nu}^{'e}}{\partial x_z^\alpha}$ | | | 9*Natom |
| 20*Natom+2+(Natom+1)*Nfreq | Gradients of \mathcal{A} [a.u] $\frac{\partial \mathcal{A}_{\mu\nu}^e}{\partial x_x^\alpha}$ $\frac{\partial \mathcal{A}_{\mu\nu}^e}{\partial x_y^\alpha}$ $\frac{\partial \mathcal{A}_{\mu\nu}^e}{\partial x_z^\alpha}$ | | | 9*Natom |
| 29*Natom+1+(Natom+1)*Nfreq | | | | |

Reduced invariants $J_{\alpha\beta,p}$ (Eq. 4.5) multiplied by $\langle f_v|Q_p|i_v\rangle^2 K_p$ are saved in a file INVAR_*.dat:

| | Natom | Natom | Natom | Natom | Natom | |
|-------------|-----------------------|---------------------------|-----------------------|----------------------------|----------------------------|-------|
| 1 | $a_{\alpha\beta,1}^2$ | $\beta_{\alpha\beta,1}^2$ | $aG'_{\alpha\beta,1}$ | $\beta_{G\alpha\beta,1}^2$ | $\beta_{A\alpha\beta,1}^2$ | Natom |
| 1*Natom+1 | $a_{\alpha\beta,2}^2$ | $\beta_{\alpha\beta,2}^2$ | $aG'_{\alpha\beta,2}$ | $\beta_{G\alpha\beta,2}^2$ | $\beta_{A\alpha\beta,2}^2$ | Natom |
| 2*Natom+1 | $a_{\alpha\beta,3}^2$ | $\beta_{\alpha\beta,3}^2$ | $aG'_{\alpha\beta,3}$ | $\beta_{G\alpha\beta,3}^2$ | $\beta_{A\alpha\beta,3}^2$ | Natom |
| 3*Natom+1 | ... | ... | ... | ... | ... | Natom |
| Nfreq*Natom | | | | | | |
| 5*Natom | | | | | | |

Molecular invariants \mathfrak{I}_p (Eq. 4.6) multiplied by K_p are saved in a file INVARsum_*.dat:

| | 1 | 1 | 1 | 1 | 1 | |
|-------|---------|-------------|---------|----------------|----------------|---|
| 1 | a_1^2 | β_1^2 | aG'_1 | β_{G1}^2 | β_{A1}^2 | 1 |
| 2 | a_2^2 | β_2^2 | aG'_2 | β_{G2}^2 | β_{A2}^2 | 1 |
| 3 | a_3^2 | β_3^2 | aG'_3 | β_{G3}^2 | β_{A3}^2 | 1 |
| 4 | ... | ... | ... | ... | ... | 1 |
| Nfreq | | | | | | |
| 5 | | | | | | |

are saved in a file `INVARpond_*.dat`:

5

and antisymmetric part are saved in a file `INVARdec_*.dat`:

15*Natom

Spectra generated by VOAPlot are saved in a file `Fit[X]*.dat`, where `X` represents the kind of simulated spectra: `X=1` corresponds to SCP backscattering, `X=2` to SCP forward scattering, and so on (according to VOAPlot's scroll menu):

Diagram illustrating a 1D lattice structure with 8 sites. The lattice is divided into two horizontal regions, 'range1' (top) and 'range2' (bottom). The sites are labeled with symbols: \tilde{v} , $d\sigma$, $-\Delta d\sigma$, RC , Δ , ρ_{\perp} , and $|\Delta d\sigma|$. Above the lattice, there are seven '1' labels centered over each of the first seven sites. A '1' label is also present to the right of the lattice, aligned with the middle of the second site. Below the lattice, a '5' label is centered under the fourth site.

The computed cartesian derivatives of α and \mathbf{G}' obtained in DALTON are saved in the output file in the same way, with dA1x meaning derivative with respect to x for atom number 1:

Derivatives of α and \mathbf{G}' (DALTON and Gaussian03)

| | | | | |
|----------|----------|----------|----------|----------|
| xx/dA1x | yx/dA1x | zx/dA1x | xy/dA1x | yy/dA1x |
| zy/dA1x | xz/dA1x | yz/dA1x | zz/dA1x | xx/dA1y |
| yx/dA1y | zx/dA1y | xy/dA1y | yy/dA1y | zy/dA1y |
| xz/dA1y | yz/dA1y | zz/dA1y | xx/dA1z | yx/dA1z |
| zx/dA1z | xy/dA1z | yy/dA1z | zy/dA1z | xz/dA1z |
| yz/dA1z | zz/dA1z | xx/dA2x | yx/dA2x | zx/dA2x |
| \vdots | \vdots | \vdots | \vdots | \vdots |

The computed cartesian derivatives of α obtained in Gaussian03¹ are saved in the formatted checkpoint file in a different way compared to what is done in DALTON. Gaussian03 evaluates the derivatives of \mathbf{G}' in the same way than for α , but prints $c_0^{1/2} \mathbf{G}'$ in the output file, where c_0 is the speed of light:

Derivatives of α and \mathbf{G}' (DALTON and Gaussian03)

| | | | | |
|----------|----------|----------|----------|----------|
| xx/dA1x | xy/dA1x | xz/dA1x | yx/dA1x | yy/dA1x |
| yz/dA1x | zx/dA1x | zy/dA1x | zz/dA1x | xx/dA1y |
| xy/dA1y | xz/dA1y | yx/dA1y | yy/dA1y | yz/dA1y |
| zx/dA1y | zy/dA1y | zz/dA1y | xx/dA1z | xy/dA1z |
| xz/dA1z | yx/dA1z | yy/dA1z | yz/dA1z | zx/dA1z |
| zy/dA1z | zz/dA1z | xx/dA2x | xy/dA2x | xz/dA2x |
| \vdots | \vdots | \vdots | \vdots | \vdots |

¹According to a private communication from James Cheesman (Gaussian03).

The computed cartesian derivatives of **A** obtained in DALTON and Gaussian03 are saved in their respective output files in different ways:

Derivatives of **A** (DALTON)

| | | | | |
|-----------|-----------|-----------|-----------|-----------|
| x,xx/dA1x | x,xx/dA1y | x,xx/dA1z | x,xx/dA2x | x,xx/dA2y |
| y,xx/dA1x | y,xx/dA1y | y,xx/dA1z | y,xx/dA2x | y,xx/dA2y |
| z,xx/dA1x | z,xx/dA1y | z,xx/dA1z | z,xx/dA2x | z,xx/dA2y |
| x,yx/dA1x | x,yx/dA1y | x,yx/dA1z | x,yx/dA2x | x,yx/dA2y |
| y,yx/dA1x | y,yx/dA1y | y,yx/dA1z | y,yx/dA2x | y,yx/dA2y |
| z,yx/dA1x | z,yx/dA1y | z,yx/dA1z | z,yx/dA2x | z,yx/dA2y |
| x,zx/dA1x | x,zx/dA1y | x,zx/dA1z | x,zx/dA2x | x,zx/dA2y |
| y,zx/dA1x | y,zx/dA1y | y,zx/dA1z | y,zx/dA2x | y,zx/dA2y |
| z,zx/dA1x | z,zx/dA1y | z,zx/dA1z | z,zx/dA2x | z,zx/dA2y |
| x,xy/dA1x | x,xy/dA1y | x,xy/dA1z | x,xy/dA2x | x,xy/dA2y |
| y,xy/dA1x | y,xy/dA1y | y,xy/dA1z | y,xy/dA2x | y,xy/dA2y |
| z,xy/dA1x | z,xy/dA1y | z,xy/dA1z | z,xy/dA2x | z,xy/dA2y |
| x,yy/dA1x | x,yy/dA1y | x,yy/dA1z | x,yy/dA2x | x,yy/dA2y |
| y,yy/dA1x | y,yy/dA1y | y,yy/dA1z | y,yy/dA2x | y,yy/dA2y |
| z,yy/dA1x | z,yy/dA1y | z,yy/dA1z | z,yy/dA2x | z,yy/dA2y |
| x,zy/dA1x | x,zy/dA1y | x,zy/dA1z | x,zy/dA2x | x,zy/dA2y |
| y,zy/dA1x | y,zy/dA1y | y,zy/dA1z | y,zy/dA2x | y,zy/dA2y |
| z,zy/dA1x | z,zy/dA1y | z,zy/dA1z | z,zy/dA2x | z,zy/dA2y |
| x,xz/dA1x | x,xz/dA1y | x,xz/dA1z | x,xz/dA2x | x,xz/dA2y |
| y,xz/dA1x | y,xz/dA1y | y,xz/dA1z | y,xz/dA2x | y,xz/dA2y |
| z,xz/dA1x | z,xz/dA1y | z,xz/dA1z | z,xz/dA2x | z,xz/dA2y |
| x,yz/dA1x | x,yz/dA1y | x,yz/dA1z | x,yz/dA2x | x,yz/dA2y |
| y,yz/dA1x | y,yz/dA1y | y,yz/dA1z | y,yz/dA2x | y,yz/dA2y |
| z,yz/dA1x | z,yz/dA1y | z,yz/dA1z | z,yz/dA2x | z,yz/dA2y |
| x,zz/dA1x | x,zz/dA1y | x,zz/dA1z | x,zz/dA2x | x,zz/dA2y |
| y,zz/dA1x | y,zz/dA1y | y,zz/dA1z | y,zz/dA2x | y,zz/dA2y |
| z,zz/dA1x | z,zz/dA1y | z,zz/dA1z | z,zz/dA2x | z,zz/dA2y |
| ⋮ | ⋮ | ⋮ | ⋮ | ⋮ |

Gaussian03 uses a different definition of \mathbf{A} , which differs from that used in DALTON by a factor of $3/2$ [140]².

Derivatives of \mathbf{A} (Gaussian03).

| | | | | |
|-----------|-----------|-----------|-----------|-----------|
| xx,x/dA1x | yy,x/dA1x | zz,x/dA1x | xy,x/dA1x | xz,x/dA1x |
| yz,x/dA1x | xx,y/dA1x | yy,y/dA1x | zz,y/dA1x | xy,y/dA1x |
| xz,y/dA1x | yz,y/dA1x | xx,z/dA1x | yy,z/dA1x | zz,z/dA1x |
| xy,z/dA1x | xz,z/dA1x | yz,z/dA1x | xx,x/dA1y | yy,x/dA1y |
| zz,x/dA1y | xy,x/dA1y | xz,x/dA1y | yz,x/dA1y | xx,y/dA1y |
| yy,y/dA1y | zz,y/dA1y | xy,y/dA1y | xz,y/dA1y | yz,y/dA1y |
| xx,z/dA1y | yy,z/dA1y | zz,z/dA1y | xy,z/dA1y | xz,z/dA1y |
| yz,z/dA1y | xx,x/dA1z | yy,x/dA1z | zz,x/dA1z | xy,x/dA1z |
| xz,x/dA1z | yz,x/dA1z | xx,y/dA1z | yy,y/dA1z | zz,y/dA1z |
| xy,y/dA1z | xz,y/dA1z | yz,y/dA1z | xx,z/dA1z | yy,z/dA1z |
| zz,z/dA1z | xy,z/dA1z | xz,z/dA1z | yz,z/dA1z | xx,x/dA2x |
| yy,x/dA2x | zz,x/dA2x | xy,x/dA2x | xz,x/dA2x | yz,x/dA2x |
| ⋮ | ⋮ | ⋮ | ⋮ | ⋮ |

²Thanks to Dr. Gérard Zuber for pointing out this differing definition.

Appendix D

Computations

This Appendix shows typical input files used in our computations of neopentane. A detailed description of the 2 files used within DALTON can be found in the thesis of Dr. Gérard Zuber [112].

***.mol file (DALTON):**

```
BASIS
aug-cc-pVDZ
This is just a dummy MOLECULE.INP file that can be used
as a starting point when the Hessian is read in.
  2   0 0
    6.   5
C001    0.0000000000    0.0000000000    0.0000000000
C002    1.6796233000    1.6796233000    1.6796233000
C003   -1.6796233000   -1.6796233000    1.6796233000
C004    1.6796233000   -1.6796233000   -1.6796233000
C005   -1.6796233000    1.6796233000   -1.6796233000
    1.   12
H006    2.8981589900    2.8981589900    0.5352665680
H007    0.5352665680    2.8981589900    2.8981589900
H008    2.8981589900    0.5352665680    2.8981589900
H009   -2.8981589900   -2.8981589900    0.5352665680
H010   -2.8981589900   -0.5352665680    2.8981589900
H011   -0.5352665680   -2.8981589900    2.8981589900
H012    2.8981589900   -2.8981589900   -0.5352665680
H013    0.5352665680   -2.8981589900   -2.8981589900
H014    2.8981589900   -0.5352665680   -2.8981589900
H015   -2.8981589900    2.8981589900   -0.5352665680
H016   -2.8981589900    0.5352665680   -2.8981589900
H017   -0.5352665680    2.8981589900   -2.8981589900
```

*.dal file (DALTON):

```

**GENERAL
.RUN PROPERTIES
.WALK
.MAX IT
  200
*WALK
.NUMERI
.PRINT
  1
.DISPLA
  0.001
**WAVE FUNCTIONS
.HF
**INTEGRALS
.NOSUP
*END OF INTEGRALS
*END OF WAVEFUNCTION
**START
.QUADRU
.VROA
.ABALNR
*ABALNR
.THRLNR
1.0D-8
.FREQUE
  1
0.08564539532
**PROPERTIES
.VROA
.ABALNR
*ABALNR
.THRLNR
1.0D-8
.FREQUE
  1
0.08564539532
**FINAL
.VROA
.ABALNR
*RESPON
.THRESH
1.0D-6
*ABALNR
.THRLNR
1.0D-8
.FREQUE
  1
0.08564539532
*END OF INPUT

```

The computation of ROA within Gaussian03 is divided in two parts, a geometry optimisation and a frequency calculation where the derivatives of the dynamic polarisability tensors are evaluated for the exciting laser wavelength (532 nm):

```
$RUNGAUSS
%mem=20MW
%chk=groa_pw_augDZ_neo
%nproc=2
#B3PW91/aug-cc-pVDZ opt test

neopentane

0 1
C 0.000000 0.000000 0.000000
C -0.889032 -0.889032 0.889032
C 0.889032 0.889032 0.889032
C -0.889032 0.889032 -0.889032
C 0.889032 -0.889032 -0.889032
H -1.536209 -1.536209 0.279167
H -0.279167 -1.536209 1.536209
H -1.536209 -0.279167 1.536209
H 1.536209 1.536209 0.279167
H 1.536209 0.279167 1.536209
H 0.279167 1.536209 1.536209
H -1.536209 1.536209 -0.279167
H -0.279167 1.536209 -1.536209
H -1.536209 0.279167 -1.536209
H 1.536209 -1.536209 -0.279167
H 1.536209 -0.279167 -1.536209
H 0.279167 -1.536209 -1.536209

--link1--
%mem=20MW
%nproc=2
%chk=groa_pw_augDZ_neo
#B3PW91/aug-cc-pVDZ freq=ROA cphf=rdfreq Geom=AllCheck Test

532nm
```


Appendix E

DALTON vs. Gaussian03

Pilot calculations of ROA have been realised in order to assess the reliability of the code implemented in Gaussian03 rev. C.01. The well known (*R*)-(+)-methyloxirane or (*R*)-(+)-propylene oxide has been chosen in this respect. The ROA spectrum obtained within Gaussian03 (trial) at the low HF/6-31G* level of theory is compared to the spectrum obtained with the same level of theory in DALTON (reference).

Fig. [E.1](#) shows that the ROA spectra obtained with both program are close to identical. The spectrum obtained by calculating the difference between the trial and reference spectra, which is two orders of magnitude smaller, is also illustrated. From these results, one can consider the Gaussian03 data as reliable.

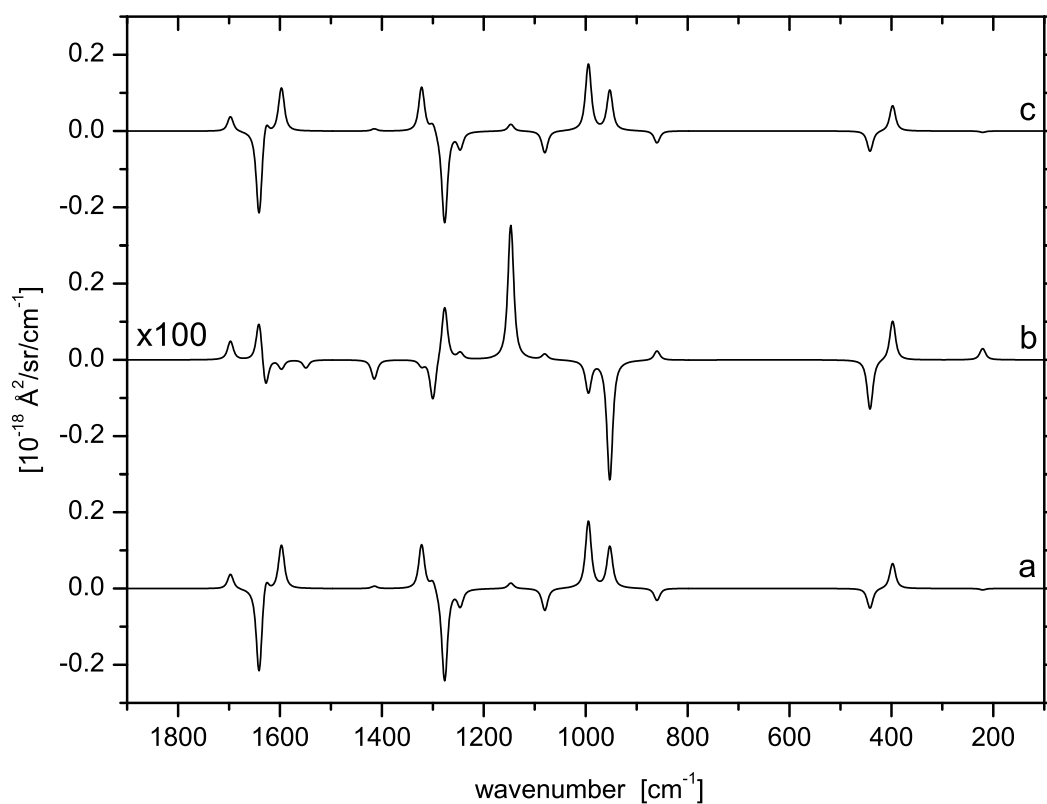


Figure E.1: Simulated ROA spectra of (*R*)-(+)-methyloxirane calculated with DALTON (a) and Gaussian03 (c). The difference spectrum between the trial and reference spectra is drawn in the middle and arises from numerical precision differences (b). Computational details: force field and electronic tensors: HF/6-31G*.

Conclusion and Outlook

The work done during this thesis covers a large spectrum of areas within the field of vibrational optical activity, and in particular ROA, from experiments to *ab initio* simulations, and their interpretations.

A novel spectrometer has been built, based on an existing reference instrument, which offers the possibility to measure ROA in SCP(π), and for the very first time also in the corresponding forward scattering scheme SCP(0). The resulting backscattering ROA spectra are reliable and of high quality, as has been proven by comparing them with data recorded on the reference spectrometer based in Zürich. The quality of the first SCP(0) ROA spectra has been compared with the only forward scattering spectrum published so far, for (-)- β -pinene, and recorded in ICP(0). The signal-to-noise ratio we obtain in our experiment is far better. The main features of these spectra are well reproduced, and a measurement mistake could be pointed out thanks to the comparison with *ab initio* simulations. A strong forward scattering ROA band has been observed for the methylene twist vibrational motion. Further measurements are being recorded to confirm this typical signal, like those of (M)-(-)-1,4-dimethylenespiropentane.

Forward scattering has been measured for the first time for biologically relevant compounds such as vitamin C or L-alanine in aqueous solutions. The recorded spectra are of very good quality, and it seems that ROA is less sensitive to the nature of the solvent when measured in forward scattering. This feature must be confirmed by measuring other compounds and by varying their

concentrations, as well as by ROA computations where the influence of solvent molecules is explicitly taken into account.

VOAView, a program with a graphical interface for the interpretation of experimental and computational VOA data, which incorporates previously but also newly developed graphical tools, has been written in Matlab. The interpretation of VOA data is now easier and more accessible. The development of a similar open source program called PyVib2, which takes advantage of the effort done for VOAView, is in progress.

(*R*)-[$^2\text{H}_1$, $^2\text{H}_2$, $^2\text{H}_3$]-neopentane, with a chiral distribution of the mass of its nuclei, obtained by isotopic substitution, has been theoretically analysed in order to assess its VOA measurability. It was found that ROA is the only method by which the absolute configuration of this compound could be determined, and that our newly developed instrument should be capable of meeting this challenge. We hope to be able to confirm this prediction with real measurements of that interesting compound, whose synthesis is still not achieved. In the mean time, Raman measurements of 2,2-dimethylpropane (neopentane) and its fully deuterated form have been performed in order to be able to correlate the vibrational spectra of all three compounds. Thanks to the implementation of temperature control, the Raman and ROA spectra could be recorded at 0°C, a temperature where neopentane is liquid, with acceptable offsets. We are therefore confident that it will be possible to measure (*R*)-[$^2\text{H}_1$, $^2\text{H}_2$, $^2\text{H}_3$]-neopentane, once it becomes available.

With the development made during this thesis, forward scattering ROA will certainly become widely used as a complementary technique to its backward scattering variety. With the advent of accessible graphical interpretation tools, ROA may finally be considered as a very powerful and reliable spectroscopic technique for the determination of the absolute configuration as well as for conformational analysis.

References

- [1] W. H. Thomson, (1884); see Lord Kelvin, *Baltimore Lectures*, London, C. J. Clay and Sons (1904), p. 436 and 619.
- [2] F. Arago, Mém. Classe Sci. Math. Phys. Inst. Impér. France **12I**, 93 (1811).
- [3] J. B. Biot, Ann. Chim. Phys., II **4**, 90 (1817).
- [4] A. Fresnel, Ann. Chim. **28**, 147 (1825).
- [5] J. H. van't Hoff, Bull. soc. chim. France **23**, 295 (1875).
- [6] J. A. Le Bel, Bull. soc. chim. France **22**, 337 (1874).
- [7] A. Kekule, Ann. **106**, 154 (1858).
- [8] R. S. Cahn, C. K. Ingold, and V. Prelog, Tetrahedron **1**, 119 (1961).
- [9] D. A. Long, *The Raman Effect* (John Wiley & Sons Ltd, Chichester, 2002).
- [10] L. D. Barron and A. D. Buckingham, Mol. Phys. **20**, 1111 (1971).
- [11] G. S. Yu and L. A. Nafie, Chem. Phys. Lett. **222**, 403 (1994).
- [12] L. A. Nafie, Annu. Rev. Phys. Chem. **48**, 357 (1997).
- [13] International Union of Pure Applied Chemistry; URL: <http://www.iupac.org/>.

- [14] L. D. Barron and A. D. Buckingham, *J. Am. Chem. Soc.* **96**, 4769 (1974).
- [15] L. D. Barron, in *Optical Activity and Chiral Discrimination*, edited by S.F. Mason (D. Reidel Publishing Company, Dordrecht, 1979).
- [16] L. D. Barron, *Molecular Light Scattering and Optical Activity* (Cambridge University Press, Cambridge, 1982).
- [17] P. L. Polavarapu, *J. Phys. Chem.* **94**, 8106 (1990).
- [18] P. K. Bose, L. D. Barron, and P. L. Polavarapu, *Chem. Phys. Lett.* **155**, 423 (1989).
- [19] P. K. Bose, P. L. Polavarapu, L. D. Barron, and L. Hecht, *J. Phys. Chem.* **94**, 1734 (1990).
- [20] P. L. Polavarapu, L. Hecht, and L. D. Barron, *J. Phys. Chem.* **97**, 1793 (1993).
- [21] P. Bouř, C. N. Tam, M. Shaharuzzaman, J. S. Chickos, and T. A. Keiderling, *J. Phys. Chem.* **100**, 15041 (1996).
- [22] P. Bouř, V. Baumruk, and J. Hanzlíková, *Collect. Czech. Chem. Commun.* **62**, 1384 (1997).
- [23] G. Zuber and W. Hug, *Helv. Chim. Acta* **87**, 2208 (2004).
- [24] T. H. Dunning, *J. Chem. Phys.* **90**, 1007 (1989).
- [25] A. J. Sadlej, *Collec. Czec. Chem. Commun.* **53**, 1995 (1988).
- [26] DALTON, a molecular electronic structure program, Release 2.0 (2005); see <http://www.kjemi.uio.no/software/DALTON/DALTON.html>.
- [27] M. J. Frisch, G. W. Trucks, H. B. Schlegel, G. E. Scuseria, M. A. Robb, J. R. Cheeseman, J. A. Montgomery, Jr., T. Vreven, K. N. Kudin, J. C.

- Burant, J. M. Millam, S. S. Iyengar, J. Tomasi, V. Barone, B. Mennucci, M. Cossi, G. Scalmani, N. Rega, G. A. Petersson, H. Nakatsuji, M. Hada, M. Ehara, K. Toyota, R. Fukuda, J. Hasegawa, M. Ishida, T. Nakajima, Y. Honda, O. Kitao, H. Nakai, M. Klene, X. Li, J. E. Knox, H. P. Hratchian, J. B. Cross, V. Bakken, C. Adamo, J. Jaramillo, R. Gomperts, R. E. Stratmann, O. Yazyev, A. J. Austin, R. Cammi, C. Pomelli, J. W. Ochterski, P. Y. Ayala, K. Morokuma, G. A. Voth, P. Salvador, J. J. Dannenberg, V. G. Zakrzewski, S. Dapprich, A. D. Daniels, M. C. Strain, O. Farkas, D. K. Malick, A. D. Rabuck, K. Raghavachari, J. B. Foresman, J. V. Ortiz, Q. Cui, A. G. Baboul, S. Clifford, J. Cioslowski, B. B. Stefanov, G. Liu, A. Liashenko, P. Piskorz, I. Komaromi, R. L. Martin, D. J. Fox, T. Keith, M. A. Al-Laham, C. Y. Peng, A. Nanayakkara, M. Challacombe, P. M. W. Gill, B. Johnson, W. Chen, M. W. Wong, C. Gonzalez, and J. A. Pople, Gaussian 03, Revision C.01, Gaussian, Inc., Wallingford, CT, 2004.
- [28] A. Cotton, *Ann. Chim. Phys.*, VII **8**, 347 (1896).
- [29] K. J. Jalkanen, R. M. Nieminen, K. Frimand, J. Bohr, H. Bohr, R. C. Wade, E. Tajkhorshid, and S. Suhai, *Chem. Phys.* **65**, 125 (2001).
- [30] S. Abdali, K. J. Jalkanen, H. Bohr, S. Suhai, and S. Nieminen, *Chem. Phys.* **282**, 219 (2002).
- [31] P. L. Polavarapu and Z. Deng, *Faraday Discuss.* **99**, 151 (1994).
- [32] Z. Deng, P. L. Polavarapu, S. J. Ford, L. Hecht, L. D. Barron, C. S. Ewig, and K. J. Jalkanen, *J. Phys. Chem.* **100**, 2025 (1996).
- [33] W.-G. Han, K. J. Jalkanen, M. Elstner, and S. Suhai, *J. Phys. Chem. B* **102**, 2587 (1998).
- [34] S. J. Ford, Z. Q. Wen, L. Hecht, and L. D. Barron, *Biopolymers* **34**, 303 (1994).

- [35] G. Wilson, L. Hecht, and L. D. Barron, *J. Chem. Soc. Faraday Trans.* **92**, 1503 (1996).
- [36] S. J. Ford, A. Cooper, L. Hecht, G. Wilson, and L. D. Barron, *J. Chem. Soc. Faraday Trans.* **91**, 2087 (1995).
- [37] G. Wilson, L. Hecht, and L. D. Barron, *J. Phys. Chem. B* **101**, 694 (1997).
- [38] I. H. McColl, E. W. Blanch, A. C. Gill, A. G. O. Rhie, M. A. Ritchie, L. Hecht, K. Nielsen, and L. D. Barron, *J. Am. Chem. Soc.* **125**, 10019 (2003).
- [39] F. Zhu, N. Isaacs, L. Hecht, and L. D. Barron, *Structure* **13**, 1409 (2005).
- [40] E. W. Blanch, L. Hecht, and L. D. Barron, *Methods* **29**, 196 (2003).
- [41] E. W. Blanch, D. J. Robinson, L. Hecht, C. D Syme, K. Nielsen, and L. D. Barron, *J. Gen. Virol.* **83**, 241 (2002).
- [42] E. W. Blanch, L. Hecht, C. D Syme, V. Volpetti, G. P. Lomonossoff, K. Nielsen, and L. D. Barron, *J. Gen. Virol.* **83**, 2593 (2002).
- [43] F. J. Devlin, P. J. Stephens, J. R. Cheeseman, and M. J Frisch, *J. Am. Chem. Soc.* **118**, 6327 (1996).
- [44] J. Costante, L. Hecht, P. L. Polavarapu, A. Collet, and L. D. Barron, *Angew. Chem. Int. Ed.* **36**, 885 (1997).
- [45] G. S. Yu, D. Che, T. B. Freedman, and L. A. Nafie, *Tetrahedron Asymmetry* **4**, 511 (1993).
- [46] A. Rauk and T. B. Freedman, *Int. J. Quantum Chem.* **28**, 315 (1994).
- [47] G. Fráter, U. Müller, and P. Kraft, *Helv. Chim. Acta* **82**, 1656 (1999).
- [48] W. Hug and G. Hangartner, *J. Raman Spectrosc.* **30**, 841 (1999).

- [49] W. Hug, Appl. Spectrosc. **57**, 1 (2003).
- [50] BioTools Inc., Wauconda, IL, USA; URL: <http://www.btools.com/>.
- [51] Critical Link Inc., Syracuse, NY, USA; URL: <http://www.criticallink.com/>.
- [52] K. Ruud, T. Helgaker, and P. Bouř, J. Phys. Chem. A **106**, 7448 (2002), URL: <http://www.kjemi.uio.no/software/DALTON/DALTON.html>.
- [53] W. Hug and M. Fedorovsky, *submitted* (2006).
- [54] W. Hug, Chem. Phys. **264**, 53 (2001).
- [55] A. Kastler, C.R. Acad. Sci. Paris **191**, 565 (1930).
- [56] H. J. Hediger and H. H. Günthard, Helv. Chim. Acta **37**, 1125 (1954).
- [57] H. R. Wyss and H. H. Günthard, Helv. Chim. Acta **49**, 660 (1966).
- [58] L. D. Barron, M. P. Bogaard, and A. D. Buckingham, J. Am. Chem. Soc. **95**, 603 (1973).
- [59] L. D. Barron, M. P. Bogaard, and A. D. Buckingham, Nature **241**, 113 (1973).
- [60] G. Holzwarth, E. C. Hsu, H. S. Mosher, T. R. Faulkaner, and A. Moscovitz, J. Am. Chem. Soc. **96**, 251 (1974).
- [61] L.A. Nafie, J. C. Cheng, and P. J. Stephens, J. Am. Chem. Soc. **97**, 3842 (1975).
- [62] W. Hug, S. Kint, G. F. Bailey, and J. R. Scherer, J. Am. Chem. Soc. **97**, 5589 (1975).
- [63] W. Hug and H. Surbeck, Chem. Phys. Lett. **60**, 186 (1979).

- [64] W. Hug, in *Raman Spectroscopy, Linear and Non-linear*, edited by eds J. Lascomb and P. Huong (Wiley-Heyden, Chichester, 1982).
- [65] L. D. Barron, L. Hecht, W. Hug, and M. J. MacIntosh, *Chem. Phys. Lett.* **158**, 341 (1989).
- [66] L. D. Barron, L. Hecht, A. R. Gargaro, and W. Hug, *J. Raman. Spectosc.* **21**, 375 (1990).
- [67] W. Hug and H. Surbeck, *J. Raman. Spectosc.* **13**, 38 (1982).
- [68] L.A. Nafie and T. B. Freedman, *Chem. Phys. Lett.* **154**, 260 (1989).
- [69] D. Che, L. Hecht, and L.A. Nafie, *Chem. Phys. Lett.* **180**, 182 (1991).
- [70] W. Hug, in *Handbook of Vibrational Spectroscopy*, edited by J. M. Chalmers and P.R. Griffiths (John Wiley & Sons Ltd, Chichester, 2002).
- [71] W. Hug, *Appl. Spectrosc.* **35**, 115 (1981).
- [72] L. Hecht, L. D. Barron, and W. Hug, *J. Am. Chem. Soc.* **111**, 8731 (1989).
- [73] L. Hecht, L. D. Barron, A. R. Gargaro, Z. Q. Wen, and W. Hug, *J. Raman. Spectosc.* **23**, 401 (1992).
- [74] L. Hecht and L. D. Barron, *Faraday Discuss. Chem. Soc.* **99**, 35 (1994).
- [75] L. Hecht and L. D. Barron, *J. Mol. Struct.* **347**, 449 (1995).
- [76] P. W. Atkins and L. D. Barron, *Mol. Phys.* **16**, 453 (1969).
- [77] L. D. Barron and J. R. Escibano, *Chem. Phys.* **98**, 437 (1985).
- [78] K. M. Spencer, T. B. Freedman, and L.A. Nafie, *Chem. Phys. Lett.* **149**, 367 (1988).
- [79] L. Hecht and L. D. Barron, *Appl. Spectrosc.* **44**, 483 (1990).

- [80] L. Hecht and L.A. Nafie, Mol. Phys. **72**, 441 (1991).
- [81] J. F. James and R. S. Sternberg, *The Design of Optical Spectrometers* (Chapman and Hall, London, 1969).
- [82] D. Che and L. A. Nafie, Appl. Spectrosc. **47**, 544 (1993).
- [83] S. C. Barden, Opt. Phot. News **47 (2)**, 35 (1996).
- [84] H. Hecht, *Optics, fourth edition* (Addison Wesley, San Francisco, 2002).
- [85] R. Fluck, I. D. Jung, G. Zhang, F. X. Kärtner, and U. Keller, IEEE J. Quantum Electron. **2**, 435 (1996).
- [86] G. Zuber and W. Hug, J. Phys. Chem. A **108**, 2108 (2004).
- [87] L. D. Barron, A. R. Gargaro, L. Hecht, and P. L. Polavarapu, Spectrochim. Acta **47A**, 1001 (1991).
- [88] G.-S. Yu, T. B. Freedman, L. A. Nafie, Deng. Z., and P. L. Polavarapu, J. Phys. Chem. **99**, 835 (1995).
- [89] L. Hecht and L. D. Barron, Spectrochim. Acta, Part A **45**, 671 (1989).
- [90] M. Diem, P. L. Polavarapu, M. Oboodi, and L. A. Nafie, J. Am. Chem. Soc. **104**, 3329 (1982).
- [91] E. Tajkhorshid, K. J. Jalkanen, and S. Suhai, J. Phys. Chem. B **102**, 5899 (1998).
- [92] A. Szent-Györgyi, Biochem. J. **22**, 1387 (1928).
- [93] L. Pauling, *How to Live Longer and Feel Better* (W. H. Freeman, New-York, 1986).
- [94] E. S. G. Barron, R. H. DeMeio, and F. Klemperer, J. Biol. Chem. **112**, 625 (1935).

- [95] J. T. Edsall and E. L. Sagall, J. Am. Chem. Soc. **65**, 1312 (1943).
- [96] J. Hvoslef and P. Klaeboe, Acta Chem. Scand. **25**, 3043 (1971).
- [97] J. Hvoslef, Acta Cryst. **B24**, 1431 (1968).
- [98] G. L. Carlson, H. Cable, and L. G. Pedersen, Chem. Phys. Lett. **38**, 75 (1976).
- [99] M. A. Mora and F. J. Melendez, J. Mol. Struct. **454**, 175 (1998).
- [100] Juhasz. J. R., L. F. Pisterzi, D. M. Gasparro, D. R.P. Almeida, and I. G. Csizmadia, J. Mol. Struct. **666**, 401 (2003).
- [101] J. Haesler and W. Hug, *to be published* (2006).
- [102] J. Oddershede, P. Jørgensen, and D. L. Yeager, Comput. Phys. Rep. **2**, 33 (1984).
- [103] P. Jørgensen, H. J. Aa. Jensen, and J. Olsen, J. Chem. Phys. **89**, 3654 (1988).
- [104] A. D. Becke, J. Chem. Phys. **98**, 5648 (1993).
- [105] C. Lee, W. Yang, and R. G. Parr, Phys. Rev. B **37**, 785 (1988).
- [106] R. Krishnan, J. S. Binkley, R. Seeger, and J. A. Pople, J. Chem. Phys. **72**, 650 (1980).
- [107] O. Quinet and B. Champagne, J. Chem. Phys. **115**, 6293 (2001).
- [108] O. Quinet, V. Liégeois, and B. Champagne, J. Chem. Theor. Comput. **1**, 444 (2005).
- [109] GAMESS, General Atomic and Molecular Electronic Structure System, see <http://www.msg.ameslab.gov/GAMESS/GAMESS.html>.

- [110] DALTON, a molecular electronic structure program, Release 1.1 (2000); see <http://www.kjemi.uio.no/software/DALTON/DALTON.html>.
- [111] MATLAB version 7.0.4.365, Release 14 SP2 (2005), The Mathworks Inc., Natick, CA, USA; see <http://www.mathworks.com/>.
- [112] G. Zuber, Ph.D. thesis, University of Fribourg, Switzerland, 2004.
- [113] J. W. Ochterski, Vibrational Analysis in Gaussian, in *Technical Support*, 1999; see http://www.gaussian.com/g_whitepap/vib.htm.
- [114] E. B. Wilson, J. C. Decius, and P. C. Cross, *Molecular Vibrations* (Dover, New York, 1955).
- [115] P. F. Flükiger, Ph.D. thesis, University of Geneva, Switzerland, 1992.
- [116] MOLEKEL, advanced interactive 3D-molecular graphics, Version 4.3 (2002); see <http://www.cscs.ch/molekel/>.
- [117] P. Schaftenaar and J. H. Noordik, *J. Comput.-Aided Mol. Design* **14**, 123 (2000).
- [118] MOLDEN, a pre- and post processing program of molecular and electronic structure, Version 4.4 (2005); see <http://www.cmbi.ru.nl/molden/molden.html>.
- [119] W. Hug and J. Haesler, *Int. J. Quantum Chem.* **104**(5), 695 (2005).
- [120] A. de Meijere, A. F. Khlebnikov, S. I. Kozhushkov, R. R. Kostikov, P. R. Schreiner, A. Wittkopp, C. Rinderspracher, D. S. Yufit, and J. A. K. Howard, *Chem. - Eur. J.* **8**, 828 (2002).
- [121] W. Hug and G. Zuber, *Helv. Chim. Acta* **84**, 1 (2001).
- [122] M. Reiher, V. Liégeois, and K. Ruud, *J. Phys. Chem. A* **109**, 7567 (2005).

- [123] M. Bounouar, Diploma work, University of Fribourg, Switzerland, 2002.
- [124] L.A. Nafie, J. Chem. Phys. **79**, 4950 (1983).
- [125] L.A. Nafie, J. Chem. Phys. **96**, 5687 (1992).
- [126] P. J., Cheeseman, M. J Frisch, F. J. Devlin, and P. J. Stephens, J. Chem. Phys. Lett. **252**, 211 (1996).
- [127] F. J. Devlin, P. J. Stephens, P. J., Cheeseman, and M. J Frisch, J. Phys. Chem. **101**, 6322 (1997).
- [128] F. J. Devlin, P. J. Stephens, P. J., Cheeseman, and M. J Frisch, J. Phys. Chem. **101**, 9912 (1997).
- [129] S. Weiss and G. E. Leroi, Spectrochim. Acta A **25**, 1759 (1969).
- [130] J. R. Durig, S. M. Craven, and J. Bragin, J. Chem. Phys. **52**, 2046 (1970).
- [131] K. S. Pitzer and J. E. Kilpatrick, Chem. Rev. **39**, 435 (1946).
- [132] J. P. A. Heuts, R. G. Gilbert, and L. Radom, J. Phys. Chem. **100**, 18997 (1996).
- [133] N. G. Mirkin and S. Krimm, J. Mol. Struct. **550-551**, 67 (2000).
- [134] M. Fedorovsky, PyVib2, a Program for Analysing Vibrational Motion and Vibrational Spectra, *unpublished work*.
- [135] S. Sportouch, C. Lacoste, and R. Gaufrès, J. Mol. Struct. **9**, 119 (1971).
- [136] D. H. Rank and E. R. Bordner, J. Chem. Phys. **3**, 248 (1935).
- [137] L. Zarkova, P. Pirgov, U. Hohm, A. Chrissanthopoulos, and B. B. Stefanov, Int. J. Thermophys. **21(6)**, 1439 (2000).

- [138] E. R. Shull, T. S. Oakwood, and D. H. Rank, J. Chem. Phys. **21**, 2024 (1953).
- [139] R. G. Snyder, Vijnana Parishad Anusandhan Patrika **14**, 139 (1953).
- [140] M. A. Spackman, Chem. Rev. **92**, 1769 (1992).

List of Abbreviations

| | |
|------|-----------------------------------------|
| AAT | : Atomic axial tensor |
| ACP | : Atomic contribution pattern |
| ADC | : Analogue to digital converter |
| AOVR | : Activité optique vibrationnelle Raman |
| APT | : Atomic polar tensor |
| CC | : Circularity converter |
| CCD | : Charge coupled device |
| CD | : Circular dichroism |
| CID | : Circular intensity difference |
| CIS | : Circular intensity sum |
| DCP | : Dual circular polarisation |
| DFT | : Density functional theory |
| DSP | : Digital signal processor |
| FPGA | : Field-programmable gate array |
| FWHM | : Full width at half maximum |
| GCM | : Group coupling matrice |
| GUI | : Graphical user interface |
| HF | : Hartree-Fock |
| ICP | : Incident circular polarisation |
| IR | : Infrared |
| LCR | : Liquid crystal retarder |
| LR | : Linear rotator |
| NM | : Nuclear motion |
| ORD | : Optical rotatory dispersion |
| ROA | : Raman optical activity |
| SCP | : Scattered circular polarisation |
| SHG | : Second harmonic generation |
| TB | : Timing block |
| TEM | : Transverse electric and magnetic mode |
| TU | : Timing unit |
| VCD | : Vibrational circular dichroism |
| VED | : Vibrational energy distribution |
| VOA | : Vibrational optical activity |
| VPH | : Volume phase holographic |

Curriculum Vitae

JACQUES HAESLER

Rte de Villars 119
1752 Villars-sur-Glâne - FR
Switzerland

Age: 28 (1977)

☎ +41 (0)79 502 76 47

☎ +41 (0)26 401 04 89

✉ Jacques.Haesler@Unifr.ch

@ Highlights of qualifications

- Extensive experience in specific spectroscopies (Raman, ROA, VCD).
- Extensive knowledge in Graphical User Interfacing (GUI) with Matlab.
- Good experience in high-level theoretical calculations and molecular modeling.
- Mother tongue: French; Good skills in English and (Swiss-)German.

@ Education

- **Ph.D. - Physical Chemistry** March 2006
University of Fribourg, Department of Chemistry, Switzerland.
- **M.Sc. - Physical & Inorganic Chemistry** March 2002
University of Fribourg, Department of Chemistry, Switzerland.
(→ Ciba Spécialité Chimique Award)
- **Federal Maturity Certificate (Type C, Scientific)** June 1997
Collège Sainte-Croix, Fribourg, Switzerland.

@ Experience

2002 - pres. **Department of Chemistry, University of Fribourg**

Research Assistant:

- Construction of a new Raman Optical Activity (ROA) spectrometer.

Student Assistant:

- Two years inorganic chemistry lab assistancy for biochemistry students.
- Development of a new Raman spectrometer for master students.

2000 - 2001 **Collège Ste-Croix**

Teacher: Chemistry teacher for students in the second and third year.

@ Informatic skills

- **Languages:** Matlab, Python, C++, HTML, SQL, PHP, \LaTeX 2 ϵ .
- **Operating Systems:** Windows 98/2000/XP, Linux, Unix.
- **Applications:** Matlab, Borland C++ Builder, LabView, Origin, Dreamweaver, Flash, MySQL.

@ Publications/Talks

- “Raman and Raman Optical Activity Spectra of Neopentane-d₀, -d₆ and -d₁₂”, manuscript in preparation.
- “Raman Optical Activity in Forward Scattering: Reduced Influence of Solvents.”, J. Haesler and W. Hug, manuscript in preparation.
- “Analysis of the VROA Signals of Helical Heptasilanes using an Atomistic Approach”, V. Liegois, O. Quinet, B. Champagne, J. Haesler, G. Zuber, W. Hug, *Vib. Spectrosc.*, in press.
- “Is the Vibrational Optical Activity of (R)-[²H₁, ²H₂, ²H₃]-Neopentane Measurable?”, W. Hug, J. Haesler, *Int. J. Quantum Chem.* **2005**, 104, 695.
- “Graphical Tools for the Analysis of Vibrational Spectra”, J. Haesler, M. Zerara, COST D26 Working Group 0010-02, April 2005, Pisa.

@ Miscellaneous

- **Interests:** sport, nutritional aspects, physiology, biomechanics, informatics, web design.
- **Activities:** sports in general (running, rollerblade, bicycle, MTB, ...).
- **Workshop:** “What a young entrepreneur should know”, IVEInstitute, Fribourg (2005).